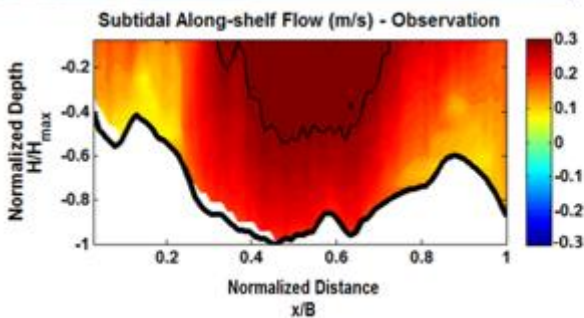# Ecological Function and Recovery of Biological Communities within Dredged Ridge-Swale Habitats in the South-Atlantic Bight

Volume 1: Final Report on the Physical Environments of the Sand Shoals

U.S. Department of the Interior
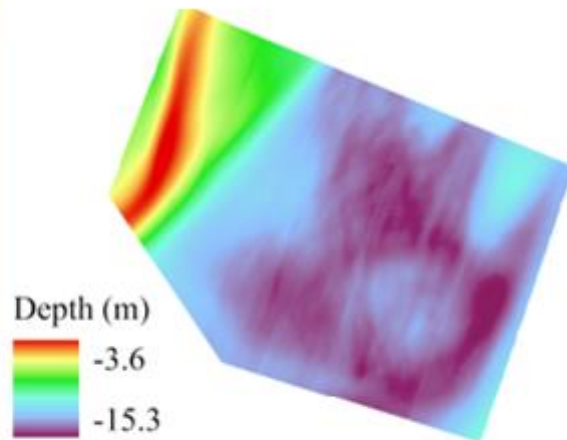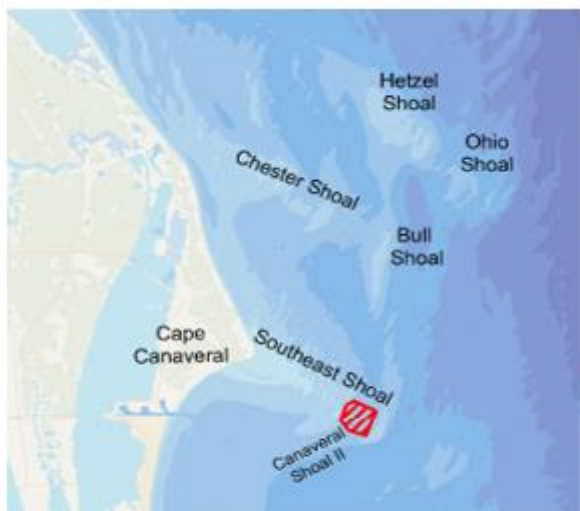**Bureau of Ocean Energy Management**
Sterling, VA

Ecological Function and Recovery of Biological Communities within Dredged Ridge-Swale Habitats in the South-Atlantic Bight

Volume 1: Final Report on the Physical Environments of the Sand Shoals

March 2024

Editors:
Debra Murie[1]
Jennifer Bucatari[2]
Deena Hansen[2]

**U.S. Department of the Interior
Bureau of Ocean Energy Management
Sterling, VA**

DISCLAIMER

REPORT AVAILABILITY

Download a PDF file of this report at https://espis.boem.gov/Final%20Reports/BOEM_2024-016.pdf. To search other studies completed by BOEM's Environmental Studies Program, visit https://www.boem.gov/environment/environmental-studies/environmental-studies-information/.

CITATION

Murie D, Bucatari J, Hansen D, editors. 2024. Ecological function and recovery of biological communities within dredged ridge-swale habitats in the South-Atlantic Bight: volume 1. Final report on the physical environments of the sand shoals. Sterling (VA): U.S. Department of the Interior, Bureau of Ocean Energy Management. 168 p. Report No.: OCS Study BOEM 2024-016. Contract No.: M13AC00012.

Chapter Citations:

Murie D, Smith, G, Jr. 2024. Chapter 1: general introduction. In: Murie D, Bucatari J, Hansen D, editors. Ecological function and recovery of biological communities within dredged ridge-swale habitats in the South-Atlantic Bight. Volume 1: final report on the physical environments of the sand shoals. Sterling (VA): U.S. Department of the Interior, Bureau of Ocean Energy Management. Report No.: OCS Study BOEM 2024-016. Contract No.: M13AC00012. p. 1–11.

Valle-Levinson A, Adams P, Paniagua-Arroyave JF, Parra S, Yousif A, So S. 2024. Chapter 2: physical oceanography surveys. In: Murie D, Bucatari J, Hansen D, editors. Ecological function and recovery of biological communities within dredged ridge-swale habitats in the South-Atlantic Bight. Volume 1: final report on the physical environments of the sand shoals. Sterling (VA): U.S. Department of the Interior, Bureau of Ocean Energy Management. Report No.: OCS Study BOEM 2024-016. Contract No.: M13AC00012. p. 12–100.

Espriella M, Lecours V, Murie D. 2024. Chapter 3: comparative changes in post-dredge shoal bathymetry and terrain morphology using multibeam echosounder surveys. In: Murie D, Bucatari J, Hansen D, editors. Ecological function and recovery of biological communities within dredged ridge-swale habitats in the South-Atlantic Bight. Volume 1: final report on the physical environments of the sand shoals. Sterling (VA): U.S. Department of the Interior, Bureau of Ocean Energy Management. Report No.: OCS Study BOEM 2024-016. Contract No.: M13AC00012. p. 101–116.

Murie D, Smith G, Jr. 2024. Chapter 4: habitat classification of the shoals and surrounding area based on direct sampling using sediment grabs. In: Murie D, Bucatari J, Hansen D, editors. Ecological

function and recovery of biological communities within dredged ridge-swale habitats in the South-Atlantic Bight. Volume 1: final report on the physical environments of the sand shoals. Sterling (VA): U.S. Department of the Interior, Bureau of Ocean Energy Management. Report No.: OCS Study BOEM 2024-016. Contract No.: M13AC00012. p. 117–135.

Dickson M, Murie D. 2024. Chapter 5: using satellite imagery to assess large-scale variation in phytoplankton productivity relative to a sand dredging event. In: Murie D, Bucatari J, Hansen D, editors. Ecological function and recovery of biological communities within dredged ridge-swale habitats in the South-Atlantic Bight. Volume 1: final report on the physical environments of the sand shoals. Sterling (VA): U.S. Department of the Interior, Bureau of Ocean Energy Management. Report No.: OCS Study BOEM 2024-016. Contract No.: M13AC00012. p. 136–143.

ABOUT THE COVER

Shoals off the coast of Cape Canaveral on the east coast of Florida, original courtesy of J. Iafrate (Naval Undersea Warfare Center [NUWC] Newport) and J. Greene (McLaughlin Research Corporation [MRC]); changes in bathymetry with dredging (V. Lecours and M. Espriella); profile of along-shelf flow (Arnoldo Valle-Levinson), and sediment types found on shoals (D. Murie).

ACKNOWLEDGMENTS

Contents (Volume 1)

List of Figures

List of Tables

List of Abbreviations and Acronyms

ADCP   Acoustic Doppler Current Profiler
ArcGIS   Aeronautical Reconnaissance Coverage Geographic Information System
AWAC   Acoustic Wave and Current
BACI   Before-After-Control-Impact
BOEM   Bureau of Ocean Energy Management
CCEOF   Concatenated Complex Empirical Orthogonal Function
CHEOF   Concatenated Hilbert Empirical Orthogonal Function
CMECS   Coastal and Marine Ecological Classification Standard
CREOF   Concatenated Real-vector Empirical Orthogonal Function
CSII   Canaveral Shoal II
CSII-BA   Canaveral Shoal II Borrow Area
CTD   Conductivity-Temperature-Depth
DOI   U.S. Department of the Interior
EFH   essential fish habitat
ESRI   Environmental Systems Research Institute
FGDC   Federal Geographic Data Committee
FRRG   Florida Research and Recovery Group
GIS   geographic information systems
GMT   Greenwich Mean Time
GOF   Goodness of Fit
GPS   Global Positioning System
HAPC   Habitat Area of Particular Concern
IDW   inverse distance weighted
LGW   long gravity wave
MLLW   Mean Low-Low Water
MODIS   Moderate Resolution Imaging Spectrometer
NDBC   National Data Buoy Center
NE   northeast
NGDC   National Geophysical Data Center
NOAA   National Oceanic and Atmospheric Administration
NW   northwest
RMSE   root mean square error
RTK   real-time kinematic
SAB   South-Atlantic Bight
SE   southeast
SEAWIFS   Sea-viewing Wide Field-of-view Sensor
SGW   short gravity wave
SW   southwest

1 General Introduction

Debra Murie and Geoffrey Smith, Jr.

> **Key Points**
> - This study monitored sand shoals off the east coast of Florida for impacts of dredging on biological communities from fall 2013 through summer 2019.
> - The overall goal was to understand the potential impacts of dredging on the dynamics of species abundance, biomass, and assemblages of phytoplankton, zooplankton, meroplankton, benthic and demersal invertebrates, and fishes.
> - Study spanned both the physical environment (oceanography, sediments) and biological communities, including shoal use by demersal fishes as determined through acoustic telemetry.
> - Impacts were assessed using a Beyond-BACI (before-after-control-impact) design, including an impact (dredge) site (CSII-BA), multiple control (reference) sites (CSII, Chester, and Bull Shoals), and temporal sampling before and after the dredging events.
> - Trophic pathways were assessed using isotope analysis, and impact of dredging on shoal ecosystems was modelled using Ecopath, an ecosystem-level model based on trophic-level biomasses.

Coastal and offshore marine habitats provide a multitude of ecosystem services that may not be directly visible to the public due to their underwater venue. Shoals consist of submerged ridges covered by sand or other unconsolidated material and the surrounding deeper relatively flat-bottomed areas, troughs, or swales (i.e., ridge-swale shoals) (Rutecki et al. 2014). They are coastal features that occur along the US Atlantic seaboard and exemplified off Florida's east coast (Figure 1-1).

These ecosystems have not been studied extensively other than in connection with dredging for coastal renourishment. They are typically rich in sand particle sizes required for beach renourishment and can occur in relatively shallow waters close to shore that allow for dredge operations. However, shoals also provide essential fish habitat (EFH) for commercial and recreational fisheries species (fishes and invertebrates), as well as threatened species or species of concern (Pickens et al. 2020). EFH serves as "those waters and substrate necessary to fish for spawning, breeding, feeding or growth to maturity," including nursery areas and migratory connections. EFH of the shoal ecosystems includes soft bottom, any hard bottom present, and the overlying water column, which together support demersal, pelagic, and migratory species. In addition, the east-central coast of Florida is designated as a Habitat Area of Particular Concern (HAPC) for Lemon Sharks, *Negaprion brevirostris,* where juveniles are known to aggregate in shallow nearshore habitat off Cape Canaveral (Reyier et al. 2008).

Previous studies have provided descriptions of species composition, abundance, and diversity of similar shoal complexes (see review by Pickens et al. 2020) but not directly in relation to contemporaneous dredging activities. Although they provide a wealth of information that can be used in monitoring impacts of dredging on these same systems, the studies have not addressed the biological functioning of these ecosystems. To do this, all trophic components (i.e., pelagic and benthic primary producers, benthic consumers, piscivores, etc.) need to be assessed at an assemblage level, as well as integrated into an ecosystem-level analysis, as is done in this study. These types of analyses link both the qualitative and quantitative trophic components of the food web, allowing for both visualization and quantification of any ecosystem-level changes potentially due to dredging activities.

1.1 Potential Sand Dredging Impacts

Sand dredging is usually perceived as having a negative impact to biological communities in the area of, or near, the dredging activities, as reviewed by Michel et al. (2013), Wenger et al. (2016), and Pickens et al. (2020). Direct negative impacts may be from physical removal of small fishes and invertebrates due to the suction of the dredge or physical removal and reshaping of the bottom habitat due to the removal of the upper layers of sand (Palmer et al. 2008). However, dredging may also have indirect impacts that can be negative. For example, increased turbidity associated with dredging can decrease light availability and hence growth of phytoplankton, which in turn decreases the abundance of zooplankton that is a primary prey resource for secondary consumers, such as larval and juvenile fishes. Turbidity can also indirectly affect juvenile and adult fish (Wenger et al. 2016), most probably through decreased foraging due to decreased visibility for sight predators (Utne-Palm 2002). Fish movements and fidelity to the shoals may also be impacted due to the physical disturbance and underwater sound production associated with dredging (Pickens et al. 2020). Indirect effects, in particular, can cascade up or down trophic levels and result in changes in species assemblages.

While most would expect negative impacts on species abundance, biomass, and assemblages due to dredging activities, there are some studies that indicate positive aspects of sand dredging. These positive scenarios include creating a bottom habitat that is more rugose and complex, and hence facilitates recruitment of invertebrates in particular (Michel et al. 2013). In addition, it has been proposed that physical disruption of the bottom, for example by bottom trawling while fishing, can resuspend nutrients in the substrate (Pilskaln et al. 1998) and make them available to a wide assortment of invertebrates, which in turn increase in abundance and provide a greater food base for fishes (Riemann and Hoffmann 1991); a similar rationale could be proposed for dredging.

1.2 Recovery from Potential Dredging Impacts

Potential impacts to biological assemblages due to dredging activities are typically associated with a recovery timeline that can be modeled relative to recovery of the assemblages observed prior to the dredging event(s) and present on control/reference (non-dredged) shoals. *Recovery* in this sense refers to assemblages returning to their former state, as indicated by the presence/return of specific organisms or species assemblages (Michel et al. 2013). This was the primary definition used throughout the current study, where impacts and recovery were assessed using changes to species assemblages.

Alternatively, however, the timeline can also be modeled relative to the recovery to biological communities that are ecologically equivalent but not identical (i.e., a microcarnivorous amphipod species is replaced with an "equivalent" but different species of microcarnivorous amphipod or other organism that serves the same function) (Michel et al. 2013).Thus, *recovery* in this sense is provided by different species with equivalent ecological trophic value. The former recovery model emphasizes preservation of the ecosystem (i.e., if the assemblages are not identical after dredging as before dredging, then the ecosystem has been negatively impacted or "damaged") versus the latter recovery model that emphasizes conservation of the ecosystem services (i.e., change is allowed as long as the ecosystem recovers equivalent biological functions).

This latter definition of recovery was used in the final integrated modeling of the study to assess the ecosystem-level changes due to dredging based on trophic-level biomasses. These two scenarios may be valued differently by various groups in our society. Dredging sand from offshore shoals and transferring it onshore to build up eroded beach habitat could protect critical infrastructure and personal property due to beach erosion from storms (such as with Hurricane Sandy), could stabilize beaches for eco-tourism and allows coastal communities to regain financial stability, and could stabilize beaches to permit nesting of threatened and endangered sea turtles. It is therefore important to fully understand the ecological function

of these shoals since offshore dredging for sand reserves most likely will continue as a necessity with coastline development, as well as coastline erosion and burgeoning storm seasons associated with climate change.

1.3 Study Framework

Our framework for understanding potential assemblage-level and ecosystem-level functional changes associated with dredging shoals off the east coast of Florida was based on using a Beyond-BACI design, including multiple control (reference) sites, an impact (dredge) site, and temporal sampling before and after the dredging events. Impact of dredging on biological communities was assessed by examining any potential changes in species abundance, biomass, and assemblages for all major trophic levels. These trophic levels included the primary producers and continued up through the food web to secondary and tertiary consumers, many of which are commercial and recreational invertebrate and fish species. The collective biomass at each trophic level was then integrated into ecosystem-level models to assess ecosystem function over time in relation to dredging events. Variation in trophic-level dynamics can have consequences to the functioning of the ecosystem because the number and biomass of producers and consumers at different trophic levels can change annually, seasonally, and diurnally (day/night) based on spatial and temporal parameters associated with both the biological and physical environment. The dynamic aspects of the physical environment of the shoals were examined through oceanographic assessment of forcing factors such as currents, tides, and bathymetry. Direct dredging impacts to the bathymetry and substate of the shoals were estimated using hydroacoustic surveys, whereas direct sampling of the substrate was used for classifying benthic habitat that could be related to fish distribution and movement using acoustic telemetry.

1.4 Goals and Objectives

Our overall goal was to understand the potential impacts of dredging on the dynamics of species abundance, biomass, and assemblages on offshore sand shoals. To accomplish this goal, this study spanned both the physical environment and the biological communities of the sand shoals. Our specific objectives were the following:

1) Characterize the coastal oceanography and environments of the sand shoals to understand the physical forcing factors;
2) Compare the bathymetry and substrate features of the shoals before and after dredging events;
3) Characterize the benthic habitat available on the shoals and surrounding area;
4) Determine the temporal variability of species assemblages (phytoplankton, zooplankton, meroplankton, benthic and demersal invertebrates, and demersal fishes) on an annual, seasonal, and diurnal basis;
5) Examine the spatial variability of these species assemblages among the shoals and between ridge and swale habitats of the shoals;
6) On a spatiotemporal basis, compare species abundance, biomass, and assemblages of the dredged shoal (CSII-BA) relative to multiple "control/reference" (non-dredged) shoals (CSII, Chester, and Bull Shoals);
7) Determine the temporal sequence of recovery of biological assemblages in the dredged area relative to the biological assemblages of the reference shoals using pre-dredge versus post-dredge comparisons;
8) Examine spatial use of key fishes associated with the shoals, site fidelity, and movement between dredged and non-dredged shoals; and
9) Discern functional, ecosystem-level services that are potentially compromised by dredging and determine the degree of potential impact, relative to the ecosystem services of reference shoals.

1.5 Study Area and Timeline

The study area was located off the east coast of Cape Canaveral, Florida, and consisted of three shoals: 1) Canaveral Shoal II (referred to as CSII); 2) Chester Shoal; and 3) Bull Shoal (Figure 1-1). Canaveral Shoal II (CSII) referenced here is one specific shoal within the Southeastern Shoal complex emanating from Cape Canaveral (Figure 1-1). The northeastern portion of CSII has a federally designated sand "borrow area," which is a permitted location consisting of beach quality sand where "sand dredging" may occur; this portion of the shoal was referred to as CSII-Borrow Area (CSII-BA) throughout the report. Chester Shoal in this study is one shoal within the Chester Shoal complex, previously identified as Shoal D in Field and Duane (1974). The non-dredged portion of CSII, as well as Chester and Bull Shoals, were all used as control or reference (non-dredged) shoals relative to CSII-BA, which has been periodically dredged since 2000 (Table 1-1).

1.5.1 Overall Sampling Design

Various components of this study (Chapters 2–17) make references to locational aspects of CSII, CSII-BA, Bull, and Chester Shoals (e.g., the northwestern swale of Bull). For clarity, the overall sampling design is outlined here with further specific aspects provided in each of the following chapters as appropriate.

Each study shoal was subdivided into ridge and swale habitats based on common criteria. For each shoal, the ridge region was defined as the area of the shoal with water depth ≤ 10 m and a slope ≤ 1.14% grade. The edge region of the shoal was characterized as the transitional zone between ridge and swale, and was defined as areas in < 10 m water depth with a gradient of > 1.14% and areas > 10 m with a gradient > 0.5%. This transition zone between the ridge and the swale was treated as a buffer zone in sampling site selections so that the two habitats could be sampled distinctly. The swale region was designated as relatively flat areas in < 18 m of water that excluded the transitional zone (edge and sides of the shoal) and extended 1 km from the outer edge of the transitional zone. Sampling occurred within the ridge and swale areas to delineate the two primary habitats associated with shoals. We characterized ridge and swale areas using ArcGIS and bathymetric charts.

We further divided each shoal (ridge and swale) into quadrants (NW, NE, SW, SE) to ensure adequate spatial coverage using a stratified-random sampling design. To do this, the ridge was divided down its spine, bisecting the west and east swale quadrants, and then divided again perpendicular to its spine, bisecting the north and south swale quadrants (Figure 1-2). The northwest quadrant of CSII was not sampled because it had very shallow water that was not accessible to a trawl vessel nor comparable to any other swale areas on any of the shoals. This sampling effort was therefore redirected towards increased sampling in CSII-BA, which was necessary because at the outset of the study the exact location of dredging within CSII-BA was unknown (i.e., sand dredging is permitted anywhere within the borrow area). To ensure that our pre-dredge sampling was done in all potential dredge areas of the borrow area, the northeast swale of CSII-BA was subdivided to form two swale sampling strata (NE1 swale and NE2 swale) (Figure 1-2). Sampling stations initially slated for the NW quadrant were therefore reallocated to the NE2 quadrant.

Temporal sampling included annual, seasonal, and diel periods. Annual sampling occurred for 6 years from November 2013 to July 2019. Seasonal sampling occurred in spring (March–May), summer (June–September), fall (October–November), and winter (December to the following February). Diurnal sampling occurred anytime between an hour after sunrise to an hour before sunset, whereas nocturnal sampling occurred between approximately an hour after sunset to an hour before sunrise (i.e., excluded periods of civil twilight).

1.5.2 Timeline of Study and Dredging and Storm Events

This study was initiated in fall 2013 and continued through summer 2019. Originally, this study was to assess the impact on biological assemblages from a dredging event that was to take place on CSII-BA in November 2013 through April 2014 (Dredge-1) (Table 1-1). However, CSII-BA was dredged a second time during this study during spring 2018 (Dredge-2). Although not an original component of the study, this second dredging event allowed for a more extensive suite of pre-dredge samples to be compared to post-dredge samples for all shoals; therefore, all the biological components of the study strived to take full advantage of this addition to the study.

In addition to potential impacts due to dredging, the area off the east coast of Florida is susceptible to intense hurricane and storm activity that could also impact biological communities, especially plankton due to the large-scale movement of water. These storm events were especially prevalent during the summer and fall during the study (Table 1-3). Storm-driven changes in biological communities therefore also were discussed when relevant.

1.6 Structure of the Report

To address the overall goal and objectives, the following volumes and chapters step through the project components:

Volume 1: Physical Environments of the Sand Shoals

- Chapter 2 details the coastal oceanography of the shoals offshore of Cape Canaveral.
- Chapter 3 describes the bathymetry and habitat complexities of the shoals based on multibeam hydroacoustic surveys.
- Chapter 4 classifies the habitat over the shoals and surrounding coastal area.
- Chapter 5 uses satellite imagery to assess large-scale phytoplankton productivity relative to the first dredging event in 2013.

Volume 2: Primary Producers and Invertebrates of the Sand Shoals

- Chapter 6 details the water quality and water chemistry associated with the shoals.
- Chapter 7 examines shoal-associated phytoplankton and bacterioplankton.
- Chapter 8 examines shoal-associated microphytobenthos (benthic microalgae).
- Chapter 9 examines shoal-associated zooplankton.
- Chapter 10 examines shoal-associated meroplankton.
- Chapter 11 examines benthic infaunal and epifaunal invertebrates from the shoals.
- Chapter 12 examines demersal invertebrates associated with the shoals.

Volume 3: Fishes and Ecosystems of the Sand Shoals

- Chapter 13 examines fish assemblages associated with the shoals.
- Chapter 14 describes movement and shoal use by fish via acoustic telemetry.
- Chapter 15 examines the isotopic niches of focal invertebrate and fish species associated with the shoals.
- Chapter 16 uses Ecopath modeling on trophic biomasses to determine ecosystem-level affects.
- Chapter 17 provides an overall summative integration of the impact of dredging on biological communities of the sand shoals.

1.7 References

BOEM (Bureau of Ocean Energy Management). 2013. Issuance of a negotiated agreement for use of outer continental shelf sand from Canaveral Shoals II in the Brevard County Shore Protection Project (SPP) North Reach and South Reach: Environmental Assessment. Herndon, VA: U.S. Department of the Interior, Bureau of Ocean Energy Management BOEM 2013-01151: 1-762.

Field M, Duane D. 1974. Geomorphology and sediments of the inner continental shelf, Cape Canaveral, Florida. Fort Belvoir, Virginia: U.S. Army, Corps of Engineers, Coastal Engineering Research Center. Technical Memorandum 42.

Michel J, Bejarano A, Peterson C, Voss C. 2013. Review of biological and biophysical impacts from dredging and handling of offshore sand. Herndon, VA: U.S. Department of the Interior, Bureau of Ocean Energy Management. OCS Study BOEM 2013-0119. 258 pp.

Palmer TA, Montagna PA, Nairn RB. 2008. The effects of a dredge excavation pit on benthic macrofauna in offshore Louisiana. Environmental Management 41(4): 573-583. doi:10.1007/s00267-007-9063-5.

Pickens B, Taylor J, Hansen D. 2020. Volume 1: Fish Habitat Associations and the Potential Effects of Dredging on Fish of the Atlantic and Gulf of Mexico Outer Continental Shelf, Literature Synthesis and Gap Analysis. Sterling, VA: US Department of the Interior, Bureau of Ocean Energy Management, OCS Study BOEM 2020-002 and NOAA NCCOS Technical Memorandum 270. 122 p.

Pilskaln C, Churchill J, Mayer L. 1998. Resuspension of sediment by bottom trawling in the Gulf of Maine and potential geochemical consequences. Conservation Biology 12(6): 1223-1229.

Reyier E, Adams D, Lowers R. 2008. First evidence of a high density nursery ground for the lemon shark, Negaprion brevirostris, near Cape Canaveral, Florida. Florida Scientist 71: 134-148.

Riemann B, Hoffmann E. 1991. Ecological consequences of dredging and bottom trawling in the Limfjord, Denmark. Marine Ecology Progress Series 69: 171-178.

Rutecki D, Dellapenna T, Nestler E, Scharf F, Rooker J, Glass C, Pembroke A. 2014. Understanding the Habitat Value and Function of Shoals and Shoal Complexes to Fish and Fisheries on the Atlantic and Gulf of Mexico Outer Continental Shelf. Literature Synthesis and Gap Analysis. Prepared for the U.S. Dept. of the Interior, Bureau of Ocean Energy Management. Contract # M12PS00009. BOEM 2015-012: 176 p.

Utne-Palm A. 2002. Visual feeding of fish in a turbid environment: physical and behavioral aspects. Marine and Freshwater Behaviour and Physiology 35: 111-128.

Wenger A, Harvey E, Wilson S, Rawson C, Newman S, Clarke D, Saunders B, Browne N, Travers M, Mcilwain J. 2016. A critical analysis of the direct effects of dredging on fish. Fish and Fisheries 2017: 1-19. doi:10.1111/faf.12218.
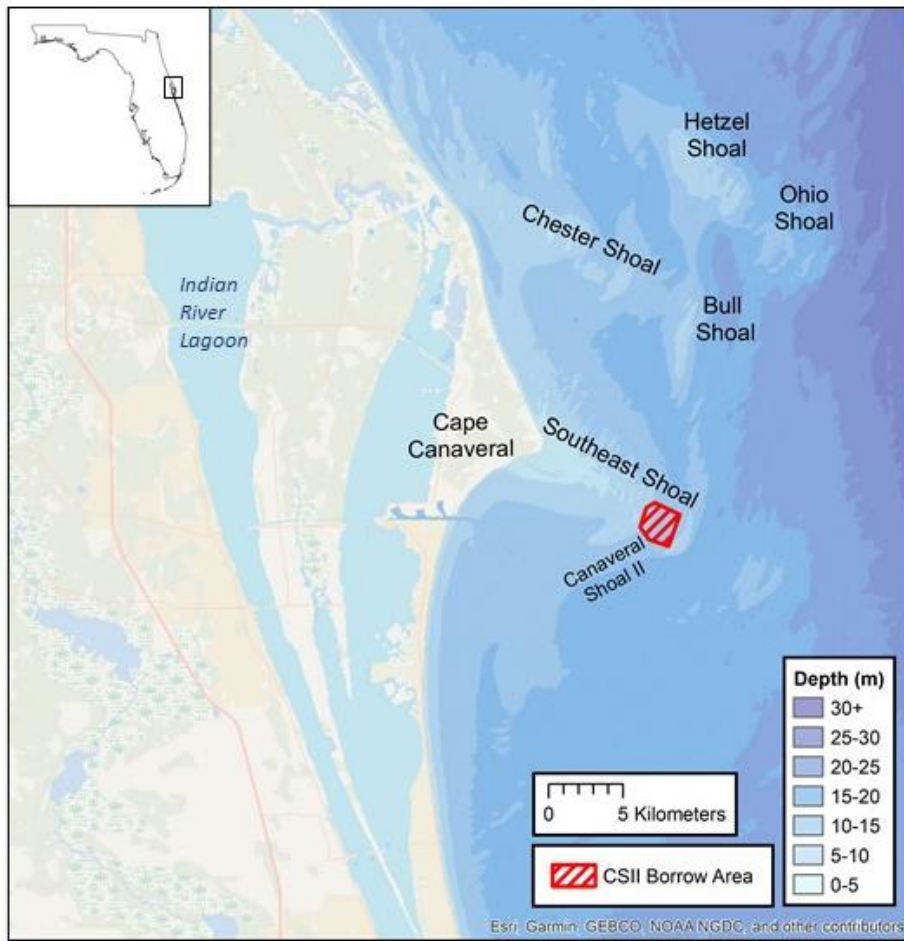
Figure 1-1. Shoals off the coast of Cape Canaveral, Florida, USA

Canaveral Shoal II (CSII) is one specific shoal in the Southeast Shoal complex off of Cape Canaveral, with the CSII Borrow Area outlined in red. Base map courtesy of J. Iafrate, Naval Undersea Warfare Center (NUWC) Newport, and J. Greene, McLaughlin Research Corporation (MRC).
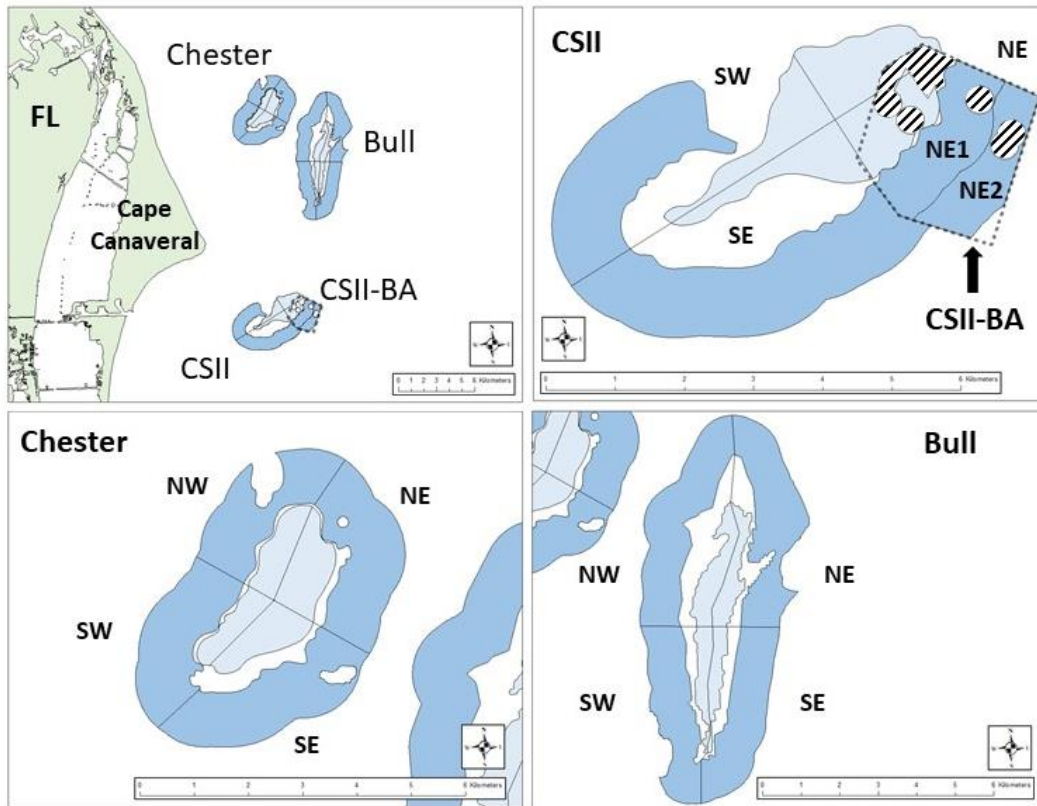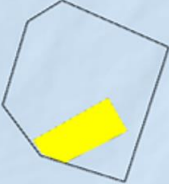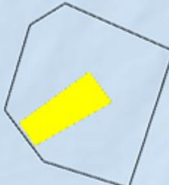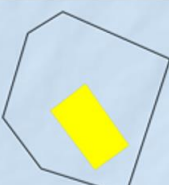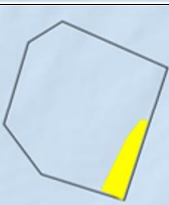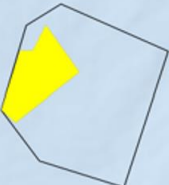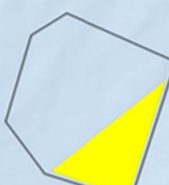
Figure 1-2. East coast of Florida showing the location of the three shoals of the study, along with detailed aspects of each shoal, including Canaveral Shoal II (CSII) with the borrow area (CSII-BA), Bull Shoal, and Chester Shoal

Ridge habitat (light blue) and swale habitat (dark blue) is shown for each shoal, which were further subdivided into quadrants (NW, NE, SW, SE) for stratified-random sampling except CSII, which only had two quadrants (SW and SE), and CSII-BA, which had one quadrant (NE). The swale of CSII-BA was further subdivided into NE1 and NE2 prior to any sampling to ensure that pre- and post-dredge sampling physically occurred in areas of CSII-BA that were dredged during the study period. Hatched areas in CSII-BA represent exclusion areas (i.e., not open to dredging or sampling) that contain National Aeronautics and Space Administration rocket cylinders (BOEM 2013).

Table 1-1. Dredging history of Canaveral Shoals II borrow area (CSII-BA) showing area dredged during each event, start and end of dredging, volume dredged, and project identification (ID) and lease number.

The area of CSII-BA is outlined in black with the footprint of each dredging event in yellow. Data obtained from BOEM Mineral Management Information System (MMIS) (https://mmis.doi.gov/boemmmis/). See site for more details and caveats on dredged volume reported.

Dredged Footprint (yellow area)	Construction Start Date	Construction Complete Date	Dredge Volume Reported (cubic yd)	Project ID and Lease Number
	1 Oct 2000	8 Apr 2001	4,800,000	Brevard County 2000 OCS-A-0454
	10 Dec 2000	16 Apr 2001	590,000	Patrick Air Force Base 2001 OCS-FL-2000
	1 Jan 2002	15 Apr 2002	50,000	Brevard County 2000 OCS-A-0454
	28 Mar 2003	1 May 2003	384,080	Brevard County 2000 OCS-A-0454
	3 Mar 2005	18 Mar 2005	321.500	Patrick Air Force Base 2005 OCS-FL-2005
	20 Mar 2005	14 May 2005	1,333,510	Brevard County 2005 OCS-A-0461
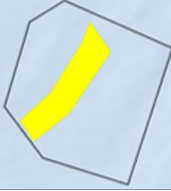
Dredged Footprint (yellow area)	Construction Start Date	Construction Complete Date	Dredge Volume Reported (cubic yd)	Project ID and Lease Number
	13 Feb 2010	17 Apr 2010	630,300	Brevard County 2009 OCS-A-00476
	27 Nov 2013	22 Apr 2014	1,724,476	Brevard County 2013 OCS-A-0493
	3 Feb 2018	11 Apr 2018	932,700	Brevard County 2018 OCS-A-0516

Table 1-2. Chronological time frame of hydroacoustic surveying events on CSII-BA, Chester Shoal, and Bull Shoal off the east coast of Florida.

Dates	Event and Location	Company and Report (if available)
1996	Single-beam hydroacoustic survey at CSII-BA	-
26 Sept 2000	Single-beam hydroacoustic survey prior to any dredging of CSII-BA	Great Lakes Dredge & Dock Company (Olsen Associates 2013)
2007	Side-scan sonar and multibeam hydroacoustic survey of CSII-BA	National Oceanographic Survey
8–11 May 2010	Single-beam hydroacoustic survey of dredged area of CSII-BA	U.S. Army Corps of Engineers, Jacksonville District (Survey # 10-079) (Olsen Associates 2013)
8 June–13 July 2013	Single-beam hydroacoustic survey of dredged area of CSII-BA	Whidden Surveying and Mapping, Royal Palm Beach, FL (for U.S. Army Corps of Engineers) (Olsen Associates 2013)
Oct–Nov 2013	Multibeam hydroacoustic survey of CSII-BA	Land & Sea Surveying (contracted by Great Lakes Dredge and Dock)
May 2014	Multibeam hydroacoustic surveys of areas of CSII-BA, Bull, and Chester Shoals	Land & Sea Surveying (this study)
May 2015	Multibeam hydroacoustic surveys of areas of CSII-BA, Bull, and Chester Shoals	Land & Sea Surveying (this study)

Table 1-3. Major hurricanes and tropical depressions/storms impacting the Cape Canaveral coast during the study period.
No major winter storms impacted the area during the study.

Year	Peak Impact	Storm Name	Category
2014	1–2 July	Arthur	tropical depression/tropical storm
2016	13–14 Sep	Julia	tropical storm
2016	6–7 Oct	Matthew	major hurricane
2017	1 Aug	Emily	tropical depression
2017	10–11 Sep	Irma	major hurricane

2 Physical Oceanography Surveys

Arnoldo Valle-Levinson, Peter Adams, Juan Felipe Paniagua-Arroyave, Sabrina Parra, Ahmad Yousif, and Sangdon So

Key Points

- Ridges and swales produce spatial variability in tidal and non-tidal (subinertial) flows over the inner continental shelf (where instruments were deployed).
- Transects with gentle slopes between ridges and swales showed Bernoulli-type hydrodynamics, i.e., flow enhancement over ridges.
- Transects with steep slopes between ridges and swales displayed frictional hydrodynamics, i.e., flow enhancement over swales.
- The critical bed slope to switch from frictional to Bernoulli-type (inertia-dominated) dynamics is equal to the non-dimensional bottom drag coefficient (typically 0.0025).
- Gulf Stream enhancements by southerly winds translate into strengthened northward inner shelf flows, and vice versa.
- The dynamics across the shelf is mostly geostrophic (water level slope balanced by Coriolis accelerations), with occasional influence from wave stresses.
- Waves with periods between 20 and 200 s are modulated by semidiurnal tidal flows in the swales exposed to the ocean (seaward of a ridge), enhancing erosion.
- Shoals dissipate and transform waves with heights > 1 m, delaying erosion.
- Tropical storm winds produce currents that distort tides and enhance erosion.
- Dredging operations dampen wave transformations over the inner shelf.
- Short wind-waves are smaller after dredging, and free long waves (infragravity) increase proportionally.
- After dredging, there is decreased generation and increased dissipation of long waves (infragravity).

2.1 Introduction

The overall goal of the study was to monitor the effects and recovery of dredging operations on biological communities within ridge-swale habitats of sand shoals offshore of Cape Canaveral; therefore, the oceanographic dynamics of these ecosystems were important to understand. This chapter characterizes the interaction between the bathymetry and the velocity field of shoals off the east coast of Florida (Figure 2-1), with oceanographic measurements during different seasonal conditions.

Initially, an oceanographic instrument was moored prior to dredging at the Canaveral Shoals II borrow area (CSII-BA; the shoal where dredging was to occur), which determined pre-dredging and post-dredging conditions at the dredging site. All other moored and towed instruments were deployed in the post-dredge period at CSII-BA, as well as at two other mooring locations, Chester Shoal and Bull Shoal, which were characterized as reference/control sites that were more than one tidal excursion away from the dredging site (Figure 2-1).

To study biophysical feedbacks on bedforms and sediment transport, mooring deployments can be used to describe the flow conditions under different forcing conditions. Underway measurements with a towed Acoustic Doppler Current Profiler (ADCP) allow determination of flow hydrographic and bathymetric characteristics in the dredging region before and after the operation. Seasonal measurements, with the combination of moored and underway measurements, provide pre-dredging and post-dredging

information with enough temporal and spatial resolution to evaluate the hydrodynamic and ecological effects of bathymetric modification. Assessment of post-dredging seasonal variations provide further information on dredging versus natural effects on flow, bathymetry, and hydrography.

The following sections accomplish these finer-scale objectives

- Section 2.2 presents the effects of ridge-swale bathymetry on tidal and subtidal hydrodynamics. Alteration to these ridges, or the swales, by dredging activities could dramatically influence flows and erosive processes.
- Section 2.3 investigates subinertial hydrodynamics, which describe variations with periods longer than 26 h (the inertial period). These periodicities provide a framework that allows inferences on long-term potential dredging alterations to ridges and swales.
- Section 2.4 addresses the influence of surface infragravity waves on sediment suspension over cape-related shoals. Inner-shelf and shoreline morphology exert control on the variability of long gravity waves (LGWs, also called infragravity waves exhibiting periods from 20 to 500 s, or 2 to 50 mHz). In turn, nearshore morphodynamics can be influenced by infragravity motions, whose behaviors are asymmetric (moving sediment in one preferred direction) but not well understood over cape-related shoals. Hurricanes have an apparent effect on the biophysical communities, especially in estuarine and coastal habitats.
- In Section 2.5, we add to the paradigm of overtides' generation by considering the effect of bottom stresses due to anomalously large current speeds related to extreme wind forcing at cape-related shoals during the passage of Hurricane Matthew. Hurricanes are common features off the east coast of Florida during the summer and fall and they drive anomalously large waves, currents, and morphological changes. These morphological changes may compare to those from dredging, at least in the short term (order of days).
- Section 2.6 discusses morphological changes of cape-related shoals in order to explore biophysical feedbacks on bedforms. Bedforms display a proportion of coarse shell material to fine sand, which may influence the hydrodynamic sorting and overall bed evolution at Canaveral Shoals. It is necessary to evaluate the magnitude of natural bedform operations versus those produced by dredging.

2.2 Tidal and Subtidal Hydrodynamics Over Ridge-Swale Bathymetry Around a Cape

2.2.1 Introduction

The inner continental shelf is a dynamic region between the surf zone and the mid-shelf, where the water depth expands from a few meters to tens of meters (Lentz and Fewings 2012). In such a region, the surface and bottom boundary layers interact with one another (Lentz 1995; Lentz and Fewings 2012). Observations have shown that across-shelf currents are constrained by bathymetry and therefore are weaker than the along-shelf currents (Lentz and Fewings 2012). This clear influence of bathymetry on the flow, particularly in inner shelves, indicates the need to further investigate its spatial influence on tidal and subtidal hydrodynamics.

The dynamics of flow have been previously investigated over rugged bathymetry such as sills (Farmer and Armi 1986; Eriksen 1991; Stenström 2003), bathymetric depressions also known as "hollows" (Salas-Monreal and Valle-Levinson 2009; Valle-Levinson and Guo 2009), channels (Winters and Seim 2000), estuaries (Wong 1994; Valle-Levinson et al. 2003), and inlets (Lwiza et al. 1991; Valle-Levinson et al. 2015). These studies have demonstrated that frictionally influenced flow has the maximum velocity values over the deepest part of the cross-section and that velocity contours are parallel to the bathymetry throughout the section. On the other hand, non-frictionally influenced flow would follow Bernoulli-type

dynamics, where it accelerates over shallower depths and decelerates over deeper depths due to mass conservation. Centrifugal or local acceleration could cause a similar result by driving the maximum flow away from the center of the cross-section (Valle-Levinson et al. 2015). It has also been noted in cases of weak frictional and advective effects that the flow may tilt to the right due to the Coriolis effect in the northern hemisphere (Valle-Levinson and O'Donnell 1996; Valle-Levinson et al. 2000, 2003).

Capes and their associated shoals are characterized by complex bathymetry, presenting abrupt changes in coastline orientation and water depth (Kumar et al. 2013). Studies have targeted current flow and sediment transport behavior around these features (McNinch and Luettich 2000; Sanay et al. 2007), as well as interactions between flow and shoaling waves (Kline et al. 2012). However, the hydrodynamics of the flow over ridge-swale bathymetry remain relatively unexplored.

The primary objective of this study was to determine the spatial structure of tidal and subtidal hydrodynamics off a cape with complex bathymetry in an inner shelf. The objective was addressed by comparing observations from vessel-based ADCPs to two analytical models: 1) a tidal model influenced by friction, local acceleration, and pressure gradient; and 2) a subtidal density-driven model influenced by friction, Coriolis, and pressure gradient. These analytical models have been developed to approximate the dynamics in channelized environments. Since the ridge-swale bathymetry forms a similar shape to a channel, the other main objective was to assess whether the hydrodynamics over ridge-swale bathymetry can be represented by those of channelized environments (Gill 1982; Armi 1986; Wong 1994; Valle-Levinson and O'Donnell 1996; Valle-Levinson et al. 2000, 2003, 2015; Salas-Monreal and Valle-Levinson 2009; Valle-Levinson and Guo 2009).

2.2.2 Methods

2.2.2.1 Study Area

The study area was located in the inner shelf adjacent to Cape Canaveral, Florida (Figure 2-1). It has a typical cape configuration that is characterized by complex bathymetry and changes in coastline orientation. It consists of a series of cape-associated shoals and shore-oblique ridges that vary several meters vertically over a horizontal scale of a few kilometers. Southeast Shoal is attached to the tip of Cape Canaveral and extends offshore southeastward for ~7 km with a width of ~5 km. Canaveral Shoal II (along with the borrow area, CSII-BA) and Shoal E are roughly parallel to the cape's shoreline orientation (Figure 2-1). Shoal E is the furthest southeast shoal and has a length of ~4 km and a width of 1.5 km. Bull Shoal and Chester Shoal (Figure 2-1) are located ~12 km northeast from the tip of Cape Canaveral. Bull Shoal (0.7 km wide by 7 km long) is east of Chester Shoal (0.7 km wide and ~4 km long), which is part of multiple, shore-oblique ridges associated with a smaller cape located ~15 km northwest of Cape Canaveral known as False Cape. Those ridges extend ~7 km offshore, southeastward of False Cape.

In this region, tides are predominantly semidiurnal. During the time period of the oceanographic study (fall 2013–summer 2016), spring tides ranged between 1.3 to 1.8 m, while neap tides ranged from 0.6 to 0.9 m. The significant wave height was ~1.2 m in winter, 1 m in spring, 0.5 m in summer, and 0.8 m in fall. The dominant wave period was ~9 s in winter, ~8 s in spring, ~7 s in summer, and ~8 s in fall. The corresponding dominant wave direction was 71 °T (from the east/northeast) in winter, 81 °T (from the east/northeast) in spring, 107 °T (from the east/southeast) in summer, and 86 °T (from the east) in fall. Clearly, the wave direction was typically easterly. The instantaneous hourly wind speed range was 1–16 m/s in winter, 1–12 m/s in spring, 1–13 m/s in summer, and 1–11 m/s in fall. The subtidal wind speed range was 1–10 m/s in winter, 1–8 m/s in spring, 2–7 m/s in summer, and 2–6 m/s in fall. The corresponding wind direction was 142 °T in winter (from the southeast), 205 °T in spring (from the southwest), 126 °T in summer (from the southeast), and 208 °T in fall (from the southwest).

2.2.2.2 Data Collection

The study area included two ~4.5-km long sampling transects: the north transect (northeast of Cape Canaveral; Figure 2-1, Plot A) and the south transect (southeast of Cape Canaveral; Figure 2-1, Plot B). The north transect had a bottom slope of 0.002, while the south transect had a bottom slope of 0.006. In order to determine the influence of cape-associated shoals on tidal and subtidal hydrodynamics, data were collected between 24 September 2013 and 29 June 2016. An ADCP was attached to a catamaran, then towed back and forth along each transect (~4.5 km) for ~12 hours. The ADCPs recorded the underway current velocity field, surface water temperature, and backscatter with a pinging rate of 2 Hz and an average ensemble of 20 profiles. The cruising speeds were 2 m/s, and the bin size was 0.5 m. Ensembles therefore had sampling intervals of 10 s and spatial resolution of 20 m. Fixed hydrographic profiles were collected from seasonal cruises between fall 2013 and summer 2016 using Castaway and Sea Bird 19 Plus conductivity-temperature-depth (CTD) profilers. Along the transects, three CTD casts were performed at the start, middle, and end of each seaward transect repetition.

2.2.2.3 Data Analysis

2.2.2.3.1 Matrix Arrangement and Compass Calibration

Current velocity data were trimmed with the following criteria that were related to the data collection: percent good among beams > 70%, absolute value of error velocity < 10 cm/s, profile discharge < 100 m^3/s, and ship speed or bottom track speed > 0.15 m/s. The method of Joyce (1989), similar to the method of Pollard and Read (1989), was used to calibrate the ADCP compass, separately for each transect repetition or pass. Correction coefficients (α and β) were obtained for each transect pass. These coefficients were used to correct the current velocity components by considering both the bottom track velocity and navigation (or ship) velocity as follows:

$$\tan{(\alpha)} = \langle u_{bt}\,v_{bt} - v_{bt}\,u_{sh} \rangle / \langle u_{bt}\,u_{sh} + v_{bt}\,v_{sh} \rangle \tag{1}$$

$$1 + \beta = [\langle u_{sh}{}^2 + v_{sh}{}^2 \rangle / \langle u_{bt}{}^2 + v_{bt}{}^2 \rangle]^{1/2} \tag{2}$$

$$u_{corr} = [1 + \beta][u\,cos(\alpha) - v\,sin(\alpha)] \tag{3}$$

$$v_{corr} = [1 + \beta][u\,sin(\alpha) + v\,cos(\alpha)] \tag{4}$$

where u_{bt} and v_{bt} were the east and north components of the bottom track velocity, respectively; u_{sh} and v_{sh} were the east and the north components of the navigation (ship) velocity (from Global Positioning System [GPS]), respectively; u and v were the east and north components of the current velocity measured by the ADCP, respectively; u_{corr} and v_{corr} were the corrected east and north components of velocity; and $<>$ indicated the average over one transect pass.

A regular matrix was then generated for u, v, and t corresponding to each transect repetition in terms of depth and distance. Each transect repetition was identified according to the time of the beginning and the end of each pass. The origin of the matrix (zero distance) was arbitrary. The distance from that origin to the location of each profile was calculated in order to generate a regular grid for u, v, and t. The end result was a group of N_p regular grids for u, v, and t , where N_p was the number of transect repetitions.

2.2.2.3.2 Least-Squares Fit to Observations

Least squares are considered one of the most powerful techniques for fitting a dependent parameter to an independent (observed input) variable (Emery and Thomson 1998). This technique determines the values of the parameters that minimize the sum of the squares of the residuals (Chapra and Canale 2015). It

decomposes the desired signals from the measured signal. Since semidiurnal tides were dominant in the region, a least-squares fit with a semidiurnal (12.42 hr) harmonic was applied to the flow. The amplitudes and phases of this harmonic were therefore calculated as

$$v_{field} = v_{Res} + A_{M_2} \sin\left(\omega_{M2} t + \phi_{M_2}\right) \tag{5}$$

where v_{field} was the along-shelf (north-south) velocity measured from the field, v_{Res} was the along-shelf residual velocity that represents the subtidal flow, A_{M_2} was the along-shelf semidiurnal amplitude of the tidal flow, ω_{M2} was the semidiurnal angular tidal frequency, t was the time, and ϕ_{M2} was the semidiurnal phase.

The subtidal velocity can be positive or negative, and its direction influences the interpretation of the driving hydrodynamics; therefore, the subtidal flow was rotated in the direction of the principal axis, which minimized the transverse velocity component.

2.2.2.3.3 Tidal Flow Analytical Model Solutions

A tidally driven analytical model can be used to solve tidal amplitude and phase for any arbitrary bathymetry (Huijts et al. 2006, 2009, 2011). Figure 2-2 provides a schematic representation of the model reference frame for one of the locations. A scaling analysis was used to simplify the governing equation and hence obtain the model momentum balance in the principal axis direction (along-shelf), as (Huijts et al. 2006, 2009, 2011):

$$\frac{\partial v_0}{\partial t} = -g \frac{\partial \eta_0}{\partial y} + A_Z \frac{\partial^2 v_0}{\partial z^2} \tag{6}$$

where $\partial v_0/\partial t$ represented local acceleration, v_0 was the model along-shelf velocity (flow in the principal axis direction), $-g(\partial \eta_0/\partial y)$ represented the pressure gradient, g was the acceleration due to gravity, η was the free surface elevation, $A_Z (\partial^2 v_0/\partial z^2)$ represented friction, A_Z was the vertical eddy viscosity, and the subzero terms (v_0 and η_0) represented the first order or dominant order solutions. The analytical model assumed that motion occurred primarily in the principal axis direction (along-shelf). It also assumed that the motion was given as a simplified momentum balance between friction, local acceleration, and the pressure gradient due to the free surface elevation. Only barotropic effects were considered. The model drawbacks were that no along-shelf variation in bathymetry was allowed and no coastline curvature was considered (Valle-Levinson et al. 2015). The model also indicated whether the tidal flow could be explained as a simple damped wave (Valle-Levinson et al. 2015).

The dominant order solution of the model simplified momentum balance (Equation 6) was obtained as (Huijts et al. 2006, 2009, 2015):

$$\alpha = \sqrt{i\omega_{M2}/A_z} \tag{7}$$

$$\frac{\partial \eta_0}{\partial y} = \frac{V\omega_{M2}A}{ig} \left[\int_0^B \frac{1}{\alpha}\{\alpha H - \tanh(\alpha H)\}dx\right]^{-1} \tag{8}$$

where B stands for the cross-sectional width, A was the cross-sectional area of the transect, V was the cross-sectional average of the tidal current amplitude, α was a frictional length scale (complex value because i equals $\sqrt{-1}$), and

$$v_0 = \frac{ig}{\omega_{M2}} \frac{\partial \eta_0}{\partial y} \left[1 - \frac{\cosh(\alpha H)}{\cosh(\alpha H)}\right] \tag{9}$$

The amplitude of v_0 ($i.e., A_{v_0}$) resembled the model along-shelf tidal amplitudes. It was a function of the vertical direction z, water depth H, gradient of the free surface elevation, and α parameter. This α parameter was dependent on the tidal frequency and the vertical eddy viscosity. As the tidal period increases, both the frequency and the alpha decrease. As the eddy viscosity increases, the alpha decreases. The alpha represents the degree of mixing or friction in the water column. Small alpha means high friction and vice versa. V and A_z were the only free parameters, and their values influenced the solution of the analytical model. Therefore, these parameters were varied, and we calculated the contour plots of the root-mean-square error ($error_{rms}$). The objective was to determine V and A_z values that had the minimum error between the model and observation. The root-mean-square error was calculated as

$$error_{rms} = \left[\frac{1}{N_s} \sum\left(A_{M2} - A_{v_0}\right)\right]^{1/2} \tag{10}$$

where N_s was the total number of samples, and A_{v_0} was the tidal model amplitude in the direction perpendicular to the transect (in the principal axis direction). More details on the analytical model solutions can be found in Huijts et al. (2006).

2.2.2.3.4 Subtidal Analytical Model Solutions

Valle-Levinson et al. (2003) developed a density-driven analytical model that extends the work of Kasai et al. (2000) to better explain exchange flows over complex bathymetry. All equations presented in this section have been introduced by Valle-Levinson et al. (2003, 2008). The same reference frame (presented previously in Figure 2-2) was used here. This model was used in our study to determine the subtidal hydrodynamics over the ridge-swale bathymetry. It described the across-shelf momentum balance as

$$-fv = -g\frac{\partial \eta}{\partial x} + \frac{g}{\rho_0}\frac{\partial \rho}{\partial x}z + A_z\frac{\partial^2 u}{\partial z^2} \tag{11}$$

where fv represented Coriolis acceleration, f was the Coriolis parameter (7 x 10^{-5} s^{-1}), ρ_0 was the reference seawater density, $-g\,(\partial \eta/\partial x)$ represented barotropic contribution, $(g/\rho_0)(\partial \rho/\partial x)\,z$ represented baroclinic contribution, and $A_z(\partial^2 u/\partial z^2)$ represented friction.

This analytical solution assumed that the motion was produced by pressure gradients and modified by Coriolis and frictional influences. The pressure gradient included the influence of free surface elevation and the density gradient. Therefore, both barotropic and baroclinic contributions were considered in this analytical model.

An important restrictive assumption in this analytical solution was that the vertical eddy viscosity was constant. It also assumed uniform along-shelf bathymetry and did not include the influence of curvature effects (Valle-Levinson et al. 2015). The Ekman layer depth was calculated as

$$D_E = \left(\frac{2A_z}{f}\right)^{1/2} \tag{12}$$

where D_E was defined as the ratio between the vertical eddy viscosity and the Coriolis parameter.

Basically, the Ekman layer depth represents the depth in which the frictional effects were dominant. In frictionally dominated cross-sections, the Ekman layer depth would be much larger than those with fewer frictional effects. This nondimensional number represents the ratio between friction and Coriolis as

$$E_k = \frac{A_z}{fH_{max}^2} \tag{13}$$

where H^2_{max} was the maximum water depth of the cross-section. Deeper cross-sections would have a smaller Ekman number, which indicates that the effect of friction only affects the very deep part of the water column. Shallower cross-sections would have a larger Ekman number, indicating that the frictional effects will extend over the entire water column.

The α parameter was calculated as

$$\alpha = \frac{(1+i)}{D_E} \tag{14}$$

The density gradient (D) was estimated as

$$D = \frac{v_{flux} - \alpha g \int_0^B N(x)[\tanh(\alpha H) - \alpha H] dx}{\int_0^B [(e^{-\alpha H} + \alpha H)\tanh(\alpha H) - (1 - e^{-\alpha H} + \alpha^2 H^2/2)] dx} \tag{15}$$

where v_{flux} was the net flux velocity (m/s) in the principal axis direction (along-shelf) and N was calculated as

$$N = -N_0(1 + ie^{-k_r^2 x^2}) \tag{16}$$

where N_0 was the slope of the water surface at the coast that decays exponentially with distance offshore. The parameter k_r was the rate of exponential decay that can be related to the internal radius of deformation R_i; $k_r = 1/R_i$. The barotropic F_1 and baroclinic F_2 contributions of the flow were calculated as

$$F_1 = \frac{I}{f}\left[1 - \frac{\cosh(\alpha z)}{\cosh(\alpha H)}\right] \tag{17}$$

and

$$F_2 = \frac{iD}{f\alpha}\left[(e^{\alpha z} - \alpha z) - (e^{-\alpha z} + \alpha H)\frac{\cosh(\alpha z)}{\cosh(\alpha H)}\right] \tag{18}$$

Therefore, the subtidal model solution had contributions from F_1 and F_2 as $v_m = gNF_1 + F_2$, where m stands for model. The subtidal flow in the principal axis direction (along-shelf) was the real part of the complex subtidal flow v_m presented in Equation 18. The free parameters in this analytical model were E_k, k_r, N_0, and v_{flux}. Optimal values of the free parameters were obtained by varying them throughout possible ranges to reduce the difference between model and observation. For more details on the analytical solution beyond this section, see Valle-Levinson et al. (2003, 2008).

2.2.3 Results

2.2.3.1 Hydrographic Data

The results of the hydrographic measurements are presented in Figure 2-3. CTD results showed that temperature decreased with depth, while salinity and density increased with depth. These results indicated a doubly stable condition. Water temperature was lowest between December and April, while highest between June and October. Although precipitation increased between June and October, more evaporation occurred, causing an increase in salinity. This phenomenon can also be associated with the influence of the warm Gulf Stream originating from the Gulf of Mexico. As it travels northward, it creates a sharp sea-surface temperature front that leads to surface wind convergence. As a result, clouds are created and precipitation occurs along the Gulf Stream (Minobe et al. 2008a; 2008b). Wind moving over the Gulf Stream causes evaporation and therefore increases the water salinity and density (Russel 2007). The location of the Gulf Stream relative to the coast may also influence salinity. As the Gulf Stream gets closer to the coast, salinity in the region is expected to increase. On the other hand, as the Gulf Stream

gets farther from the coast, salinity in the region is expected to decrease. Seasons with an overall location of the Gulf Stream closer to the coast are expected to have higher salinity than seasons with an overall location of the Gulf Stream farther from the coast. Also, the Gulf Stream flowrate is influenced by seasonality. According to Geosat altimetry results, the Gulf Stream flowrate is maximum in fall and minimum in spring, which is in phase with the north and south shifts from its mean position (Kelly and Gille 1990; Zlotnicki 1991). However, the strength of the flowrate does not necessarily have a direct influence on salinity near the coast, as the location of the relatively stronger Gulf Stream may be farther offshore.

The temperature/salinity diagram (Figure 2-3) showed that, for all CTD casts, salinity ranged between 33.4 kg/m^3 and 35.8 kg/m^3, while temperature ranged between 17.3 °C and 30 °C. The smaller incremental change in salinity had more influence on density than temperature. The temperature/salinity diagram also showed that water masses during the colder months were similar to one another. The water temperature during these months ranged between 18 °C and 21 °C, while salinity ranged between 33.4 kg/m^3 and 34 kg/m^3. Likewise, the water masses during the warmer months were similar to each other. The water temperature during these months ranged between 25.7 °C and 29 °C, while salinity ranged between 35.4 kg/m^3 and 35.7 kg/m^3. Since October was a transition month, the corresponding water mass exhibited properties between those of the warmer and colder seasons. In general, density in the region had a similar trend in the north and south transects. However, some discrepancies were noted in June of 2014, when density at the north transect was changing more with depth than the one at the south transect (Figure 2-3). This observation was related to the rapid change in temperature with depth at the north transect, whereas it was more uniform at the south transect. Similar discrepancy in density was noted between the north and south transect during September and October of 2013 due to the rate of change in temperature with depth at each location. The small incremental change in salinity with depth at the south transect during September of 2013 (Figure 2-3) could have also been a factor.

2.2.3.2 Tidal Model Versus Observation

In order to obtain the model tidal amplitudes, the free parameters (V and A_z) in the analytical model were varied until the minimum root-mean-squared error was achieved. The best parameters were then used to create a contour plot of the model's semidiurnal amplitudes. These contours were compared with those derived from field observations. It was important to acknowledge and appreciate the limitations as well as the capabilities of this model. The model was unable to perfectly reproduce the observation. However, very useful information could be achieved by keeping track of the V and A_z values.

A comparison between the tidal model and observation amplitudes is provided in Figures 2-4 to 2-7. The comparison was in terms of the root-mean-squared error, the corresponding V and A_z values, and the contour plots of semidiurnal amplitudes.

Two types of configurations were observed. In the north transect, the maximum tidal flow (i.e., velocity amplitude) was located over the shoals (Figure 2-4), while, in the south transect, the maximum flow was located in the channel (over the deepest part of the cross-section; Figures 2-5 to 2-7). In order to use the tidal model to represent the observations, the vertical eddy viscosity (A_z) had to be decreased in the north transect while increased in the south transect. Increasing or decreasing A_z affects friction A_Z ($\partial^2 v_0/\partial z^2$). Therefore, the flow in the north transect was more influenced by local acceleration, such that inertial effects also caused acceleration over shallower depths. On the other hand, the flow in the south transect was dominated by friction, such that the maximum flow was located in the channel.

2.2.3.3 Subtidal Model Versus Observation

To obtain the model subtidal velocities, the free parameters (E_k, k_r, N_0, and v_{flux}) in the analytical model were varied (by trial and error) until the best match between the model and observation was

achieved. As with the tidal model, it was important to acknowledge and appreciate the limitations as well as the capabilities of the model. The model was unable to perfectly reproduce the observation. However, very useful information was achieved by keeping track of the E_k, k_r, N_0, and v_{flux} values.

A comparison between the subtidal model and observation velocities is provided in Figures 2-8 to 2-14. The comparison was in terms of the subtidal velocities' contour plots and the corresponding values of E_k, k_r, N_0, and v_{flux}.

Two types of configurations were also observed here. In the north transect, the maximum subtidal flow was located over the shoals (Figures 2-8 to 2-10), while in the south transect the maximum flow was located in the channel (Figures 2-11 to 2-14). To best approximate the subtidal model to represent the observations, the Ekman number (E_k), which indicated the frictional effects on the water column, had to be decreased in the north transect and increased in the south transect. This indicated that the effect of friction in the north transect was restricted only to the very deep part of the water column. Therefore, the flow in the north transect was more influenced by Coriolis (early geostrophic dynamics) or advection (i.e., Bernoulli-type dynamics). On the other hand, the frictional effects in the south transect extended over the entire water column, and the flow was dominated by friction. This observation was consistent with the strongest flows appearing over the ridges in the north transect and in the swale in the south transect.

2.2.4 Discussion

2.2.4.1 Tidal Model

In general, the vertical eddy viscosity (A_z) had a larger influence on the shape of the contours than the sectional average tidal amplitude (V). As A_z increased, friction [$A_z\,(\partial^2 v_0/\partial z^2)$] increased, and the maximum flow tended to be located over the deepest part of the cross-section (x/B= ~0.3 to 0.7; Figures 2-5 to 2-7). The model tidal amplitude contours also tended to be parallel to the bathymetry throughout the section. This behavior has been seen in estuaries (Wong 1994; Valle-Levinson et al. 2003) and inlets (Valle-Levinson et al. 2015). On the other hand, as A_z got smaller, friction decreased, and local acceleration became more important. Therefore, the maximum flow was driven away from the center of the cross-section (over the shoals; Figure 2-4) (Valle-Levinson et al. 2015).

The south transect was dominated by friction and had larger A_z values (5e-2 m²/s to 2.1e-1 m²/s). This result was expected in inner shelves where both the surface and bottom boundary layers overlap (Lentz 1995; Lentz and Fewings 2012). By contrast, the north transect, which had a more influential local acceleration, had a smaller A_z value by one or two orders of magnitude (1e-3 m²/s). These results can be directly linked to the bathymetry at each location. The north transect, with a slope of 0.002, tended to have gentler bathymetry. The effect of friction will affect only the very deep part of the water column ('H/H_{max}'= ~0.3 from the bottom). Therefore, it makes sense that the cross-section had a smaller A_z, and local acceleration had more influence. The south transect, however, had a steeper bathymetry with a slope of 0.006, forming the shape of a channel. Therefore, frictional effects extend over the entire water column, and A_z becomes larger. The discrepancies between the model and observed tidal amplitudes in Figure 2-4 could be attributed to the restrictive model assumptions. It may also indicate that there were more forces influencing the north transect other than local acceleration. The tidal model used for this study was originally developed for channelized flow, while our observations were in the open shelf. Despite that, the model was still very useful in representing the essence of the flow at each location and helped to determine the dominant hydrodynamics.

2.2.4.2 Subtidal Model

In general, Ekman number (E_k) had larger influence on the shape of the contours than the rate of exponential decay (k_r), slope at the coast (N_0), and net flux velocity (v_{flux}). Since E_k is a function of A_z

and H (see Equation 9), smoother cross-sections, such as the north transect, would have a smaller Ekman number (1.5e-4 to 2.3e-4), which indicated that the effect of friction only affected the very deep part of the water column ('H/H_{max}'= ~0.2 from the bottom). On the other hand, more complex bathymetry with a steeper cross-section, such as the south transect, would have a larger Ekman number (6e-2 to 7e-2), indicating that the frictional effects extended over the entire water column, which was expected in inner shelves where both the surface and bottom Ekman layers overlap (Li and Weisberg 1999). Therefore, the south transect was dominated by friction and the strongest currents were located over the deepest part of the cross-section (x/B= ~0.3 to 0.7; Figures 2-11 to 2-14) (Wong 1994; Valle-Levinson et al. 2003).

Also, the model's subtidal velocity contours were parallel to the bathymetry throughout the section (Lwiza et al. 1991; Valle-Levinson et al. 2015). On the other hand, the north transect had smaller E_k values by two orders of magnitude. Examination of the north transect's cross-sectional area, when the flow traveled southward and the maximum current tilted to the right (looking northward), suggests the influence of Coriolis (Figures 2-8 to 2-10) (Valle-Levinson and O'Donnell 1996; Valle-Levinson et al. 2000, 2003). This southward motion of the flow can be associated with the along-shelf wind. The southward along-shelf wind causes the nearshore flow to deflect towards the coast (to the right) due to Coriolis influence. This Coriolis influence is balanced with a sea-surface slope to keep a geostrophic balance. The result is a negative nearshore sea-surface slope that drives the nearshore flow southward.

Furthermore, closer examination of the north transect's cross-sectional area, when the flow moved northward and the maximum current tilted to the left (looking forward, Figure 2-9, i.e., tilted toward the coast or against Coriolis accelerations), suggests that the flow was not influenced by Coriolis, but rather followed Bernoulli-type dynamics. When the flow is following Bernoulli-type dynamics, it accelerates over shallower depths and decelerates over deeper depths due to mass conservation.

Since the subtidal model considered only the contribution of friction, Coriolis, and pressure gradient, the exact hydrodynamics causing such behavior could not be determined. It was also noted that the values of net flux velocity (v_{flux}) at the north transect (2.7e-3 m/s to 5.5e-3) were larger than the ones at the south transect by two orders of magnitude (0.74e-5 m/s to 1.4e-5 m/s). This could be related to the higher frictional influence of the complex bathymetry at the south transect, which decelerates the passing flowrates.

The discrepancies between the model and observed subtidal currents in Figures 2-8 to 2-10 could be attributed to the restrictive model assumptions or influential forces that were not considered in the model. Similar to the tidal model, the subtidal model used for this study was originally developed for channelized flow, while our observations were in the open shelf. Despite that, the model was still very useful in representing the flow at each location and helped to determine the dominant hydrodynamics.

2.2.4.3 Implications for Dredging

Inner continental shelf bathymetry consisting of ridges and swales produces spatial variability in tidal and non-tidal (subinertial) flows. Transects with gentle slopes between ridges and swales showed Bernoulli-type hydrodynamics, i.e., tidal and subtidal flow enhancement over ridges. Transects with steep slopes between ridges and swales displayed frictional hydrodynamics, i.e., flow enhancement over swales. It is evident that any alteration to a swale or ridge can modify the hydrodynamics by influencing friction and inertia. Because erosion will develop where strongest flows appear, any dredging alteration will also shift the erosional processes accordingly.

2.2.5 Conclusion

This study examined the influence of the ridge-swale bathymetry on tidal and subtidal hydrodynamics. The north transect had a smoother bathymetry and a bottom slope of 0.002. The effect of friction was

restricted to the bottom boundary layer, which was a small portion of the water column ('H/H_{max}'= ~0.2-0.3 from the bottom). Therefore, tidal hydrodynamics were more influenced by local acceleration, and subtidal hydrodynamics were either influenced by Coriolis or followed Bernoulli-type dynamics. This was consistent with previous studies on flows passing over variable bathymetries with less frictional influence. Since the subtidal model only considered the contribution of friction, Coriolis, and pressure gradient, the exact hydrodynamics causing the flow to follow Bernoulli-type dynamics could not be determined.

On the other hand, the south transect had a steeper bottom slope of 0.006 and a bathymetry that delineated a channel. Frictional effects could therefore extend over the entire water column, which was expected in inner shelves where both the surface and bottom boundary layers overlap. As a result, the south transect was dominated by friction, and the maximum flow was located over the deepest part of the cross-section (x/B= ~0.3 to 0.7). Also, the modeled principal axis contours were parallel to the bathymetry throughout the section. This behavior has been seen elsewhere with frictionally influenced flow.

The tidal and subtidal analytical model solutions support one another and highlight the influence of ridge-swale bathymetry on tidal and subtidal hydrodynamics, similar to what is observed in shallow-water systems. It was clear that dredging modifications to a swale or ridge should modify the hydrodynamics by influencing frictional and inertial effects that determine where the strongest flows develop, and where subsequent erosional processes appear.

2.2.6 References

Armi L. 1986. The hydraulics of two flowing layers with different densities. Journal of Fluid Mechanics 163: 27-58. doi:10.1017/S0022112086002197.

Chapra S, Canale R. 2015. Numerical methods for engineers. New York, NY: McGraw-Hill Education.

Emery W, Thomson R. 1998. Data analysis methods in physical oceanography. 1st ed. New York, NY: Elsevier.

Eriksen CC. 1991. Observations of amplified flows atop a large seamount. Journal of Geophysical Research: Oceans 96(C8): 15227-15236. doi.org/10.1029/91JC01176.

Farmer DM, Armi L. 1986. Maximal two-layer exchange over a sill and through the combination of a sill and contraction with barotropic flow. Journal of Fluid Mechanics 164: 53-76. doi:10.1017/S002211208600246X.

Gill A. 1982. Atmosphere-ocean dynamics. New York, NY: Elsevier. 662 p.

Huijts K, de Swart H, Schramkowski G, Schuttelaars H. 2011. Transverse structure of tidal and residual flow and sediment concentration in estuaries. Ocean Dynamics 61(8): 1067-1091. doi:10.1007/s10236-011-0414-7.

Huijts K, Schuttelaars H, de Swart H, Friedrichs C. 2009. Analytical study of the transverse distribution of along-channel and transverse residual flows in tidal estuaries. Continental Shelf Research 29: 89-100. doi:10.1016/j.csr.2007.09.007.

Huijts K, Schuttelaars H, de Swart H, Valle-Levinson A. 2006. Lateral entrapment of sediment in tidal estuaries: An idealized model study. Journal of Geophysical Research: Oceans 111(C12016). doi:10.1029/2006JC003615.

Joyce TM. 1989. On In Situ "Calibration" of Shipboard ADCPs. Journal of Atmospheric and Oceanic Technology 6(1): 169-172. doi:10.1175/1520-0426(1989)006<0169:Oisosa>2.0.Co;2.

Kasai A, Hill AE, Fujiwara T, Simpson JH. 2000. Effect of the Earth's rotation on the circulation in regions of freshwater influence. Journal of Geophysical Research: Oceans 105(C7): 16961-16969. doi.org/10.1029/2000JC900058.

Kelly KA, Gille ST. 1990. Gulf Stream surface transport and statistics at 69W from the Geosat altimeter. Journal of Geophysical Research 95(C3): 3149-3161.

Kline SW, Adams PN, Plant NG, MacKenzie RA, Jaeger JM. 2012. Effect of a shore-oblique ridge on beach and bar morphodynamics at Kennedy Space Center, Cape Canaveral, Florida. In: American Geophysical Union Fall Meeting; 2012/12/1; San Francisco, CA. p EP33B-0867. https://ui.adsabs.harvard.edu/abs/2012AGUFMEP33B0867K.

Kumar N, Voulgaris G, List JH, Warner JC. 2013. Alongshore momentum balance analysis on a cuspate foreland. Journal of Geophysical Research: Oceans 118(10): 5280-5295. doi.org/10.1002/jgrc.20358.

Lentz S. 1995. Sensitivity of the inner-shelf circulation to the form of the eddy viscosity profile. Journal of Physical Oceanography 25(1): 19-28. doi:10.1175/1520-0485(1995)025<0019:Sotisc>2.0.Co;2.

Lentz S, Fewings MR. 2012. The wind- and wave-driven inner-shelf circulation. Annual Review of Marine Science 4(1): 317-343. doi:10.1146/annurev-marine-120709-142745.

Li Z, Weisberg RH. 1999. West Florida continental shelf response to upwelling favorable wind forcing: Dynamics. Journal of Geophysical Research 104: 23427-23442.

Lwiza K, Bowers D, Simpson J. 1991. Residual and tidal flow at a tidal mixing front in the North Sea. Continental Shelf Research 11: 1379-1395. doi:10.1016/0278-4343(91)90041-4.

McNinch JE, Luettich RA. 2000. Physical processes around a cuspate foreland: implications to the evolution and long-term maintenance of a cape-associated shoal. Continental Shelf Research 20(17): 2367-2389. doi.org/10.1016/S0278-4343(00)00061-3.

Minobe S, Kuwano-Yoshida A, Komori N, Xie S-P, Small RJ. 2008a. Influence of the Gulf Stream on the troposphere. Nature 452(7184): 206-209. doi:10.1038/nature06690.

Minobe S, Kuwano-Yoshida A, Komori N, Xie S-P, Small RJ. 2008b. The Gulf Stream's pathway to impact climate. International Pacific Research Center Climate 8(1): 1-8.

Pollard R, Read J. 1989. A method for calibrating shipmounted acoustic doppler profilers and the limitations of gyro compasses. Journal of Atmospheric and Oceanic Technology 6(6): 859-865.

Russel R. 2007. Thermohaline ocean circulation. [accessed 7 July]. https://www.windows2universe.org/?page=%2Fearth%2FWater%2Fthermohaline_ocean_circulation.html.

Salas-Monreal D, Valle-Levinson A. 2009. Continuously stratified flow dynamics over a hollow. Journal of Geophysical Research: Oceans 114 (C03021) doi.org/10.1029/2007JC004648.

Sanay R, Voulgaris G, Warner J. 2007. Influence of tidal asymmetry and residual circulation on sediment transport in linear sandbanks: A processes-oriented numerical study. Journal of Geophysical Research 112. doi:10.1029/2007JC004101.

Stenström P. 2003. Mixing and recirculation in two-layer exchange flows. Journal of Geophysical Research 108: 3256.

Valle-Levinson A. 2008. Density-driven exchange flow in terms of the Kelvin and Ekman numbers. Journal of Geophysical Research: Oceans 113 (C4001) doi.org/10.1029/2007JC004144.

Valle-Levinson A, Guo X. 2009. Asymmetries in tidal flow over a Seto Inland Sea scour pit. Journal of Marine Research 67(5): 619-635. doi:10.1357/002224009791218850.

Valle-Levinson A, Huguenard K, Ross L, Branyon J, Macmahan J, Reniers A. 2015. Tidal and nontidal exchange at a subtropical inlet: Destin Inlet, Northwest Florida. Estuarine, Coastal and Shelf Science 155: 137-147. doi:10.1016/j.ecss.2015.01.020.

Valle-Levinson A, O'Donnell J. 1996. Tidal interaction with buoyancy-driven flow in a coastal plain estuary. In: Aubrey DG, Friedrichs C, editors. Buoyancy Effects on Coastal and Estuarine Dynamics. American Geophysics Union, Washington, DC. p. 265-281. https://agupubs.onlinelibrary.wiley.com/doi/abs/10.1029/CE053p0265.

Valle-Levinson A, Reyes C, Sanay R. 2003. Effects of bathymetry, friction, and rotation on estuary–ocean exchange. Journal of Physical Oceanography 33(11): 2375-2393. doi:10.1175/1520-0485(2003)033<2375:Eobfar>2.0.Co;2.

Valle-Levinson A, Wong K-C, Lwiza KMM. 2000. Fortnightly variability in the transverse dynamics of a coastal plain estuary. Journal of Geophysical Research: Oceans 105(C2): 3413-3424. doi.org/10.1029/1999JC900307.

Winters KB, Seim HE. 2000. The role of dissipation and mixing in exchange flow through a contracting channel. Journal of Fluid Mechanics 407: 265-290. doi:10.1017/S0022112099007727.

Wong K-C. 1994. On the nature of transverse variability in a coastal plain estuary. Journal of Geophysical Research: Oceans 99(C7): 14209-14222. doi.org/10.1029/94JC00861.

Zlotnicki V. 1991. Sea level differences across the Gulf Stream and Kuroshio Extension. Journal of Physical Oceanography 21: 599-609.
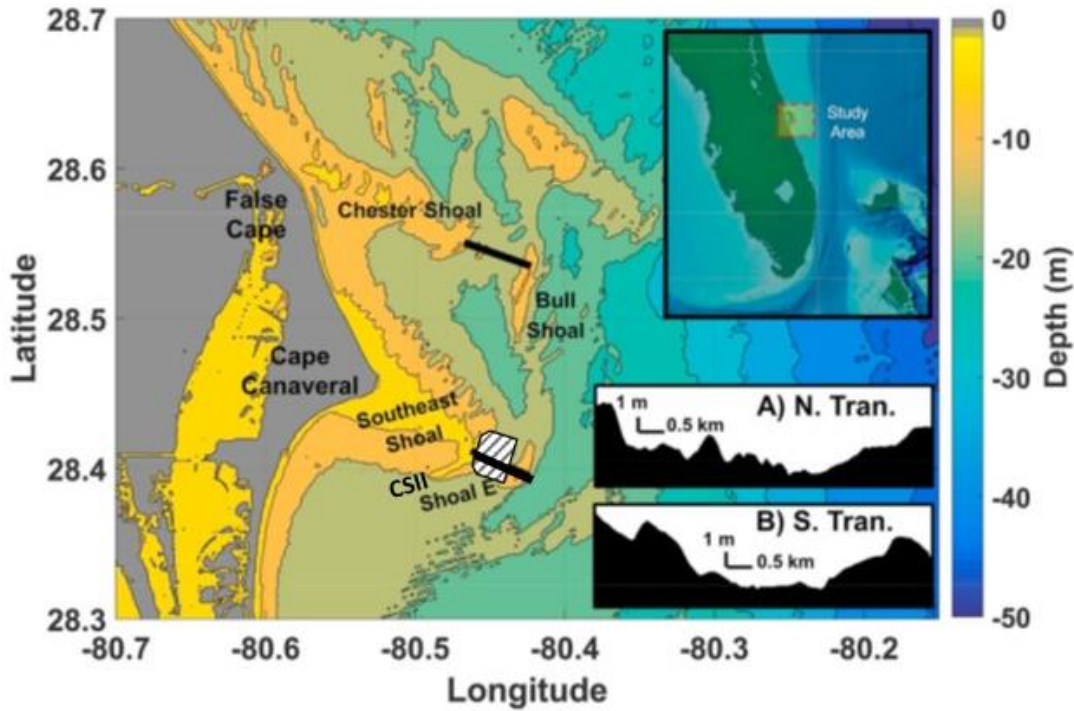
Figure 2-1. Bathymetric map of Cape Canaveral with the location of the two ADCP transects surveyed between 24 September 2013 and 29 June 2016.
The red dotted line in the inset map shows the location of the study area relative to Florida. In the main figure, the thick black lines represent the paths of the two transects. The striped area is the borrow area (CSII-BA) of Canaveral Shoal II (CSII); CSII-BA was the area where dredging was permitted. Plots A) and B) show the bathymetry of the north transect and south transect, respectively.
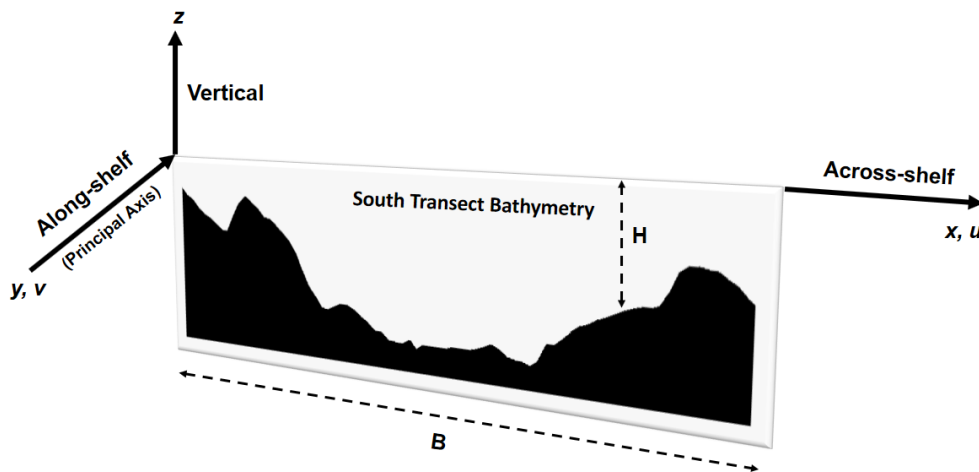
Figure 2-2. Schematic representation of the model reference frame for the south transect bathymetric profile.
B was the cross-sectional width, H was water depth, and the arrows show the along-shelf and across-shelf directions. The same reference frame was used for the north transect.

25
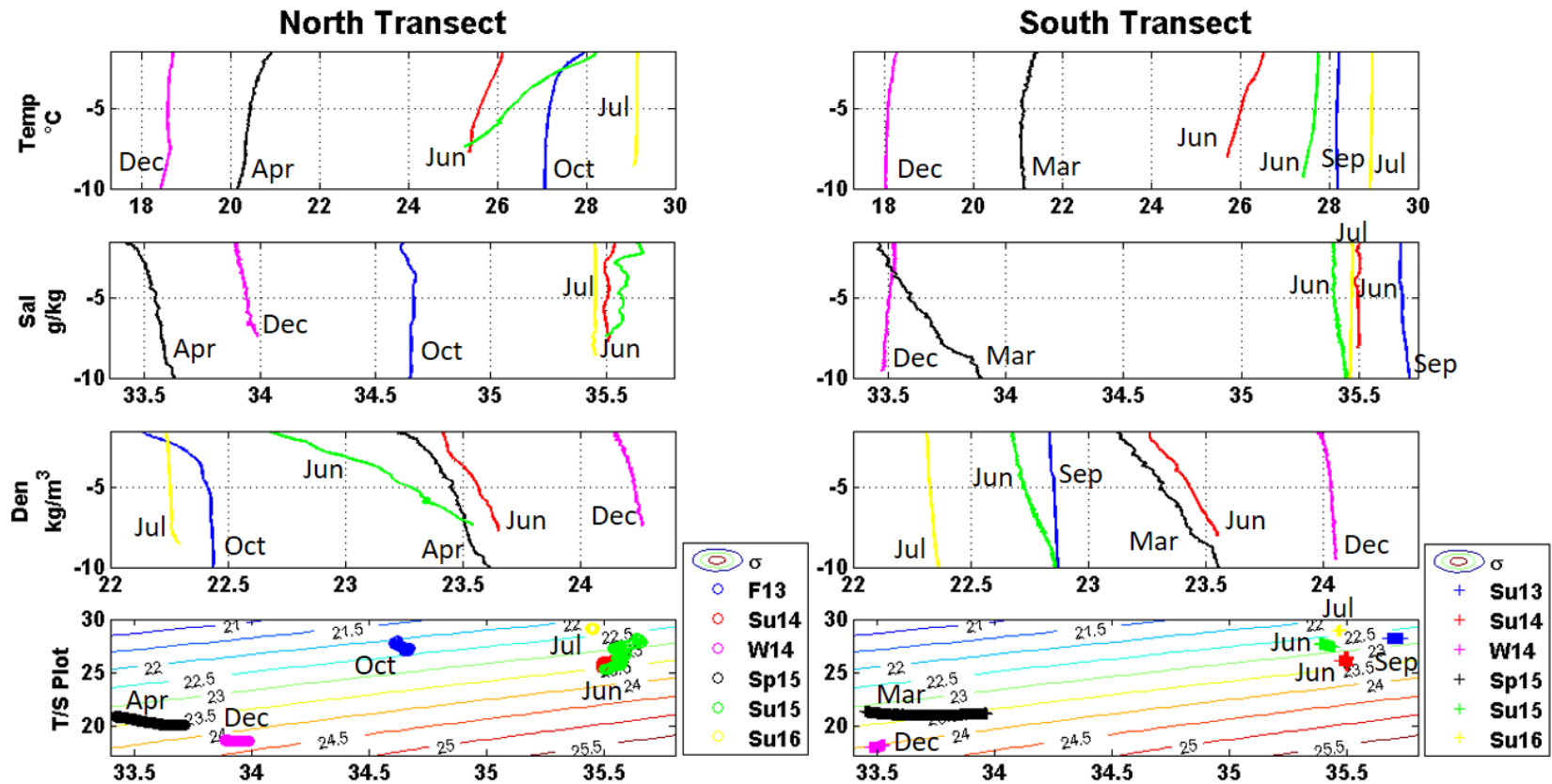
Figure 2-3. Hydrographic data for the north and south transects during all tows performed between fall 2013 and summer 2016.
The first row shows temperature (°C) profiles at the two locations; the second row shows salinity (g/kg); the third row shows density (kg/m³); and the last row gives the temperature/salinity diagrams. Season and year legend includes Sp (spring), Su (summer), F (fall), and W (winter).
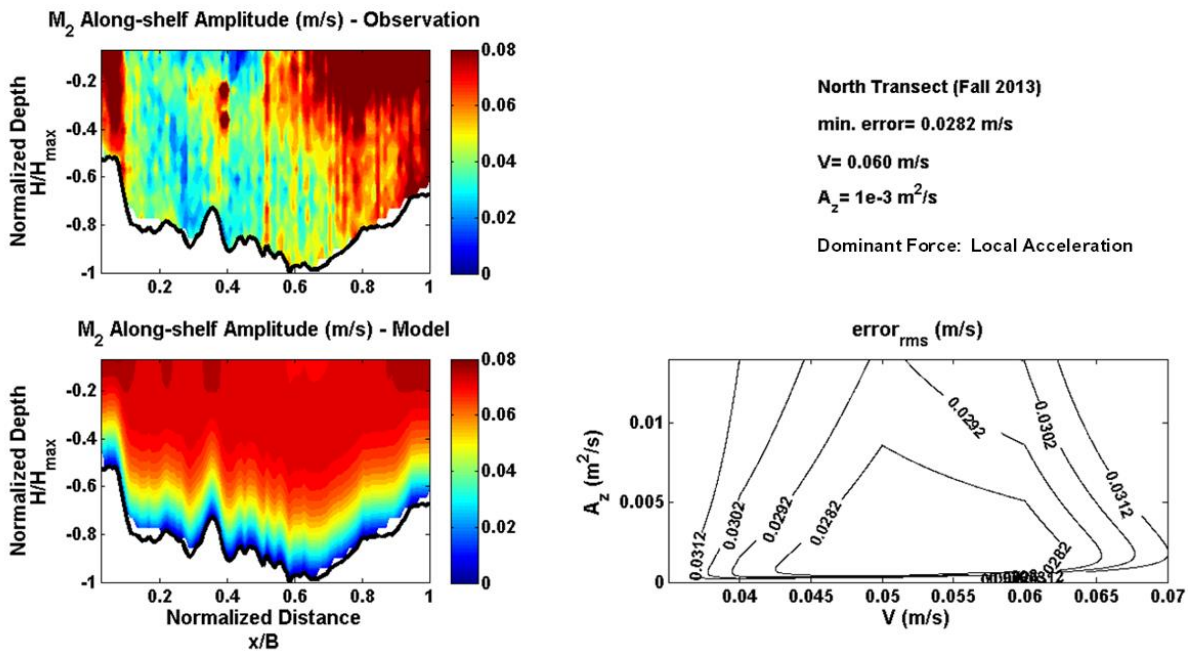
Figure 2-4. A comparison between the observation (top) and tidal model (bottom) amplitudes for the north transect during fall 2013.

Left panels: thick black line at the bottom represents bathymetry. Contours of root-mean-squared error (lower right panel) shows the best combination of V and A_z values, where V = sectional average tidal current amplitude and A_z = vertical eddy viscosity.
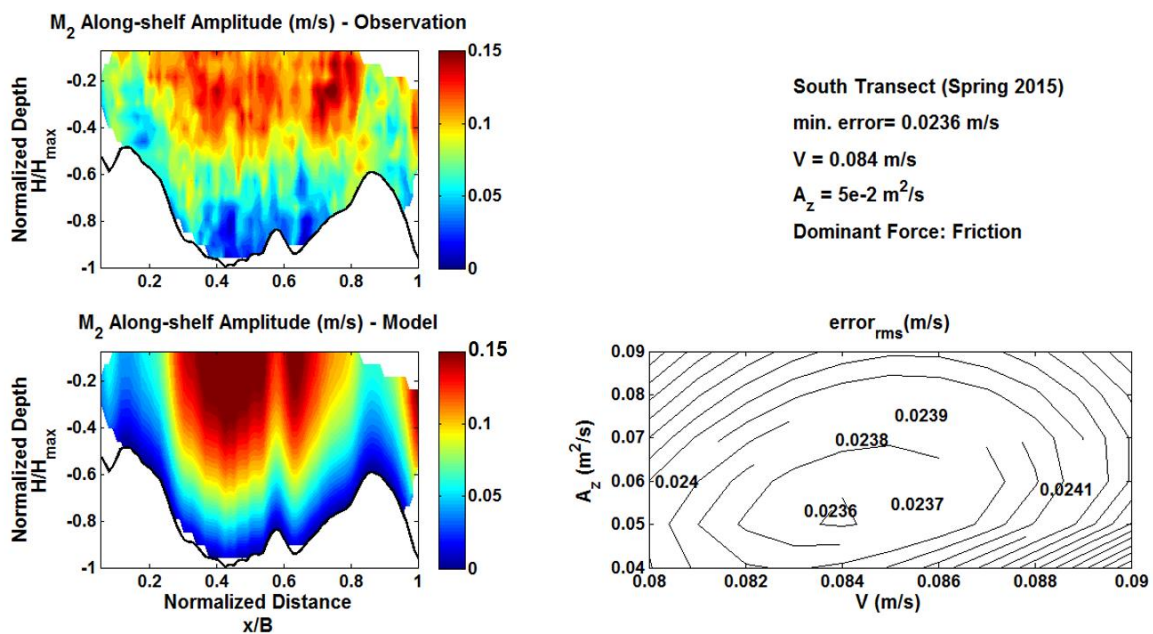
Figure 2-5. A comparison between the observation (top) and tidal model (bottom) amplitudes for the south transect during spring 2015.

Notation as in Figure 2-4.
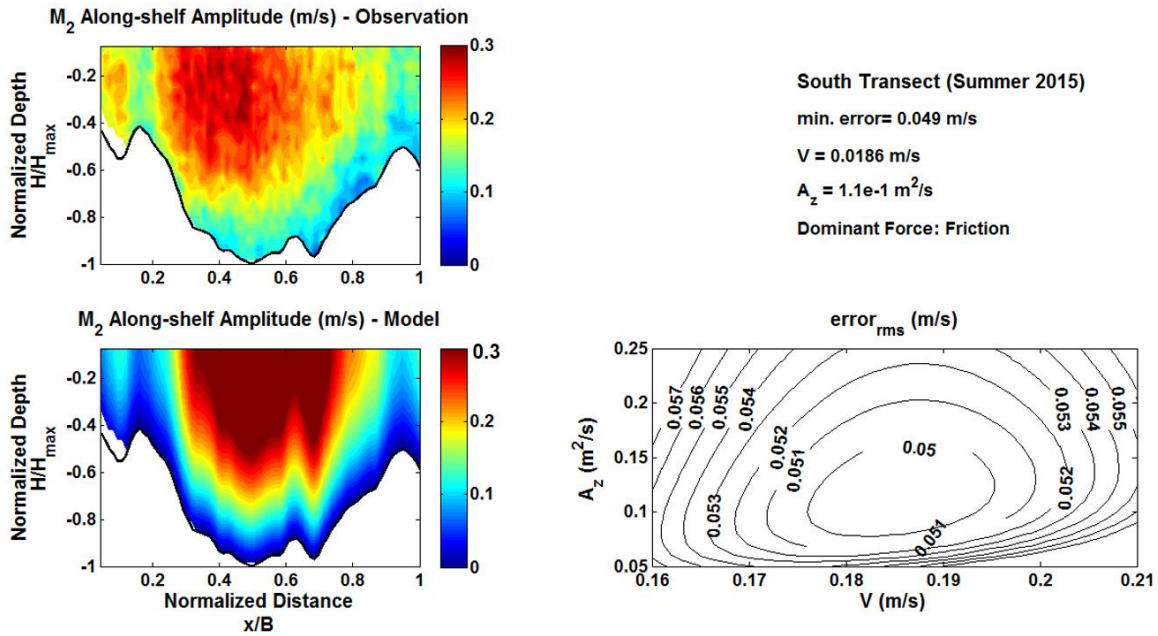
Figure 2-6. A comparison between the observation (top) and tidal model (bottom) amplitudes for the south transect during summer 2015.
Notation as in Figure 2-4.
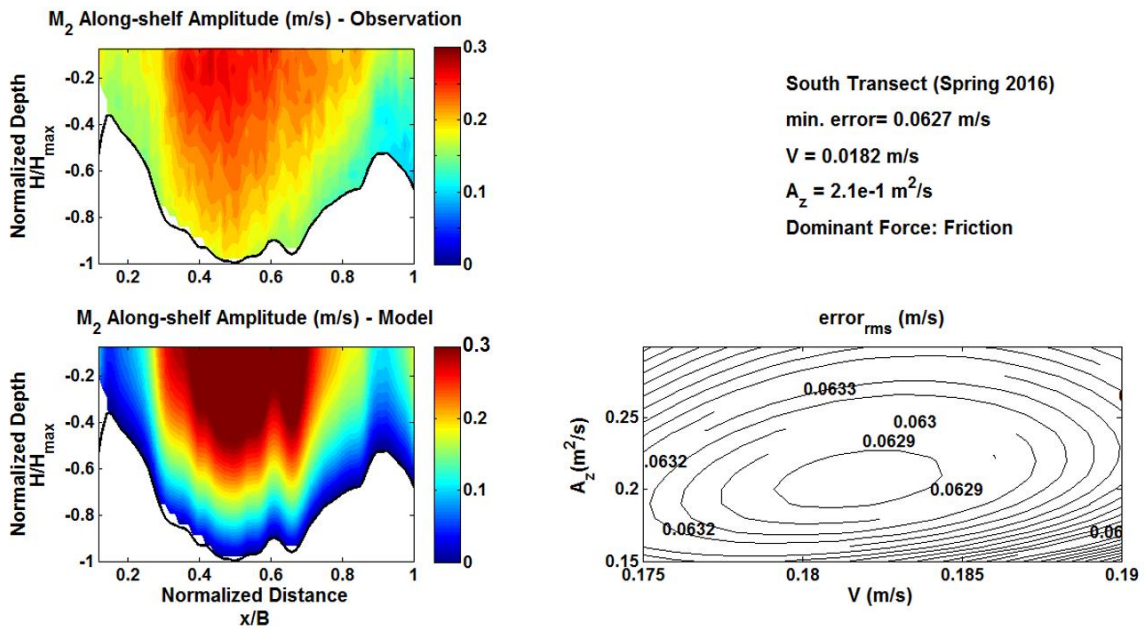
Figure 2-7. A comparison between the observation (top) and tidal model (bottom) amplitudes for the south transect during spring 2016.
Notation as in Figure 2-4.
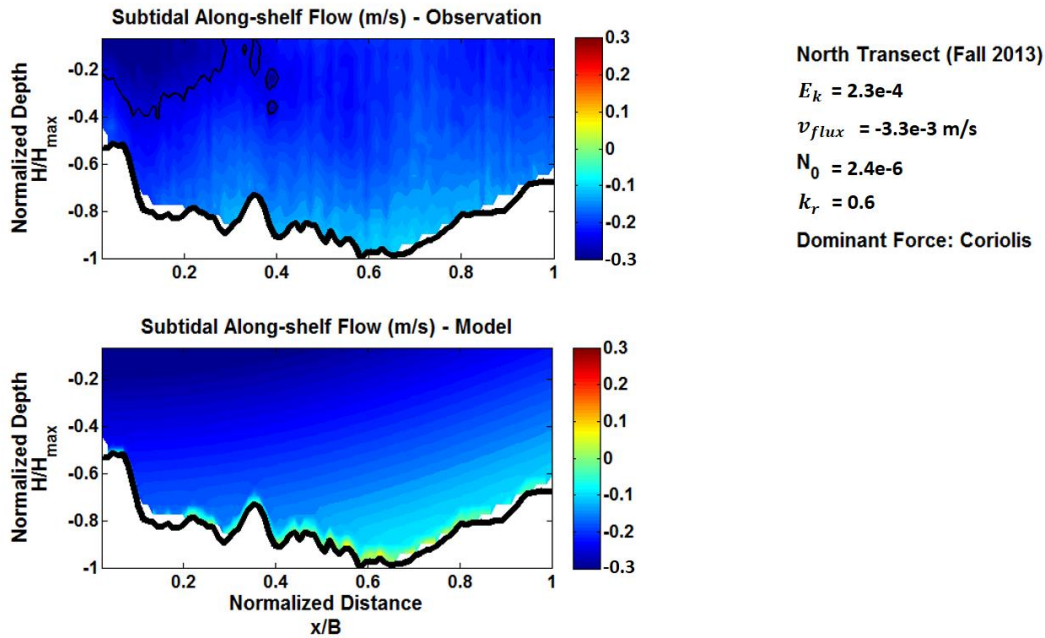
Figure 2-8. A comparison between the observation (top) and subtidal model (bottom) velocities for the north transect during fall 2013.

The black line at the bottom represents bathymetry, while the black contour represents the location of the strongest currents. Variables are given in Section 2.2.2.3.4.
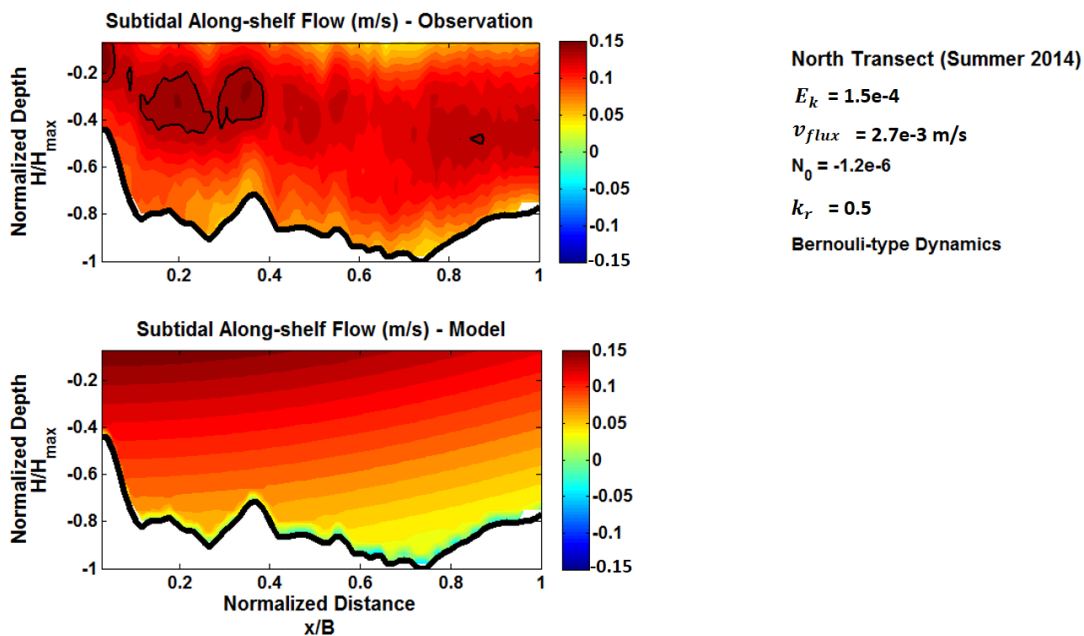
Figure 2-9. A comparison between the observation (top) and subtidal model (bottom) velocities for the north transect during summer 2014.

Notation as in Figure 2-8.
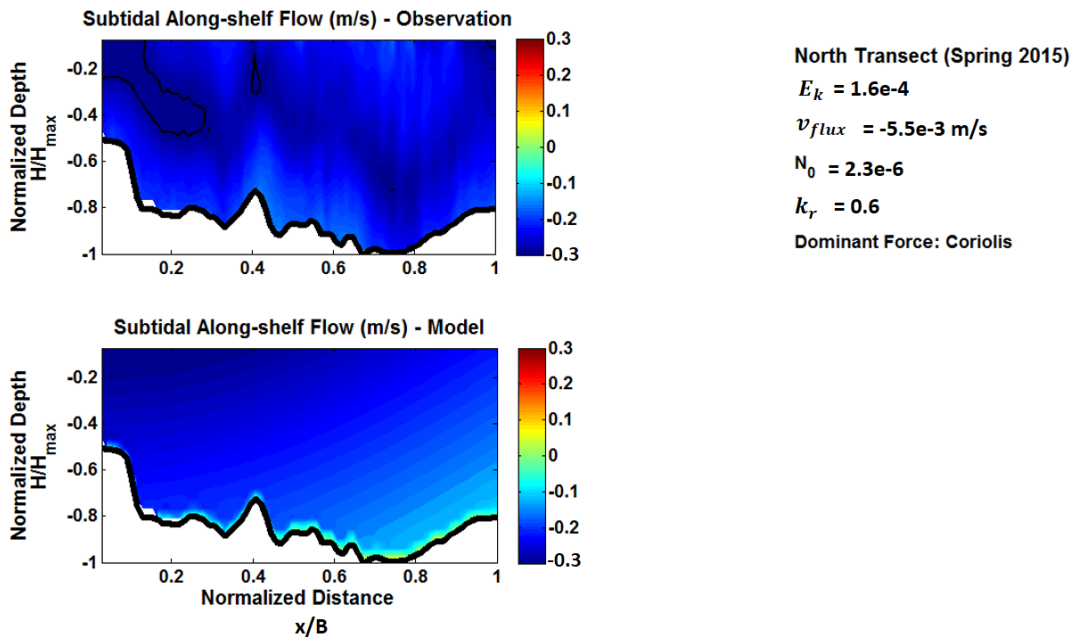
Figure 2-10. A comparison between the observation (top) and subtidal model (bottom) velocities for the north transect during spring 2015.

Notation as in Figure 2-8.
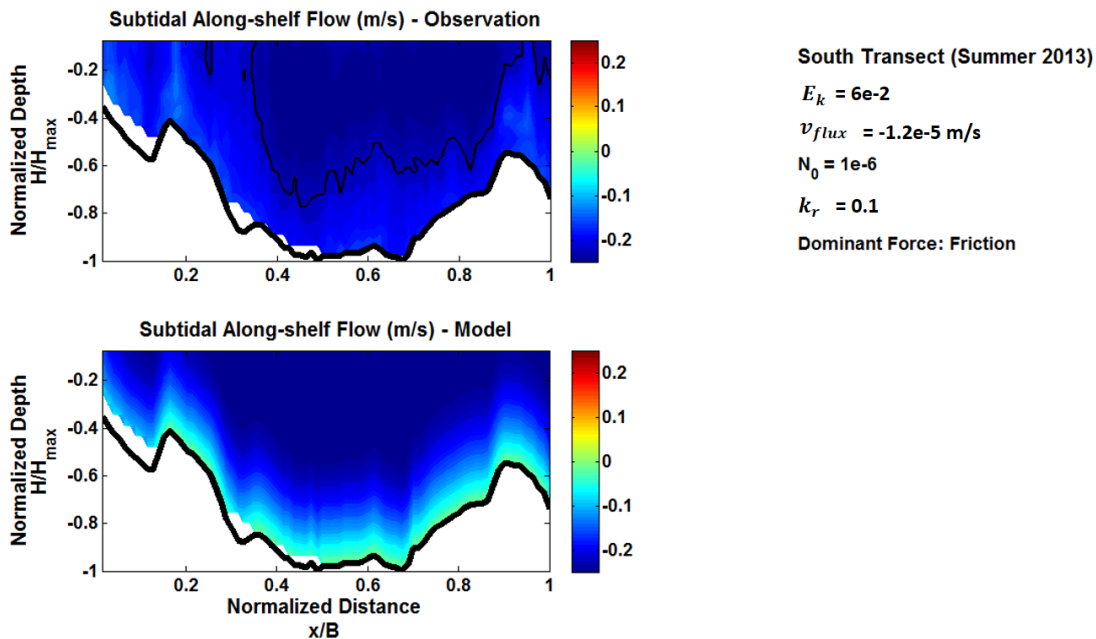
Figure 2-11. A comparison between the observation (top) and subtidal model (bottom) velocities for the south transect during summer 2013.

Notation as in Figure 2-8.
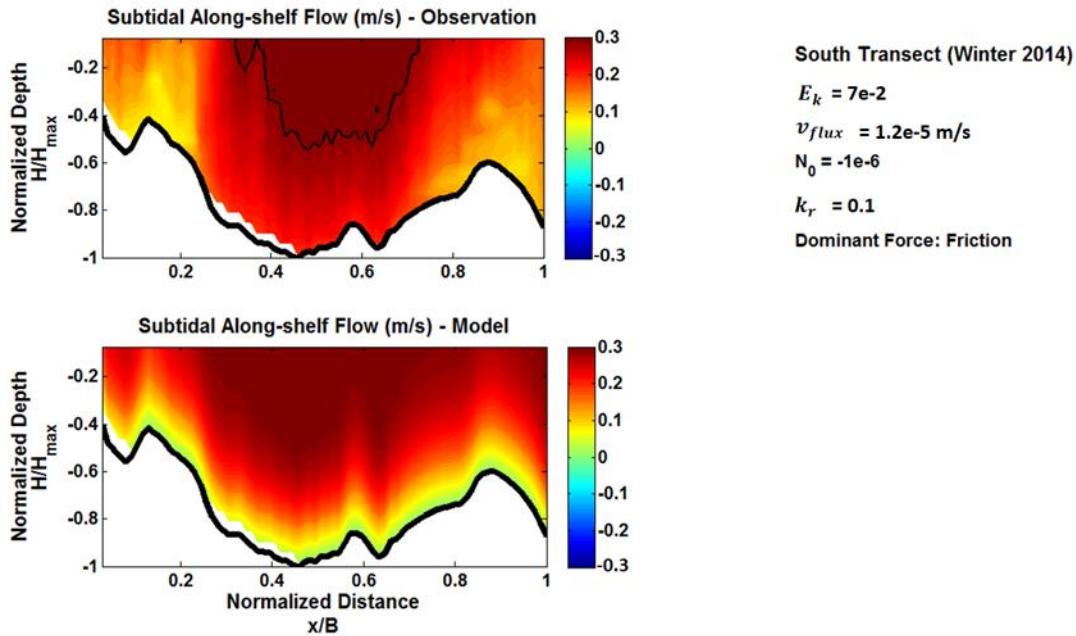
Figure 2-12. A comparison between the observation (top) and subtidal model (bottom) velocities for the south transect during winter 2014.
Notation as in Figure 2-8.
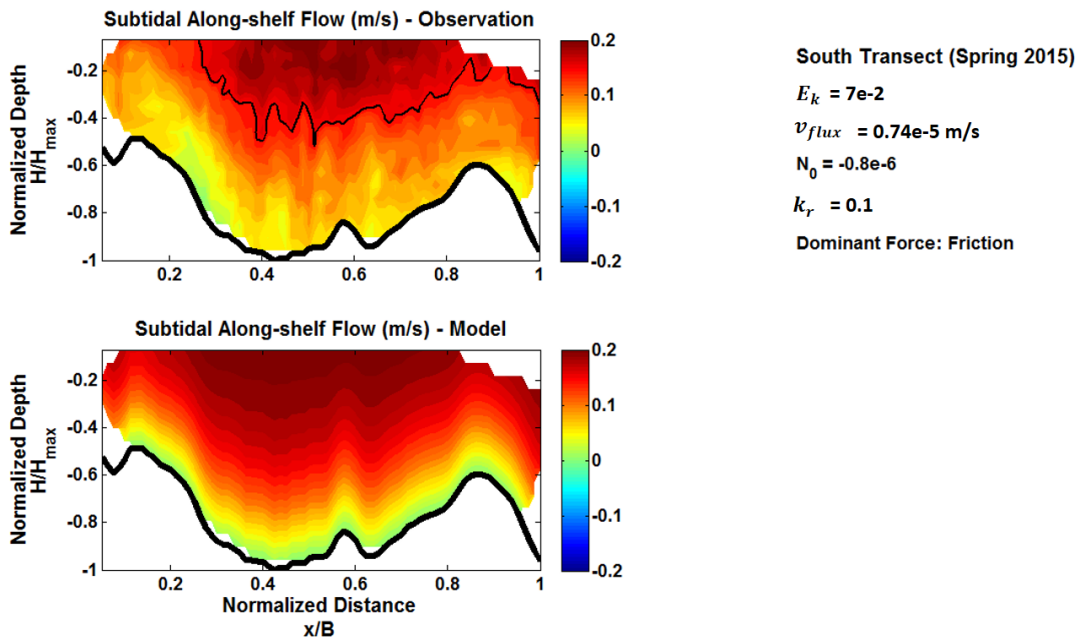
Figure 2-13. A comparison between the observation (top) and subtidal model (bottom) velocities for the south transect during spring 2015.
Notation as in Figure 2-8.
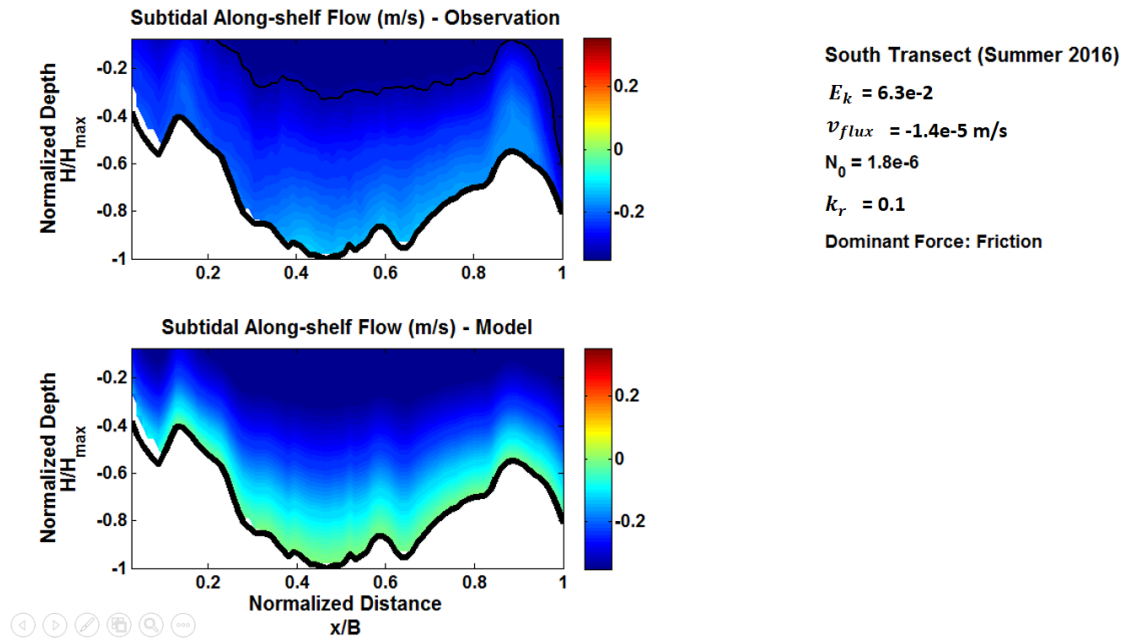
Figure 2-14. A comparison between the observation (top) and subtidal model (bottom) velocities for the south transect during summer 2016.
Notation as in Figure 2-8.

2.3 Subinertial Hydrodynamics Over Ridge-swale Bathymetry Around a Cape

2.3.1 Introduction

Previous studies performed on inner, mid, and outer shelves indicated that the across-shelf momentum balance was predominantly geostrophic (Allen and Kundu 1978; Noble et al. 1983; Lee et al. 1984, 1989; Brown et al. 1985; Thompson and Pugh 1986; Brown et al. 1987; Lentz et al. 1999; Li and Weisberg 1999a; 1999b; Shearman and Lentz 2003; Liu and Weisberg 2005; Fewings and Lentz 2010). While the along-shelf momentum was expected to be more frictional, the pressure gradient was mainly balanced by surface and bottom stresses (Lentz et al. 1999; Li and Weisberg 1999b; Liu and Weisberg 2005; Fewings and Lentz 2010; Lentz and Fewings 2012).

Inner-shelf morphology and hydrodynamics can be modified by capes. Capes and their associated shoals are characterized by complex bathymetry, as they represent a sudden change in the coastline orientation (Kumar et al. 2013) and water depth. Kline et al. (2012) performed a study to gain a better understanding on the interaction of the ridge-swale bathymetry off Cape Canaveral in Florida, particularly with the incoming deep-water waves and their role in redistributing the wave energy along and across the shore. However, the effect of such bathymetry on the subtidal/subinertial circulation processes remains unexplored (Kumar et al. 2013). The objective of this study was to determine the subinertial hydrodynamics off a cape with a ridge-swale bathymetry that was located in an inner shelf by a) using statistical techniques to assess the response of the subinertial flow to different forcings and b) calculating the momentum balance along and across the shelf. Because ridges transform the dynamic (i.e., momentum balance) relevance of wind waves via wave stresses, it is essential to determine the contribution of wave stresses to existing conditions on the shelf (c.f., Equation 21). Dredging operations that alter ridges would also affect the impact of waves on the hydrodynamics and their consequence on erosion.

2.3.2 Methods

2.3.2.1 Study Area

This study focused on CSII-BA (the borrow area of Canaveral Shoals II), Shoal E directly east of CSII, and Chester Shoal (Figure 2-15), as described previously in Section 2.2.2. Tidal conditions in this region were summarized previously in Section 2.2.2, and temperature and salinity interactions relative to the Florida Current were summarized previously in Section 2.2.4.

2.3.2.2 Data Collection

We deployed ADCPs at Shoal E and Chester Shoal to determine the subinertial hydrodynamics of the ridge-swale bathymetry. Two sites were at each side of Chester Shoal (named Chester swale west and Chester swale east, respectively) and another two were at each side of Shoal E (named Shoal E swale west and Shoal E swale east, respectively), for a total of four sites (Figure 2-15). The ADCP at Shoal E swale west was located in the borrow area of Canaveral Shoal II (i.e., CSII-BA) (Figure 2-15). Data were collected during spring 2014 for 31 days, between 6 May and 6 June 2014. The bottom-mounted ADCPs recorded water bottom temperature, pressure, current profiles, and wave heights and direction. More details on the locations of the ADCP moorings and the data sampling schemes are provided in Table 2-1.

Hydrographic data were collected from seasonal cruises between fall 2013 and summer 2016 using Castaway and Sea Bird 19 Plus CTD profilers. Three CTD casts were taken along two transects seaward. The location of these transects relevant to the ADCP moorings is shown in Figure 2-15. Records of the hourly winds for the period of the deployment were collected from the National Oceanic and Atmospheric

Administration's (NOAA's) National Data Buoy Center (NDBC) station 41009, located at 28.52° N and 80.18° W (data available at http://www.ndbc.noaa.gov/). The station is approximately 25 km east of Bull Shoal over a water depth of ~45 m (Figure 2-15). Hourly sea-level records at Trident Pier were collected from the NOAA's National Ocean Service tidal gauge (data available at https://opendap.co-ops.nos.noaa.gov/) at station TRDF1 (ID# 8721604), located at Canaveral Port inlet (28.42° N, 80.59° W). The daily mean transport of the Florida Current was measured by NOAA's Atlantic Oceanographic and Meteorological Laboratory (data available at www.aoml.noaa.gov/phod/floridacurrent/) using a submarine cable spanning from West Palm Beach, Florida, to Eight Mile Rock, Bahamas (Figure 2-15). It is located ~200 km southeast of Cape Canaveral, Florida. Bathymetric data for the region were obtained from NOAA's National Geophysical Data Center (NGDC) using the United States Coastal Relief Model (data available at https://ngdc.noaa.gov/mgg/coastal/crm.html).

2.3.2.3 Data Analysis

2.3.2.3.1 Filtering

Low-frequency time series were obtained by filtering the measured observations with a 30-hour low-pass Lanczos filter to remove the oscillations associated with tidal motion (of ~12 hr) and inertial oscillations (of ~25 hr). Time series at different depths only describe the variance at subtidal and subinertial periods.

2.3.2.3.2 Concatenated Hilbert Empirical Orthogonal Function (CHEOF)

CHEOF was used to obtain the dominant modes of the subinertial currents at the four locations along with their spatial and temporal structures. The along- and across-shelf velocity components at the four locations were concatenated into one matrix to see how they interacted with each other. The real part of the complex time series was the original observation, and the imaginary part was phase shifted by $\pi/2$. The principal modes of covariation were determined by finding the eigenvalues and eigenvectors of the complex co-variance matrix (Emery and Thomson 1998). CHEOF was used instead of the Concatenated Real-vector Empirical Orthogonal Function (CREOF) because CHEOF has a better phase. Concatenated Complex Empirical Orthogonal Function (CCEOF) was not used in this study because it does not preserve the vector nature and therefore may have direction ambiguity in the eigenstructures (Kaihatu et al. 1998).

2.3.2.3.3 Wavelet Analysis

Unlike the spectral analysis, the wavelet analysis is very helpful for analyzing nonstationary time series in which the amplitudes and phases may be changing in time or space (Emery and Thomson 1998). Wavelet transform was calculated as the following (Grinsted et al. 2004):

$$W_n^x(s) = \sqrt{\frac{\delta t}{s}} \sum_{n'=1}^{N} x_{n'} \psi_0 \left[(n' - n) \frac{\delta t}{s} \right] \tag{19}$$

where the wavelet transform of a time series (x_n, $n = 1, \ldots, N$) with uniform time steps δt was defined as the convolution of x_n with the scaled and normalized wavelet $W_n^x(s)$. In Equation 19, ψ_0 stands for Morlet wavelet, s stands for the scale, and n stands for time index. Wavelet coherence can determine the periods at which two time series (X and Y) have high common power, whether they were coherent at those periods, and their phase (Grinsted et al. 2004). Wavelet Coherence, $R_n^2(s)$, was calculated as the following (Grinsted et al. 2004):

$$R_n^2(s) = \frac{\left| S\left(s^{-1} W_n^{XY}(s)\right) \right|^2}{S\left(s^{-1} |W_n^X(s)|^2\right) * S\left(s^{-1} |W_n^Y(s)|^2\right)} \tag{20}$$

where S was a smoothing operator in time and frequency, W^X and W^Y were the wavelets of each time series, W^{XY} was the cross wavelet, the terms $|W_n^X(s)|^2$, $|W_n^Y(s)|^2$, and $|W_n^{XY}(s)|^2$ represented the power, and s^{-1} was used to convert to energy density. The wavelet coherence had values between 0 and 1, with its direction representing the phase. Arrows pointing to the right (90° clockwise from the top) mean that X and Y were in 0° phase. Arrows pointing to the left (270° clockwise from the top) mean that X and Y were out-of-phase by 180°. Arrows pointing downward (180° clockwise from the top) mean X was leading Y by 90º, while arrows pointing upward mean Y was leading X by 90º. Using wavelet analysis techniques to compare the time series of the most dominant mode of CHEOF with different forcings helps us to understand their relationship and how they interact with one another.

2.3.2.3.4 Depth-averaged Along-Shelf Momentum Balance

The depth-averaged along-shelf momentum balance was calculated to determine the dominant forces driving the along-shelf subinertial currents around the nearshore bathymetric features. The equation was as follows (Lentz and Fewings 2012):

$$\frac{\partial \bar{V}}{\partial t} + \bar{U}\frac{\partial \bar{V}}{\partial x} + \bar{V}\frac{\partial \bar{V}}{\partial y} + f(\bar{U} + \bar{U}_{st}) = -g\frac{\partial \eta}{\partial y} + \frac{\tau_{sy}-\tau_{by}}{\rho_o h} - \frac{1}{\rho_o h}\left(\frac{\partial S_{xy}}{\partial x} + \frac{\partial S_{yy}}{\partial y}\right) - \frac{\tau_{bwy}}{\rho_o h} \tag{21}$$

where $\bar{V}$ was the depth-averaged along-shelf current, $\bar{U}$ was the across-shelf current, $\bar{U}(\partial \bar{V}/\partial x) + \bar{V}(\partial \bar{V}/\partial y)$ were the along-shelf nonlinear advection terms, $f = 2\Omega sin\theta_{lat}$ was the Coriolis frequency, Ω was the Earth's angular rotation rate, θ_{lat} was the latitude (28.5°), $\bar{U}_{st}$ was the across-shelf Stokes drift velocity, g was the acceleration due to gravity, η was the sea level, $g(\partial \eta/\partial y)$ was the along-shelf barotropic pressure gradient, τ_{sy} was the along-shelf wind stress, τ_{by} was the along-shelf bottom stress, ρ_o was a reference seawater density, h was the undisturbed water depth, S_{xy} and S_{yy} were radiation stresses due to incident waves, τ_{bwy} was the along-shelf bottom stress due to waves, and the overbar represents depth averages for the current velocity terms.

Only the barotropic pressure gradient was considered in the momentum balance since the hydrographic data showed a small change in density within the area of study. This consideration justified the assumption of a homogenous water column and neglecting the baroclinic component.

The across-shelf Stokes drift velocity was estimated using linear wave theory (Stokes 1847; Mei 1983; Xu and Bowen 1994; Fewings et al. 2008; Lentz et al. 2008; Fewings and Lentz 2010; Lentz and Fewings 2012):

$$\bar{U}_{st} = \frac{H_s^2 \omega k}{16} \frac{cosh[2k(z+h)]}{sinh^2(kh)} cos\theta_w \tag{22}$$

where H_S was the significant wave height, ω was the angular wave frequency, k was the wavenumber, z was the vertical coordinate with $z = 0$ at the mean water surface, and θ_w was the direction the waves were propagating, measured counterclockwise from the positive x-direction, so $\theta_w = 0$ for waves propagating onshore (Longuet-Higgins and Stewart 1964; Mei 1983; Lentz and Fewings 2012).

The along-shelf surface stress was estimated as in Smith (1988):

$$\tau_{sy} = \rho_a C_a |W| W_y \tag{23}$$

where ρ_a was the density of air (1.23 kg/m³, according to the International Standard Atmosphere), W was the wind velocity, W_y was the along-shelf velocity component, and C_a was the air-water drag coefficient considered to be $1.2x10^{-3}$ when $W < 11$ m/s and calculated as $(0.49 + 0.065W)x10^{-3}$ for $11 \leq W <$

25 m/s (Large and Pond 1981). Bottom stress was calculated using the quadratic drag formula (Lee et al. 1984; Geyer et al. 2000; Liu and Weisberg 2005; Fewings and Lentz 2010):

$$\tau_{by} = \rho_0 C_D |\overline{\boldsymbol{U}_b}| \overline{V}_b \tag{24}$$

where $\overline{\boldsymbol{U}_b} = (\overline{U}_b, \overline{V}_b)$ was the bottom velocity vector and C_D was the nondimensional bottom drag coefficient, generally $2.5x10^{-3}$ for sandy bottoms (Lee et al. 1984; Valle-Levinson et al. 2003, 2015; Liu and Weisberg 2005; Salas-Monreal and Valle-Levinson 2009).

The radiation stresses were estimated using linear wave theory as follows (Longuet-Higgins and Stewart 1964; Lentz and Fewings 2012):

$$S_{yy} = E \left[\frac{c_g}{c} (sin^2\,\theta_w + 1) - \frac{1}{2} \right] \tag{25}$$

$$S_{xx} = E \left[\frac{c_g}{c} (cos^2\,\theta_w + 1) - \frac{1}{2} \right] \tag{26}$$

$$S_{xy} = E \frac{c_g}{c} cos\,\theta_w\,sin\,\theta_w \tag{27}$$

where $E = \rho_o g H_s^2 / 16$ was the wave energy, $H_{rms} = \frac{1}{\sqrt{2}} H_s$ was the root-mean-square wave height, c_g was the wave group velocity, and c was the phase speed of the waves. The gradients were estimated using a finite difference approximation between locations. The along-shelf bottom stress due to the waves was estimated as follows (Longuet-Higgins 1953; Xu and Bowen 1994; Lentz et al. 2008):

$$\tau_{bwy} = \frac{H_s^2 \omega^2 k}{16\,sinh^2(kh)} \left[(-\beta z'sin\beta z' + (\beta z' - 1)cos\beta z')e^{-\beta z'} - e^{-2\beta z'} \right] sin\theta_w \tag{28}$$

where $\beta = \sqrt{\omega/2A_z}$, A_z was the vertical eddy viscosity used to represent the turbulent Reynolds stresses, and $z' = h + z$ was the height above the bottom.

2.3.2.3.5 Depth-averaged Across-Shelf Momentum Balance

The depth-averaged across-shelf momentum balance was calculated to determine the dominant forces driving the across-shelf subinertial currents around the nearshore bathymetric features. The equation was as follows (Lentz and Fewings 2012):

$$\frac{\partial \overline{U}}{\partial t} + \overline{U} \frac{\partial \overline{U}}{\partial x} + \overline{V} \frac{\partial \overline{U}}{\partial y} - f(\overline{V} + \overline{V}_{st}) = -g \frac{\partial \eta}{\partial x} + \frac{\tau_{sx} - \tau_{bx}}{\rho_o h} - \frac{1}{\rho_o h} \left(\frac{\partial S_{xx}}{\partial x} + \frac{\partial S_{xy}}{\partial y} \right) - \frac{\tau_{bwx}}{\rho_o h} \tag{29}$$

where $\overline{U}(\partial \overline{U}/\partial x) + \overline{V}(\partial \overline{U}/\partial x)$ were the across-shelf nonlinear advection terms, $\overline{V}_{st}$ was the along-shelf Stokes drift velocity, $g(\partial \eta/\partial x)$ was the across-shelf pressure gradient, τ_{sx} was the across-shelf surface stress due to the winds, τ_{bx} was the across-shelf bottom stress, and τ_{bwx} was the across-shelf bottom stress due to the waves. The along-shelf Stokes drift velocity was estimated using linear wave theory (Stokes 1847; Mei 1983; Xu and Bowen 1994; Fewings et al. 2008; Lentz et al. 2008; Fewings and Lentz 2010; Lentz and Fewings 2012):

$$\overline{V}_{st} = \frac{H_s^2 \omega k}{16} \frac{cosh[2k(z+h)]}{sinh^2(kh)} sin\,\theta_w \tag{30}$$

The across-shelf surface stress was estimated as Smith (1988):

$$\boldsymbol{\tau}_{sx} = \rho_a C_a |\boldsymbol{W}| W_x \tag{31}$$

where W_x was the across-shelf velocity component.

The across-shelf bottom stress was calculated using the quadratic drag law (Lee et al. 1984; Geyer et al. 2000; Liu and Weisberg 2005; Fewings and Lentz 2010):

$$\boldsymbol{\tau_{bx}} = \rho_0 C_D |\boldsymbol{\bar{U}_b}| \bar{U}_b \tag{32}$$

The across-shelf near-bottom stress generated by waves was estimated as follows (Xu and Bowen 1994; Lentz et al. 2008):

$$\tau_{bwx} = \frac{H_s^2 \omega^2 k}{16\,sinh^2(kh)} \left[(-\beta z' sin\beta z' + (\beta z' - 1)cos\beta z')e^{-\beta z'} - e^{-2\beta z'} \right] cos\theta_w \tag{33}$$

2.3.2.3.6   Geostrophic Balance

The influence of the Florida Current on sea level can be quantified using the following geostrophic balance equation between Coriolis acceleration and the barotropic pressure gradient:

$$f\bar{V}_{FC} = g\frac{\Delta\eta}{\Delta x} = g\frac{\eta_{FC}-\eta_{coast}}{x_{FC}-x_{coast}} \tag{34}$$

where $\bar{V}_{FC}$ was the Florida Current transport (m/s), $\Delta\eta$ was the difference in sea level across-shelf, Δx was the change in location across-shelf, η_{FC} was the sea level at the location of the Florida Current (x_{FC}), and η_{coast} was the coastal sea level obtained from the tidal gauge located at Trident Pier (x_{coast}).

Equation 34 shows a direct correlation between the Florida Current and sea-level slope. As the Florida Current gets stronger, the Coriolis force becomes stronger. Therefore, the sea-surface slope has to increase in order to keep a balance of forces. In other words, the sea level at the location of the Florida Current has to increase, while the sea level at the coast has to decrease to maintain a geostrophic balance. In contrast, as the Florida Current gets weaker, the Coriolis force becomes weaker as well. Consequently, the sea-surface slope has to decrease and the sea level at the coast has to increase.

2.3.2.3.7   Ekman Dynamics

In deep water, an Ekman spiral is developed due to the Coriolis effect. The wind moves the surface water 45° east of the wind in the northern hemisphere due to the Coriolis effect. Likewise, deeper layers of water molecules are dragged and deflected by the Coriolis effect. Each deeper layer moves slower than the layer above it creating a spiral effect. As a result, net water transport is generated 90° from the wind (Ekman 1905). The depth of the Ekman layer, along which an Ekman spiral effect is noted, can be calculated as follows (Valle-Levinson et al. 2003; Valle-Levinson 2008):

$$D_E = \left(\frac{2A_z}{f}\right)^{1/2} \tag{35}$$

The shallowness of water in inner shelves relative to the surface and bottom boundary layer thicknesses allows those boundaries to fill the entire water column (Fewings and Lentz 2010). Thus, inner shelves are often described as the regions where the surface and bottom boundary layers overlap (Lentz 1995; Lentz and Fewings 2012) or where the surface and bottom Ekman layers overlap (Li and Weisberg 1999b). Therefore, the water depth at the locations of the deployments (9 m to 14 m) on each side of the shoals may not have required as strong wind stress to influence the subinertial flow, nor did it allow the complete formation of the Ekman spiral. Using an analytical model to predict the vertical eddy viscosity (A_z) in the region (Huijts et al. 2006, 2009, 2011), the values were in the range of $1x10^{-3}$ to $2x10^{-1}$ m²/s. Therefore, the Ekman depth in the region according to Equation 17 was between 5.4 m and 78 m. The average depth was ~42 m, which was much larger than the water depth in the study area (9 m to 14 m).

As a result, the currents in the region were expected to be highly influenced by the wind. Also, the wind-driven currents that deflect due to Coriolis effects have to be balanced by the sea-surface slope to maintain a geostrophic balance.

2.3.3 Results

2.3.3.1 Subinertial Parameters

Cross-shelf currents were much smaller than the along-shelf currents due to bathymetry (Figure 2-16). A clear pattern was noted between the depth-averaged subinertial along-shelf currents and the along-shelf wind (Figure 2-16). The flow was traveling in the same direction of the along-shelf wind. As wind traveled northward, the sea level at the coast decreased; in contrast, as the wind traveled southward, the sea level at the coast increased. This trend was associated with Ekman dynamics and geostrophic balance, which was explained previously in Section 2.3.2.3.7. Due to the in-phase relationship between the subinertial flow and along-shelf wind, an inverse relationship was noted between the along-shelf current and the sea level at the coast. Also, an inverse relationship was noted between the Florida Current and the sea level at the coast. As the Florida Current increased, the sea level at the coast decreased, and vice versa. This trend was associated with the geostrophic balance, which was explained in Section 2.3.2.3.6. It was also noted in Figure 2-16 that the northward along-shelf wind enhanced the Florida Current, while the southward along-shelf wind weakened the Florida Current.

2.3.3.2 CHEOF and Wavelet Coherence

CHEOF was used to determine the temporal and spatial principal modes of the subinertial flow measured in the four locations of the study area. The CHEOF results were mainly influenced by the along-shore current due to bathymetry. In Figure 2-17, the temporal variability of CHEOF Mode 1 accounted for a higher percentage of the total variance (95.25%). The spatial variability associated with CHEOF Mode 1 was positive and unidirectional throughout the duration of the deployment. Wavelet analysis techniques were then used between the principal mode of the subinertial flow (CHEOF Mode 1) and the subintertial forcings to determine the periods and phase at which they were coherent.

As previously noted in Figure 2-16, the results of the wavelet coherence analysis (Figures 2-18 to 2-20) showed high coherency between CHEOF Mode 1, the along-shelf wind, the sea level at the coast, and the Florida Current. In Figure 2-18, CHEOF Mode 1 was highly coherent and in phase with the Florida Current and the along-shelf wind. It was also highly coherent, but out-of- phase, with the sea level at the coast. At the same periods of high in-phase coherency between the Florida Current and CHEOF Mode 1 (at periods of 4–8 days; Figure 2-18), high out-of-phase coherency was observed between the Florida Current and the sea level at the coast (Figure 2-19). Similarly, the along-shelf wind had high in-phase coherency with CHEOF Mode 1 (Figure 2-18) at the same periods it had high out-of-phase coherency with the sea level at the coast (at periods of 4–8 days; Figure 2-19). Also, the Florida Current had high in-phase coherency with the along-shelf wind (Figure 2-20) at the same periods it had high out-of-phase coherency with the sea level at the coast (at periods 4–8 days; Figure 2-19).

2.3.3.3 Along-Shelf Momentum Balance

The depth-averaged along-shelf momentum balance was calculated to determine the dominant forces driving the along-shelf subinertial current around the shoals. Time series of along-shelf momentum balance during spring conditions are provided in Figure 2-21. Results shows that the along-shelf momentum balance was mainly frictional (pressure gradient balanced by bottom stress). However, other forces in the momentum balance were similar in magnitude and could still be influential on the along-shelf hydrodynamics.

2.3.3.4 Across-Shelf Momentum Balance

The depth-averaged across-shelf momentum balance was calculated to determine the dominant forces driving the across-shelf subinertial current around the shoals. Time series of the across-shelf momentum balance during spring conditions is provided in Figure 2-22. Results show that the along-shelf momentum balance was mainly geostrophic (pressure gradient balanced by Coriolis). Since the across-shelf momentum balance was clearly geostrophic while the along-shelf momentum balance was mainly frictional, these trends suggested that the dynamics in the region were semi-geostrophic.

2.3.3.5 Using Standard Deviation to Compare the Momentum Terms

The standard deviation can be used to compare the size of the fluctuation of each momentum term (Lee et al. 1984; Liu and Weisberg 2005; Fewings and Lentz 2010; Lentz and Fewings 2012). A larger standard deviation means larger variability and therefore a contributing force throughout the duration of the deployment. A summary of the results for the depth-averaged momentum balance (along- and across-shelf) using the standard deviation is provided in Figure 2-23. These results clarify and support the findings obtained with along- and across-shelf momentum balances that the region was semi-geostrophic during this deployment.

2.3.4 Discussion

The influence of the cape-associated shoals on the subinertial currents was very clear in Figures 2-16 and 2-17. High coherency between the along-shelf wind and the subinertial flow have been seen before by Lee et al. (1984, 1989) when studying the South-Atlantic Bight (SAB) and the South Carolina shelf during winter conditions. Mitchum and Sturges (1982) also found high coherency among the currents, sea level, and along-shelf wind while studying the West Florida Shelf in winter. The nearshore bathymetry was forcing the flow to travel primarily along-shelf. Also, the along-shelf wind had a clear influence on the subinertial flow direction (Figures 2-16 and 2-18). This influence was expected in inner shelves, where the surface and bottom Ekman layers overlap. As a result, the influence of the along-shelf wind can fill the entire water column and the subinertial flow travels in the same direction of the along-shelf wind.

The Florida Current was also influenced by the along-shelf wind (Figure 2-20). When both the Florida Current and along-shelf wind were traveling in the same direction, the Florida Current strength increased and vice versa (Figure 2-24).

As the Florida Current increased, the Coriolis force increased as well. As a result, the sea-surface slope offshore increased to keep a geostrophic balance. At the same time, the northward along-shelf wind caused the flow nearshore to deflect offshore due to Coriolis influence. This Coriolis influence had to be balanced with a sea surface to keep the system balanced. The result was a positive across-shelf sea-surface slope that drove the flow northward (Figure 2-24). On the other hand, as the Florida Current decreased, the Coriolis influence decreased and the sea-surface slope offshore relaxed to keep a geostrophic balance. At the same time, the southward along-shelf wind caused the nearshore flow to deflect towards the coast due to Coriolis influence. This Coriolis influence was balanced with a sea-surface slope to keep the system balanced. The result was a negative nearshore sea-surface slope that drove the nearshore flow southward and a positive but more relaxed offshore sea-surface slope that drove the offshore flow northward (Figure 2-24).

Two exceptions to the process explained previously were noted in days 133 and 138 (Figure 2-18). Comparing day 133 with 145, both had southward along-shelf wind of ~3.5 m/s. However, the southward along-shelf wind caused a reduction in the Florida Current transport of ~0.6 Sv in day 133 and a reduction in Florida Current transport of ~3 Sv in day 145. Consequently, the sea level at the coast increased to 0.01 m in day 133, while it increased to 0.04 m in day 145. Therefore, the corresponding nearshore sea-

surface slope in day 133 caused a reduction in the northward subinertial flow strength but did not change the flow direction. On the other hand, the corresponding nearshore sea-surface slope in day 145 caused the subinertial flow to travel southward. In day 138, a decrease in the strength of the southward along-shelf wind caused an increase in the Florida Current transport. As a result, the sea level at the coast decreased and the corresponding nearshore sea-surface slope caused a reduction in the southward subinertial flow strength but did not change the flow direction.

The results from the across-shelf momentum balance in Figures 2-22 and 2-23 strengthen the conclusion derived from the wavelet coherence analysis about the important role of geostrophic balance in driving the flow around the ridges. It was very clear that the across-shelf momentum balance was dominated by Coriolis and the pressure gradient throughout the duration of the deployment during spring conditions. This result was consistent with previous studies performed in inner, mid, and outer shelves (Allen and Kundu 1978; Noble et al. 1983; Lee et al. 1984, 1989; Brown et al. 1985, 1987; Thompson and Pugh 1986; Lentz et al. 1999; Li and Weisberg 1999a; 1999b; Shearman and Lentz 2003; Liu and Weisberg 2005; Fewings and Lentz 2010). On the other hand, the along-shelf momentum balance, as shown in Figures 2-21 and 2-23, was mainly frictional (the pressure gradient balanced by bottom stress), as found in previous studies on inner shelves (Lentz et al. 1999; Li and Weisberg 1999b; Liu and Weisberg 2005; Fewings and Lentz 2010; Lentz and Fewings 2012). However, other terms in the along-shelf momentum balance were similar in magnitude and could still have an influence on the along-shelf hydrodynamics. This makes the along-shelf momentum balance more complicated by including terms that are usually found to be influential in surfzone, inner shelves, or mid-shelves. It also suggested that the region was semi-geostrophic.

2.3.4.1 Implications for Dredging

It was evident that waves associated with ridges can play a dynamic and morphodynamic role in a region of swale-ridge bathymetry. Modifications to ridges or swales by dredging could also alter the wave regime through transformation processes such as infragravity distortions, refractions, diffractions, reflections and shoaling (see Section 2.4). Potential enhancement of these processes by dredging would likely increase the dynamic relevance of wind-waves with consequential exacerbation of erosion.

2.3.5 Conclusion

The bathymetry in the inner shelf adjacent to Cape Canaveral was considered complex due to its series of shoals and shore-oblique ridges. The flow over this bathymetry mainly moved along-shelf. As the along-shelf wind and the Florida Current traveled in the same direction, the Florida Current transport increased. As a result, a positive across-shelf sea-surface slope developed, dragging inner-shelf water in the same direction of the western boundary current. This motion suggested that an across-shelf geostrophic balance was driving the subinertial flow. On the other hand, as the along-shelf wind and the Florida Current were in opposite directions, the Florida Current decreased. Consequently, the positive offshore sea-surface slope relaxed to keep a geostrophic balance, which dragged the offshore flow in the same direction as the Florida Current. At the same time, the southward along-shelf wind created a negative nearshore sea-surface slope that dragged the nearshore flow in the same direction as the along-shelf wind. The across-shelf momentum balance result showed that the subinertial flow was dominated by the pressure gradient and Coriolis (geostrophic balance). This result was consistent with the result obtained from the wavelet coherence analysis. Similar to previous studies on inner shelves, the along-shelf momentum balance was mainly frictional (pressure gradient balanced by bottom stress); however, other terms were similar in magnitude and not negligible. Modifications to ridges or swales by dredging also could alter the wave regime through transformation processes. Potential enhancement of these processes by dredging would likely increase the dynamic relevance of wind-waves with consequential augmentation of morphodynamic evolution.

2.3.6 References

Allen JS, Kundu PK. 1978. On the momentum, vorticity and mass balance on the Oregon Shelf. Journal of Physical Oceanography 8(1): 13-27. doi:10.1175/1520-0485(1978)008<0013:Otmvam>2.0.Co;2.

Brown WS, Irish JD, Winant CD. 1987. A description of subtidal pressure field observations on the Northern California Continental Shelf during the Coastal Ocean Dynamics Experiment. Journal of Geophysical Research 92: 1605-1635.

Brown WS, Pettigrew NR, Irish JD. 1985. The Nantucket Shoals Flux Experiment (NSFE79). Part II: The structure and variability of across-shelf pressure gradients. Journal of Physical Oceanography 15(6): 749-771. doi:10.1175/1520-0485(1985)015<0749:Tnsfep>2.0.Co;2.

Ekman V. 1905. On the influence of the earth's rotation on ocean-currents. Arkiv for Matematik, Astronomi och Fysik 2(11): 1-52.

Emery W, Thomson R. 1998. Data analysis methods in physical oceanography. 1st ed. New York, NY: Elsevier.

Fewings M, Lentz S. 2010. Momentum balances on the inner continental shelf at Martha's Vineyard Coastal Observatory. Journal of Geophysical Research: Oceans 115 (C12023). doi.org/10.1029/2009JC005578.

Fewings M, Lentz S, Fredericks J. 2008. Observations of cross-shelf flow driven by cross-shelf winds on the inner continental shelf. Journal of Physical Oceanography 38(11): 2358-2378. doi:10.1175/2008jpo3990.1.

Geyer WR, Trowbridge JH, Bowen MM. 2000. The dynamics of a partially mixed estuary. Journal of Physical Oceanography 30(8): 2035-2048. doi:10.1175/1520-0485(2000)030<2035:Tdoapm>2.0.Co;2.

Grinsted A, Moore JC, Jevrejeva S. 2004. Application of the cross wavelet transform and wavelet coherence to geophysical time series. Nonlinear Processes in Geophysics 11(5/6): 561-566. doi:10.5194/npg-11-561-2004.

Huijts K, de Swart H, Schramkowski G, Schuttelaars H. 2011. Transverse structure of tidal and residual flow and sediment concentration in estuaries. Ocean Dynamics 61(8): 1067-1091. doi:10.1007/s10236-011-0414-7.

Huijts K, Schuttelaars H, de Swart H, Friedrichs C. 2009. Analytical study of the transverse distribution of along-channel and transverse residual flows in tidal estuaries. Continental Shelf Research 29: 89-100. doi:10.1016/j.csr.2007.09.007.

Huijts K, Schuttelaars H, de Swart H, Valle-Levinson A. 2006. Lateral entrapment of sediment in tidal estuaries: An idealized model study. Journal of Geophysical Research: Oceans 111(C12016). doi:10.1029/2006JC003615.

Kaihatu J, Handler R, Marmorino G, Shay L. 1998. Empirical orthogonal function analysis of ocean surface currents using complex and real-vector methods. Journal of Atmospheric and Oceanic Technology 15(4): 927-941.

Kline SW, Adams PN, Plant NG, MacKenzie RA, Jaeger JM. 2012. Effect of a shore-oblique ridge on beach and bar morphodynamics at Kennedy Space Center, Cape Canaveral, Florida. In: American

Geophysical Union Fall Meeting; 2012/12/1; San Francisco, CA. p EP33B-0867. https://ui.adsabs.harvard.edu/abs/2012AGUFMEP33B0867K.

Kumar N, Voulgaris G, List JH, Warner JC. 2013. Alongshore momentum balance analysis on a cuspate foreland. Journal of Geophysical Research: Oceans 118(10): 5280-5295. doi.org/10.1002/jgrc.20358.

Large WG, Pond S. 1981. Open ocean momentum flux measurements in moderate to strong winds. Journal of Physical Oceanography 11(3): 324-336. doi:10.1175/1520-0485(1981)011<0324:Oomfmi>2.0.Co;2.

Lee TN, Ho WJ, Kourafalou V, Wang JD. 1984. Circulation on the continental shelf of the southeastern United States. Part I: Subtidal response to wind and Gulf Stream forcing during winter. Journal of Physical Oceanography 14(6): 1001-1012. doi:10.1175/1520-0485(1984)014<1001:Cotcso>2.0.Co;2.

Lee TN, Williams E, Wang JD, Evans RH, Atkinson L. 1989. Response of South Carolina continental shelf waters to wind and Gulf Stream forcing during winter of 1986. Journal of Geophysical Research 94: 10715-10754.

Lentz S. 1995. Sensitivity of the inner-shelf circulation to the form of the eddy viscosity profile. Journal of Physical Oceanography 25(1): 19-28. doi:10.1175/1520-0485(1995)025<0019:Sotisc>2.0.Co;2.

Lentz S, Fewings M, Howd P, Fredericks J, Hathaway K. 2008. Observations and a model of undertow over the inner continental shelf. Journal of Physical Oceanography 38(11): 2341-2357. doi:10.1175/2008jpo3986.1.

Lentz S, Fewings MR. 2012. The wind- and wave-driven inner-shelf circulation. Annual Review of Marine Science 4(1): 317-343. doi:10.1146/annurev-marine-120709-142745.

Lentz S, Guzu R, Elgar S, Feddersen F, Herbers T. 1999. Momentum balances on the North Carolina inner shelf. Journal of Geophysical Research: Oceans 104(C8): 18205-18226. doi.org/10.1029/1999JC900101.

Li Z, Weisberg RH. 1999a. West Florida continental shelf response to upwelling favorable wind forcing: Dynamics. Journal of Geophysical Research 104: 23427-23442.

Li Z, Weisberg RH. 1999b. West Florida shelf response to upwelling favorable wind forcing: Kinematics. Journal of Geophysical Research: Oceans 104(C6): 13507-13527. doi.org/10.1029/1999JC900073.

Liu Y, Weisberg RH. 2005. Momentum balance diagnoses for the West Florida Shelf. Continental Shelf Research 25(17): 2054-2074.

Longuet-Higgins MS. 1953. Mass transport in water waves. Philosophical Transactions of the Royal Society of London Series A, Mathematical and Physical Sciences 245(903): 535-581.

Longuet-Higgins MS, Stewart RW. 1964. Radiation stresses in water waves; a physical discussion, with applications. Deep Sea Research and Oceanographic Abstracts 11(4): 529-562. doi.org/10.1016/0011-7471(64)90001-4.

Mei CC. 1983. The applied dynamics of ocean surface waves. New York, NY: Wiley. http://books.google.com/books?id=uOdOAAAAMAAJ.

Mitchum GT, Sturges W. 1982. Wind-driven currents on the West Florida Shelf. Journal of Physical Oceanography 12(11): 1310-1317. doi:10.1175/1520-0485(1982)012<1310:Wdcotw>2.0.Co;2.

Noble M, Butman B, Williams E. 1983. On the longshelf structure and dynamics of subtidal currents on the eastern United States continental shelf. Journal of Physical Oceanography 13(12): 2125-2147. doi:10.1175/1520-0485(1983)013<2125:Otlsad>2.0.Co;2.

Salas-Monreal D, Valle-Levinson A. 2009. Continuously stratified flow dynamics over a hollow. Journal of Geophysical Research: Oceans 114 (C03021) doi.org/10.1029/2007JC004648.

Shearman RK, Lentz SJ. 2003. Dynamics of mean and subtidal flow on the New England shelf. Journal of Geophysical Research: Oceans 108 (C8, 3281) doi.org/10.1029/2002JC001417.

Smith SD. 1988. Coefficients for sea surface wind stress, heat flux, and wind profiles as a function of wind speed and temperature. Journal of Geophysical Research: Oceans 93(C12): 15467-15472. doi.org/10.1029/JC093iC12p15467.

Stokes G. 1847. On the theory of oscillatory waves. Transactions of the Cambridge Philosophical Society 8: 441-455.

Thompson KR, Pugh DT. 1986. The subtidal behaviour of the Celtic Sea-II. Currents. Continental Shelf Research 5(3): 321-346. doi.org/10.1016/0278-4343(86)90002-6.

Valle-Levinson A. 2008. Density-driven exchange flow in terms of the Kelvin and Ekman numbers. Journal of Geophysical Research: Oceans 113 (C4001) doi.org/10.1029/2007JC004144.

Valle-Levinson A, Huguenard K, Ross L, Branyon J, Macmahan J, Reniers A. 2015. Tidal and nontidal exchange at a subtropical inlet: Destin Inlet, Northwest Florida. Estuarine, Coastal and Shelf Science 155: 137-147. doi:10.1016/j.ecss.2015.01.020.

Valle-Levinson A, Reyes C, Sanay R. 2003. Effects of bathymetry, friction, and rotation on estuary–ocean exchange. Journal of Physical Oceanography 33(11): 2375-2393. doi:10.1175/1520-0485(2003)033<2375:Eobfar>2.0.Co;2.

Xu Z-g, Bowen AJ. 1994. Wave- and wind-driven flow in water of finite depth. Journal of Physical Oceanography 24: 1850-1866.
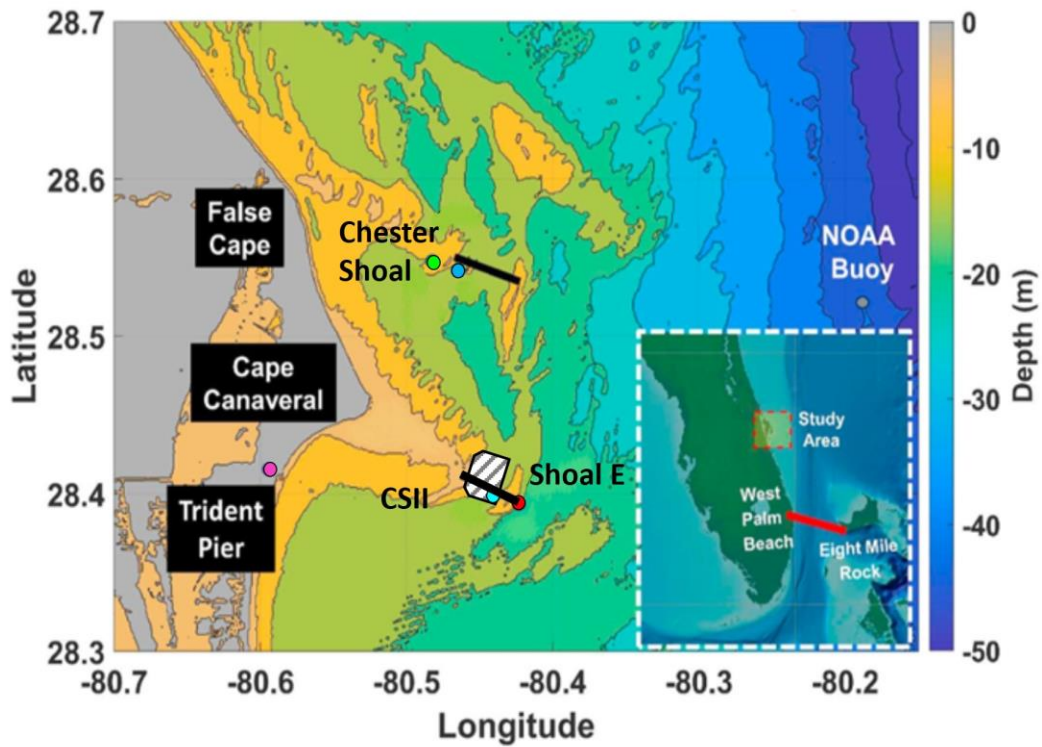
Figure 2-15. Bathymetric map of Cape Canaveral area showing the locations of the four ADCP moorings during spring conditions between 6 May and 6 June 2014.

Moorings at Chester Shoal were in the west swale (green dot) and in the east swale (blue dot); moorings at Shoal E were in the west swale (cyan dot) and in east swale (red dot). Striped area is the borrow area (CSII-BA) of Canaveral Shoal II (CSII). The NOAA water level station at the Trident Pier is given by the magenta dot. The solid black lines show the location of the two transects along which hydrographic data were collected (Section 2.2). The red solid line in the inset map of Florida shows the location of a profile along which the rate of the Florida Current transport was measured by the submarine cables.
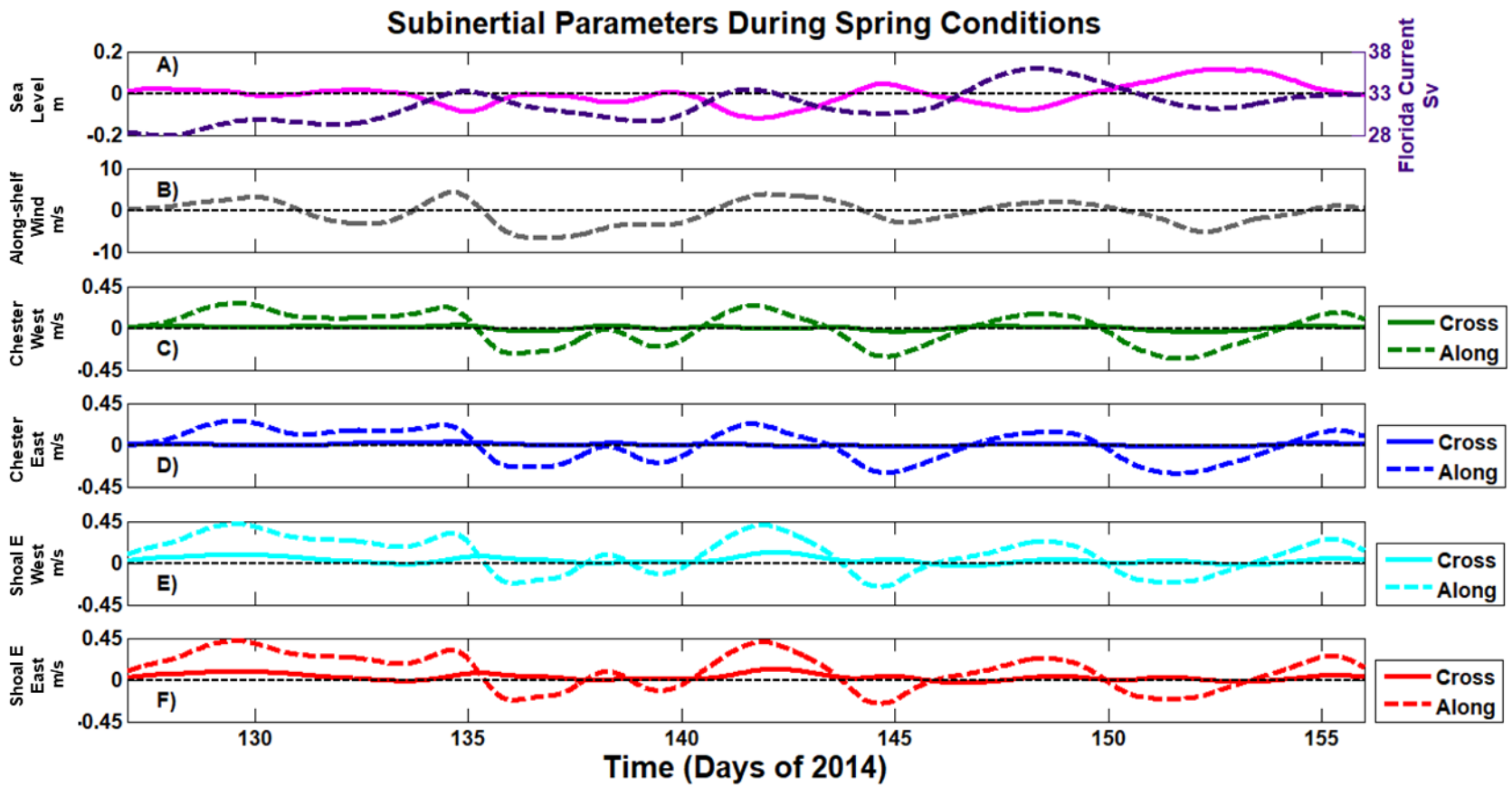
Figure 2-16. The subinertial parameters during spring conditions around shoals associated with Cape Canaveral and False Cape.
A) Subinertial sea level at the Trident Pier (magenta) (left y-axis) and the estimated transport rate of the Florida Current (dashed purple) (right y-axis); B) Along-shelf wind component in the direction of propagation; and the depth-averaged subinertial currents at C) Chester swale west, D) Chester swale east, E) Shoal E swale west and F) Shoal E swale east.
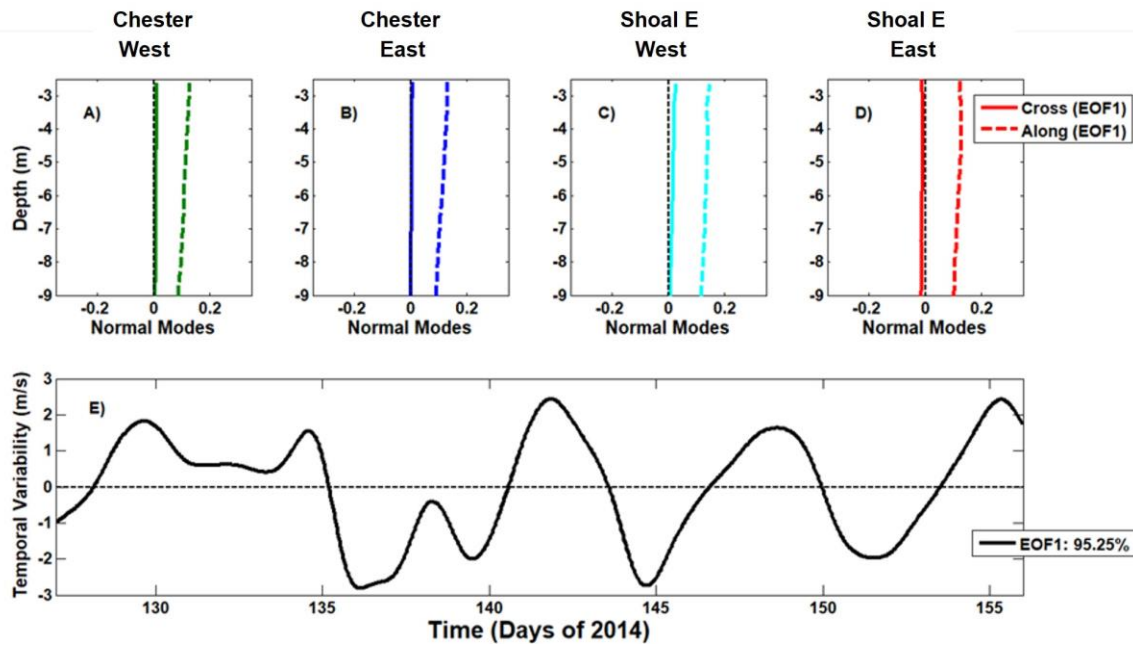
Figure 2-17. Results of CHEOF during spring 2014 conditions.
The spatial variability of Mode 1 across-shelf (solid line) and along-shelf (dashed line) for each location as follows: A) Chester swale west, B) Chester swale east, C) Shoal E swale west, and D) Shoal E swale east, and E) the temporal variability of CHEOF Mode 1 (solid black). The spatial structure of CHEOF Mode 1 was positive and unidirectional throughout the deployment. Therefore, positive temporal variability of CHEOF Mode 1 means that the flow was traveling northward, while negative temporal variability of CHEOF Mode 1 means that the flow was traveling southward.
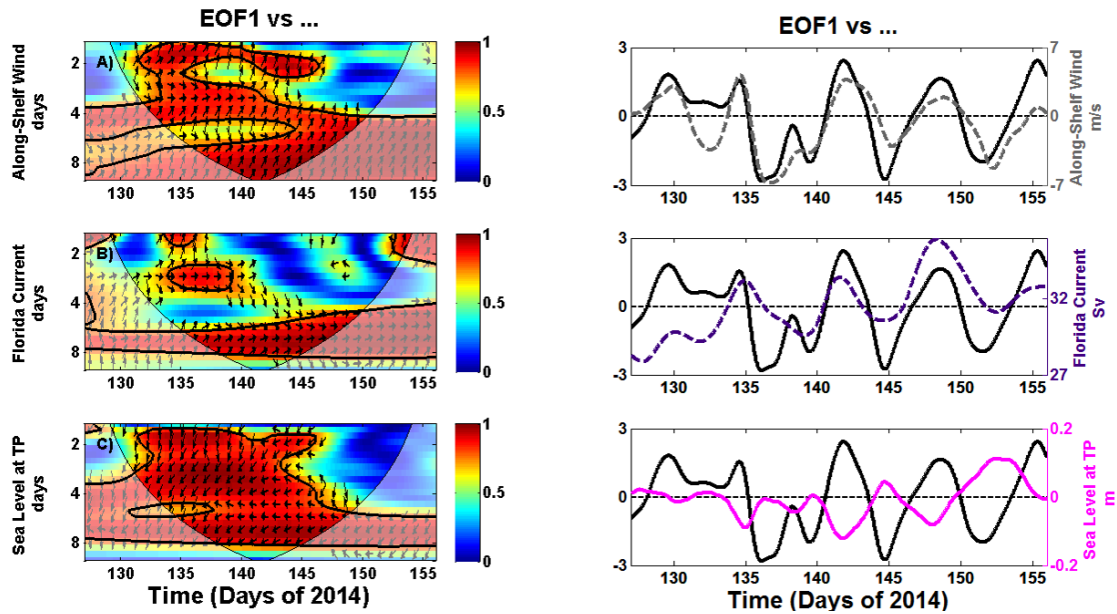
Figure 2-18. Wavelet coherences results between CHEOF Mode 1 and different forcings during spring 2014.

Left panel: CHEOF 1 vs A) along-shelf wind, B) the Florida Current transport, and C) coastal sea level at Trident Pier. The red and blue contours represent high and low coherency, respectively. The bold black contour represents a 95% confidence level. The enclosed areas within the cone of influence represent significant coherence, whereas shaded areas outside the cone of influence were below the significance level. Right panel: Temporal variability of CHEOF Mode 1 (solid black line) together with environmental forcings (dashed/colored lines).
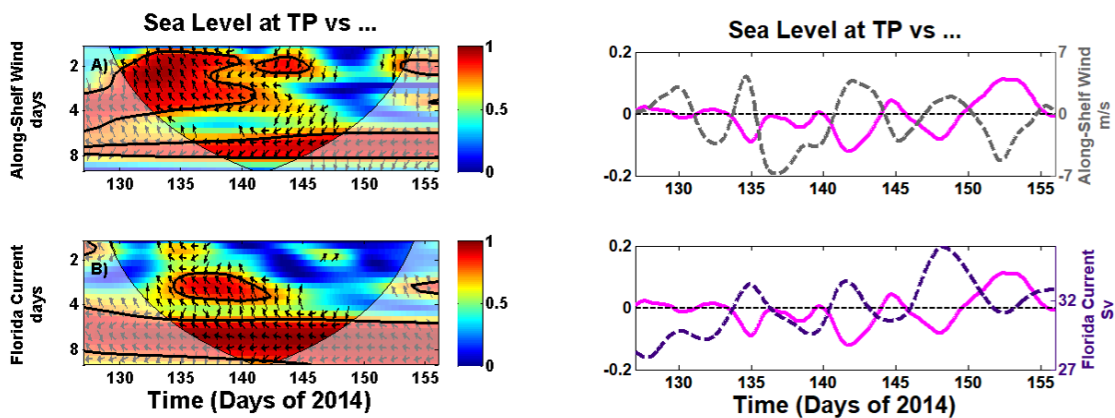
Figure 2-19. Wavelet coherence results between the sea level at Trident Pier and the along-shelf wind and the Florida Current during spring 2014.

Left panel: Notation as for Figure 2-18. Right panel: Temporal variability of the sea level at Trident Pier (solid magenta line) together with the along-shelf wind (gray dashed line) and the Florida Current (purple dashed line).
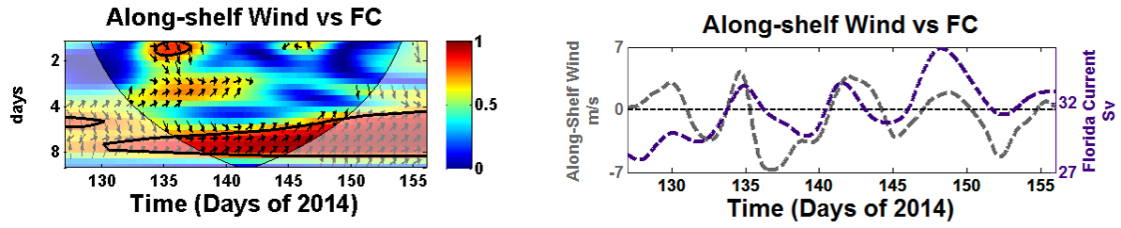
Figure 2-20. Wavelet coherence results between the Florida Current and the along-shelf wind during spring 2014.

Left panel: Notation as for Figure 2-18. Right panel: Temporal variability of along-shelf wind (gray dashed line) together with the Florida Current (purple dashed line).
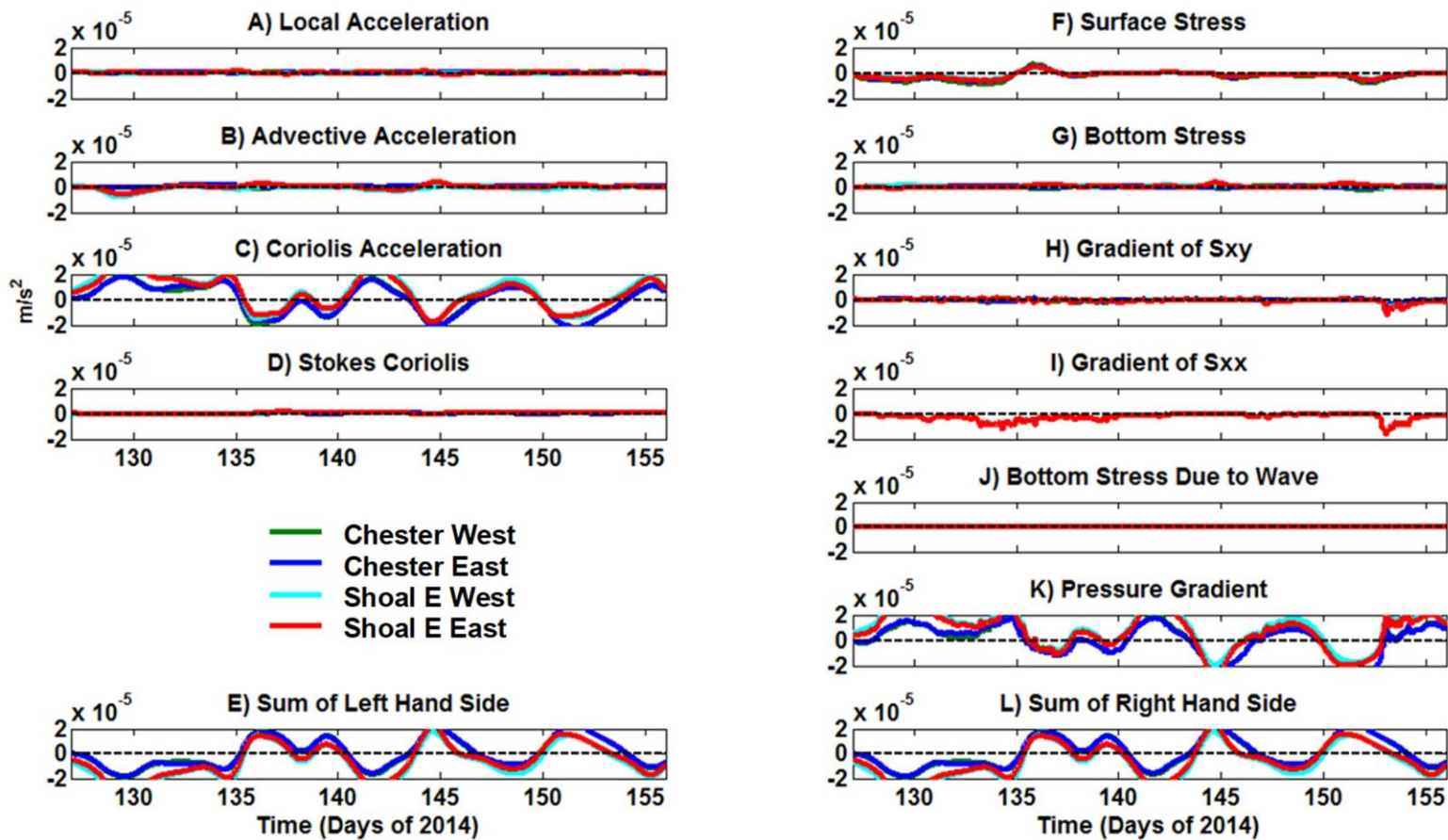
Figure 2-21. Time series of the along-shelf momentum balance during spring 2015.

A) Local acceleration $\frac{\partial \overline{V}}{\partial y}$; B) advective acceleration ($\overline{U}\frac{\partial \overline{V}}{\partial x} + \overline{V}\frac{\partial \overline{V}}{\partial y}$); C) Coriolis acceleration $f\overline{U}$; D) Stokes Coriolis $f\overline{U}_{st}$; E) sum of left-hand side; F) surface stress $\frac{\tau_{sy}}{\rho_o h}$; G) bottom stress $\frac{-\tau_{by}}{\rho_o h}$; H) gradient of the radiation stress of x-component in the y-direction $-\frac{1}{\rho_o h}\frac{\partial S_{xy}}{\partial x}$; I) gradient of the radiation stress of y-component in the y-direction $-\frac{1}{\rho_o h}\frac{\partial S_{yy}}{\partial y}$; J) bottom stress due to waves $-\frac{\tau_{bwy}}{\rho_o h}$; K) pressure gradient $-g\frac{\partial \eta}{\partial y}$, ; and L) sum of the right-hand side for Shoal E West Swale (cyan), Shoal E East Swale (red), Chester West Swale (green), and Chester East Swale (blue). All units on the 'y' axes are force per unit mass (or accelerations—m/s²).
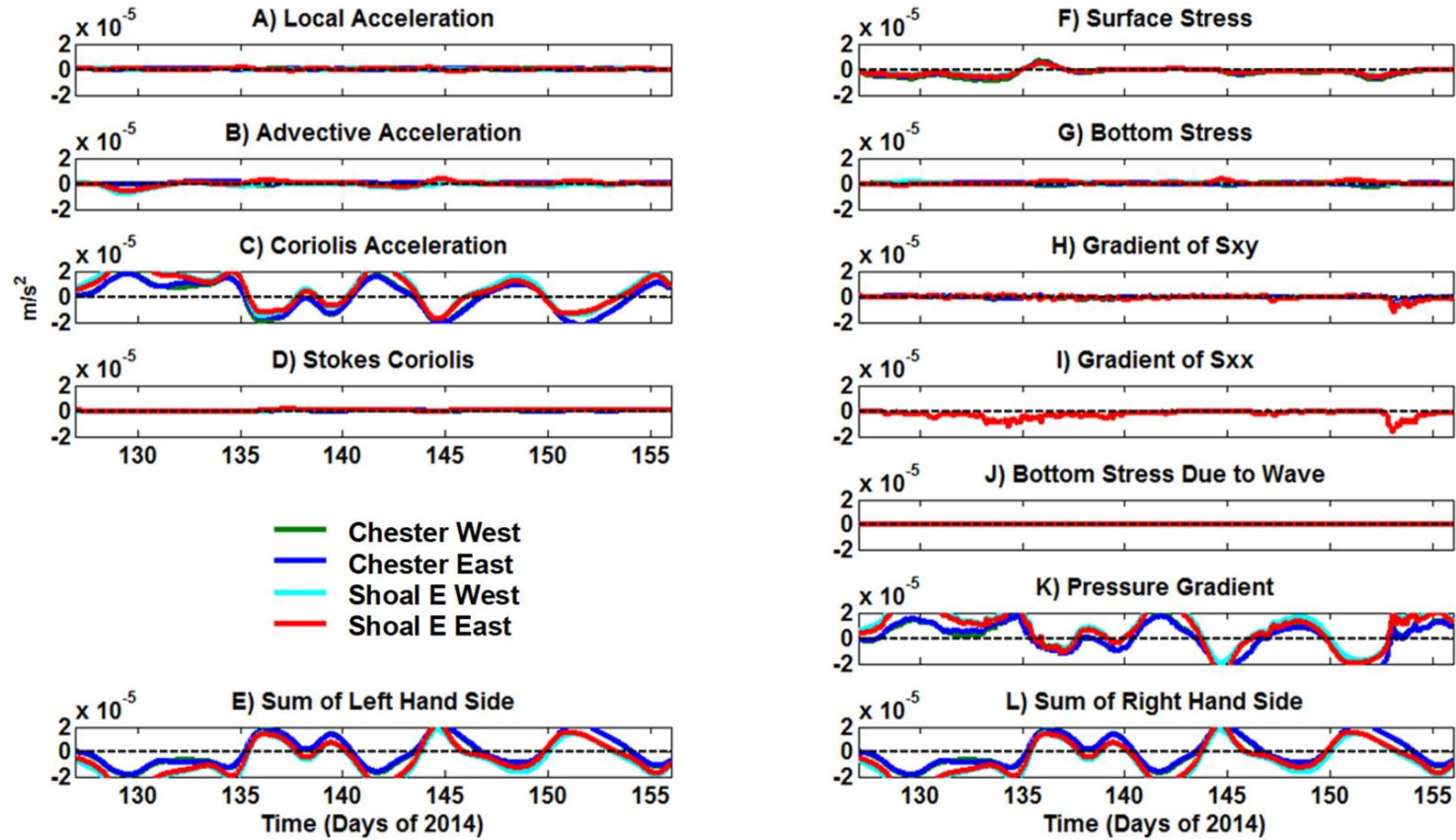
Figure 2-22. Time series of the across-shelf momentum balance during spring 2014.

A) Local acceleration $\frac{\partial \bar{U}}{\partial t}$; B) Advective acceleration $\bar{U}\frac{\partial \bar{U}}{\partial x} + \bar{V}\frac{\partial \bar{U}}{\partial y}$; C) Coriolis acceleration $-f\bar{V}$; D) Stokes Coriolis $-f\bar{V}_{st}$; E) Sum of left-hand side; F) Surface stress $\frac{\tau_{sx}}{\rho_o h}$;

G) Bottom stress $\frac{-\tau_{bx}}{\rho_o h}$; H) Gradient of the radiation stress of x-component in the y-direction $-\frac{1}{\rho_o h}\frac{\partial S_{xy}}{\partial y}$; I) Gradient of the radiation stress of x-component in the x-direction

$-\frac{1}{\rho_o h}\frac{\partial S_{xx}}{\partial x}$; J) Bottom stress due to waves $-\frac{\tau_{bwx}}{\rho_o h}$; K) Pressure gradient $-g\frac{\partial \eta}{\partial x}$; and L) Sum of the right-hand side for Shoal E Swale West (cyan), Shoal E Swale East (red), Chester

Swale West (green), and Chester Swale East (blue).

50
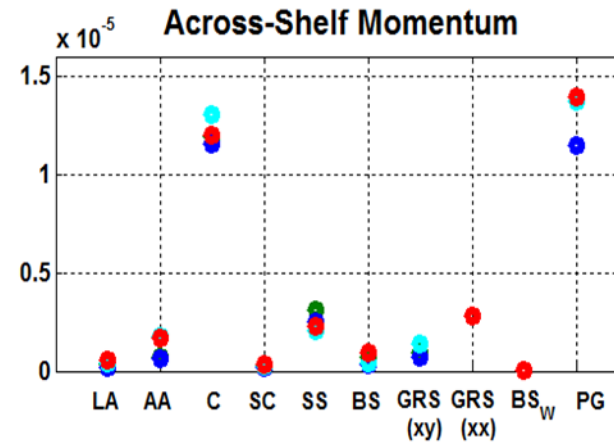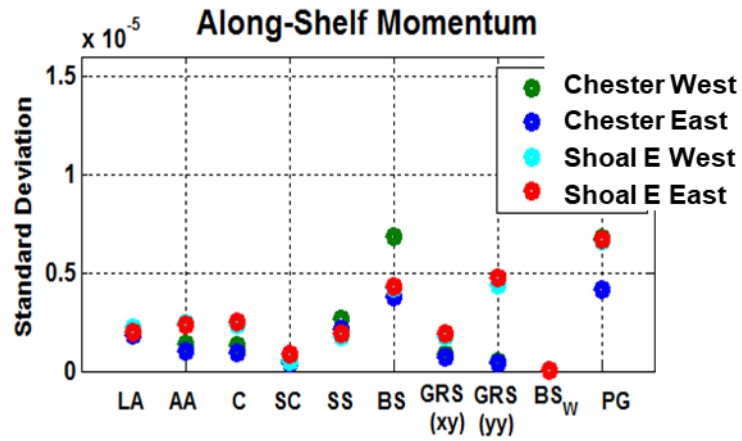
Figure 2-23. The standard deviation for each term of the along-shelf and across-shelf momentum balance during spring conditions.
Shoals included Chester Swale West (green dot), Chester Swale East (blue dot), Shoal E Swale West (cyan dot), and Shoal E Swale East (red dot). LA stands for Local Acceleration, AA stands for Advective Acceleration, C stands for Coriolis, SC stands for Stokes Coriolis, SS stands for Surface Stress, BS stands for Bottom Stress, GRS_{xx} stands for Gradient of Radiation Stress S_{xx}, GRS_{xy} stands for Gradient of Radiation Stress S_{xy}, GRS_{yy} stands for Gradient of Radiation Stress S_{yy}, BS_w stands for Bottom Stress Due to Waves, and PG stands for pressure gradient.

- W_{AS} and V_{FC} in the same direction:
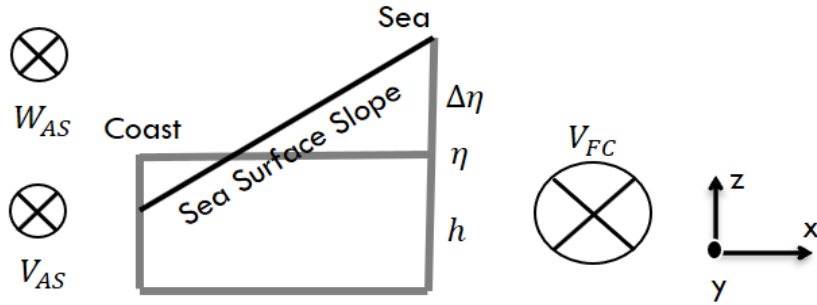
- W_{AS} and V_{FC} in opposite direction:
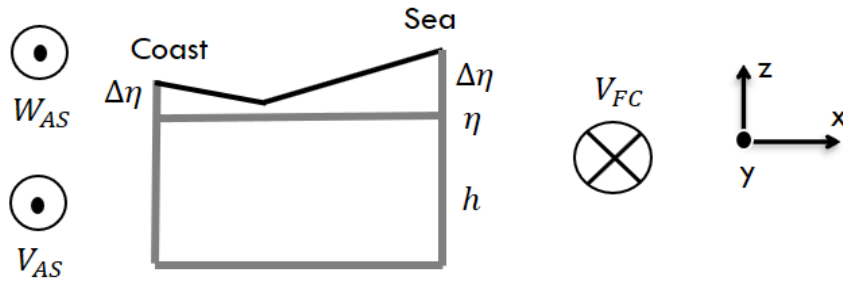
Figure 2-24. Schematic diagram of the subinertial circulation in the inner shelf adjacent to Cape Canaveral, FL.
W_{AS} stands for along-shelf wind, V_{FC} stands for the Florida Current transport, V_{AS} Stands for along-shelf current, $\Delta\eta$ stands for the slope in sea-surface elevation, η stands for equilibrium (flat) surface elevation, h stands for depth, the cross means that the direction of propagation was northward, and the dot means that the direction of propagation was southward. The diagram is for illustration purposes and not to scale.

Table 2-1. Details of the ADCPs at the four mooring positions during spring 2014.

Feature	Chester Shoal	Chester Shoal	Shoal E (=CSII-BA)	Shoal E
Location	Swale West	Swale East	Swale West	Swale East
Latitude, 28°N	33.01'	32.64'	23.99'	23.64'
Longitude, 80°W	28.95'	27.80'	26.33'	25.42'
Instrument	RDI Workhorse	RDI Workhorse	Nortek Aquadopp	Nortek AWAC
Depth (m)	9	12	14	13
Start date (GMT)	6-May-14	6-May-14	6-May-14	6-May-14
Start time	15:30:00	14:10:00	20:10:00	18:42:00
End date	6-Jun-14	6-Jun-14	6-Jun-14	6-Jun-14
End time	15:10:00	14:00:00	19:40:00	18:51:00
Total time span (days)	31	31	31	31
Waves: Burst interval (minutes)	120	-	60	60
Waves: Samples per burst	2,400	-	2,400	2,400
Waves: Sampling rate (Hz)	2	-	2	2
Currents: Blanking distance (m)	1.1	1.1	0.2	0.4
Currents: Interval (minutes)	10	10	30	24
Currents: Number of cells (bins)	30	25	40	40
Currents: Cell size (m)	0.5	0.5	0.5	0.5

2.4 Generation of Infragravity Waves by Asymmetric Shoaling and Dissipation of Short-wave Groups Over Cape-related Shoals

2.4.1 Introduction

Inner-shelf morphology controls the scattering and dissipation of waves within the incident band. Nearshore conditions and morphodynamics depend upon such transformations as they dictate the amount of energy available to transport sediment, pollutants, nutrients, and organisms (Rodriguez et al. 1995; Hoefel and Elgar 2003; Clark et al. 2011; Schratzberger and Larcombe 2014 and many others). Furthermore, the long-term evolution of sandy shorelines is determined by spatial gradients in longshore sediment transport (Komar 1971; Ashton and Murray 2006; Kaergaard and Fredsoe 2013), which are highly dependent upon complicated inner-shelf bathymetry (Bender and Dean 2003; Limber et al. 2017 and references therein).

Short gravity waves (SGWs, frequencies 0.05 to 0.3 Hz or periods from 3 to 20 s) are modeled as rays of frequency-dispersive sinusoidal waves that conserve their energy flux and follow Snell's law of refraction during propagation over straight and parallel depth contours. SGW height increases, while celerity and wavelength decrease, as wave rays shoal and converge due to refraction by ambient currents and changes in water depth (Mei et al. 2005 section 3.3; Cavaleri et al. 2007 section 7), consistent with observations of ray divergence over submarine canyons and convergence at cuspate forelands (e.g., Davidson-Arnott 2010 section 5.3.2).

Although this approach provides the bulk spatial distribution of wave energy, its main assumption of negligible nonlinearity does not hold near the shoreline. In the nearshore, frequency dispersion $(\kappa h)^2$ diminishes, while amplitude dispersion - nonlinearity (a/h) increases, where κ is the wavenumber, h is the water depth, and a is the waveform amplitude (Whitham 1999 section 13.11). This competition between frequency dispersion and nonlinearity can be represented by the Ursell number, given (in terms of wave statistics) by

$$Ur = \alpha \frac{H_{SGW}}{h}\left(\frac{L}{h}\right)^2 \tag{36}$$

where $\alpha = \left(3\sqrt{2}\right)/(64\pi^2)$ and H_{SGW} was the SGW significant height (Ursell 1953; Doering and Bowen 1986) (see Appendices B and C for details). In deep water, $Ur \ll O(1)$ and frequency dispersion dominates over nonlinearity. Over the inner shelf, where $Ur \approx O(1)$, weakly nonlinear conditions prevail and the accurate modeling of nearshore morphodynamics require the inclusion of nonlinear processes typically well-identified for $Ur \gg O(1)$ in the surf zone (Young and Eldeberky 1998). These nonlinear processes include the diffraction at caustics (diffraction caused by oblique wave incidence) that may occur over complicated bathymetry (e.g., Kirby and Dalrymple 1983; Yoo and O'Connor 1988), sea-swell breaking (e.g., Elgar and Guza 1985; Filipot et al. 2010), and LGW generation and transformation (e.g., Elgar et al. 1992; Herbers et al. 1994).

The theory and application of LGWs (frequencies from 2 to 50 mHz, or 20 to 500 s, also referred to as *infragravity* waves) have generated considerable scientific interest during the last 60 years. From early studies that found correlations between sea-swell and oscillations at frequencies in the lower portion of the gravity band (i.e., surf beats) (Munk 1949; Tucker 1950), subsequent contributions corroborated that LGWs play an important role in nearshore morphodynamics. Theoretical developments, as well as field and laboratory experiments, have demonstrated the relevance of LGWs to sediment transport in surf and swash zones (Guza and Thornton 1982; Aagaard and Greenwood 2008; Alsina et al. 2016 and others), beach cusp formation via nearshore-trapped edge waves (e.g., Bowen and Guza 1978; Guza and Thornton 1982; Coco et al. 2003), instabilities in longshore currents (Feddersen 2014), wave-breaking (Clark et al. 2012), water-level variations in harbors (Bowers 1977; Bellotti and Franco 2011; Diaz-Hernandez et al.

2015), and coastal erosion during storms (Guza and Thornton 1982; van Thiel de Vries et al. 2008; Roelvink et al. 2009; Young et al. 2012).

Considering only irrotational motions, nearshore LGWs result from the combination of free and forced waves (Okihiro et al. 1992; Rijnsdorp et al. 2015 and others). Forced LGWs (i.e., surf beats) are oscillations bound to wave groups due to nonlinear, difference interactions in triads of sea-swell waves (Herbers et al. 1994). Within a group of dispersive SGWs exists a spatial variability in wave heights and therefore period-averaged stresses related to wave orbital velocities (*wave radiation stresses*) (Longuet-Higgins and Stewart 1964). For horizontal bottoms and wave groups that are long compared to the water depth, the spatial gradient in radiation stresses generates a spatially varying wave set-down, or "surf beat," with a mass transport opposed to the wave group propagation (Longuet-Higgins and Stewart 1962). In addition, on sloping bottoms the difference in water depth within the group induces a spatially oscillatory forced wave and a dynamic set-up, i.e., free LGWs that propagate both in the direction of wave groups and the opposite direction (Baldock 2006; Zou 2011). Forced infragravity waves are typically small in deep water with amplitudes $O(10^{-3}\ m)$ but can be larger in the surf and swash zones with amplitudes ranging $O(10^{-1}\ m)$ to $O(1\ m)$ (e.g., Ruessink 1998).

In addition to forced motions, free LGWs that follow the shallow-water dispersion relation—$(\omega/\kappa)^2 = gh$, where ω is the radian frequency, κ is the wavenumber, and g is the acceleration due to gravity—have been found to be either locally or remotely generated. Remote sources refer to shoreline reflections across the ocean (Herbers et al. 1995). Local sources include reflections from nearby shorelines, the aforementioned dynamic set-up produced by the shoaling of wave groups (Mei and Benmoussa 1984; Liu 1989; Zou 2011), and the time-varying breaking of short waves within groups (Symonds et al. 1982; Schäffer 1993). The dominance of breaking- over shoaling-induced generation of LGWs, or vice versa, has been suggested to depend upon short-wave characteristics and on the ratio of bottom steepness to surf-beat wavelength. It has been suggested that shoaling dominates when short waves reach shallow water before breaking, or $\kappa h_b > \pi/10$. Breaking-induced LGWs dominate if short waves break before shallow-water (resonant) conditions (Baldock 2006). The shoaling-breaking LGW generation has been represented by the combination of two parameters: (1) short-wave steepness $\sqrt{H_{SGW,b}/L_{SGW,b}}$, where L_{SGW} is the short-wave wavelength, and b represents "at breaking conditions"; and (2) the relative importance of the bottom slope on the wave group propagation given by the normalized bed slope $\beta_{norm} = (h_x/\omega_{LGW})\sqrt{gh}$, where h_x is the bottom slope, and ω_{LGW} the radian frequency of the infragravity wave (Battjes et al. 2004). The surf-beat similarity parameter, $\xi_{surfbeat}$, was then proposed to account for the shoaling-breaking dichotomy as (Baldock 2012):

$$\xi_{surfbeat} = \beta_{norm}\sqrt{\frac{H_{SGW}}{L_{SGW}}} = \frac{h_x}{\omega_{LGW}}\sqrt{\frac{g}{h}}\sqrt{\frac{H_{SGW}}{L_{SGW}}} \tag{37}$$

Large (small) values of $\xi_{surfbeat}$ have been associated with the dominance of the breaking (shoaling) mechanism at a particular location (e.g., Contardo and Symonds 2013). Here, however, we opt to use the Ursell parameter instead of $\sqrt{H_{SGW,b}/L_{SGW,b}}$ to represent the short-wave shoaling in $\xi_{surfbeat}$ (see the Discussion).

Bathymetry exerts control on infragravity motions via variations in water depth (h), bottom slope (h_x), and bottom curvature (h_{xx}), and also influences the level of energy transfer between the sea-swell and the surf-beat frequencies (e.g., Janssen et al. 2006 Equation A1). This phenomenon has been extensively studied (Hasselmann 1962; Elgar et al. 1993; Herbers et al. 1994, 2000; de Bakker et al. 2016 and others) and found to depend on bottom sedimentary material (Torres-Freyermuth and Hsu 2014) and overall profile shape (Battjes et al. 2004; Henderson et al. 2006; Thomson et al. 2006; Zou 2011; de Bakker et al. 2016).

In addition, bottom morphology influences free LGWs variability via trapping, partial reflections, and short-wave breaking. Passive-margin, wide continental shelves can trap free LGWs (Herbers et al. 1995), whereas submarine canyons can partially reflect incoming infragravity waves (Thomson et al. 2005, 2007). In turn, short-wave breaking dominates LGW variability at fringing reef lagoons (Pomeroy et al. 2012). However, at locations characterized by complicated inner-shelf bathymetry near to high-curvature shorelines, like cape-related shoals near cuspate forelands (e.g., Davis et al. 1993; McNinch and Luettich 2000; Kumar et al. 2013), the variability of LGWs has not been explored. The presence of capes and associated shoals at settings of relatively high socioeconomic importance (Murray and Ashton 2013 and references therein) highlight the need for understanding in situ LGW hydrodynamics, which likely influence the long-term evolution of adjacent shorelines (McNinch and Luettich 2000; Thompson et al. 2015).

Our overall goal was to combine field-observed pressure and velocity data with wave theory to analyze the effect of cape-related shoals on LGW variability. We hypothesize that LGWs are affected by the complex bathymetry offshore of cuspate forelands through three mechanisms: 1) shoaling and dissipation of short and long waves, 2) partial reflection, and 3) trapping. The latter two mechanisms are connected as the reflection may lead to standing wave formation between the shoal ridge and the turning point (Huntley et al. 1981; Sheremet et al. 2005; Rijnsdorp et al. 2015). Isolated, cape-related shoals may affect free LGWs via partial reflection in analogy to the potential-well problem in quantum mechanics. In this mechanism, the electron motion through a region of change in potential requires the incident momentum to be divided into reflected and transmitted waves (Bohm 1989 section 11.7). Analytical solutions for long-wave propagation over shoals include ridges represented as rectangular sections (Mei et al. 2005 section 4.4), trapezoidal sections (Lin and Liu 2005), and steps with curvilinear slopes (Liu et al. 2013). These solutions assume mass and momentum conservations for linear waves and highly idealized 2D profiles. Moreover, a higher order solution is available for the general case of short-wave group shoaling over more complex topography that includes additional forced and free LGWs (Mei and Benmoussa 1984; Zou 2011).

We further argue that short wave breaking may generate free LGW via the time-varying breakpoint process (Schäffer 1993). We also speculate that shore-attached shoals (with water depths ~10 m found 15 km offshore) may prevent most of the wave energy from reaching the shoreline and that the high-curvature-coastline (cape and false cape) might reflect and trap free LGWs in a manner similar to convex mirrors. However, a detailed analysis of the aforementioned concepts was beyond the scope of our experiments and should be considered for future studies.

2.4.2   Methods

2.4.2.1   Study Area

Canaveral Shoals occupy depths between 5 and 25 m offshore of Cape Canaveral, on the Atlantic coast of Florida, whereas shore-attached Southeast and Chester Shoals appear as offshore extensions of Cape Canaveral and False Cape, respectively (Figure 2-25). Isolated shoals are separated from the aforementioned attached shoals by shallow basins that are ~20 m deep. The isolated shoal examined in this study was Shoal E, located ~3 km from Southeast Shoal (Field and Duane 1974; Thompson et al. 2015). Previous studies in this region (Olsen Associates 2013) and similar locations (McNinch and Luettich 2000; Thieler et al. 2013) found that shoals can migrate at rates $O(10 \text{ m/yr})$ and might experience active reworking by oceanographic processes, such as tidal rectification and associated residual flow (Signell and Geyer 1991; Geyer 1993; Berthot and Pattiaratchi 2005; 2006), wind-related flows, and surface gravity waves (McNinch and Luettich 2000; Kumar et al. 2013). Canaveral Shoals are thought to be a nearshore sediment sink, a hypothesis supported by ooids found at shoals and adjacent beaches (Field and Duane 1974).

Water levels in the southeastern USA are dominated by semidiurnal (M_2 and S_2), and diurnal (K_1) tidal constituents. Around Cape Canaveral, spring tidal ranges are ~1 m and neap ranges are ~0.4 m. Wave climate exhibits seasonal variability. During summer months (June to August) the wave field is mildly energetic, with $H_{SGW} \approx 0.5\ m$ and $T_p \approx 8\ s$, propagating from the east ($D_p \approx 90°$), while during winter and spring (October to April) Nor'easter activity tends to dominate ($H_{SGW} \approx 2\ m$, $T_p \approx 10\ s$) with waves coming from the north-northeast ($D_p < 60°$ and $D_p > 330°$) (Kline 2013). Seasonality in wave climate also includes tropical storm-hurricane activity during summer and early fall (June through November). During hurricanes, wave conditions at the shoals can reach values $H_{SGW} \approx 6\ m$ and $T_p \approx 10\ s$. Infragravity frequencies ranged from 5 to 50 mHz (or 20 to 200 s), comparable to other locations along the US Atlantic Coast (Herbers et al. 1994), and LGWs significant wave heights ranged from 0.02 to 0.2 m.

2.4.2.2 Data Collection and Processing

Observations of water velocity and near-bottom pressure were obtained from upward-looking ADCPs at the inner and outer swales on either side of Shoal E (Figure 2-25). Field experiments were conducted during fall 2013, spring 2014, and fall 2014. Only one ADCP deployed in fall 2013 recorded data prior to the dredging event in winter 2013–14/spring 2014. Pressure and velocity data were recorded in bursts of 1,200; 2,048; 2,400; or 3,600 measurements at a sampling frequency of 2 Hz. Pressure was measured ~1 m above the bed, while wave orbital velocities were obtained at one depth, between 3 and 7 m above the bed (see Paniagua et al. 2017 for details in experimental set-up).

Data processing included the screening for anomalous values in time when instruments were not submerged, when spikes occurred, and when there were low correlations among velocities measured by different transducers (Goring and Nikora 2002; RD Instruments 2011). Given the water depths and wave characteristics (typically $Ur < 0.1$), observed deviations from linear wave theory were considered negligible (Elgar et al. 2005). To quantify wave parameters and analyze the LGW energy variability, power spectra with frequency resolutions $df = 4\ mHz$ (hereafter referred as "low resolution") and $df = 1\ mHz$ ("high resolution") were calculated for pressure burst data packets that were de-meaned and de-trended. Because sampling frequencies were instrument specific, we assembled bursts into 3-hr time spans and assumed stationarity over each of those intervals. To reduce the Gibbs phenomenon, we tapered (with a Hann function) and 75 %-overlapped data windows of $2^{10} = 1,024$ and $2^{11} = 2,048$ elements to calculate the low- and high-resolution spectra, respectively (Thomson and Emery 2014 section 5.4.6). See Table 2-2 for additional details about the spectral calculation.

2.4.2.3 Long-Gravity Energy Fluxes

Seaward and landward cross-shoal LGW energy fluxes were estimated from time series of pressure P and velocity $\vec{q} = (u, v)$, where u and v were the East-West and North-South velocity components, respectively. Cross- and along-shoal velocities were calculated as the projections of $\vec{q}$ to a coordinate system aligned with the angle of the shoal axes (i.e., ~22° of azimuth). As such, velocities in the shoal coordinate system were defined as $\vec{Q} = (U, V)$, with U and V being the along- and cross-shoal velocities, respectively. Assuming cross-shoal propagation only, the energy fluxes $\mathcal{F}^\pm(f)$ at each location (with "+" being landward and "−" seaward) were calculated from the momentum balance in shallow water as the following (Sheremet et al. 2002):

$$\mathcal{F}^\pm(f) = \frac{\sqrt{gh}}{4}\left[Co_{PP}(f) + \frac{h}{g}Co_{VV} \pm 2\sqrt{\frac{h}{g}}Co_{PV}(f)\right] \tag{38}$$

where $Co_{xy}(f)$ corresponded to the coincident spectrum – the real part of the cross-spectrum between time series x and y (e.g., Thomson and Emery 2014 section 5.6.5). Bulk energy fluxes $F^\pm$ were then

quantified as the integral sum of $\mathcal{F}^{\pm}(f)$ within the long gravity band (0.5 50 mHz). From seaward- and landward-oriented LGW energy fluxes, the cross-shoal reflection coefficient, R^2, was calculated as

$$R^2 = \frac{F^-}{F^+} \tag{39}$$

This symbology for the reflection coefficient, R^2, was chosen to be consistent with Sheremet et al. (2002) and should not be confused with the coefficient of determination, r^2, to be used later in this chapter.

2.4.3 Results

2.4.3.1 Spectral Analysis and LGW Variability

The spectrograms (the time series of low-resolution spectra) and the significant wave heights for the short-gravity band, H_{SGW}, are given in Figure 2-26. The spectral density values (in m²/Hz) represent the variance at different frequencies. Most of this variance (i.e., relatively bigger oscillations) were measured at frequencies between 50 and 300 mHz, or 3 to 20 s. When waves were relatively large within this band, approximately corresponding to when $H_{SGW} > 1.5$ m, oscillations were correspondingly more prominent at frequencies below 50 mHz (cf. Figure 2-26 A and B around dates 5 and 14 November of 2013). The inverse of this relationship was also found; during events when $H_{SGW} < 0.3$ m variances within the LGW band (around 10 mHz) were approximately 10^{-4} m²/Hz (see Figure 2-26 C and D at 25 May, or E and F at 30 October). Moreover, during instances when oscillations were negligible at frequencies ~10 mHz, LGW variance at 3 mHz was relatively high. These observations suggest the partition of forced and free LGWs found elsewhere (e.g., Herbers et al. 1994, 1995).

To analyze the dependence of LGWs on SGWs and obtain an approximate distribution of forced and free LGWs, we calculated the coefficients of determination between the time series of spectral densities (in m²/Hz) at each frequency within the LGW band and the SGW (sea-swell) variance, $m_{0,SGW}$ (Okihiro and Guza 1995). Overall, ~50% of the variance at LGWs frequencies between ~5 mHz (200 s) and 50 mHz (20 s) was explained by the variability of $m_{0,SGW}$ at the 99% confidence level (Figure 2-27, A for the inner swale, and B for the outer swale). For example, at frequencies lower than ~5 mHz (or periods higher than 200 s), ~10% of LGW variance variability was explained by variations in $m_{0,SGW}$. During fall 2013 at the outer swale, H_{SGW} explained nearly 75% of LGW variability (red line in Figure 2-27 B), in contrast to 60% explained at the inner swale (Figure 2-27 A).

Figures 2-27 C and D illustrate the mean spectra (from "high-resolution" spectra). The mean spectra were computed by averaging in time the spectral densities at each frequency for all high-resolution spectra (cf. Figure 2-26). The infragravity band was therefore defined between 1 and 50 mHz (or 20 to 1,000 s) by the valley in mean spectral density in the sea-swell band, defined between 50 and 300 mHz, or 3 to 20 s (cf. all panels in Figure 2-26, and Figures 2-27 C, inner swale, and 2-27 D, outer swale). This frequency band separation agrees with studies carried along the U.S. North Atlantic Coast (e.g., Herbers et al. 1994).

2.4.3.2 Infragravity Energy Fluxes Between Swales

To test the hypothesis that the cape-related shoal exerts control on the spatial evolution of the infragravity waves, we compared cross-shoal seaward- (F^-) and landward-directed (F^+) LGW energy fluxes at inner and outer swales of Shoal E (Figure 2-28). Overall, three spatial variabilities were identified. In comparison to outer swale fluxes, we observed larger fluxes at the inner swale during fall 2013 (Figure 2-28 A and B), nearly comparable fluxes at the inner swale during spring 2014 (Figure 2-28 C and D), and smaller fluxes at the inner swale during fall 2014 (Figure 2-28 E and F). Differences in fluxes suggested that the source (or sink) of LGW energy between the swales may be related to short-wave shoaling and breaking over the shoal.

As supported by coefficients of determination between fluxes at inner and outer swales, approximately 5%, 24%, and 14% of variability of both seaward- and landward-directed fluxes ($F^{\pm}$) at the inner swale were explained by $F^{\pm}$ variations at the outer swale during fall 2013, spring 2014, and fall 2014, respectively. These determination coefficients suggested that LGW fluxes at the inner swale were independent from LGW fluxes at the outer swale, and variability was likely related to processes occurring over Shoal E. In addition, ~50% of variability in LGW energy fluxes or less was explained by changes in H_{SGW} during all experiments (Table 2-3). These levels of determination between H_{SGW} and LGW energy fluxes suggested a background of free infragravity oscillations (Herbers et al. 1994).

In addition, we quantified the cross-shoal bulk LGW reflection coefficients (R^2) at inner and outer swales of Shoal E (Figure 2-29). Mean reflection coefficients at the outer swale were not equal to those at the inner swale at the 99% of statistical confidence. Table 2-4 summarizes the results from the inference analyses to R^2 means between swales. R^2 values were typically larger at the outer swale during all experiments (see Appendix D for details in the statistical analysis).

Figure 2-29 illustrates D_p- and T_p- sorted values of R^2 and H_{LGW} versus Ur. In general, $R^2 \approx 1$ when $5 \times 10^{-4} < Ur < 5 \times 10^{-3}$ and $T_p < 8\ s$. R^2 ranged from 0.4 to 3 for $T_p > 10\ s$ and followed wave propagation with respect to the shoal. Reflection coefficients were less than 1 when waves came from $67° < D_p < 157°$ of azimuth (i.e., landward direction across shoal), whereas $R^2 > 1$ were associated to $247° < D_p < 337°$ of azimuth (i.e., seaward-directed waves). Opposite tendencies in R^2 values between fall 2013 and fall 2014 for $Ur > 2 \times 10^{-2}$ may be explained as an artifact of the orientation chosen for F^- as seaward and F^+ as landward (cf. Figures 2-29 A and E). When waves with $Ur > 5 \times 10^{-2}$ came from $247° < D_p < 337°$ during fall 2014, values of R^2 were typically larger than 1. This tendency suggested $F^- > F^+$, as expected in the deep-water zone (Sheremet et al. 2002). However, if the incoming-outgoing roles were interchanged (i.e., F^+ represents seaward fluxes), $F^{\pm}$ directions were reversed according to wave propagation over the shoal when $Ur > 5 \times 10^{-2}$ during fall 2014; values of $R^2 < 1$ and the shoal may be located in the shoaling zone as in during fall 2013. In general, values of R^2 suggest that fluxes directed opposite to the short-wave propagation were smaller than fluxes in the direction of the sea-swell for $Ur > 5 \times 10^{-2}$. In addition, values of H_{LGW} were $\sim 10^{-2}\ m$ for relatively frequency-dispersive waves ($T_p < 5\ s$ and $Ur \approx 10^{-3}$) and $O(1\ m)$ for relatively weakly nonlinear waves ($Ur \approx 0.2$).

2.4.4 Discussion

We hypothesized that the complex bathymetry related to cuspate forelands affects LGWs via shoaling, dissipation, reflection, and trapping. Differences in $F^{\pm}$ between swales and higher R^2 values at the outer swale of Shoal E suggested the presence of a source (sink) of seaward (landward) cross-shoal LGW energy flux. Seasonality may play a role in LGW variability since observations during both fall experiments followed similar trends and differed from spring results.

2.4.4.1 Shoaling and Breaking of SGWs over Cape-related Shoals

Shoaling and breaking of wave groups was one mechanism that could generate LGWs over cape-related shoals. Infragravity waves can be produced over shoals by the amplification of the dynamic set-up generated due to depth differences within a short-waves group (Mei and Benmoussa 1984) that are enhanced over sloping bottoms (Baldock 2006), by the time-varying short-wave breaking at LGW frequencies (Schäffer 1993), and via extra energy transfers from sea-swell (Beji and Battjes 1993).

2.4.4.1.1 Shoaling of Short-Wave Groups

The variability of R^2 with Ur resembled the dependency of wave biphase, asymmetry, and skewness on Ur (Doering and Bowen 1995) and suggested that $R^2s \approx 0.5$ were related to weakly nonlinear waves with relatively important triad interactions among the spectral peak and its harmonics (Young and Eldeberky 1998). Parameterizations of the skewness S_{ww}, asymmetry A_{ww}, and biphase β_{ww} were given in terms of Ur as the following (Doering and Bowen 1995 Eqs. 4.9 through 4.11):

$$S_{ww} = [0.8 + 0.62\log(Ur)]\cos\left[-90° + 90°\tanh\left(\frac{0.73}{Ur}\right)\right] \tag{40}$$

$$A_{ww} = [0.8 + 0.62\log(Ur)]\sin\left[-90° + 90°\tanh\left(\frac{0.73}{Ur}\right)\right] \tag{41}$$

and

$$\beta_{ww} = -90° + 90°\tanh\left(\frac{0.73}{Ur}\right) \tag{42}$$

These parameters represent the relative importance of triad interactions in the formation of superharmonics, which are related to velocity and acceleration skewness and breaking (Hoefel and Elgar 2003). Table 2-5 shows values of skewness, asymmetry, and biphase for the maximum value of Ur during each experiment. These values suggest that as Ur was ~0.1, SGWs remained frequency-dispersive, and asymmetry and skewness were negligible.

However, over Shoal E proper at $h \approx 5\ m$, with $H_{SGW} \approx 2.5\ m$, $T_P \approx 10\ s$, and $Ur \approx 0.6$, the parameterization resulted in values $S_{ww} = 0.64$, $A_{ww} = -0.17$, and $\beta_{ww} = -15°$. This biphase refers to superharmonics not locked to the main spectral peak. Asymmetry and skewness different from zero may indicate relatively more energy transfers to the LGWs, as expected in shallower water over Shoal E (Elgar and Guza 1985). Moreover, during hurricanes ($H_{SGW} \approx 6\ m$, $T_p \approx 12\ s$, and $Ur \approx 2.1$) $S_{ww} = 0.49$, $A_{ww} = -0.88$, and $\beta_{ww} = -60°$. During storms, sea-swell over Shoal E ridge may behave comparatively more amplitude dispersive.

Considering the relation between landward- and seaward-oriented infragravity energy fluxes, Figure 2-30 shows the reflection coefficients measured during each experiment in the context of studies performed in gently sloping beaches. Values $R^2 \approx 1$ may indicate negligible dissipation and trapping (as edge waves) between the reflector and the measurement location. Values $R^2 < 1$ ($R^2 > 1$) suggest either the generation of seaward- (landward-) oriented LGWs, or the dissipation of landward- (seaward-) oriented LGWs. In gently sloping beaches (Figure 2-30 A), values ~0.5 were found in the shoaling region when onshore-oriented LGW energy flux increases, while variations in offshore-directed flux were orders of magnitude smaller (Sheremet et al. 2002). At Cape Canaveral Shoals, values of $R^2 \approx 0.5$ during fall 2013 (Figure 2-29 A, and red star and bar in Figure 2-30 B) suggest the shoaling of short-wave groups close to the breaking location where F^+ was maximum. Values of $R^2 > 1$ for $247° < D_p < 337°$ during fall 2014 corresponded to $R^2 \approx 0.5$ in the opposite direction and suggested, in terms of short-wave shoaling, conditions similar to the fall 2013 experiment.

2.4.4.1.2 Dichotomy Between Shoaling and Breaking in LGW Generation

The discernment between shoaling and breaking in LGWs generation has been represented by the surf-beat similarity parameter, $\xi_{surfbeat}$. This parameter was defined as the product of the surf-beat length relative to the bottom slope and the short-wave steepness (Battjes et al. 2004; Baldock 2012). Breaking-induced surf beat was thought to dominate when $\xi_{surfbeat}$ was large (i.e., for steep short waves and steep beach slopes), whereas low short-wave steepness and mild beach slopes produced small values of

$\xi_{surfbeat}$ during which the shoaling mechanism dominates. In other words, the dominance depends upon whether short-wave groups propagate in shallow water before breaking or not. If not, the breaking mechanism dominates (Contardo and Symonds 2013).

Given water depths found at the swales (~13 m) and the ridge (~5 m) of Shoal E, we propose that both mechanisms generate free LGWs. Under the assumption of frequency dispersive ($a/h \ll 1$) and infinitesimal waves ($a\kappa \ll 1$), shallow-water conditions are achieved when $h/L < 0.05$, with $L = 2\pi/\kappa$. For the case of a sinusoidal wave train with $H_{SGW} = 0.5\ m$ and $T_p = 8\ s$ propagating over constant water depths of 13 m, $a/h \approx 0.04$, wavelength $L \approx 78\ m$ ($f \approx 0.125\ Hz$), $a\kappa \approx 0.01$, and $h/L \approx 0.17$. In this case, the shallow-water limit was theoretically found at $h \approx 4\ m$. These calculations support the idea that short waves found at the shoals of Cape Canaveral do not propagate in shallow water over the shoals. However, what happens when a/h is not $\ll 1$? In such a case, shallow-water conditions should be evaluated by means of complete parameterizations (i.e., Ur).

Wave steepness in $\xi_{surfbeat}$ ($a\kappa$ or H/L) determines whether gravity waves propagate as shallow water waves only when $a/h \ll 1$. When this condition does not hold, determining wave behavior would require the comparison between amplitude and frequency dispersion as it is represented by Ur (Ursell 1953). Waves behave as in shallow water (or tend to be amplitude dispersive) when $Ur > 1$. In published results that use β_{norm} and $\xi_{surfbeat}$ (Battjes et al. 2004; Baldock 2012; Contardo and Symonds 2013), a/h was considered negligible, and frequency dispersion was assumed to capture SGWs behavior. Actually, frequency dispersion plays a more prominent role than wave steepness in the Ursell parameterization as can be seen in a modified version of Ur:

$$Ur = \frac{3}{32\pi^2}\frac{H}{L}\left(\frac{L}{h}\right)^3 \tag{43}$$

We suggest that, if used, the $\xi_{surfbeat}$ should include Ur to avoid ambiguities in the shoaling-breaking discernment in LGWs generation. We tentatively propose a modified surf-beat similarity parameter ξ_{LGW} as the following:

$$\xi_{surfbeat} = \beta_{norm}Ur = \frac{h_x}{\omega_{LGW}}\sqrt{\frac{g}{h}}\,\alpha\frac{H_{SGW}}{h}\left(\frac{L}{h}\right)^2 \tag{44}$$

Similar to $\xi_{surfbeat}$, large values of ξ_{LGW} indicate breaking dominance in LGW generation. For energetic conditions at Shoal E ridge ($H_{SGW} \approx 2.5\ m$, $T_p \approx 10\ s$, and $h \approx 5\ m$), $\xi_{surfbeat} \approx 0.01$ and $\xi_{LGW} \approx 0.05$. These values corresponded to shoaling dominance (Baldock 2012). For extreme values found at Shoal E ridge during hurricanes ($H_{SGW} \approx 6\ m$, $T_p \approx 12\ s$, and $h \approx 5\ m$), $\xi_{surfbeat} \approx 0.02$ and $\xi_{LGW} \approx 0.16$. The surf-beat similarity parameter suggests shoaling mechanism dominates over breaking. In contrast, the LGW similarity suggests short-wave breaking dominates. The inclusion of Ur (≈ 2 during hurricanes) in $\xi_{surfbeat}$ allows for the consideration of waves that are not steep but behave as amplitude dispersive given water depths over Shoal E ridge.

However, it is worth offering a word of caution: although individually, Ur and β_{norm} each may be regarded to have a physical basis, $\xi_{surfbeat}$ and ξ_{LGW} are not supported by a physical formalism. They appear as combinations of parameters that exhibit similar numeric tendencies according to short- and long-wave conditions. This behavior does not imply that the terms are physically connected. Therefore, the discernment of mechanisms involved in LGWs generation over shoals should be based on a complete picture of the phenomenon. This endeavor may be attained by using dense instrumentation (e.g., Herbers et al. 1994 section 2) and extending analytical solutions of wave scattering in infragravity wave generation to three dimensions (e.g., Zou 2011) and secondary wave variability (e.g., Belibassakis et al. 2011).

2.4.4.1.3 Variable Forcing Due to Short-wave Scattering over Shoal E

A complete picture of sea-swell transformations over shoals should consider both wave field scattering and dissipation. "Scattering" refers to short-wave refraction, diffraction, and reflection (Bender and Dean 2003), which likely exert control on the long-term maintenance of cuspate forelands (Limber et al. 2017). The partial reflection of LGWs by complicated bathymetry has been theorized for several idealized profiles (Liu et al. 2013 and references therein) and has been confirmed at submarine canyons (Thomson et al. 2005, 2007). Over cape-related shoals, LGW reflection may be analogous to the transmission of a stream of electrons through an attractive, square well potential (Bohm 1989; Mei et al. 2005), and analytical solutions for smooth topographies have been already proposed (Zou 2011; Liu et al. 2012).

In two dimensions, the scattering of short-wave groups over shoals may generate LGWs via three mechanisms: depth variations induce second-order forced LGWs, changes in long-wave volume flux, and spatial gradients in stresses related to wave orbital velocities (*radiation stresses*) (cf. Zou 2011 section 5). These mechanisms depend upon topographic characteristics: water depth, slope, and curvature. Figure 2-25 D shows the Shoal E profile, which was not symmetric. Outer slopes and curvatures were steeper and negative, respectively, whereas inner slopes and curvature were milder and positive. These geometrical characteristics likely produced asymmetries in LGW generation and might explain differences in fluxes between swales. Low coefficients of determination between fluxes of the same orientation at two swales (cf. Figure 2-28) suggest fluxes were unrelated to one another, and energy was added/lost over Shoal E by the aforementioned processes that were not dependent on fluxes variability. Further analysis would be required to refine these ideas (e.g., Thomson et al. 2005 supplementary information).

2.4.4.2 Net Spatial Gradients in Energy Fluxes: Implications for the Long-term Maintenance of Capes

Figure 2-31 shows the time series of the bulk infragravity source terms, $\bar{S}$, and the net gradient in LGW energy fluxes, $\Delta F_{LGW}/\Delta x$ (see Appendix E for details), including the wavelet coherence (WTC) between these time series. During fall 2013 (Figure 2-31 A and B), values of $\bar{S}$ oscillated around zero, while net fluxes $\Delta F_{LGW}/\Delta x$ were mostly positive. Large oscillations in $\bar{S}$ were associated to $\Delta F_{LGW}/\Delta x > 0$ most of the time, with some notable exceptions (see Figure 2-31 B between 1 and 16 days of period).

Landward propagation also occurred during spring 2014. However, values of $\bar{S}$ and $\Delta F_{LGW}/\Delta x$ were only coherent for ~2 days near 12 May 2014 (cf. Figure 2-31 D between 1 and 3 days of period). The lack of coherence suggests changes in LGW energy fluxes did not depend upon short-wave transformation over Shoal E. The inverse effect on $\Delta F_{LGW}/\Delta x$ was calculated for fall 2014 data given that short-wave propagation was dominantly seaward across Shoal E.

In general, these results suggest Shoal E exerted control on LGW variability by increasing the net energy flux at the "outgoing" swale (i.e., the swale located "after" the shoal with respect to short-wave propagation). Consider the net cross-shoal flux, F_{LGW}, which reads as follows (Sheremet et al. 2002):

$$F_{LGW} = F^+ - F^- \tag{45}$$

Larger net fluxes at the outgoing swale imply either the dissipation of F^- or the enhancement of F^+ due o short-wave propagation over Shoal E. The enhancement option would be supported by an increase in the proportion of free LGWs at the inner swale by short-wave shoaling (and possible breaking) during the fall 2013 experiment (cf. Figure 2-27 A and B).

In synthesis, we speculate that cape-related shoals initiate the energy transfer from SGWs to LGWs further offshore compared to a typical, gently sloping beach physiography (Figure 2-32 A). This LGW forcing implies that short-wave breakers near cuspate coastlines migrate further onshore as the surfzone

narrows. Also, free LGWs should be reflected from the shoreline in patterns similar to convex mirrors (cf. Figure 2-32 B and Whitham 1999 Figure 7.9), and both incoming and outgoing LGWs would be dissipated by the shore-attached shoal (cf. Figure 2-25 D). Over time scales of years to centuries, these mechanisms may exert control on the maintenance of cuspate forelands. In addition to the high-angle instability (Ashton and Murray 2006; Limber et al. 2017), a minimization in transport capacity at the cape tip provides an additional source for gradients in longshore sediment transport. Short waves may force infragravity motions via triad interactions (shoaling) and breaking over isolated and shore-attached shoals. These mechanisms illustrate how the energy from the short-gravity band transfers to LGW energy. Therefore, infragravity and tidal motions, and interactions among them, ought to dominate water circulation over cape-related shoals.

2.4.4.3 Potential Trapping of LGWs: Methodological Limitations

The main limitation in our methods relates to assuming cross-shoal propagation, which simplifies the physics but may hold only when SGWs propagate in directions close to perpendicular to the Shoal E axis ($67° < D_p < 157°$ or $247° < D_p < 337°$). Along-shoal reflection coefficients, i.e., those quantified using along-shoal velocities U, varied in the same manner as cross-shoal R^2 values. Reflection coefficients were larger at the outer swale during fall 2013, not different during spring 2014, and smaller at the outer swale during fall 2014. These results suggested that common processes were affecting both cross- and along-shoal energy fluxes. A summary of the statistical inference analysis is given in Table 2-6.

The sparsity of locations of measurements over the shoals provided an incomplete picture of the LGWs variability over the shoal. Our experiments did not consider along-shoal changes, likely governed by trapped edge waves and partial reflections in several directions (Eckart 1951; Huntley et al. 1981; Thomson et al. 2007; Rijnsdorp et al. 2015 and others). Values of $R^2 < 1$ suggested that the dissipation of energy during weakly nonlinear conditions may be attributed in part to these phenomena. Future research should focus on analyzing cross- and along-shoal LGWs dynamics with field data derived from arrays of instruments (Herbers et al. 1994; Sheremet et al. 2005).

2.4.4.4 Implications of Dredging

Because we have limited data under pre-dredging conditions, we can only speculate on the implications of these results. Wave-related energy fluxes at SGW and LGW change seasonally and from swale to swale. Comparisons of pre-dredging to after-dredging conditions at the site of the one mooring with data suggest changes that can be grouped into three categories: 1) susceptibility for wave transformation caused by subinertial water-level variability; 2) infragravity (LGW) wave forcing by short waves (SGW); and 3) generation and dissipation of LGW over ridges. With respect to (1), susceptibility for wave transformations decreased after dredging. In reference to (2), there was decreased forcing of SGW after dredging and an increased proportion of free LGW. Related to (3), there was decreased generation and increased generation of LGW after dredging.

Therefore, any alterations to the sea bed through dredging, either to ridge or to swale, will necessarily produce alterations to wave-related energy fluxes and the amount of erosional LGW energy that reaches the shore. These alterations will have effects on morphodynamic equilibrium and on erosional and depositional horizons. Dredging consequences could potentially be further addressed with process-oriented numerical simulations.

2.4.5 Conclusions

We compared LGW energy fluxes between inner and outer swales of Shoal E, offshore Cape Canaveral, to confirm that shoals exert control on infragravity wave variability. Three regimes were observed: larger fluxes at the inner swale, same order of magnitude in fluxes, and larger fluxes at the outer swale. Larger

differences were observed during fall 2013 and fall 2014 seasons, despite being reversed in direction. This reversal was explained by seaward-oriented short-wave propagation during fall 2014. Larger fluxes at "outgoing" swales were explained by two mechanisms: (1) LGW forcing over Shoal E by asymmetric shoaling and breaking of short waves, and (2) partial reflection and trapping of free LGWs. In general, these mechanisms suggest short-wave energy may be transferred to LGWs at isolated and shore-attached shoals and prevented from reaching the cape and adjacent shorelines. This transformation should influence the long-term maintenance of cape morphology. However, the complete LGW motion structure was not resolved, which likely includes trapped edge waves and partially reflected motions in different directions.

Our findings and limitations highlight the need to further study LGWs dynamics over cape-related shoals and how they influence the overall morphodynamics near cuspate forelands. Dredging alterations to ridge or swale were grouped into three categories associated with short-wave transformations into infragravity waves. Bed alterations will necessarily modify the amount of infragravity wave (LGW) energy that reaches the coastline and, hence, the morphodynamic changes at the shore.

2.4.6   References

Aagaard T, Greenwood B. 2008. Infragravity wave contribution to surf zone sediment transport — The role of advection. Marine Geology 251(1): 1-14. doi.org/10.1016/j.margeo.2008.01.017.

Alsina JM, Padilla EM, Cáceres I. 2016. Sediment transport and beach profile evolution induced by bi-chromatic wave groups with different group periods. Coastal Engineering 114: 325-340. doi.org/10.1016/j.coastaleng.2016.04.020.

Ashton AD, Murray AB. 2006. High-angle wave instability and emergent shoreline shapes: 1. Modeling of sand waves, flying spits, and capes. Journal of Geophysical Research: Earth Surface 111(F4). doi.org/10.1029/2005JF000422.

Baldock TE. 2006. Long wave generation by the shoaling and breaking of transient wave groups on a beach. Proceedings of the Royal Society A: Mathematical, Physical and Engineering Sciences 462: 1853 - 1876.

Baldock TE. 2012. Dissipation of incident forced long waves in the surf zone—Implications for the concept of "bound" wave release at short wave breaking. Coastal Engineering 60: 276-285.

Battjes JA, Bakkenes HJ, Janssen TT, van Dongeren AR. 2004. Shoaling of subharmonic gravity waves. Journal of Geophysical Research: Oceans 109 (C02009). doi.org/10.1029/2003JC001863.

Beji S, Battjes JA. 1993. Experimental investigation of wave propagation over a bar. Coastal Engineering 19(1): 151-162. doi.org/10.1016/0378-3839(93)90022-Z.

Belibassakis KA, Gerostathis TP, Athanassoulis GA. 2011. A coupled-mode model for water wave scattering by horizontal, non-homogeneous current in general bottom topography. Applied Ocean Research 33(4): 384-397. doi.org/10.1016/j.apor.2011.05.004.

Bellotti G, Franco L. 2011. Measurement of long waves at the harbor of Marina di Carrara, Italy. Ocean Dynamics 61(12): 2051-2059. doi:10.1007/s10236-011-0468-6.

Bender CJ, Dean RG. 2003. Wave field modification by bathymetric anomalies and resulting shoreline changes: a review with recent results. Coastal Engineering 49: 125-153.

Berthot A, Pattiaratchi C. 2005. Maintenance of headland-associated linear sandbanks: Modelling the secondary flows and sediment transport. Ocean Dynamics 55: 526-540. doi:10.1007/s10236-005-0010-9.

Berthot A, Pattiaratchi C. 2006. Mechanisms for the formation of headland-associated linear sandbanks. Continental Shelf Research 26(8): 987-1004. doi.org/10.1016/j.csr.2006.03.004.

Bohm D. 1989. Quantum Theory. New York, NY: Dover Publications.

Bowen AJ, Guza RT. 1978. Edge waves and surf beat. Journal of Geophysical Research: Oceans 83(C4): 1913-1920. doi.org/10.1029/JC083iC04p01913.

Bowers EC. 1977. Harbour resonance due to set-down beneath wave groups. Journal of Fluid Mechanics 79: 71 - 92.

Cavaleri L, Alves JHGM, Ardhuin F, Babanin A, Banner M, Belibassakis K, Benoit M, Donelan M, Groeneweg J, Herbers THC, Hwang P, Janssen PAEM, Janssen T, Lavrenov IV, Magne R, et al. 2007. Wave modelling – The state of the art. Progress in Oceanography 75(4): 603-674. doi.org/10.1016/j.pocean.2007.05.005.

Clark DB, Elgar S, Raubenheimer B. 2012. Vorticity generation by short-crested wave breaking. Geophysical Research Letters 39 (L24604). doi.org/10.1029/2012GL054034.

Clark DB, Feddersen F, Guza RT. 2011. Modeling surf zone tracer plumes: 2. Transport and dispersion. Journal of Geophysical Research: Oceans 116 (C11028). doi.org/10.1029/2011JC007211.

Coco G, Burnet TK, Werner BT, Elgar S. 2003. Test of self-organization in beach cusp formation. Journal of Geophysical Research: Oceans 108 (C3, 3101). doi.org/10.1029/2002JC001496.

Contardo S, Symonds G. 2013. Infragravity response to variable wave forcing in the nearshore. Journal of Geophysical Research: Oceans 118(12): 7095-7106. doi.org/10.1002/2013JC009430.

Davidson-Arnott R. 2010. Introduction to Coastal Processes and Geomorphology. Cambridge, UK: Cambridge University Press. https://books.google.com/books?id=L2qgzQEACAAJ.

Davis RA, Klay J, Jewell P. 1993. Sedimentology and stratigraphy of tidal sand ridges Southwest Florida inner shelf. Journal of Sedimentary Research 63(1): 91-104. doi:10.1306/d4267a9b-2b26-11d7-8648000102c1865d.

de Bakker ATM, Tissier MFS, Ruessink BG. 2016. Beach steepness effects on nonlinear infragravity-wave interactions: A numerical study. Journal of Geophysical Research: Oceans 121(1): 554-570. doi.org/10.1002/2015JC011268.

Diaz-Hernandez G, Mendez FJ, Losada IJ, Camus P, Medina R. 2015. A nearshore long-term infragravity wave analysis for open harbours. Coastal Engineering 97: 78-90. doi.org/10.1016/j.coastaleng.2014.12.009.

Doering JC, Bowen AJ. 1986. Shoaling surface gravity waves: A bispectral analysis. In: Coastal Engineering Proceedings, 20th International Conference in Coastal Engineering, January 1986; 150-162 p.

Doering JC, Bowen AJ. 1995. Parametrization of orbital velocity asymmetries of shoaling and breaking waves using bispectral analysis. Coastal Engineering 26(1): 15-33. doi.org/10.1016/0378-3839(95)00007-X.

Eckart C. 1951. Surface waves on water of variable depth, Lecture notes, fall semester, 1950-51. Scripps Institution of Oceanography.

Elgar S, Guza RT. 1985. Observations of bispectra of shoaling surface gravity waves. Journal of Fluid Mechanics 161: 425-448. doi:10.1017/S0022112085003007.

Elgar S, Guza RT, Freilich MH. 1993. Observations of nonlinear interactions in directionally spread shoaling surface gravity waves. Journal of Geophysical Research: Oceans 98(C11): 20299-20305. doi.org/10.1029/93JC02213.

Elgar S, Herbers THC, Okihiro M, Oltman-Shay J, Guza RT. 1992. Observations of infragravity waves. Journal of Geophysical Research: Oceans 97(C10): 15573-15577. doi.org/10.1029/92JC01316.

Elgar S, Raubenheimer B, Guza RT. 2005. Quality control of acoustic Doppler velocimeter data in the surfzone. Measurement Science and Technology 16(10): 1889-1893. doi:10.1088/0957-0233/16/10/002.

Feddersen F. 2014. The generation of surfzone eddies in a strong alongshore current. Journal of Physical Oceanography 44: 600-617.

Field M, Duane D. 1974. Geomorphology and sediments of the inner continental shelf, Cape Canaveral, Florida. Fort Belvoir, Virginia: U.S. Army, Corps of Engineers, Coastal Engineering Research Center. Technical Memorandum 42.

Filipot J-F, Ardhuin F, Babanin AV. 2010. A unified deep-to-shallow water wave-breaking probability parameterization. Journal of Geophysical Research: Oceans 115 (C04022). doi.org/10.1029/2009JC005448.

Geyer WR. 1993. Three-dimensional tidal flow around headlands. Journal of Geophysical Research: Oceans 98(C1): 955-966. doi.org/10.1029/92JC02270.

Goring DG, Nikora VI. 2002. Despiking acoustic doppler velocimeter data. Journal of Hydraulic Engineering 128: 117-126.

Guza RT, Thornton EB. 1982. Swash oscillations on a natural beach. Journal of Geophysical Research: Oceans 87(C1): 483-491. doi.org/10.1029/JC087iC01p00483.

Hasselmann KF. 1962. On the non-linear energy transfer in a gravity-wave spectrum Part 1. General theory. Journal of Fluid Mechanics 12: 481 - 500.

Henderson SM, Guza RT, Elgar S, Herbers THC, Bowen AJ. 2006. Nonlinear generation and loss of infragravity wave energy. Journal of Geophysical Research: Oceans 111 (C12007). doi.org/10.1029/2006JC003539.

Herbers THC, Elgar S, Guza RT. 1994. Infragravity-frequency (0.005-0.05 hz) motions on the shelf: Part I: Forced waves. Journal of Physical Oceanography 24: 917-927.

Herbers THC, Elgar S, Guza RT, O'Reilly WC. 1995. Infragravity-frequency (0.005–0.05 Hz) motions on the shelf. Part II: Free waves. Journal of Physical Oceanography 25(6): 1063-1079. doi:10.1175/1520-0485(1995)025<1063:Ifhmot>2.0.Co;2.

Herbers THC, Russnogle NR, Elgar S. 2000. Spectral energy balance of breaking waves within the surf zone. Journal of Physical Oceanography 30(11): 2723-2737. doi:10.1175/1520-0485(2000)030<2723:Sebobw>2.0.Co;2.

Hoefel F, Elgar S. 2003. Wave-induced sediment transport and sandbar migration. Science 299(5614): 1885-1887. doi:doi:10.1126/science.1081448.

Huntley DA, Guza RT, Thornton EB. 1981. Field observations of surf beat: 1. Progressive edge waves. Journal of Geophysical Research: Oceans 86(C7): 6451-6466. doi.org/10.1029/JC086iC07p06451.

Janssen TT, Herbers THC, Battjes JA. 2006. Generalized evolution equations for nonlinear surface gravity waves over two-dimensional topography. Journal of Fluid Mechanics 552: 393-418. doi:10.1017/S0022112006008743.

Kaergaard K, Fredsoe J. 2013. A numerical shoreline model for shorelines with large curvature. Coastal Engineering 74: 19-32. doi.org/10.1016/j.coastaleng.2012.11.011.

Kirby JT, Dalrymple RA. 1983. A parabolic equation for the combined refraction–diffraction of Stokes waves by mildly varying topography. Journal of Fluid Mechanics 136: 453-466. doi:10.1017/S0022112083002232.

Kline SW. 2013. Influence of wave energy dissipation on the geomorphic behavior of rocky and sandy coasts. Gainesville, FL: Dissertation. University of Florida, Gainesville, FL.

Komar PD. 1971. The mechanics of sand transport on beaches. Journal of Geophysical Research (1896-1977) 76(3): 713-721. doi.org/10.1029/JC076i003p00713.

Kumar N, Voulgaris G, List JH, Warner JC. 2013. Alongshore momentum balance analysis on a cuspate foreland. Journal of Geophysical Research: Oceans 118(10): 5280-5295. doi.org/10.1002/jgrc.20358.

Limber PW, Adams PN, Murray AB. 2017. Modeling large-scale shoreline change caused by complex bathymetry in low-angle wave climates. Marine Geology 383: 55-64. doi.org/10.1016/j.margeo.2016.11.006.

Lin P, Liu H. 2005. Analytical study of linear long-wave reflection by a two-dimensional obstacle of general trapezoidal shape. Journal of Engineering Mechanics 131: 822-830.

Liu H, Luo J, Lin P, Liu R. 2013. Analytical solution for long-wave reflection by a general breakwater or trench with curvilinear slopes. Journal of Engineering Mechanics 139: 229-245. doi:10.1061/(ASCE)EM.1943-7889.0000483.

Liu H, Yang J, Lin P. 2012. An analytic solution to the modified mild-slope equation for wave propagation over one-dimensional piecewise smooth topographies. Wave Motion 49(3): 445-460. doi.org/10.1016/j.wavemoti.2012.01.002.

Liu PLF. 1989. A note on long waves induced by short-wave groups over a shelf. Journal of Fluid Mechanics 205: 163-170. doi:10.1017/S0022112089001989.

Longuet-Higgins MS, Stewart RW. 1962. Radiation stress and mass transport in gravity waves, with application to 'surf beats'. Journal of Fluid Mechanics 13(4): 481-504. doi:10.1017/S0022112062000877.

Longuet-Higgins MS, Stewart RW. 1964. Radiation stresses in water waves; a physical discussion, with applications. Deep Sea Research and Oceanographic Abstracts 11(4): 529-562. doi.org/10.1016/0011-7471(64)90001-4.

McNinch JE, Luettich RA. 2000. Physical processes around a cuspate foreland: implications to the evolution and long-term maintenance of a cape-associated shoal. Continental Shelf Research 20(17): 2367-2389. doi.org/10.1016/S0278-4343(00)00061-3.

Mei CC, Benmoussa C. 1984. Long waves induced by short-wave groups over an uneven bottom. Journal of Fluid Mechanics 139: 219-235. doi:10.1017/S0022112084000331.

Mei CC, Stiassnie M, Yue D. 2005. Theory and applications of ocean surface waves. Part I: Linear aspects. Hackensack, NJ: World Scientific.

Munk WH. 1949. Surf beats. Transactions American Geophysical Union 30(6): 849-854. doi.org/10.1029/TR030i006p00849.

Murray AB, Ashton AD. 2013. Instability and finite-amplitude self-organization of large-scale coastline shapes. Philosophical Transactions of the Royal Society A: Mathematical, Physical and Engineering Sciences 371(2004): 20120363. doi:10.1098/rsta.2012.0363.

Okihiro M, Guza RT. 1995. Infragravity energy modulation by tides. Journal of Geophysical Research: Oceans 100(C8): 16143-16148. doi.org/10.1029/95JC01545.

Okihiro M, Guza RT, Seymour RJ. 1992. Bound infragravity waves. Journal of Geophysical Research: Oceans 97(C7): 11453-11469. doi.org/10.1029/92JC00270.

Olsen Associates. 2013. Brevard County, Florida, Federal Shore Protection Project, South Reach: 3-Year post-construction monitoring of the Canaveral Shoals II offshore borrow area (June 2013). Jacksonville, Florida: 15 p.

Paniagua -A, JF, Admas P, Valle-Levinson A, Parra S. 2017. Infragravity energy fluxes at inner and outer swales of Shoal E, Cape Canaveral, Florida: Experimental set-up. Sustainable Environment through Actionable Data (SEAD).

Pomeroy A, Lowe R, Symonds G, Van Dongeren A, Moore C. 2012. The dynamics of infragravity wave transformation over a fringing reef. Journal of Geophysical Research: Oceans 117(C11). doi.org/10.1029/2012JC008310.

RD Instruments. 2011. Acoustic doppler current profiler principles of operation: a practical primer. Poway, CA.

Rijnsdorp DP, Ruessink G, Zijlema M. 2015. Infragravity-wave dynamics in a barred coastal region, a numerical study. Journal of Geophysical Research: Oceans 120(6): 4068-4089. doi.org/10.1002/2014JC010450.

Rodriguez A, Sánchez-Arcilla A, Redondo JM, Bahia E, Sierra JP. 1995. Pollutant dispersion in the nearshore region: Modelling and measurements. Water Science and Technology 32(9): 169-178. doi.org/10.1016/0273-1223(96)00088-1.

Roelvink D, Reniers A, van Dongeren A, van Thiel de Vries J, McCall R, Lescinski J. 2009. Modelling storm impacts on beaches, dunes and barrier islands. Coastal Engineering 56(11): 1133-1152. doi.org/10.1016/j.coastaleng.2009.08.006.

Ruessink BG. 1998. Bound and free infragravity waves in the nearshore zone under breaking and nonbreaking conditions. Journal of Geophysical Research: Oceans 103(C6): 12795-12805. doi.org/10.1029/98JC00893.

Schäffer HA. 1993. Infragravity waves induced by short-wave groups. Journal of Fluid Mechanics 247: 551-588. doi:10.1017/S0022112093000564.

Schratzberger M, Larcombe P. 2014. The role of the sedimentary regime in shaping the distribution of subtidal sandbank environments and the associated meiofaunal nematode communities: An example from the southern North Sea. PLOS ONE 9(10): e109445. doi:10.1371/journal.pone.0109445.

Sheremet A, Guza RT, Elgar S, Herbers THC. 2002. Observations of nearshore infragravity waves: Seaward and shoreward propagating components. Journal of Geophysical Research: Oceans 107 (C8, 3095). doi.org/10.1029/2001JC000970.

Sheremet A, Guza RT, Herbers THC. 2005. A new estimator for directional properties of nearshore waves. Journal of Geophysical Research: Oceans 110 (C01001). doi.org/10.1029/2003JC002236.

Signell RP, Geyer WR. 1991. Transient eddy formation around headlands. Journal of Geophysical Research: Oceans 96(C2): 2561-2575. doi.org/10.1029/90JC02029.

Symonds G, Huntley D, Bowen A. 1982. Two-dimensional surf beat: Long wave generation by a time-varying breakpoint. Journal of Geophysical Research 87: 492-498. doi:10.1029/JC087iC01p00492.

Thieler E, Foster D, Himmelstoss E. 2013. Geologic framework of the northern North Carolina, USA inner continental shelf and its influence on coastal evolution. Marine Geology 348: 113-130. doi:10.1016/j.margeo.2013.11.011.

Thompson DM, Plant NG, Hansen ME. 2015. Analysis of bathymetric surveys to identify coastal vulnerabilities at Cape Canaveral, Florida. Reston, VA: 31 pp p. Report No.: 2015-1180. http://pubs.er.usgs.gov/publication/ofr20151180.

Thomson J, Elgar S, Herbers T, Raubenheimer B, Guza R. 2007. Refraction and reflection of infragravity waves near submarine canyons. Journal of Geophysical Research 112 (C10009). doi:10.1029/2007JC004227.

Thomson J, Elgar S, Herbers THC. 2005. Reflection and tunneling of ocean waves observed at a submarine canyon. Geophysical Research Letters 32 (L10602). doi.org/10.1029/2005GL022834.

Thomson J, Elgar S, Raubenheimer B, Herbers THC, Guza RT. 2006. Tidal modulation of infragravity waves via nonlinear energy losses in the surfzone. Geophysical Research Letters 33 (L05601). doi.org/10.1029/2005GL025514.

Thomson RE, Emery WJ. 2014. Data analysis methods in physical oceanography. 3rd ed. Waltham, MA: Elsevier.

Torres-Freyermuth A, Hsu T-J. 2014. On the mechanisms of low-frequency wave attenuation by muddy seabeds. Geophysical Research Letters 41(8): 2870-2875. doi.org/10.1002/2014GL060008.

Tucker MJ. 1950. Surf beats: sea waves of 1 to 5 min. period. Proceedings of the Royal Society of London Series A Mathematical and Physical Sciences 202: 565 - 573.

Ursell F. 1953. The long-wave paradox in the theory of gravity waves. Mathematical Proceedings of the Cambridge Philosophical Society 49(4): 685-694. doi:10.1017/S0305004100028887.

van Thiel de Vries JSM, van Gent MRA, Walstra DJR, Reniers AJHM. 2008. Analysis of dune erosion processes in large-scale flume experiments. Coastal Engineering 55(12): 1028-1040. doi.org/10.1016/j.coastaleng.2008.04.004.

Whitham G. 1999. Linear and nonlinear waves. New York, NY: Wiley-Interscience. https://onlinelibrary.wiley.com/doi/abs/10.1002/9781118032954.fmatter.

Yoo D, O'Connor B. 1988. Diffraction of waves in caustics. Journal of Waterway, Port, Coastal, and Ocean Engineering 114: 715-731.

Young AP, Guza RT, Adams PN, O'Reilly WC, Flick RE. 2012. Cross-shore decay of cliff top ground motions driven by local ocean swell and infragravity waves. Journal of Geophysical Research: Oceans 117 (C06029). doi.org/10.1029/2012JC007908.

Young IR, Eldeberky Y. 1998. Observations of triad coupling of finite depth wind waves. Coastal Engineering 33(2): 137-154. doi.org/10.1016/S0378-3839(98)00006-4.

Zou Q. 2011. Generation, transformation, and scattering of long waves induced by a short-wave group over finite topography. Journal of Physical Oceanography 41: 1842-1859. doi:10.1175/2011JPO4511.1.
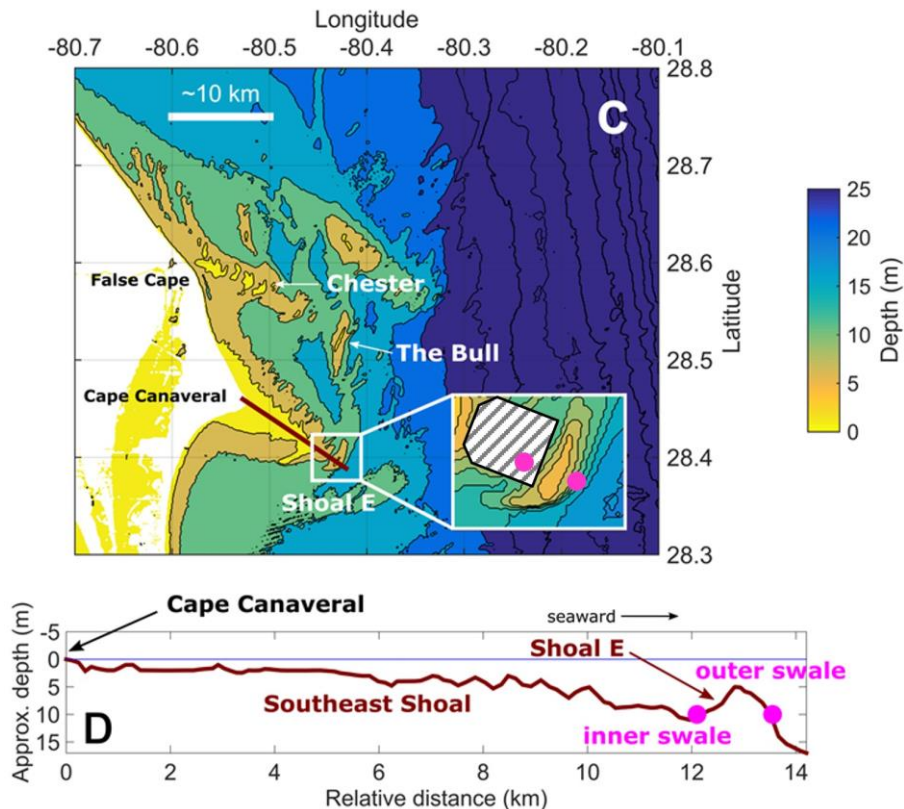
Figure 2-25. Location of ADCPs at Shoal E.
(A) Inner-shelf bathymetry near Cape Canaveral with an inset highlighting Shoal E and CSII-BA (the borrow area of CSII, indicated by the hatched area). Magenta-filled circles represent the approximate ADCP locations at the outer and inner swales of Shoal E (water depths ~13 m). (B) An approximate bottom profile across Southeast Shoal and Shoal E, given by the solid brown line.
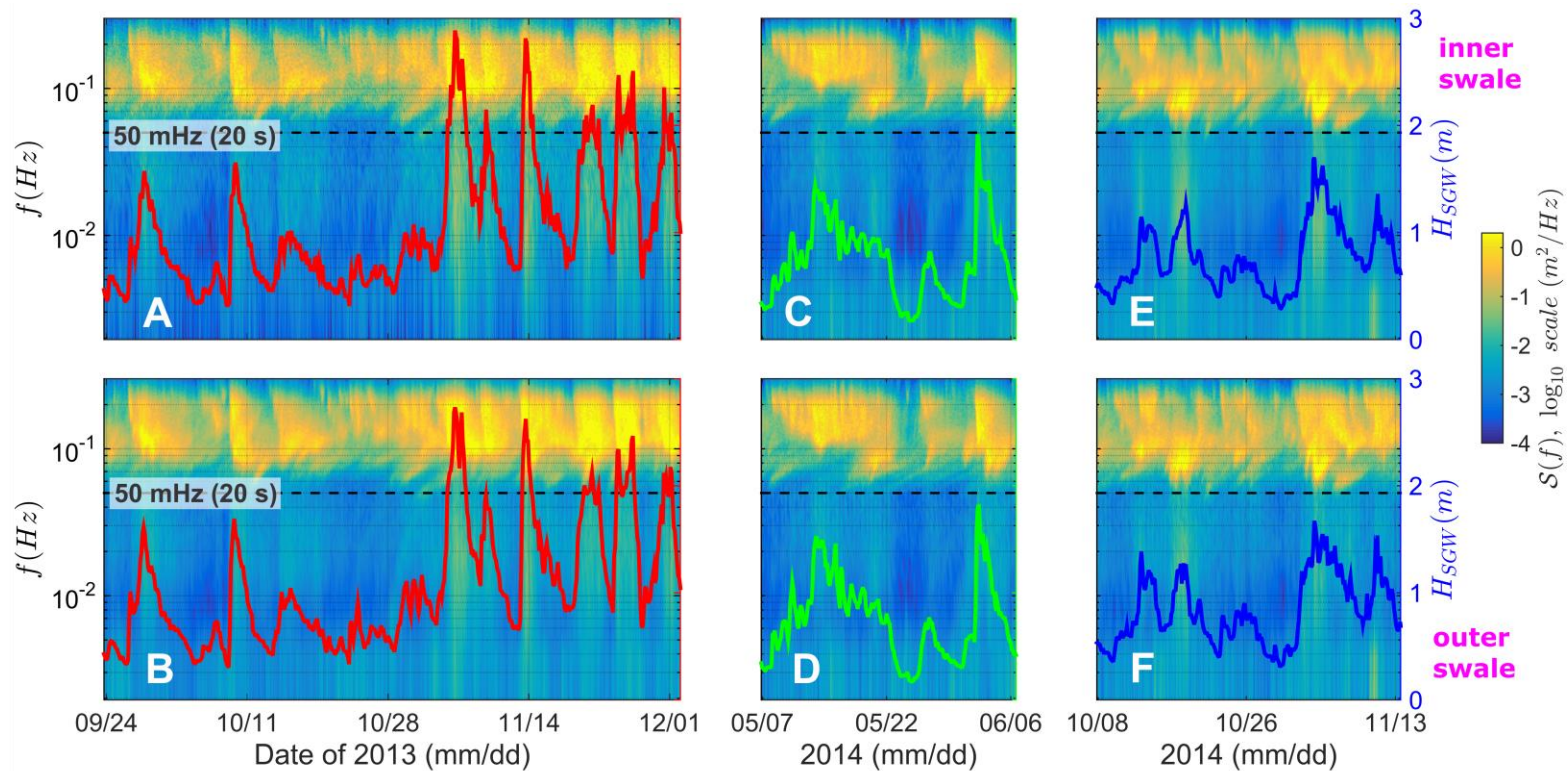
Figure 2-26. Spectrograms show unsteady variance at the long gravity (infragravity) band (frequencies below 50 mHz, or above 20 s) at inner and outer swales of Shoal E.

Upper panels correspond to experiments at the inner swale of Shoal E, whereas lower panels correspond to the outer swale of Shoal E. Experiments were conducted during fall 2013 (A and B), spring 2014 (C and D), and fall 2014 (E and F). Each "low-resolution" spectrum was calculated from detrended, Hanning-windowed, 75% overlapped, and attenuation-corrected pressure values measured during 3-hour intervals. Red, green, and blue lines correspond to SGW significant heights, H_{SGW} (cf. Appendix C), for fall 2013, spring 2014, and fall 2014, respectively.
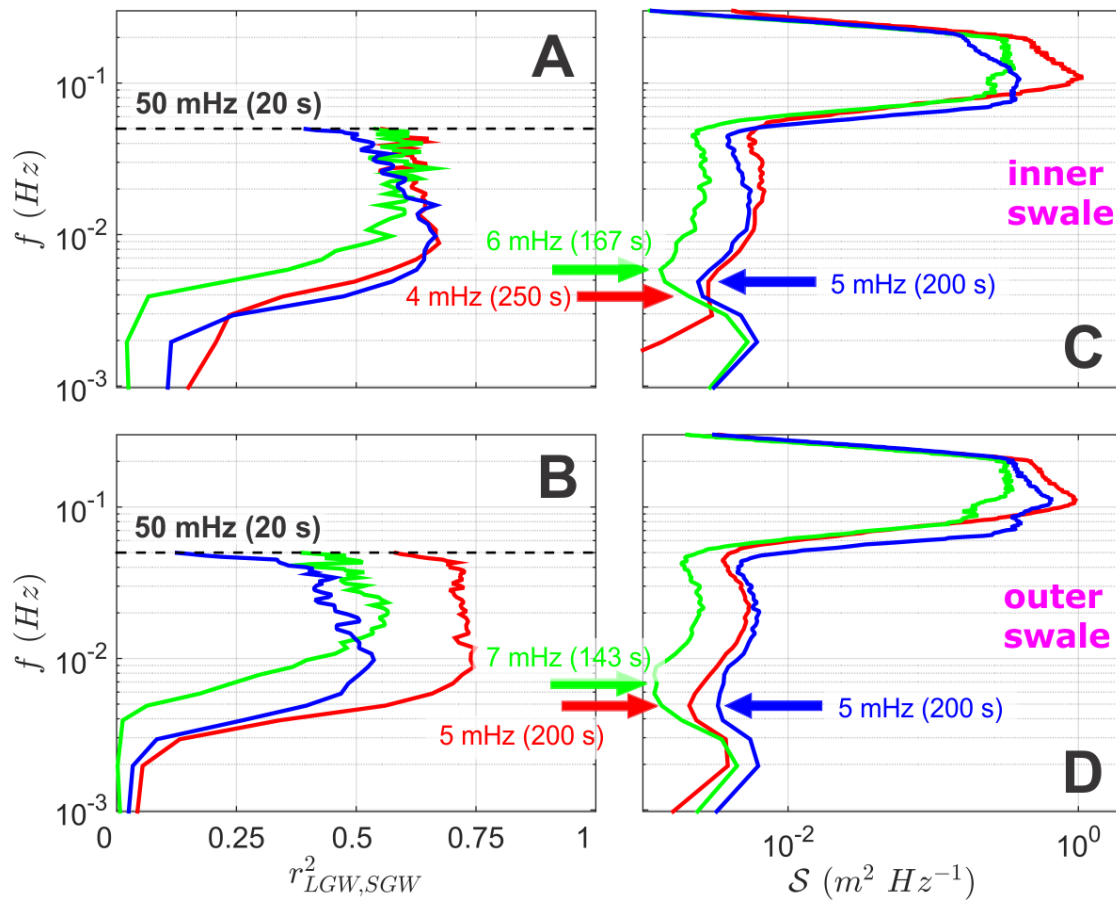
Figure 2-27. (A and B) Coefficients of determination between significant wave height of short waves (H_{SGW}) and time series of infragravity spectral densities at each frequency, $r^2{}_{LGW,SGW}$; and (C and D) mean spectra (S).

Coefficients of determination suggest that sea-swell typically explained ~50% of LGW variability between ~6 mHz (~166 s) and 50 mHz (20 s), and ~10% below ~6 mHz (above 166 s). During fall 2013 (red lines) the difference between the outer (~0.75) and inner swale (~0.62) suggests an increase in the free LGWs proportion with respect to forced LGWs at the inner swale. This difference was inverse during fall 2014 (blue lines) and may support the previous idea since short waves propagated seaward across Shoal E. Mean spectra suggest two LGW sub-bands as shown by drops in mean spectral density at ~50 mHz and ~6 mHz, which correspond to the two groups with different correlations with H_{SGW}. Red, green, and blue lines represent fall 2013, spring 2014, and fall 2014 experiments, respectively.
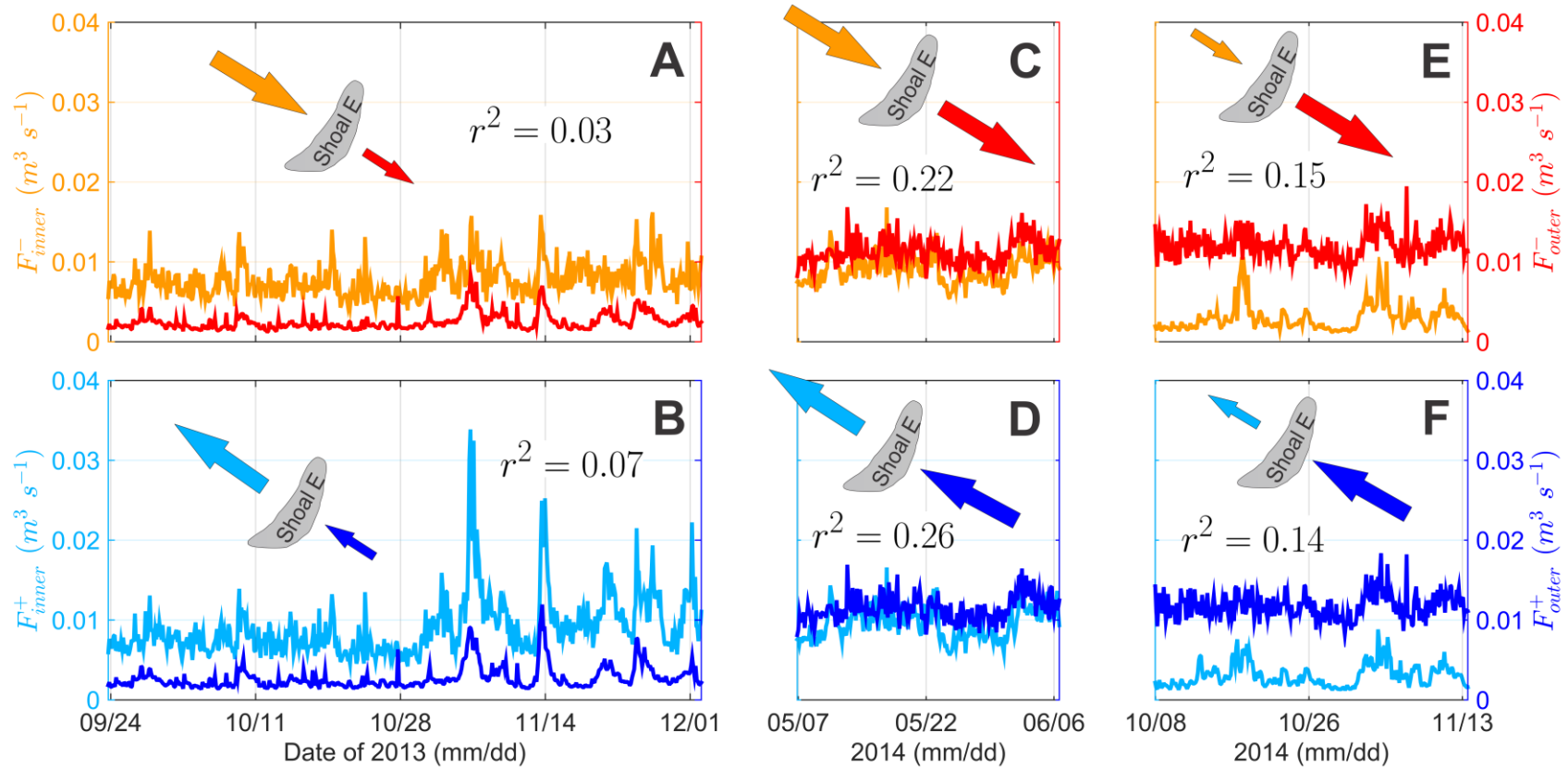
Figure 2-28. Time series plots of seaward- and landward-directed, cross-shoal long gravity wave energy fluxes for inner and outer swales of Shoal E.

Panels A, C, and E correspond to seaward-directed (F^-) cross-shoal LGW energy fluxes, whereas B, D, and F show landward-directed (F^+) cross-shoal LGW energy fluxes for the inner swale (orange and turquoise lines) and outer swale (red and blue lines) of Shoal E, which suggested loss (gain) of seaward-(landward) oriented flux. During fall 2013 (A and B) and fall 2014 (E and F), both fluxes decreased in the direction of SGW propagation and suggested that Shoal E was in the shoaling zone close to the surfzone. During spring 2014, both fluxes had similar values at the two swales, which suggested that Shoal E was in the mid-shoaling zone. Instruments registered a variable shoaling zone width.
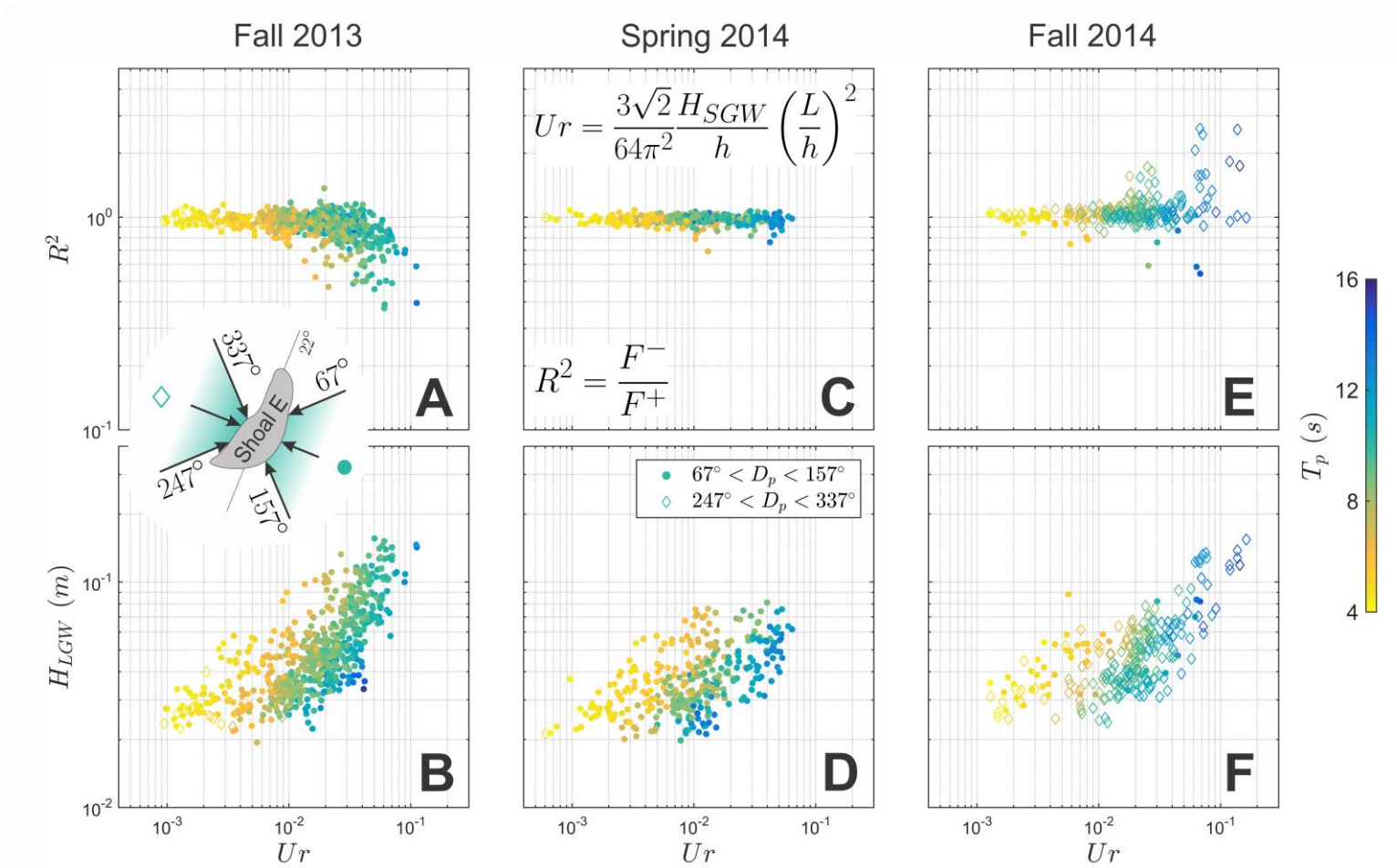
Figure 2-29. Reflection coefficients R^2 versus Ursell parameters, Ur, sorted by peak periods, T_p, and peak directions, D_p , relative to shoal orientation (in azimuth).

Results indicated Shoal E was in the shoaling zone when waves were higher and longer. Generally, short waves propagated across Shoal E in the landward direction during fall 2013 (A and B) and spring 2014 (C and D), and in the seaward direction during fall 2014 (E and F). For $Ur > 2 \times 10^{-2}$, $R^2 > 1$ corresponded to $247° < D_p < 337°$ (fall 2014), while $R^2 < 1$ occurred when $67° < D_p < 157°$ during fall 2013 and spring 2014. (B, D, and F). Long gravity significant wave heights, H_{LGW}, were proportional to Ur and T_p, and ranged from 2×10^{-2} to 1.5×10^{-1} m.
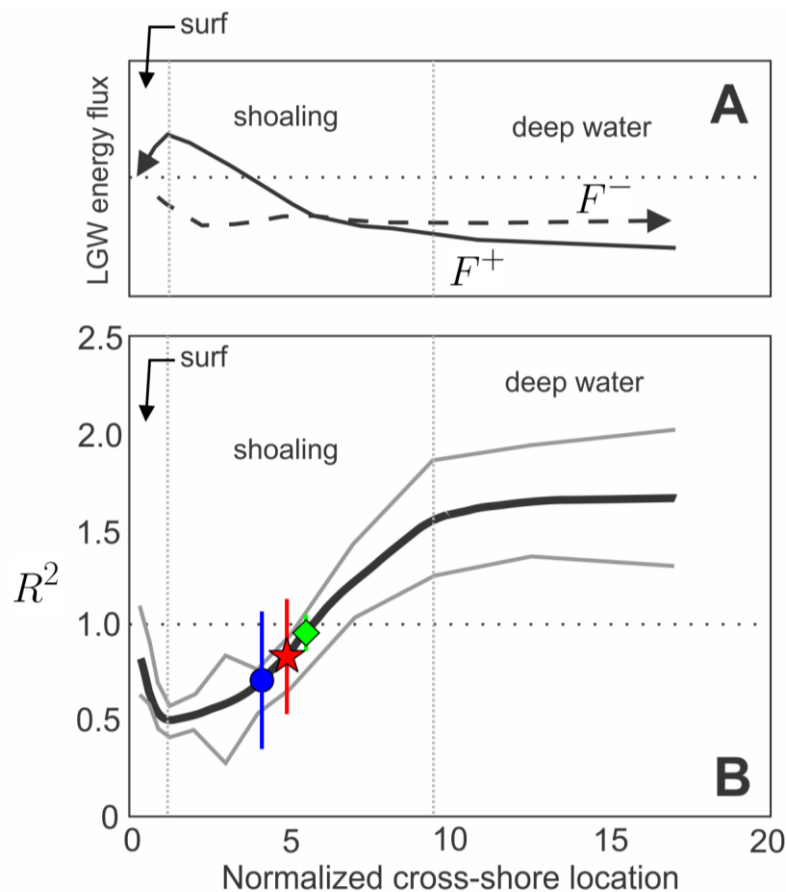
Figure 2-30. Zonation of LGW forcing in sloping beaches indicates reflection coefficients (R^2) ≈ 0.5 in the transition from shoaling to surf zone.

(A) Typical spatial variability in $F^{\pm}$ as found in field studies. F^{+} was negligible in deep water then increased in the shoaling zone due to energy transfers to long frequencies via triad interactions up to the point of short-wave breaking, where F^{+} was maximum. $F^{-} \approx F^{+}$ at the shoreline due to reflection, decreased seaward due to nearshore trapping, and then was nearly constant over deep water. (B) Reflection coefficients (black line) vary in space according to the relation in fluxes: nearly constant and larger than 1-in-deep water, decreasing in the shoaling zone, increasing in the surfzone. Gray lines show the limit of scatter in data from which the figure was originally created. Underlying figure was modified from Sheremet et al. (2002, their Figures 3d and 8). Red star and bar, green diamond and bar, and blue circle and bar represent mean (±r 1 SE) reflection coefficients for fall 2013, spring 2014, and fall 2014 experiments, respectively.
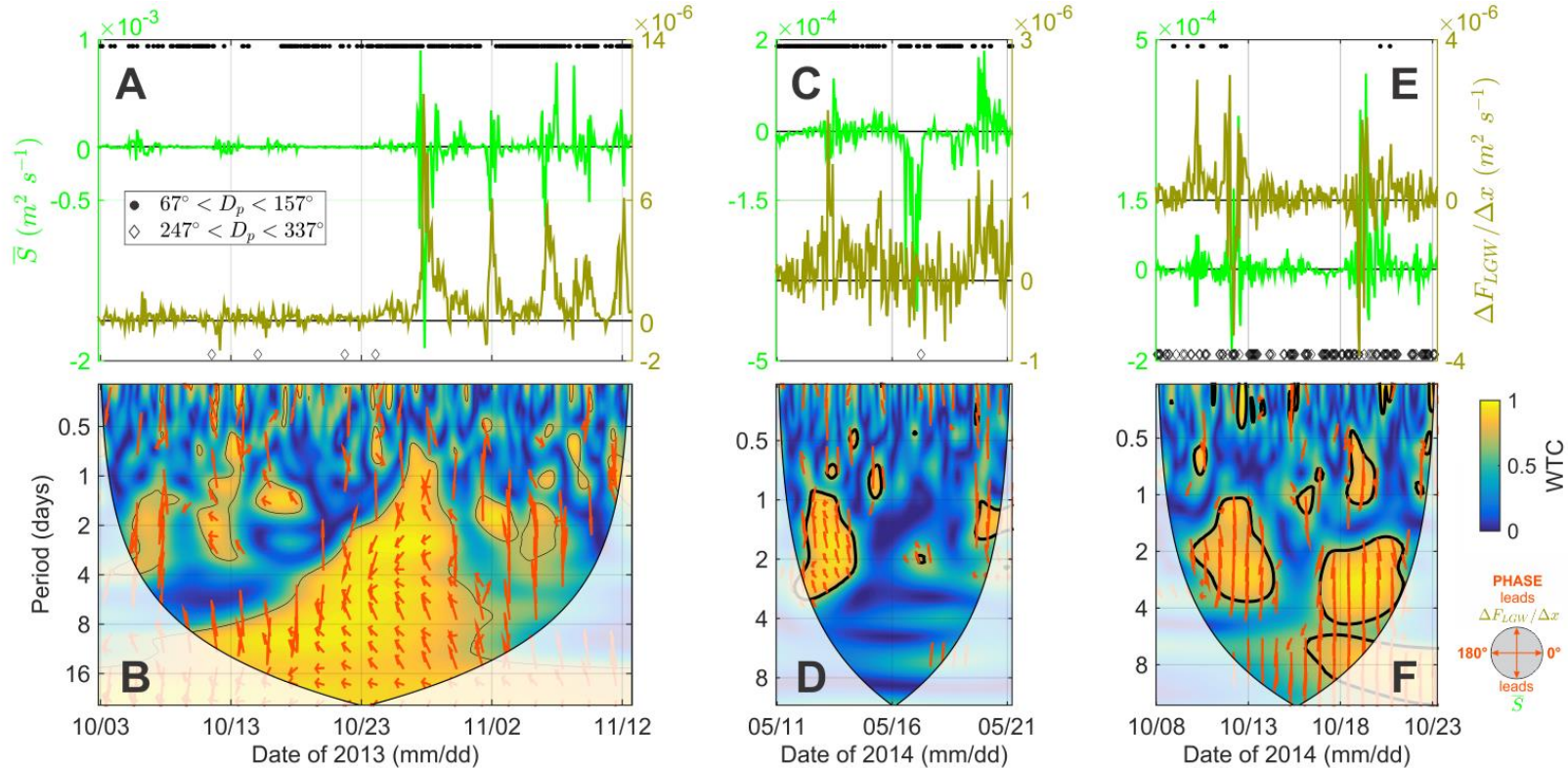
Figure 2-31. Time series (A, C, and E) and wavelet coherence spectra (B, D, and F) between the averaged bulk source term, $\bar{S}$, and the mean spatial gradient in net LGW energy flux between swales.

$\Delta F_{net}/\Delta x$ suggest differences in fluxes were linked to triad interactions and bottom friction at subtidal periods between 2 and 16 days. (Top panels) Light green lines and left Y-axes correspond to $\bar{S}$, while dark green lines and right Y-axes show values of $\Delta F_{net}/\Delta x$. Filled circles and hollow diamonds represent moments at which waves propagated almost perpendicularly to Shoal E in the landward and seaward directions, respectively. Positive $\Delta F_{net}/\Delta x$ values suggest a net landward gain in LGW energy flux. Negative (positive) $\bar{S}$ values indicate the loss (gain) of LGW due to triad interactions and bottom friction. (Bottom panels) Wavelet coherence levels and phases suggest $\Delta F_{net}/\Delta x$ values led $\bar{S}$ by 90° to 180° (during fall 2013 and spring 2014), and $\bar{S}$ led $\Delta F_{net}/\Delta x$ by approximately −90° (fall 2014). If the phase was calculated using the inverse multiples of $\Delta F_{net}/\Delta x$ values, i.e., accounting for an opposite propagation across Shoal E, phase variability among experiments would be relatively similar. Black contours represent the level of statistical confidence at the 95%. Red arrows show the phase between time series, while shaded areas indicate the area of influence of edge effects (see Appendix D for details about the wavelet coherence analysis).
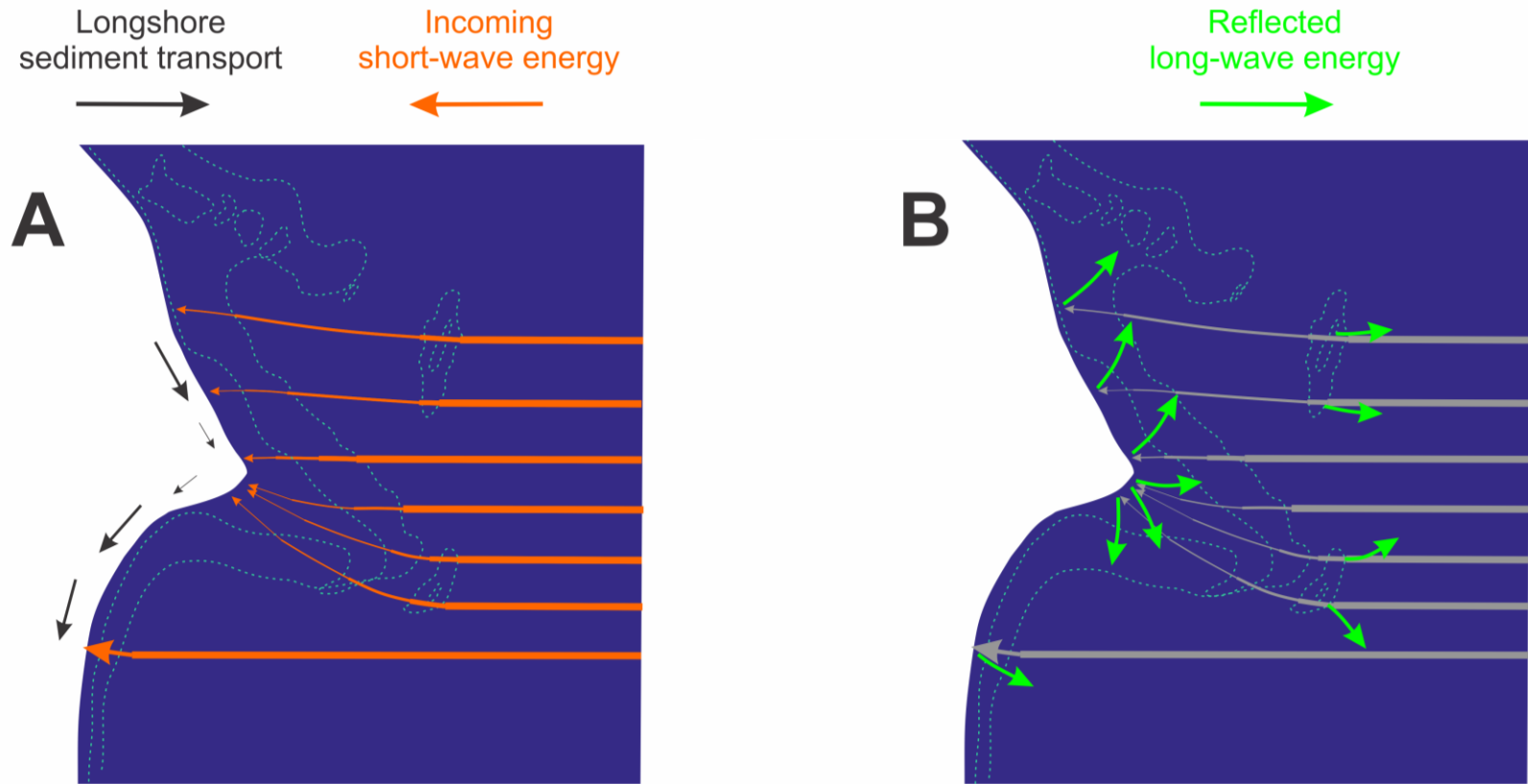
Figure 2-32. Wave energy distribution near capes may be decisively influenced by shoaling and dissipation over shoals.
(A) Landward-oriented, short-wave rays refract and transfer energy to LGWs, which diminishes transport capacity at the cape tip. Latter reduction further enhances spatial gradients in longshore sediment transport at the shoreline. (B) Incoming LGWs energy is reflected and spread in different directions from Shoal E and the shoreline, with subsequent nearshore and shoal trapping as edge waves.

Table 2-2. Parameters of spectral calculations for each experiment at Shoal E.

Experiment	Swale	Number of elements (Burst)	Number of elements (3-hr package)	DOFs (Low resolution)	DOFs (High resolution)
Fall 2013	Inner	1,200[a]	3,600	36	20
Fall 2013	Outer	2,048[b]	12,288	180	84
Spring 2014	Inner	2,400[a]	7,200	100	36
Spring 2014	Outer	2,400[a]	7,200	100	36
Fall 2014	Inner	21,600[c]	21,600	324	148
Fall 2014	Outer	2,400[a]	7,200	100	36

Notes: [a]One burst at 2 Hz measured every hour; [b]Burst at 2 Hz measured every 32 min; [c]Data continuously measured at 2 Hz. DOFs: degrees of freedom (Thomson and Emery 2014 section 5.4.6).

Table 2-3. Coefficients of determination between short-gravity significant wave height (H_{SGW}) and long gravity wave energy fluxes at Shoal E.

Experiment	Swale	$r^2_{(SGW,F^+)}$	$r^2_{(SGW,F^-)}$
Fall 2013	Inner	0.55[a]	0.27
Fall 2013	Outer	0.56	0.52
Spring 2014	Inner	0.43	0.33
Spring 2014	Outer	0.21	0.19
Fall 2014	Inner	0.59	0.54
Fall 2014	Outer	0.22	0.26

Notes: Coefficients of determination ($r^2_{(SGW,F^\pm)}$) suggest that ~50% or less of LGW variability was explained by variations in H_{SGW}. Correlation coefficients (r) were positive and significant at the 99% of statistical confidence for all experiments (Bendat and Piersol 2010 section 4.6.1). Infragravity waves that were not correlated to H_{SGW} were considered "free": either edge waves trapped near the shoal, or leaky waves reflected from the shoreline and the shoal. In such case, the percentage of free waves would be $(1 - r^2) \times 100$.

Table 2-4. Statistical inference of cross-shoal reflection coefficient values at outer (eastern) and inner (western) swales of Shoal E.

Experiment	Swale	N	Mean	STD	z^b	P-value
Fall 2013	Outer	1,046	0.96	0.12	8.8	<0.001
Fall 2013	Inner	566	0.90	0.14	-	-
Spring 2014	Outer	247	0.99	0.04	7.3	<0.001
Spring 2014	Inner	247	0.96	0.05	-	-
Fall 2014	Outer	611	1.02	0.06	2.4	(0.009)[c]
Fall 2014	Inner	885	1.00	0.31	-	-

Notes:
Larger reflection coefficients (R^2) were found at the outer location[a]; N = number of samples; STD = standard deviation; P-values in brackets indicate values not significantly different at the 99% level of confidence.
[a]At the 99% of statistical confidence with $z_{crit,0.005} = 2.58$, see Devore and Berk (2012, section 10.1); [b]Positive z-values indicated larger R^2 values at the outer swale; [c] R^2 values did not differ at 99%, but differed at 95% level of confidence.

Table 2-5. Values of biphase, skewness, and asymmetry correspondent to the maximum values in Ursell parameters over Shoal E.

Experiment	Ursell parameter (max. Ur)	Biphase (β_{ww})	Skewness (S_{ww})	Asymmetry (A_{ww})
Fall 2013	0.12	-9.4×10^{-4}	0.23	-3.7×10^{-6}
Spring 2014	0.07	-1.6×10^{-7}	0.08	-2.3×10^{-10}
Fall 2014	0.25	-0.52	0.43	-0.004

Note:
Ur suggest short gravity waves behaved as frequency-dispersive waves during all experiments over the swales of Shoal E.

Table 2-6. Statistical inference of along-shoal reflection coefficients values at outer (eastern) and inner (western) swales of Shoal E.

Experiment	Swale	N	Mean	STD	z[b]	P-value
Fall 2013	Outer	1,046	1.09	0.14	7.9	<0.001
Fall 2013	Inner	566	1.04	0.14	-	-
Spring 2014	Outer	247	1.00	0.04	1.96	(0.03)
Spring 2014	Inner	247	1.00	0.05	-	-
Fall 2014	Outer	611	1.02	0.07	-11.9	<0.001
Fall 2014	Inner	885	1.16	0.34	-	-

Notes:
Larger reflection coefficients (R^2) were found at the outer location[a]; N = number of samples; STD = standard deviation; P-values in brackets indicate values not significantly different at the 99% level of confidence.
[a]At the 99% of statistical confidence with $z_{crit,0.005} = 2.58$, see Devore and Berk (2012 section 10.1) ; [b]Positive z-values indicates larger R^2 values at the outer swale.

2.5 Tidal Distortions Associated with Extreme Flows Over Cape-related Shoals

2.5.1 Introduction

Tides influence cape-related shoals morphodynamics via direct transport (Berthot and Pattiaratchi 2006), residual flows (McNinch and Luettich 2000), and secondary circulation (Geyer 1993). Tidal flows have been the subject of extensive study during the last two centuries due to their role in water, sediment, and nutrient exchange in estuaries (Le Provost 2001). Recent applications include power extraction (Neill et al. 2014), eco-morphological evolution (Stark et al. 2017), and morphodynamic studies (Guo et al. 2014) in which tidal distortions play an essential role. Tidal distortion has been a well-known phenomenon since the late 1800s and has been extensively studied via theoretical developments (Friedrichs and Aubrey 1988) and observations (Stanev et al. 2015). Nevertheless, the role of tidal distortions in particulate transport over cape-related shoals is not well understood.

This study focuses on the inner-shelf hydrodynamics during the passage of Hurricane Matthew, which traveled northward in 2016 along the east coast of Florida, passing by the shoals of Cape Canaveral. We focus on extraordinarily distorted tidal waves related to an increase in bottom friction caused by a wind-generated current, whose speed ranged from 1 to 2.7 m/s at the inner swale of a cape-related shoal (Shoal E). This connection adds to the paradigm of overtides formation by demonstrating how indirect, extreme atmospheric forcing over the inner shelf can produce tidal distortions.

2.5.2 Methods

2.5.2.1 Field Observations and Data Analysis

Barometric pressure, wind velocity and direction, and water levels were measured at the NOAA Trident Pier station near Cape Canaveral (Figure 2-15). Water motions (profiles of velocity and pressure) were measured at the bottom of the inner swale of Shoal E (28° 23.998'N, 80° 26.337'W; Figure 2-25) using a Nortek Acoustic Waves and Currents (AWAC) ADCP. The 1-MHz instrument had a recording range of ~30 m and pointed upward. Its position was near the slope break directly off of the ridge that is considered as the top of Shoal E in ~13 m depth. The instrument was active from 30 September 2016 at 15:36 GMT to 4 November 2016 at 15:54 GMT on a frame at a mean depth of 12 m. Data were collected in 0.5-m cells as 60 sec averages of velocity (at each cell) and pressure separated by 3 min. Vertically averaged velocities, $\bar{u}(t)$, were calculated as $\bar{u}(t) = \frac{1}{Z}\int_{z_b}^{z_s} u(t,z)\,dz$, where z_b corresponded to the vertical distance from the instrument to the first measurement cell, z_s was the vertical distance to the furthest measurement cell, $u(t,z)$ was the velocity at each time step for each cell, and dz was the cell size, and $Z = z_s - z_b$. Velocity directions at the surface and bottom, $\alpha_s(t)$ and $\alpha_b(t)$, were calculated as $\alpha_z(t) = \arctan[u(t,z)/v(t,z)]$, where z was a vertical distance from the instrument, and subindices s and b corresponded to the near-surface and near-bottom cell positions, respectively.

Water levels (i.e., converted and demeaned pressure values) were reconstructed using harmonic analysis by means of least square fit for different constituents depending on the period analyzed (Codiga 2011). The reconstruction skill was evaluated using the root mean square error, $RMSE = \sqrt{\frac{1}{N}\sum_{i=1}^{N}(x_i - x_{r,i})^2}$ and the goodness of fit, $GOF = (\sum_{i=1}^{N}(\bar{x} - x_{r,i})^2)/(\sum_{i=1}^{N}(\bar{x} - x_i)^2)$, where N referred to the number of elements in the time series, x_i corresponded to the element i in the time series, $x_{i,r}$ was the i element of the series reconstructed using harmonic analysis, and $\bar{x} = \frac{1}{N}\sum_{i=1}^{N}x_i$ (Devore and Berk 2012). Echo intensity anomalies, I', were calculated as $I'(z,t) = I(z,t) - \bar{I}(z)$, where $I(z,t) = 10\log_{10} RSSI(z,t)$,

where $RSSI(z,t)$ was the time series of profiles of received signal strength indicator values (given in counts from the ADCP), and $\bar{I}(z) = \frac{1}{N}\sum_{i=1}^{N} I(z, t_i)$ (Valle-Levinson et al. 2014).

The level of asymmetric effects by the river presence were represented by the Fourier transformation of the frictional term $\vec{u}|\vec{u}|$ as the following (Parker 1984; 2007):

$$a_1 = \left| \frac{4}{\pi} u_1{}^2 \left\{ \frac{u_0}{u_1} \arcsin\left(\frac{u_0}{u_1}\right) + \frac{1}{3}\left[\left(\frac{u_0}{u_1}\right)^2 + 2\right]\left[1 - \left(\frac{u_0}{u_1}\right)^2\right]^{1/2} \right\} \right| \tag{46}$$

and

$$a_2 = \left| \frac{1}{\pi} u_1{}^2 \left\{ \arcsin\left(\frac{u_0}{u_1}\right) + \frac{1}{3}\frac{u_0}{u_1}\left[5 - 2\left(\frac{u_0}{u_1}\right)^2\right]\left[1 - \left(\frac{u_0}{u_1}\right)^2\right]^{1/2} \right\} \right| \tag{47}$$

and

$$a_3 = \left| \frac{8}{15\pi} u_1{}^2 \left\{ \left[1 - 2\left(\frac{u_0}{u_1}\right)^2 + \left(\frac{u_0}{u_1}\right)^4\right]\left[1 - \left(\frac{u_0}{u_1}\right)^2\right]^{1/2} \right\} \right| \tag{48}$$

where u_0 corresponded to the subtidal flow (river) speed and u_1 to the maximum tidal flow speed.

2.5.3 Results

As measured by the NOAA meteorological station at Trident Pier (Port Canaveral, Florida), from 6 October at 18:00 hr to 8 October at 12:00 hr, barometric pressure decreased from ~101 to ~100 kPa in ~12 hr, then dropped dramatically from ~100 to ~97 kPa in ~7 hr, and finally increased to ~101 kPa in ~29 hr (Figure 2-33). This valley in pressure coincided with an increase in wind speeds from 5 to 20 m/s (gusting up to 30 m/s), and a counterclockwise shift in wind direction from ~20°, coming from north-northeast, to ~210°, coming from the southwest. Then, wind direction remained at ~220° during the subsequent 21 hr.

Water levels above mean low-low water (MLLW) showed an offset of ~0.4 m from the predicted water levels (Figure 2-33). This offset was enhanced before the pressure valley due to relatively strong distortions in the high tide, which lasted ~6 hr. Then, water levels went to low tide in ~3 hr, which under regular conditions takes ~6 hr. This variability was also measured by our instrument at the inner shelf (Figure 2-34).

The variability of bottom pressure mirrored the change in water levels at Trident Pier, in which the distortions were evident during the two high tides immediately before and after a peak in vertically averaged water velocities (Figure 2-34). The magnitudes of vertically averaged velocities followed the variation in barometric pressure and wind speed. Southwestward velocities varied from ~0.2 m/s to ~1 m/s in 15 hr and then increased to ~2.7 m/s in ~2 hr. After the valley in pressure, velocities veered counterclockwise from southwestward to northeastward directed in ~7 hr and attained 1 m/s. Lastly, velocities diminished to ~0 m/s in ~20 hr.

The differences between measured and reconstructed water levels were positive when wind was from the north-northeast (from 0° to 25°) between 6 October at 12:00 hr and 7 October at 10:00 hr, and negative when wind was from the southwest (from 180° to 270° until 8 October at 12:00 hr) (Figure 2-34).

The anomalously high winds and currents, as well as the offset in the mean water level, generated asymmetries in bottom friction. These asymmetries produced tidal wave distortions via decreasing the group celerity and attenuating the tidal wave amplitude. Tidal distortions can be represented by the generation of superharmonics (overtides) and interactions among harmonics (compound tides). Even harmonics, e.g., M_4 and M_6, form due to changes in mean water level, which make bottom friction asymmetric with respect to tidal stage (i.e., attenuation is smaller for larger depths during high tide). Similarly, M_6 and odd harmonics arise from the addition of a mean current velocity, which augmented or diminished friction depending upon the tidal stage favored by the current (Parker 2007). Water levels were reconstructed using the principal lunar semidiurnal M_2, solar diurnal K_1, and shallow-water (overtides) tidal constituents and compound tides of M_2 and K_1 (i.e., M_3, M_4, $2MK_5$, M_6, $3MK_7$, and M_8) (Goodness of Fit [GOF] = 76.7%, root mean square error [RMSE] = 0.15 m, Table 2-7). The amplitudes of superharmonics were larger for the reconstruction of the tidal cycle during the hurricane and corresponded to M_4, M_6, M_8, M_{10}, M_{12}, ST_{16}, and ST_{35} constituents (GOF = 99.8%, RMSE = 0.01 m, Table 2-8).

2.5.4   Discussion

2.5.4.1   Unusual Atmospheric Forcing

Hurricane Matthew resulted in ~USD6 billion in damages, caused 43 deaths, and increased the likelihood of vector-borne viruses' outbreaks due to winds ~20 m/s and flooding (Carr 2016; Rice 2016; Ahmed and Memish 2017).

The hurricane-related, river-like current along the inner shelf presented here had similar speeds to the peak surface speed of the Gulf Stream, ~2 m/s (Leaman et al. 1989), and twice the hurricane-induced current speed previously found at the Florida inner shelf, ~0.95 m/s (Smith 1982).

The differences between measured and reconstructed water levels could be attributed either to the settling of our instrument's frame or to a change in Ekman dynamics (i.e., from upwelling during southwestward wind to downwelling for the northeastward wind). Given the hurricane path, offset in water level was unlikely to have been created by storm surge. This argument was supported by the differences between near-surface and near-bottom velocity directions, $\alpha_s - \alpha_b$. These differences suggest Ekman layer formation during some instances. If the difference was negative, it suggests the development of an Ekman surface-friction layer by the wind-driven current. If positive, it may indicate the presence of an inverse bottom-friction layer. If close to zero, surface and bottom-friction layers overlapped (Pedlosky 1987).

Three situations were identified: (1) oscillations of amplitudes ~40° at ~1 cycle/hr (possibly caused by overtides) between 5 October at 15:00 hr to 7 October at 06:00 hr; (2) oscillations close to zero from 7 October at 06:00 hr to 8 October at 12:00 hr (unidirectional, river-type flow); and (3) highly variable oscillations between 8 October at 12:00 hr and 9 October at 06:00 hr. Notice $\alpha_s - \alpha_b \approx 0$ when wind velocities were >5 m/s (i.e., situation 2). Variability in water velocities with depth (Figure 2-34) showed unidirectional flow during the time span considered. Echo intensity anomalies, I', showed an increase in acoustic signal return during the intense winds, especially at the surface. This increase in I' was probably related to bubbles or whitecapping at the surface.

Instances when tidal motions were slightly distorted resembled conditions found at friction-dominated, well-mixed estuaries characterized by $\eta_1/h > \sim 0.1$ (where η_1 was the main tidal harmonic amplitude and h the water depth) and tidal velocities ~0.5 m/s (Friedrichs and Madsen 1992). These conditions may be found during calm periods over Canaveral Shoals that typically exhibit $\eta_1 \approx 1\,m$, $h \approx 13\,m$ (so $\eta_1/h \approx 0.08$), and tidal velocities ~0.2 m/s. During Hurricane Matthew, conditions instead resembled well-mixed estuaries with a large river discharge. Theoretical treatments for frictionally dominated estuaries support that the ratio of the mean flow (river) speed u_0, to the maximum current speed of the main tidal harmonic,

u_1, dictates the level of overtides generation, a_n for the n harmonic. Under typical conditions at Canaveral Shoals, $u_0/u_1 \approx 1$, $a_1 \approx 0.12 \ m^2/s^2$, $a_2 \approx 0.03 \ m^2/s^2$, and $a_3 \approx 0$. During Hurricane Matthew, distortions that were associated to $u_0/u_1 \approx 10$ were supported by theoretical results $a_1 \approx 24.6 \ m^2/s^2$, $a_2 \approx 128.7 \ m^2/s^2$, and $a_3 \approx 1,034.7 \ m^2/s^2$ (Parker 2007).

The >2 m/s currents related to the hurricane should decisively exert control on cape-related shoal particle or sediment dynamics. These processes would also be influenced by the extreme distortions caused by anomalously strong currents to tidal flows. Although we provide evidence for an extreme case of water-level distortions, the influence of typical subtidal currents on tidal propagation over cape-related shoals is still elusive. Direct implications of both regular and extreme conditions to long-term bed changes, planktonic and benthic habitats, and nutrient dynamics remain not well understood.

2.5.4.2 Implications from Dredging

Effects of extreme forcing, like a tropical storm or hurricane, cause distortions on the tidal elevation and currents that are likely to be greater than those produced from dredging operations. However, the morphological changes brought about by such atmospheric forcing may be opaqued by dredging activities. This aspect could be addressed further with targeted and process-oriented numerical simulations.

2.5.5 References

Ahmed QA, Memish ZA. 2017. The public health planners' perfect storm: Hurricane Matthew and Zika virus. Travel Medicine and Infectious Disease 15: 63-66. doi.org/10.1016/j.tmaid.2016.12.004.

Berthot A, Pattiaratchi C. 2006. Mechanisms for the formation of headland-associated linear sandbanks. Continental Shelf Research 26(8): 987-1004. doi.org/10.1016/j.csr.2006.03.004.

Carr A. Hurricane Matthew leaves 43 dead in the U.S.; Flooding crises continues in North Carolina. The Weather Channel (13 October 2016).

Codiga DL. 2011. Unified tidal analysis and prediction using the UTide Matlab functions. Technical Report 2011-01. Graduate School of Oceanography, University of Rhode Island, Narragansett, RI.

Devore JL, Berk KN. 2012. Modern mathematical statistics with applications. 2nd ed. New York, NY: Springer.

Friedrichs CT, Aubrey DG. 1988. Non-linear tidal distortion in shallow well-mixed estuaries: a synthesis. Estuarine, Coastal and Shelf Science 27(5): 521-545. doi.org/10.1016/0272-7714(88)90082-0.

Friedrichs CT, Madsen OS. 1992. Nonlinear diffusion of the tidal signal in frictionally dominated embayments. Journal of Geophysical Research: Oceans 97(C4): 5637-5650. doi.org/10.1029/92JC00354.

Geyer WR. 1993. Three-dimensional tidal flow around headlands. Journal of Geophysical Research: Oceans 98(C1): 955-966. doi.org/10.1029/92JC02270.

Guo L, van der Wegen M, Roelvink JA, He Q. 2014. The role of river flow and tidal asymmetry on 1-D estuarine morphodynamics. Journal of Geophysical Research: Earth Surface 119(11): 2315-2334. doi.org/10.1002/2014JF003110.

Le Provost C. 2001. Ocean tides. In: Fu L-L, Cazenave A, editors. Satellite altimetry and earth sciences: A handbook of techniques and applications. Academic Press, San Diego, CA. 6; p. 267-303. https://www.sciencedirect.com/science/article/pii/S0074614201801510.

Leaman KD, Johns EM, Rossby T. 1989. The average distribution of volume transport and potential vorticity with temperature at three sections across the Gulf Stream. Journal of Physical Oceanography 19: 36-51.

McNinch JE, Luettich RA. 2000. Physical processes around a cuspate foreland: implications to the evolution and long-term maintenance of a cape-associated shoal. Continental Shelf Research 20(17): 2367-2389. doi.org/10.1016/S0278-4343(00)00061-3.

Neill S, Hashemi MR, Lewis M. 2014. The role of tidal asymmetry in characterizing the tidal energy resource of Orkney. Renewable energy 68: 337-350. doi:10.13140/2.1.4738.4966.

Parker BB. 1984. Frictional effects on the tidal dynamics of a shallow estuary. Dissertation. Baltimore, MD: John Hopkins University, Baltimore, MD. 292 pp.

Parker BB. 2007. Tidal analysis and prediction. Silver Spring, MD: NOAA Special Publication NOS COOPS 3. NOAA, NOS Center for Operational Oceanographic Products and Services.

Pedlosky J. 1987. Geophysical fluid dynamics. New York, NY: Springer-Verlag. http://books.google.com/books?id=TiBRAAAAMAAJ.

Rice D. Hurricane Matthew economic damage nears $6 billion. USA Today (8 October 2016).

Smith NP. 1982. Response of Florida Atlantic shelf waters to Hurricane David. Journal of Geophysical Research: Oceans 87(C3): 2007-2016. doi.org/10.1029/JC087iC03p02007.

Stanev E, Al-Nadhairi R, Valle-Levinson A. 2015. The role of density gradients on tidal asymmetries in the German Bight. Ocean Dynamics 65: 77-92. doi:10.1007/s10236-014-0784-8.

Stark J, Meire P, Temmerman S. 2017. Changing tidal hydrodynamics during different stages of eco-geomorphological development of a tidal marsh: A numerical modeling study. Estuarine, Coastal and Shelf Science 188: 56-68. doi.org/10.1016/j.ecss.2017.02.014.

Valle-Levinson A, Castro L, Cáceres M, Pizarro O. 2014. Twilight vertical migrations of zooplankton in a Chilean fjord. Progress in Oceanography 129: 114-124. doi.org/10.1016/j.pocean.2014.03.008.
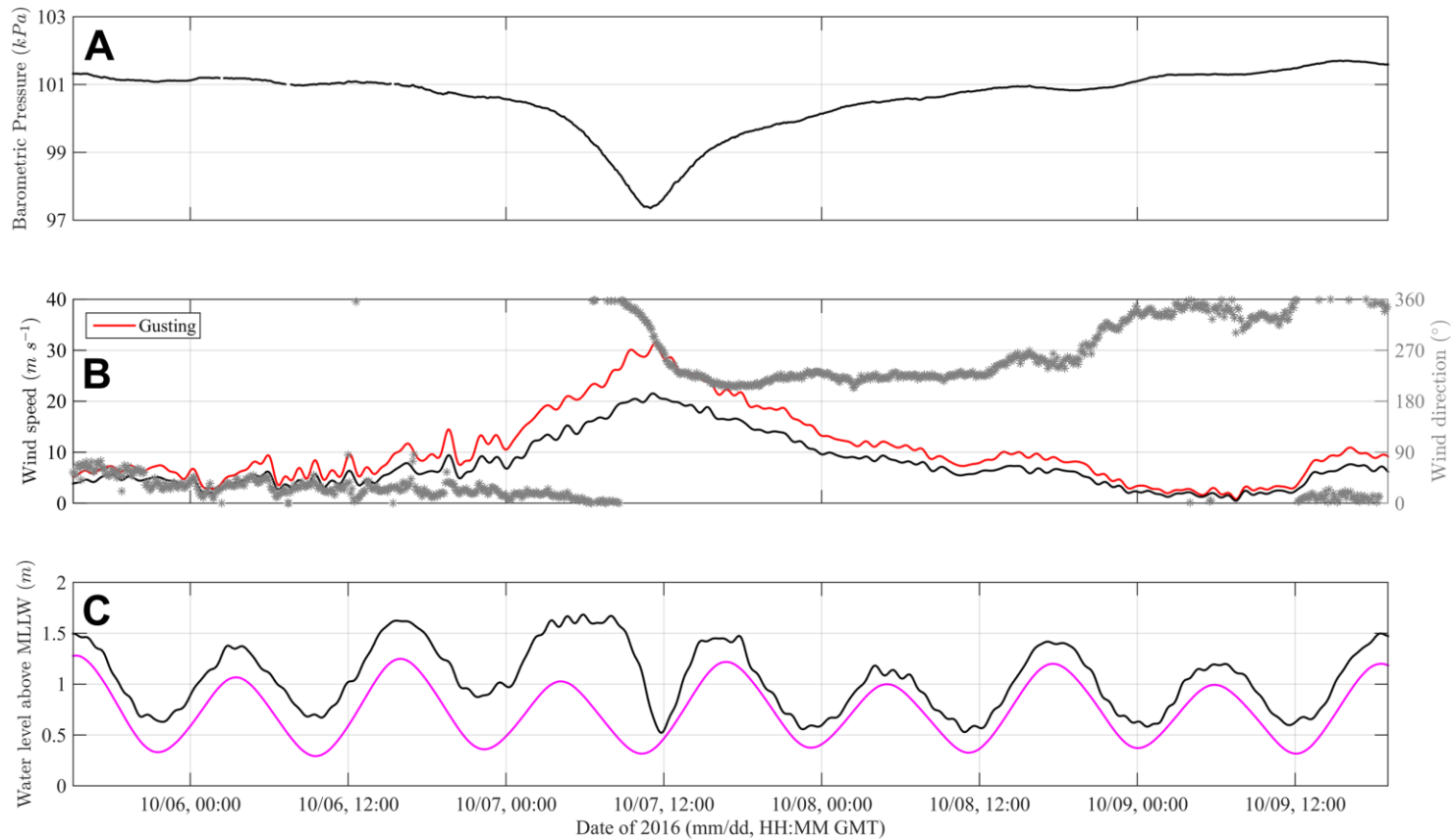
Figure 2-33. Atmospheric conditions measured at the Trident Pier (Port Canaveral, Florida) during the passage of Hurricane Matthew.
Observations showed a valley in barometric pressure that coincided with a peak in wind speed and gusting, change in wind direction, and highly distorted water levels.
A) Barometric pressure; B) wind; and C) predicted (magenta) and measured (black) water levels.
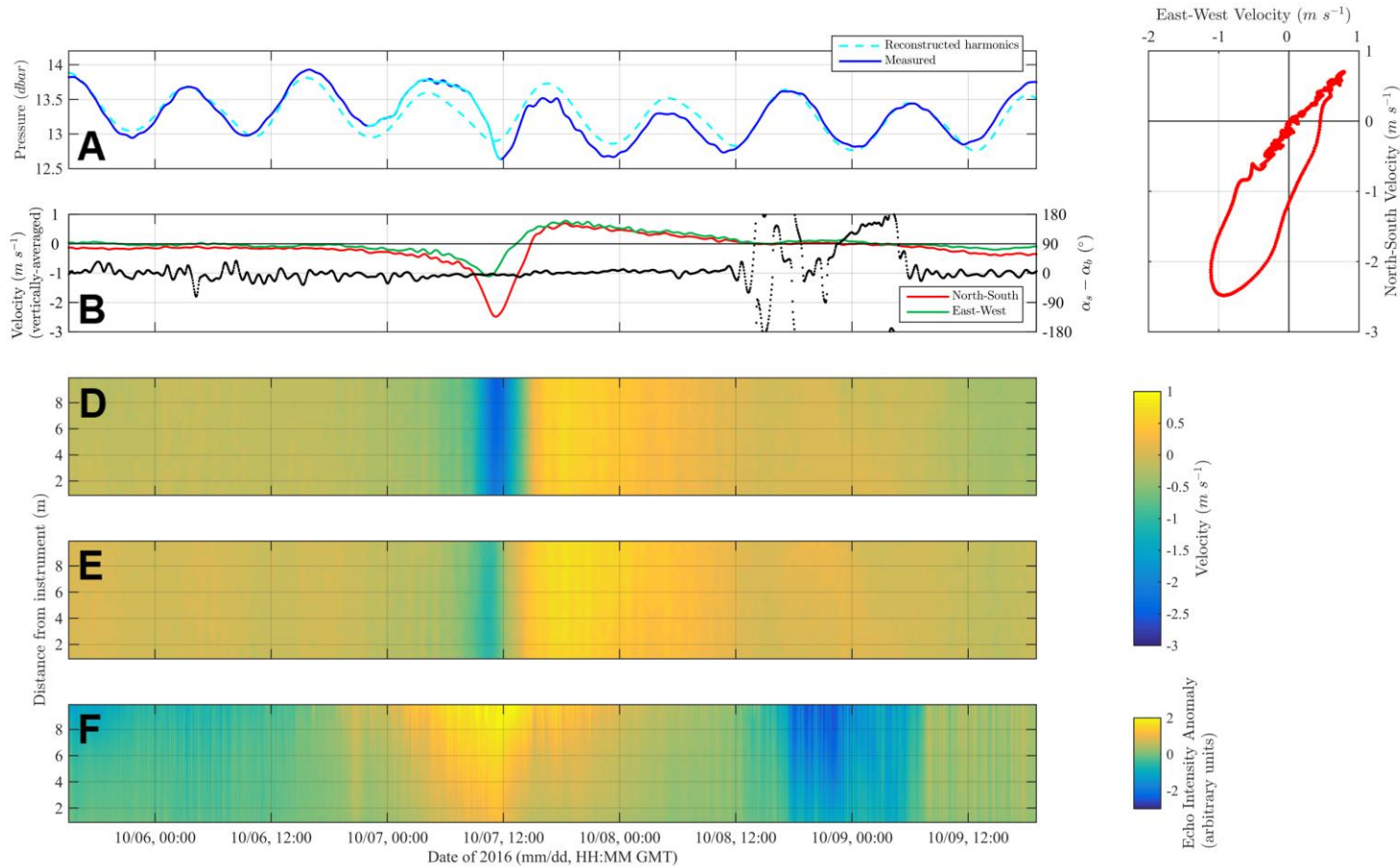
Figure 2-34. Bottom pressure at the inner swale of Shoal E during the passage of Hurricane Matthew.
Observations showed atypical, extreme distortion of tidal motions over the inner shelf due to the river-type current of 2 m/s. A) Measured and reconstructed pressure values; B) vertically averaged components of water velocities and differences in direction between near-surface and near-bottom velocities; C) east-west and north-south components of vertically averaged velocities; D and E) time series of velocity profiles that show unidirectional flow; and F) time series of echo intensity anomaly profiles.

Table 2-7. Amplitudes and phases for tidal constituents.

Constituent	Period (hr)[a]	Amplitude (m)	Phase (°)[b]
M_2	12.4206	0.362	352
K_1	23.9345	0.072	154
M_3	8.2804	0.034	328
M_4	6.2103	0.028	252
$2MK_5$	4.9309	0.012	296
$3MK_7$	3.5296	0.007	174
M_6	4.1402	0.006	142
M_8	3.1052	0.004	358

Notes: Calculations suggest water levels at the outer swale of Shoal E followed a Stokes expansion of the main harmonic M_2 (GOF = 76.7%, RMSE = 0.15 m).
[a]Parker (2007)
[b]Phase lag with respect to Greenwich Meridional Time.

Table 2-8. Amplitudes and phases for tidal constituents for the tidal stage during Hurricane Matthew.

Constituent	Period (hr)	Amplitude (m)	Phase (°)[a]
M_2	12.4206	0.351	15
ST_{35}	2.0516	0.308	187
ST_{16}	3.5325	0.232	297
M_{12}	2.0701	0.231	278
M_6	4.1402	0.132	331
M_4	6.2103	0.114	202
M_8	3.1052	0.097	326
M_{10}	2.4841	0.029	123

Notes: Observations indicate M_2 overtides enhancement (GOF = 99.8%, RMSE = 0.01 m).
[a]Phase lag with respect to Greenwich Meridional Time.

2.6 Quantifying Bed Changes at Canaveral Shoals

2.6.1 Introduction

Over cape-related shoals, where sand is customarily extracted for beach nourishment purposes, variability in particulate transport and related bed form evolution remains unclear. From studies performed at relatively similar locations, we infer that the morphodynamics of shoals depend upon interactions among hydrodynamic processes influenced by shallow bathymetry. Processes responsible would be tidal flows and their distortions (overtides and headland-related residual and secondary flows), surface gravity waves (resuspension over ripples, Stokes drift, and infragravity motions), and subtidal currents (wind-driven flows) (Geyer 1993; Nittrouer and Wright 1994; McNinch and Luettich 2000; Kumar et al. 2013 and references therein). This section analyzes bed elevation changes at ridges and swales of three isolated shoals offshore of Cape Canaveral.

2.6.2 Methods

2.6.2.1 Study Site

This study focused on CSII-BA (the borrow area of Canaveral Shoals II), Shoal E directly east of CSII, Chester Shoal, and Bull Shoal (Figure 2-15), as described previously in Section 2.2.2. Tidal conditions in this region were summarized previously in Section 2.2.2, and temperature and salinity interactions relative to the Florida Current were summarized previously in Section 2.2.4.

2.6.2.2 Bed Changes from Downward-pointing ADCPs

We obtained bed elevation changes, $\partial\eta/\partial t$, at several locations within Canaveral Shoals during different seasons. Data were collected at CSII-BA ridge, the inner swale of Shoal E, the outer swale and ridge of Chester Shoal (Shoal D in Field and Duane 1974), and Bull Shoal (Figure 2-35). We conducted a total of seven deployments, each with roughly three moorings (for a total of 22 moorings), during summer A & B of 2015, fall A & B 2015, winter 2015–2016, and fall 2016 (i.e., all after the first dredging event in winter 2013/spring 2014) (see Appendix A).

Profiles of acoustic echo intensities and hydrodynamics were measured by upward- and downward-pointing ADCPs that were moored ~1.5 m above the bed (for data collection details see Paniagua-Arroyave 2018). The tilt of the instruments remained stable as indicated by their pitch and roll. Distances from the ADCP to the bed were measured as the distance to the cell where the (anomalously) maximum value in echo intensity was found. Bed changes were calculated from the 10-min average of bed distances as the variation of bed distances in time. From $\partial\eta/\partial t$ values, time series of cumulative bed change, η_{cml}, and values of total bed change per deployment, η_{tot}, were quantified as

$$\eta_{cml}(t) = \int_{t_{ini}}^{t} \frac{\partial\eta}{\partial t}(t)\, dt \qquad (49)$$

and

$$\eta_{tot} = \int_{t_{ini}}^{t_{end}} \frac{\partial\eta}{\partial t}(t)\, dt \qquad (50)$$

where t refers to an instance in the time series, t_{ini} and t_{end} to the initial and ending times, and dt represents the time step (1 s). Note that $\eta_{cml}(t)$ represents the cumulative bed change at the time t, so the integral would be evaluated from t_{ini} to t and the calculation results in a time series per deployment. The variable, η_{tot}, corresponds to the definite integral between initial and ending times, and it results in a value per deployment (i.e., the relative bed change when each deployment finalized). Values of $\partial\eta/\partial t$, η_{cml}, and η_{tot} were considered different from zero (stable bed) by means of statistical tests to normally

distributed variables for a data number > 40 (Devore and Berk 2012 section 9.2), and when absolute values of η_{cml} and η_{tot} were larger than 0.025 m (as we consider 2.5 cm the measurement uncertainty).

2.6.3 Results

2.6.3.1 Spatial Patterns in Bed Elevation Changes

Figure 2-36 shows the cumulative bed level changes, η_{cml}, and instantaneous bed level changes, $\partial\eta/\partial t$, in the spatial context of each shoal for every deployment. Central-value statistics at the 95% of confidence indicated that all η_{cml} values were different from zero, and $\partial\eta/\partial t$ values were not different from zero. A summary of mean and total η_{cml} (the final values of η_{cml} for each period) allowed us to assess the average morphological response at each location for every deployment.

During summer A 2015, CSII-BA ridge and Shoal E inner swale were stable, while Chester Shoal (Shoal D) ridge and outer swale evidenced accretion and erosion, respectively. During summer B 2015, CSII-BA ridge and Shoal E evidenced erosion and accretion, respectively (Figures 2-36 and 2-37). Those responses were also evidenced during that deployment (in that order) at Bull Shoal ridge and outer swale. During fall A and B of 2015, all locations were stable. During winter 2015–2016, CSII-BA and Bull Shoal outer swale evidenced erosion, while Shoal E inner swale was stable. During summer 2016, Chester Shoal (Shoal D) ridge and outer swale were stable, while CSII-BA ridge evidenced erosion. Lastly, during fall 2016, CSII-BA was stable, while Shoal E inner swale evidenced accretion (Figures 2-36 and 2-37). Mean values of η_{cml} and η_{tot} suggested two relationships among locations: (1) at contiguous locations, morphological responses were either both stable or of opposite sign (i.e., erosion and accretion), e.g., during summer A 2015 at Chester Shoal (Shoal D); and (2) responses were similar among shoals (i.e., ridges eroded while swales evidenced accretion), e.g., during summer B 2015.

We can confidently say that the combination of tides, waves, and wind-driven currents produced these changes. We summarize them as "current-wave interactions," but a deeper analysis is in order. For example, these morphological changes were likely driven by current-wave interactions through turbulence. However, time limitation prevented us from exploring turbulence calculations to explore these dynamics further. In essence, the turbulence that links to bed changes could be quantified through the Shields number (i.e., using physics to analyze the changes). However, the data sets were enormous and would require dedicated time to calculate the turbulence parameters.

2.6.3.2 Temporal Variability in Bed Elevation Changes

Figure 2-37 shows the time series of cumulative bed elevation changes (η_{cml}) for each deployment. Data are organized per season and location according to each row of panels and colors. The gray band on each color represents the bed stability (i.e., when η_{cml} values were not different than zero). Cumulative bed changes during summer seasons varied between ~–0.6 and 0.9 m. During summer A 2015 changes were significant at Chester Shoal (Shoal D) and varied from ~0.025 to 0.2 m at the ridge, while at the other swale bed changes remained constant at ~0.05 m. Bed changes at Shoal E inner swale and CSII-BA ridge were not significantly different than zero. Bed changes during summer B 2015 at Shoal E inner swale and Bull Shoal ridge were not different than zero for ~16 days and were stable between 0.05 and –0.05 m for ~4 days, respectively. Changes at CSII-BA ridge were ~0.05 m. At Bull Shoal outer swale, η_{cml} changes followed a semidiurnal, oscillatory pattern between ~0 and 0.8 m. During summer 2016 changes at the CSII-BA ridge were constant at ~0.1 m, while changes at the outer swale of Chester Shoal (Shoal D) were negligible most of the time, although they exhibited three events of erosion up to –0.7 m.

During fall A 2015, bed changes were close to the gray band (i.e., η_{cml} values not different than zero). For Chester Shoal (Shoal D) outer swale bed changes were zero, while for Shoal E inner swale negligible changes were punctuated by events of erosion and deposition (although final bed change was not different

than zero). During fall B 2015, values of η_{cml} were characterized by events of erosion and deposition around stability depending on the location. At Shoal E inner swale, bed changes were negligible with several events of deposition. At Chester Shoal (Shoal D) outer swale, events of erosion occurred, but overall bed level was stable.

During fall 2016, CSII-BA ridge exhibited erosion up to ~–0.05 m, while Shoal E inner swale was stable. After time series at these locations were concurrent, bed changes at Shoal E inner swale oscillated between ~0.05 and 0.2 m, with a final change of ~0.1 m. Finally, during winter 2015–2016, bed changes were negligible at Shoal E inner swale, exhibited net erosion of –0.2 m at Bull Shoal outer swale, and showed cumulative erosion up to –0.4 m at CSII-BA ridge. See Table 2-9 for a compilation of ranges in bed elevation changes.

2.6.4   Discussion

2.6.4.1   Spatial and Temporal Variability in Bed Elevation Changes

We used downward-pointing ADCPs to measure bed elevation changes at six locations within Canaveral Shoals to quantify their morphological variability. Results do not directly reflect a comprehensive assessment of the shoals' morphological variability, but, rather, they provide time intensive bed changes of ridges and swales that describe morphological change during different seasons. Thus, we presented results in two broad categories: spatial patterns and temporal variability. Spatial patterns were represented by central tendency statistics of bed changes during each season for ridge-swale locations of each shoal. Temporal variability was shown as time series of bed changes available for each season. A discussion of the results provided some context for future studies.

In summary, values of η_{cml} and η_{tot} support the hypothesis of active reworking at Cape Canaveral shoals suggested by other authors (Field and Duane 1974) and observed in other studies (Olsen Associates 2013; Thieler et al. 2013). Three relationships were observed between bed changes at contiguous ridge-swale locations: (1) null change at both locations; (2) bed changes of opposite sign between ridge and swale of a shoal, i.e., erosion versus accretion; and (3) bed changes positive or negative versus null among ridges and swales of a shoal. Among shoals, two relationships were observed: (a) null changes at CSII-BA and Shoal E and changes at Chester Shoal (Shoal D) during summer A 2015, and (b) eroding ridges and accreting swales at CSII-BA/Shoal E and Bull Shoals during summer B 2015 (Table 2-10).

2.6.4.2   Bed Changes in Perspective: Decadal Evolution of Cape Shoals

Patterns of shoals' morphological evolution—whether shoals are growing or shrinking, migrating, or rotating—could be deduced from spatially dense observations of bed changes. In this case, data density did not allow inferences about detailed morphological change. Instead, it facilitated the estimation of patterns and tendencies of morphological change. In general, changes were not restricted to a specific season. Therefore, we present results as short term (multi-seasonal) and decadal evolution.

Bed elevation variability has been monitored by other authors at the inner swale of Shoal E and the CSII-BA by means of repeated acoustic sonar surveys (Olsen Associates 2013). From these observations, it was proposed that the ridge position fluctuates with migration rates of ~30 to 60 m/yr. A migration pattern could be deduced from alternating positive-negative changes observed at ridge-swale locations. If the ridge-swale feature is migrating, we expect to see a decrease in bed elevation at the ridge, with a simultaneous increase in bed elevation at the swale. This scenario was consistent with observations from bathymetric surveys immediately following the dredging event in winter 2014/spring 2015 compared to survey 1-year later (Chapter 3). The former could also produce negligible bed changes: when the bed lowers (or rises) at a location, the other could display minimal changes.

Over decadal time scales, alternating positive and negative bed elevation changes might indicate net bedform migrations like those observed at similar locations. Decadal changes observed at the so-called "shoal retreat massifs" of the North Carolina inner shelf (Swift et al. 1978; Thieler et al. 2013) were calculated from the comparison of bathymetric contours obtained in 1870s, 1970s, and 2000s. Overall, bedform migrations were found to be $O(1\ m/yr)$ to $O(10\ m/yr)$, which are comparable with shoals' migrations found offshore of Cape Canaveral.

Observations in our study did not allow comparisons of multi-seasonal changes in bed elevation *per se*. In other words, changes were not monitored across seasons and data correspond to changes within time spans of ADCP moorings. This sampling approach hindered quantification of bed elevation variability from deployment to deployment because the bed elevation was "reset" and started at zero with each deployment. However, we could infer that the measurements during a season "inherited" bed conditions measured during a previous season. The seasonal interchange of positive and negative values therefore supports our speculation that shoals either recovered or migrated, agreeing with migration rates estimated from bathymetric observations.

The "reset" also affects our understanding of dredging effects. Our observations support the hypothesis of the shoals being morphologically dynamic. However, we cannot assess from our results what would occur if a dredging event were to take place. We envision two possible avenues to explore dredging effects: (1) to link bed changes to oceanographic processes within a morphodynamic (physical-mathematical) model that enables exploring the effects of synthetic bed changes (dredging); or (2) to develop a data-driven (statistical) model to quantify the likely sequences of bed changes after a synthetic bed change (dredging).

2.6.4.3 Reworking by Modern Oceanographic Processes

Considering Canaveral Shoals' sediment reworking by modern oceanographic processes (e.g., McNinch and Luettich 2000), preliminary analyses suggest that surface gravity waves have the potential to resuspend sediments under a range of conditions. Wave orbital velocities were compared to critical threshold velocities for typical sediments found at Cape Canaveral shoals at depths of 5 m (ridge) and 10 m (swale). Wave spectra data from NDBC buoy 41009 were used to estimate the representative bottom orbital velocity, ubr, as the following (Wiberg and Sherwood 2008 their Equation 7):

$$u_{br} = \sqrt{2}\left\{\sum_i \frac{4\pi^2}{T_i^2 \sinh^2(\kappa_i h)} S_{\eta,i}\Delta f_i\right\}^{1/2} \tag{51}$$

where $S_{\eta,i}$ was the wave spectral surface value at each frequency i, Δf was the spectrum frequency resolution, T_i was the wave period for each frequency i, κ_i was the wave number associated with each frequency for linear wave theory, and h was the water depth. Values of bottom orbital velocities were ~0.2 m/s at 10 m (with peak values reaching between 1 and 2 m/s), and ~0.3 at 5 m depth (with peak values reaching between 2 and 4 m/s).

Estimates from Equation 51 were compared to critical threshold velocities for sediment sizes found at the shoals (Field and Duane 1974; Jaeger et al. 2011). The range of grain sizes was 0.177 to 0.841 mm and critical threshold velocities at 1 m above the bed, $u1cr$, were calculated for extreme grain sizes using (Miller et al.'s 1977) approach for particle sizes smaller than 0.2 mm as (see also Wang and Gao 2001):

$$u_{1cr} = 122.6(D)^{0.29} \tag{52}$$

where u_{1cr} was given in cm/s and D (the non-cohesive grain size) in cm. Critical threshold velocities were 0.38 m/s for D=0.177 mm, and 0.60 m/s for D=0.841 mm.

In general, wave bottom orbital velocities calculated exceeded the critical values for incipient bed load transport at 10 m depth between 4 and 16% of the time, and at 5 m depth between 20 and 50% of the time. In addition to waves, subtidal currents are thought to play an important role in the sedimentary dynamics at this location. Maximum subtidal currents could be 1.5 to 2 times larger than the average wave-induced bottom orbital velocities and can be present throughout the water column to 15 m depth. Subtidal currents respond mainly to local winds and variations in the speed of the Gulf Stream (Parra et al. n.d. manuscript in preparation). Although implications for sediment transport by subtidal currents are still unknown, we envision that the wave-current induced turbulent kinetic energy, including vortex shedding from orbital and anorbital ripples, ought to dominate sediment resuspension at Canaveral Shoals (Amoudry et al. 2016 and references therein). Further investigations would be based on velocity profiles measured with the downward-facing ADCPs.

2.6.4.4 Implications and Conclusions

Previous studies have documented decadal changes of inner-shelf sand banks and cape shoals along the U.S. Atlantic Coast. We have addressed the possibility of morphological change of the ridge-swale bathymetry of Cape Canaveral Shoals by analyzing bed elevation changes at six locations within the shoal complex. In general, our results give evidence of active reworking of Canaveral Shoals by modern oceanographic processes. Bed elevation changes were between –0.9 and 0.8 m, with changes typically occurring during summer and winter deployments. During summer deployments, erosion and deposition were found alternatively at ridges and swales: erosion at ridge and accretion at swale (summer B 2015) and accretion at ridge and erosion at swale (summer A 2015).

We observed three patterns in bed changes: when ridges eroded, swales either accreted or were inactive; when ridges accreted, swales eroded; and when ridges were inactive, swales were also inactive. This spatial and temporal variability in bed changes suggest isolated shoal migrations, in agreement with previous studies at Canaveral Shoals and other sand banks in the U.S. Atlantic Coast. Comparison of transport by waves further suggests that the smallest sand at ridges (~5 m depth) was resuspended by waves between 20 and 50% of the time. Our results were limited by spatial coverage and lack of temporal continuity. However, they provide direct evidence of morphological changes at cape shoals and should constitute a launch point for future morphodynamic studies, especially in consideration of the active dredging activities on these sand shoals.

2.6.5 References

Amoudry LO, Souza AJ, Thorne PD, Liu PL-F. 2016. Parameterization of intrawave ripple-averaged sediment pickup above steep ripples. Journal of Geophysical Research: Oceans 121(1): 658-673. doi.org/10.1002/2015JC011185.

Devore JL, Berk KN. 2012. Modern mathematical statistics with applications. 2nd ed. New York, NY: Springer.

Field M, Duane D. 1974. Geomorphology and sediments of the inner continental shelf, Cape Canaveral, Florida. Fort Belvoir, Virginia: U.S. Army, Corps of Engineers, Coastal Engineering Research Center. Technical Memorandum 42.

Geyer WR. 1993. Three-dimensional tidal flow around headlands. Journal of Geophysical Research: Oceans 98(C1): 955-966. doi.org/10.1029/92JC02270.

Jaeger JM, Adams PN, Mackenzie IR, Kline SW, Maibauer B, Kirchner T, Lesnek A, Harris-Parks E, Lovering J. 2011. Monitoring shoreline and beach morphologic change at Kennedy Space Center, Cape Canaveral, Florida. Annual Report Phase 2, May 2009-May 2011. Gainesville, FL: Department of Geological Sciences, University of Florida.

Kumar N, Voulgaris G, List JH, Warner JC. 2013. Alongshore momentum balance analysis on a cuspate foreland. Journal of Geophysical Research: Oceans 118(10): 5280-5295. doi.org/10.1002/jgrc.20358.

McNinch JE, Luettich RA. 2000. Physical processes around a cuspate foreland: implications to the evolution and long-term maintenance of a cape-associated shoal. Continental Shelf Research 20(17): 2367-2389. doi.org/10.1016/S0278-4343(00)00061-3.

Miller MC, McCave IN, Komar PD. 1977. Threshold of sediment motion under unidirectional currents. Sedimentology 24(4): 507-527. doi.org/10.1111/j.1365-3091.1977.tb00136.x.

Nittrouer CA, Wright LD. 1994. Transport of particles across continental shelves. Reviews of Geophysics 32(1): 85-113. doi.org/10.1029/93RG02603.

Olsen Associates. 2013. Brevard County, Florida, Federal Shore Protection Project, South Reach: 3-Year post-construction monitoring of the Canaveral Shoals II offshore borrow area (June 2013). Jacksonville, Florida: 15 p.

Paniagua-Arroyave JF. 2018. Hydrodynamic processes associated with the evolution of cape-related shoals [Dissertation, University of Florida, Gainesville, Florida. 143 p.]. University of Florida, Gainesville, Florida.

Swift DJP, Sears PC, Bohlke B, Hunt R. 1978. Evolution of a shoal retreat massif, North Carolina Shelf: Inferences from areal geology. Marine Geology 27(1): 19-42. doi.org/10.1016/0025-3227(78)90072-5.

Thieler E, Foster D, Himmelstoss E. 2013. Geologic framework of the northern North Carolina, USA inner continental shelf and its influence on coastal evolution. Marine Geology 348: 113-130. doi:10.1016/j.margeo.2013.11.011.

Wang YP, Gao S. 2001. Modification to the Hardisty equation, regarding the relationship between sediment transport rate and particle size. Journal of Sedimentary Research 71: 118-121.

Wiberg PL, Sherwood CR. 2008. Calculating wave-generated bottom orbital velocities from surface-wave parameters. Computers and Geosciences 34(10): 1243-1262. doi.org/10.1016/j.cageo.2008.02.010.
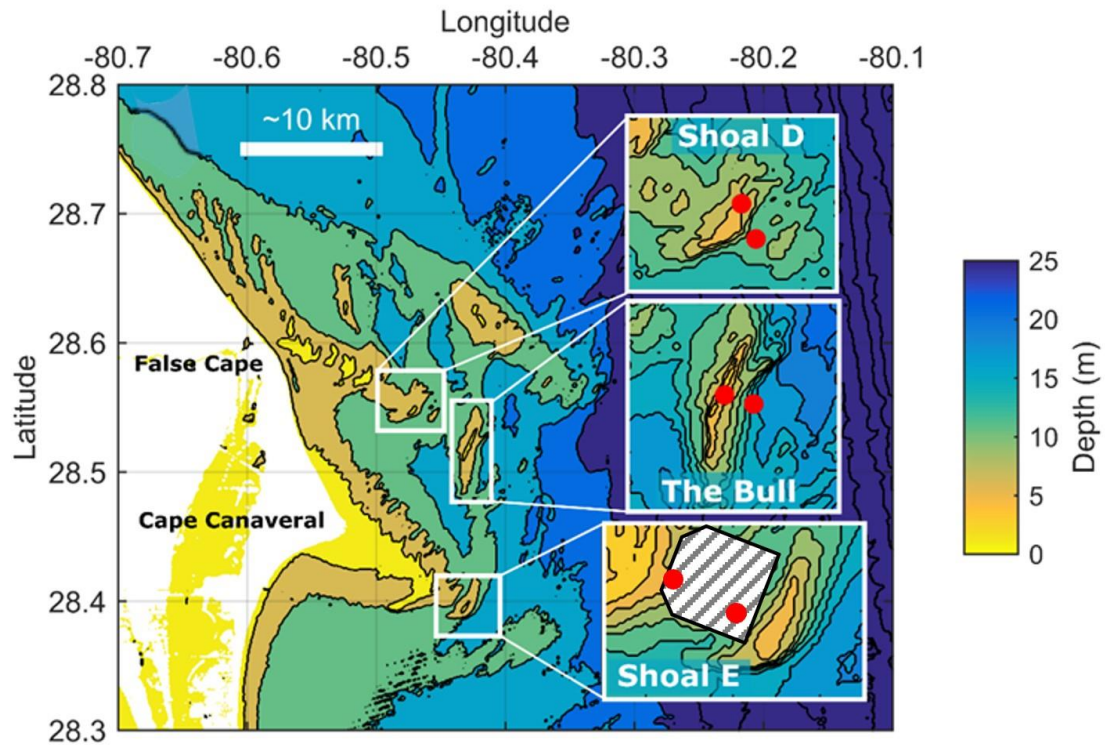
Figure 2-35. Location of ADCPs at shoals offshore of Cape Canaveral during the bed changes experiment.
Map shows the inner-shelf bathymetry near Cape Canaveral with an inset highlighting Shoal D (Chester Shoal), Shoal E (including CSII-BA denoted by hatched area), and Bull Shoal. Red-filled circles represent the approximate locations of the ADCPs.
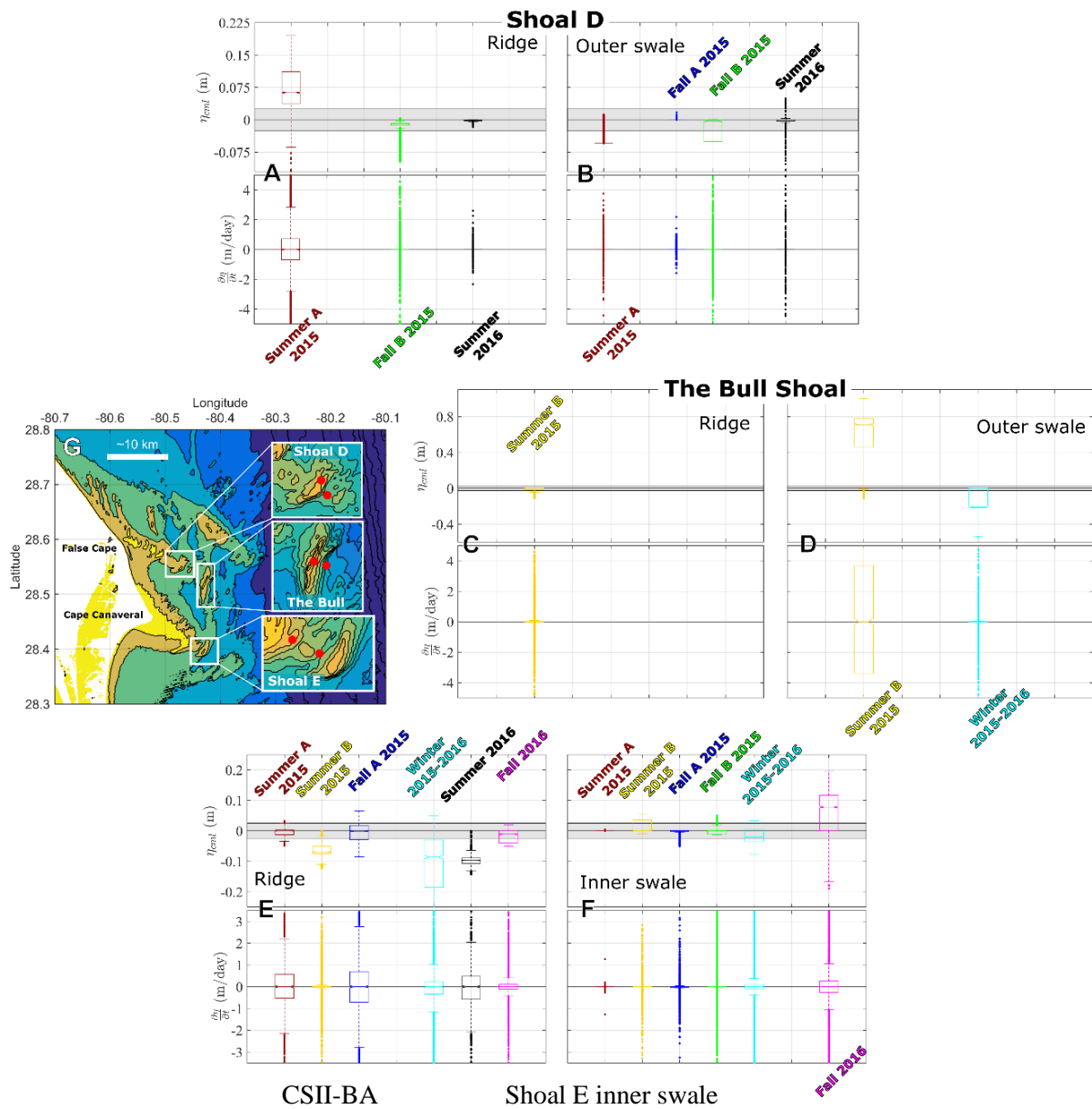
Figure 2-36. Bed elevation changes and cumulative bed elevation changes in their spatial context.
Each box whisker plot represents the collection of values for all deployments at any one location, with colors representing different deployments. Each subplot shows, respectively, the bed elevation changes ($\partial\eta/\partial t$) and cumulative bed elevation changes (η_{cml}). A and B show ridge and outer swale of Chester Shoal (Shoal D); C and D show ridge and outer swale of Bull Shoal; E and F show CSII-BA ridge and Shoal E inner swale; and G shows each shoal in the context of Cape Canaveral, with red dots indicating the approximate ADCP mooring locations. The gray band on each plot represents the bed stability (i.e., when η_{cml} values were not different than zero). Deployments were for summer A & B of 2015, fall A & B 2015, winter 2015–2016, summer 2016, and fall 2016.
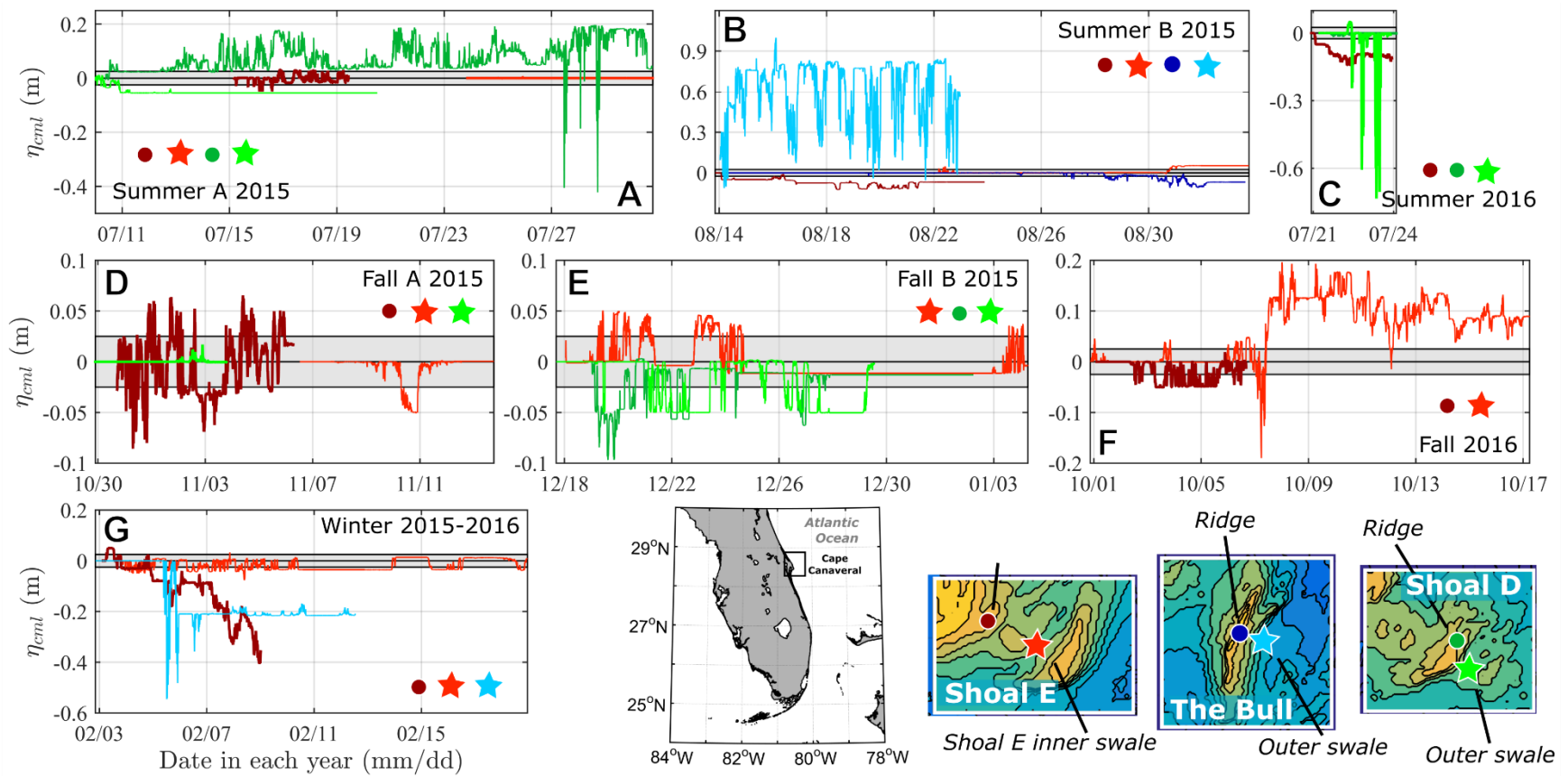
Figure 2-37. Time series of cumulative bed elevation changes, η_{cml}, during summer, fall, and winter for CSII-BA, Shoal E, Bull Shoal, and Chester Shoal (Shoal D).

(A) summer A 2015, (B) summer B 2015, (C) summer 2016, (D) fall A 2015, (E) fall B 2015, (F) fall 2016, and (G) winter 2015–2016. Gray band indicates instrument resolution (~0.05 m). Locations are color-coded and shown in the lower-right corner. Note different vertical scales for each subplot.

Table 2-9. Compilation of bed elevation changes at Canaveral Shoals per location and deployment given by season and year.

Shoal	Ridge or Swale	Summer A 2015	Summer B 2015	Fall A 2015	Fall B 2015	Winter 2015-16	Summer 2016	Fall 2016
CSII-BA	Ridge	0.00	-0.05	-0.10 to 0.05	ND	-0.40 to 0.05	0.10	0.00 to -0.04
Shoal E	Inner swale	0.00	0.00	-0.04 to 0.00	0.00 to 0.04	0.00	ND	-0.20 to 0.20
Chester (Shoal D)	Ridge	-0.40 to 0.20	ND	ND	-0.10 to 0.00	ND	0.00	ND
Chester (Shoal D)	Outer swale	0.05	ND	0.00	-0.05 to 0.00	ND	-0.70 to 0.00	ND
Bull	Ridge	ND	-0.05 to 0.05	ND	ND	ND	ND	ND
Bull	Outer swale	ND	0.00 to 0.80	ND	ND	-0.50 to 0.00	ND	ND

Notes: Positive indicates accretion, while negative represents erosion, with all values in meters. Deployments without data are represented by a dash.

Table 2-10. Summary of final cumulative and total bed changes at Canaveral Shoals per location and deployment given by season and year.

Shoal	Ridge or Swale	Summer A 2015	Summer B 2015	Fall A 2015	Fall B 2015	Winter 2015-16	Summer 2016	Fall 2016
CSII-BA	Ridge	0	(-)	0	ND	(-)	(-)	0
Shoal E	Inner swale	0	(+)[a]	0	0	0	ND	(+)
Chester (Shoal D)	Ridge	(+)[b]	ND	ND	0	ND	0	ND
Chester (Shoal D)	Outer swale	(-)	ND	0	0	ND	0	ND
Bull	Ridge	ND	(-)[a]	ND	ND	ND	ND	ND
Bull	Outer swale	ND	(+)	ND	ND	(-)	ND	ND

Notes: Positive suggests accretion, while negative indicates bed lowering, with all values in meters. Deployments without data are represented by ND.

a Total bed changes different than zero, cumulative bed changes not different than zero (95%).
b Cumulative bed changes different than zero, total bed changes not different than zero (95%).

2.7 Overall Conclusions with Application to Dredging

The effects of ridge-swale bathymetry on tidal and subtidal hydrodynamics were presented in Section 2.2, where vessel-based ADCP measurements were compared to two analytical models that yield tidal and subtidal solutions. The seasonal towed-ADCP measurements were obtained at two locations: a north transect at Chester Shoal (a reference shoal) and a south transect between CSII-BA (the dredged shoal) and the adjacent shoal, Shoal E. The north transect had relatively smoother bathymetry with a bottom slope of 0.002. Tidal hydrodynamics at the north transect were more influenced by local acceleration than frictional effects, while subtidal hydrodynamics were influenced either by Coriolis or by inertia (Bernoulli-type dynamics). The south transect had a better-defined swale with a bottom slope of 0.006. Frictional effects dominated in the south transect, where the maximum flow was located over the deepest part of the cross-section. Results of the tidal and subtidal analytical model solutions demonstrated the variable influence of ridge-swale bathymetry in inner shelves. In addition, the analysis of the underway measurements examined the applicability of open channel concepts to inner-shelf dynamics.

Subinertial hydrodynamics were investigated in Section 2.3 with a ridge-swale bathymetry during the spring season. This section focused on Chester Shoal and Shoal E, the latter encompassing the Canaveral Shoals II borrow site (CSII-BA) in its west (inner) swale. Four ADCPs were moored at an east swale and a west swale of each of the shoals. The bathymetry in the region steered the current flow, which moved mainly along-shelf. As a result, most of the variance in currents was accounted for by Concatenated Hilbert Empirical Orthogonal Function (CHEOF) Mode 1 (95.25%). The vertical structure of the flow was unidirectional at the four locations. Wavelet coherence analysis techniques were used to explore relationships between the CHEOF Mode 1 and different forcings. When the along-shelf wind and the Florida Current were in the same direction, this coincided with an increase in Florida Current transport and vice versa. The along-shelf wind enhanced the subinertial flow motion. The across-shelf momentum showed that the subinertial flow was in geostrophic balance throughout the deployment. The along-shelf momentum was dominated by pressure gradient, bottom stress, and the gradient of radiation stresses, while other terms were still influential. Enhancement of the Florida Current was associated with increased offshore sea-surface slope generated by geostrophic balance. This increase caused the subinertial flow on the shelf to move in the same direction as the western boundary current. On the other hand, southward winds coincided with weakening of the Florida Current. As a result, a negative nearshore sea-surface slope was triggered by the geostrophic balance and the nearshore flow thus moved southward.

The influence of surface infragravity waves on sediment suspension over cape-related shoals was addressed in Section 2.4. In order to study the effects of shoals on infragravity-wave variability, water-level and velocity data were collected during fall 2013, spring 2014, and fall 2014 at swales on either side of Shoal E, directly east of Canaveral Shoals II. Landward- and seaward-oriented cross-shoal infragravity energy fluxes were calculated from the auto- and coincident spectra of pressure and cross-shoal velocities. Bulk infragravity reflection coefficients were then quantified as the ratio of seaward- to landward-oriented bulk infragravity energy fluxes. Reflection coefficients and spatial variations in infragravity fluxes indicated that the moorings were located in the shoaling zone during fall 2013 and fall 2014. Net flux differences measured at inner and outer swales suggested Shoal E acts as a source of long gravity waves energy fluxes. Differences in wave characteristics on either side of Shoal E could be attributed to asymmetric short-wave shoaling and breaking, partial reflection, and trapping near the shoal. However, by assuming cross-shoal propagation, we did not resolve along-shoal motions (edge waves) that might be significant over the shoal. Our results broadly characterize the variability of infragravity energy forcing and potential short-wave dissipation over cape-related shoals. Such behavior may provide a positive mechanism for the long-term maintenance of cuspate forelands by preventing the maximum wave energy from reaching the shoreline.

Hurricanes have an apparent effect on the biophysical communities, especially in nearshore habitats. In Section 2.5, we added to the paradigm of overtides' generation by considering the effect of bottom stresses due to anomalously large current speeds related to extreme atmospheric forcing at cape-related shoals. Moderate tidal distortions at the inner swale of Shoal E (encompassing CSII-BA) were documented during conditions with subtidal flows ~0.3 m/s. Extreme tidal distortions were also measured close to Shoal E and at a nearby inlet, during the passage of Hurricane Matthew in October of 2016. Near-bottom pressure and velocity profiles evidenced extreme water-level distortions during instances with a depth-averaged flow that veered counterclockwise from going to SW (~2.7 m/s) to going to NE (~1 m/s). Subtidal currents three-fold larger than the tidal flow speed significantly increased momentum transfers from the main tidal constituent to its superharmonics. These extreme conditions measured during along-shelf propagating hurricanes indicated the highly variable nature of particulate transport dynamics at inner shelves, both in space and time.

In order to study the potential for biophysical feedbacks on bedforms, morphological changes of cape-related shoals were quantified by upward- and downward-pointing ADCPs in Section 2.6. Our results give evidence of active reworking of Canaveral Shoals by modern oceanographic processes. Bed elevation changes were between –0.9 and 0.8 m, with changes typically occurring during summer and winter deployments. During summer deployments, erosion and deposition were found alternatively at ridges and swales: erosion at ridge and accretion at swale (summer B 2015), and accretion at ridge and erosion at swale (summer A 2015). We observed three patterns in bed changes: when ridges eroded, swales either accreted or were inactive; when ridges accreted, swales eroded; and when ridges were inactive, swales were also inactive. This spatial and temporal variability in bed changes suggest isolated shoal migrations. The smallest sand at ridges (~5 m depth) was resuspended by waves between 20% and 50% of the time. Our results were limited by spatial coverage and lack of temporal continuity. However, they provide direct evidence of morphological changes at cape shoals and should constitute a launch point for future morphodynamic studies, especially when considering active dredging activities on these sand shoals.

2.8 Acknowledgments

3 Comparative Changes in Post-Dredge Shoal Bathymetry and Terrain Morphology Using Multibeam Echosounder Surveys

Michael Espriella, Vincent Lecours, and Debra Murie

Key Points

- Multibeam surveys of CSII-BA (the borrow area of Canaveral Shoals II) immediately post-dredge (May 2014) showed clearly distinguishable draghead lines (furrows) from the trailing suction hopper dredge; furrows were less pronounced 1 year following dredging (June 2015).
- Multibeam surveys of CSII-BA immediately post-dredge also showed that the dredging activity was contained solely within the swale area of CSII-BA.
- Of the surveyed area of CSII-BA, 15% experienced some sediment removal or loss in the year following dredging, with the majority of the area showing deposition (63%) or no change (22%); the overall average change in bathymetry was + 0.11 m.
- Comparatively, Chester and Bull Shoals (the reference shoals) experienced 73% and 77% sediment loss, respectively, in the year following dredging. However, the average sediment loss for both reference shoals was only -0.09 m, indicating very little change over time.
- Multibeam surveys immediate post-dredge and 1 year after dredging showed a filling-in and smoothing of the dredged area of CSII-BA, and no or minor change in bathymetric profile and terrain characteristics of slope and aspect for Bull and Chester Shoals.
- Both CSII-BA and Chester Shoals had a slight but noticeable migration of their ridge crest to the southeast from May 2014 to June 2015, which is a natural occurring phenomenon with these dynamic sand shoals.

3.1 Introduction

Changes in bathymetry and habitat features of sand shoals that are subject to dredging can have important impacts on species assemblages through habitat preferences, forage species availability, and recruitment processes, to name but a few (Wenger et al. 2016). Dredging of seafloor sediments is generally considered to be detrimental to the abundance and diversity of non-mobile marine invertebrates in particular, although deeper dredged areas may also fill in with finer sediments that are preferred by some benthic invertebrates (Michel et al. 2013). Changes in species abundance and diversity can also affect the forage base for consumers that occupy higher trophic levels, including recreational and commercially important fish species.

In addition, bathymetry can be used to derive terrain attributes using principles from geomorphometry. Geomorphometry is the quantitative characterization of terrain characteristics and is increasingly used as a means to describe seafloor geomorphology that can serve as benthic habitats (Lecours et al. 2016). Continuous terrain characteristics, like slope and terrain roughness, have been shown to act as surrogates of species distribution, and discrete seafloor features (e.g., geoforms, morphometric features) are often found to support distinct biological assemblages (Harris and Baker 2019). Quantifying the changes in bathymetry and terrain characteristics associated with dredging events is therefore an important component of assessing potential changes in species assemblages and ecosystem functioning of offshore sand shoals.

The northeastern quadrant of Canaveral Shoal II off the east coast of Florida has been dredged and surveyed on multiple occasions (see Tables 1-1 and 1-2); this region of CSII is referred to as CSII-BA (i.e., the borrow area of CSII) (Figure 3-1). The purpose of the present study was to compare bathymetry and habitat features of CSII-BA immediately post-dredge to those features a year after dredging to observe a timeline of changes. To compare these changes relative to natural changes occurring on non-dredged (reference) shoals at the same time, multibeam bathymetric surveys were also conducted in comparable areas on Chester and Bull Shoals in May 2014 (immediately after the completion of the dredging activity on CSII-BA). These surveys were repeated on the shoal areas again 1 year later (June 2015) to provide an annual timeframe for comparison. To our knowledge, the natural changes that occur in the bathymetry and terrain features of non-dredged, ridge-swale shoals over an annual cycle compared contemporaneously with those of a dredged shoal have not been documented previously in the SAB.

3.2 Methods

3.2.1 Study Sites and Data Acquisition

Multibeam echosounder bathymetric data were collected on CSII-BA and similar-sized areas and positions on Chester Shoal and Bull Shoal, which were categorized as reference shoals (Figure 3-1). General information on the shoals is provided in Chapter 1, but relevant here is that the overall range in depths were also similar among the sampled areas: 4–16 m for CSII-BA, 6–15 m for Chester Shoal, and 5–20 m for Bull Shoal. CSII-BA was dredged from November 2013 to April 2014. Multibeam bathymetric data were collected from all three shoal areas in May 2014, immediately following the dredging event, as well as 1 year later in June 2015.

Surveys were done under contract by Land & Sea Surveying Concepts Inc., Merritt Island, Florida. Data were collected using a Reason Seabat 7125 400 kHz multibeam echosounder. The echosounder produces 512 beams with a swath capability of 140°. The sonar head was mounted on a 40-foot survey vessel. Positioning for the system was from the Ashtech Proflex with motion adjustments and real-time kinematic (RTK) GPS correction from a motion reference unit (Kongsberg MRU5). The data were collected using PDS2000 acquisition software, and parallel survey lines were performed across the three survey areas with a 5% overlap among adjacent lines. Sound velocity profiles were taken by observing salinity readings taken by the Odom Hydrographics DigibarPro and applied to the data to reduce refraction errors. Additionally, patch tests were used to calibrate the system and determine static offsets for heave, pitch, and roll on the multibeam system.

3.2.2 Data Processing

Raw multibeam soundings were processed in the PDS2000 processing software. Offsets from the patch tests were applied to the vessel configuration in the software. Navigation, positioning, and motion data from the RTK GPS and motion reference unit were then applied to the raw soundings to account and correct for dynamic heave, pitch, and roll. We note that the use of RTK positioning captures, and therefore directly accounts for, vertical changes caused by tidal variations. Corrected soundings were then interpolated to produce 3 x 3 ft (cell size) raster grids for each of the three surveyed areas for 2014 and 2015, and exported as machine-readable ASCII files. The North American Datum (NAD) 1983, HARN State Plane Florida East and the North American Vertical Datum (NAVD) 1988 were used as horizontal and vertical geographic frames of reference. The vertical uncertainty of the surveys was reported by the surveying company as ± 0.1 ft (± 0.03048 m).

3.2.3 Change and Geomorphometric Analyses

ASCII files of the bathymetric surfaces were imported into ArcGIS Pro v2.4. The files were converted to show recorded depths in meters instead of feet, a condition for generating accurate terrain attributes like

local slope in geographic information systems (GIS). The raster calculator tool within ArcGIS Pro was then used to compare year-to-year differences in bathymetry at all three survey sites (i.e., raster representing the 2014 bathymetry was subtracted from the 2015 bathymetry raster, resulting in a raster depicting the change). The difference rasters were then reclassified to identify areas where depth increased or decreased more than the combined vertical uncertainty of the surveys being compared (± 0.2 ft or ± 0.06096 m), generating maps showing areas that did not change relative to areas of positive change (i.e., accretion or shallower) and negative change (i.e., erosion or deeper).

Eighteen terrain attributes were derived using focal analysis GIS tools with a 3 x 3 window of analysis, including many measures of curvatures (i.e., whether an area is concave or convex in given directions), rugosity measures, slope, aspect (i.e., the direction of the slope), and various statistical terrain characteristics. Table 3-1 gives the complete list of derived terrain attributes. Correlations were calculated among terrain attributes, and nine of them were selected as uncorrelated and characteristic of the areas. These terrain attributes included easterness and northerness (which can be combined to represent aspect), profile normal curvature, relative deviation from mean value (a measure of relative position that identifies local peaks and pits), the surface area to planar area ratio (a measure of rugosity), slope, the slope of slope (a measure of variability), a vector ruggedness measure, and tangential curvature (Table 3-1).

3.3 Results

Bathymetric surveys of CSII-BA in 2014 and 2015 showed similar depth distributions (Figure 3-2 A and C) and showed little change in depth within the swale area that was dredged (Figure 3-2 D). The most noticeable change in CSII-BA was the shift in the crest of the ridge slightly to the southeast, as evidenced by the deepening (red) and deposition (blue) changes in the most western portion of the surveyed area in Figure 3-2 D. Another notable feature in the bathymetry of CSII-BA was the parallel draghead lines made by the suction hopper dredge, which were evident in the 2014 survey that was done immediately post-dredge (Figure 3-2 B). Some draghead furrows were still apparent in 2015, whereas others were at least partially filled in, based on the changes in bathymetry compared to 2014 (Figure 3-2 D).

Bull Shoal bathymetric surveys showed little difference between 2014 and 2015 (Figure 3-3 A and B). The similarity was also reflected in the overall change map, with only a small portion of its northeastern ridge showing some erosion (Figure 3-3 C). Chester Shoal also showed little to no differences in bathymetry in the eastern portion of the area surveyed in 2014 and 2015 (Figure 3-3 D and E). The western portion of the surveyed area, however, showed some movement of sediment to the southeast (i.e., accretion observed at the leading edge of the ridge (blue) followed by deepening (red)) (Figure 3-3F).

In addition, the difference maps for all shoals displayed significant artifacts based on the survey lines in a northeast to southwest orientation (see these denoted in Figures 3-2 and 3-3). These artifacts are the cumulative effect of various inaccuracies in ancillary data measurements (e.g., positioning, motion, sound velocity) and are commonly found in such datasets (e.g., Lucieer et al. 2012; Georgian et al. 2014). However, correcting such errors in digital terrain models like bathymetric data is very challenging (Hughes Clarke 2003; Lindsay and Creed 2006) and rarely performed, in particular because the magnitude of artifacts is usually within hydrographic error standards and thus considered acceptable (Hughes Clarke 2003; Roman and Singh 2006).

Overall, relative to the combined maximum vertical uncertainty of the compared surveys (± 0.6096 m), approximately 15% of the surveyed CSII-BA area experienced at least some level of sediment loss or direct removal from 2014 to 2015, most notably from the ridge crest (Figure 3-4 A). Most of the

surveyed area of CSII-BA showed deposition (63%) or no change (22%). During the same timeline (2014 to 2015), 73% of the surveyed area on Chester experienced erosion deeper than -0.6096 m (the uncertainty of measured change) (Figure 3-4 B), while 77% of the Bull Shoal area surveyed experienced erosion (Figures 3-4 C). Table 3-2 quantifies these differences with the summary statistics for each difference map. The CSII-BA difference map between 2014 and 2015 represented the most variability, with a standard deviation of 0.194 m. The skewness of the statistical distributions of difference values for all areas was negative. Negative skewness indicated a tendency towards sediment loss between 2014 and 2015. Measures of kurtosis of the statistical distribution of difference values for all areas were all high and positive, indicating more values tending towards the means, which are all close to 0 (i.e., few high absolute values of change). The kurtosis value was lower for Bull than the other areas, indicating a wider dispersion of change values around the mean. The maximum local accretion between 2014 and 2015 was observed at Chester Shoal (+1.856 m) due to the migration of the ridge crest, and the maximum sediment loss was observed at CSII-BA (-1.146 m) (Table 3-2).

The different terrain attributes showed that the study areas were relatively flat and did not present much terrain variability or rugosity. Results for slope and aspect (Figures 3-5 and 3-6) provided the most visual representation of the terrain changes and were plotted for each shoal and year; note that the scales in the terrain plots for slope were specific to each study shoal to highlight relative changes.

Although the surveyed areas of the shoals were relatively flat, regions with comparatively higher local slope (yet generally low with < 7.8° on Bull Shoal and <14° on Chester Shoal) remained constant for Bull and Chester Shoals between 2014 and 2015. In 2014, the dredged areas of CSII-BA had a comparatively higher slope (yet generally low with < 9°), and the draghead lines were clearly visible and created rugosity in the area (Figure 3-5). This observation was expected given that the 2014 survey was done immediately following the dredging event. However, it was notable that the slope terrain a year later, in terms of magnitude and region, showed that the dredged area had been "smoothed" in the intervening time between the 2014 and 2015 surveys, which was also visible in the reduced draghead lines in 2015 (Figure 3-5). Of note, terrain attributes like slope are extremely scale-dependent; in this case, slope values were measured using a focal window of 3 x 3 raster cells, meaning that slope values were measured over areas of 2.7432 m by 2.7432 m. The slope surfaces displayed in Figure 3-5 thus only show local slope and do not capture a more regional slope that may be affected by natural and anthropogenic processes.

Aspect (the orientation of the slope) also demonstrated no notable changes in seafloor morphology for the areas surveyed on Bull and Chester Shoals from 2014 to 2015 (Figure 3-6). Within the dredged area of the swale on CSII-BA, aspect values were more variable in 2014 immediately following the dredging but, as with slope, showed a smoothed morphology by the survey in 2015 a year after dredging.

Some of the terrain attributes were enhanced artificially due to the presence of motion artifacts in the multibeam data, which have been shown to propagate and amplify in the process of deriving terrain attributes (Lucieer et al. 2016; Lecours et al. 2017a). However, these motion artifacts were distinct as multiple parallel lines following the survey transects running through the entire survey area in a northeast to southwest direction (denoted on Figure 3-5 in the panel of CSII-BA 2015).

Bathymetric profiles of each surveyed shoal area showed virtually no measurable change on Bull Shoal (Figure 3-7A). On Chester Shoal, the profiles were similar between years with the 2015 bathymetry showing only a slight offset from 2014 (Figure 3-7B). This difference was mostly noticeable in the leading crest of the ridge, showing the shoal shifting to the southeast, which was also noted in Figure 3-3F. A slight shift of the ridge crest to the southeast was also observed in the bathymetric profile of CSII-BA from 2014 to 2015 (Figure 3-7C). Most notable, however, was the irregular profile showing rugosity caused by the fine-scale disturbance of the swale area of CSII-BA immediately following dredging in 2014, which was smoothed out by 2015. This area was also smooth in 2013 before dredging. It had a

higher volume (i.e., it was shallower) in 2013 and had a similar volume between 2014 and 2015 (after dredging). Overall, the bathymetric profiles highlighted that the broader-scale features of all three shoals remained unchanged from 2014 to 2015.

3.4 Discussion

Overall, when viewing the bathymetry maps and profile for CSII-BA, it appeared that the dredging activity in winter 2013–spring 2014 was confined to the swale of CSII-BA (i.e., the ridge area was not dredged) (Figure 3-2). The bathymetric profiles across CSII-BA given in Figure 3-7 also show that there was a removal of sediment in 2014 in the swale region only. The most recent dredging event prior to the 2013–2014 dredging was from February to April 2010, which dredged only the western portion of the swale of CSII-BA (Olsen Associates 2014, their Figure 6). Comparatively, the previous 2010 dredged area of CSII-BA overlapped with only a small proportion of the area dredged in 2013–2014 (Figure 1-1).

Another major attribute of the bathymetry on CSII-BA that was most obvious in the immediate post-dredge (2014) survey was the criss-crossing lines from the dragheads of the trailing suction hopper dredge; these lines were visually apparent in the borrow area immediately following dredging activities (Figure 3-2). The draghead lines were clearly distinguishable from the parallel survey lines that were an artifact of the survey methodology itself. The rugosities created by the draghead lines were less evident 1 year later in June 2015, indicating that the dredged area had been smoothed out by natural tidal and current processes in the intervening year. This increased rugosity of the bottom due to dredging followed by smoothing over in the following years was also apparent in a previous dredging event for CSII-BA during 2010 (Olsen Associates 2013; their Figure 7 A-A'). Bathymetric profiles for this 2010-dredging event showed that the post-2010 bathymetric profile had a higher seafloor rugosity than either the pre-2010 profile or a profile taken 3 years after the dredging event (3-yr post-2010 in their Figure 7 A-A'). From the bathymetric profiles of the dredging event reported in our study, it would appear that most of the smoothing over of the aea with higher rugosity created by the dredging itself is done within the first year following the dredging event (Figure 3-7 C).

Comparing CSII-BA between 2014 and 2015 indicated that only relatively small bathymetric changes had occurred in the dredged area in the intervening year after dredging (Figures 3-2 and 3-7). The ridge area of CSII-BA appeared to experience some accretion on its northeastern side and erosion on the northwestern side in 2015 relative to 2014, shifting the shoal ridge to the southeast. In monitoring surveys for the previous 2010 dredging event, the 3-year follow-up survey showed a migration of the shoal ridge by ~500 ft in the opposite direction, to the northwest, over the 3-year period (Olsen Associates 2013). However, the ridge of CSII-BA has also been shown to migrate to the southeast previously, as reported in monitoring surveys done between 2000–2010 (Olsen Associates 2013). The ridge of CSII-BA therefore appears to be a dynamic feature of the shoal, which migrates back and forth over the years. Olsen Associates (2013) estimated that the movement could be in the order of 100–200 ft per year.

Swale areas on Chester and Bull Shoals in 2014 and 2015 did not experience major changes in bathymetry, nor did the ridge of Bull Shoal (Figure 3-3). The ridge area on Chester Shoal, however, experienced deposition and deepening of the ridge crest, showing a small movement of the ridge to the southeast (Figure 3-3 F), a similar situation as observed in CSII-BA. This trend would indicate that the shoals, whether dredged or not, naturally migrate small distances to the northwest or southeast over time.

From 2014–2015, CSII-BA experienced less erosion compared to the reference shoals, with an average deposition that exceeded the reference shoals (Figure 3-4, Table 3-2). Other than the ridge of CSII-BA, which was not dredged, the area that experienced any erosion at all was contained within the footprint of the actual dredging activity and erosion outside of that area was not observed (Figure 3-4A). Therefore,

within a 1-year period post-dredge, there was no evidence to suggest that dredging had precipitated any further scouring or erosion of the swale area. This trend was also observed in the previous 2010 dredging event where, at 3 years post-dredge, there was no pronounced erosion or scouring of the swale beyond the original removal level of sediments, as evidenced by the 3-yr post-2010 bathymetric profile line not dipping below the post-2010 bathymetric profile line (Olsen Associates 2013, their Figure 7).

Slope and aspect both demonstrated notable changes in the seafloor morphology for CSII-BA immediately following dredging in 2014 but were reduced significantly 1 year later. Fine-scale slope has implications for the stability of sediments and the local acceleration of currents, which affects food supply and exposure (Lecours et al. 2016). Aspect can indicate the direction of dominant geomorphic processes and the degree of exposure to dominant and/or local currents from specific directions; it has implications for food supply, sedimentation, and larval dispersal, among other elements (Lecours et al. 2016). Changes in slope on the reference shoals of Bull and Chester were nominal from 2014–2015. Aspect for each of the shoals for each surveyed year (Figure 3-6) demonstrated that the reference shoals (Bull and Chester Shoals) remained largely unchanged in terms of aspect in the surveyed area. In contrast, CSII-BA demonstrated significant aspect variability in 2014 in the dredged swale area. However, as with slope, aspect variability was reduced significantly on CSII-BA by 2015.

One major caveat of this analysis was that the areas surveyed on each shoal were relatively small compared to the entire size of each shoal (with its ridge and surrounding swale) (see Figure 3-1). It was not monetarily feasible to survey entire shoals using multibeam echosounder surveys. Therefore, representative areas on the reference shoals of Bull and Chester were chosen to be as similar as possible in position to the area on CSII-BA that was opened to dredging. This method allowed us to observe relatively large, localized areas of change or no change, but did not allow for observations on a much larger scale, such as landscape-level changes (i.e., a whole shoal functioning at the ecosystem level).

In summary, the surveyed areas of CSII-BA, Chester, and Bull Shoals all maintained their large-scale shoal features over a 1-year period of time. Changes in the finer-scale features associated with the physical removal of sediment from the CSII-BA swale were dynamic and over a year's timeline the swale showed deposition and smoothing of the dredge furrows. Fine-scale terrain morphology, quantified by slope and aspect, among other terrain characteristics, was also conserved on the reference shoals over a 1-year time frame and over the areas of CSII-BA that were not dredged. Fine-scale terrain morphology was also flattened within 1 year in the dredged swale on CSII-BA.

3.5 Acknowledgments

3.6 References

BOEM (Bureau of Ocean Energy Management). 2013. Issuance of a negotiated agreement for use of outer continental shelf sand from Canaveral Shoals II in the Brevard County Shore Protection Project (SPP) North Reach and South Reach: Environmental Assessment. Herndon, VA: U.S. Department of the Interior, Bureau of Ocean Energy Management BOEM 2013-01151: 1-762.

Georgian SE, Shedd W, Cordes EE. 2014. High-resolution ecological niche modelling of the cold-water coral *Lophelia pertusa* in the Gulf of Mexico. Marine Ecology Progress Series 506: 145-161.

Harris P, Baker E. 2019. Seafloor geomorphology as benthic habitat: GeoHab atlas of seafloor geomorphic features and benthic habitats. 2nd ed. Harris P, Baker E, editors. Amsterdam, The Netherlands: Elsevier. 1076 p.

Hughes Clarke JE. 2003. Dynamic motion residuals in swath sonar data: Ironing out the creases. The International Hydrographic Review 4 (1). https://journals.lib.unb.ca/index.php/ihr/article/view/20600(1). [accessed 2022/08/04].

Jenness JS. 2004. Calculating landscape surface area from digital elevation models. Wildlife Society Bulletin 32 (3): 829-839.

Lecours V, Devillers R, Lucieer V, Brown CJ. 2017a. Artefacts in marine digital terrain models: A multiscale analysis of their impact on the derivation of terrain attributes. IEEE Transactions on Geoscience and Remote Sensing 55: 5391-5406.

Lecours V, Devillers R, Simms A, Lucieer V, Brown CJ. 2017b. Towards a framework for terrain attribute selection in environmental Studies. Environmental Modelling Software 89: 19–30.

Lecours V, Dolan M, Micallef A, Lucieer V. 2016. A review of marine geomorphometry, the quantitative study of the seafloor. Hydrology and Earth System Sciences 20: 3207-3244.

Lindsay JB, Creed IF. 2006. Distinguishing actual and artefact depressions in digital elevation data. Computers and Geosciences 32: 1192-1204.

Lucieer V, Barrett N, Hill N, Nichol SL. 2012. Characterization of shallow inshore coastal reefs on the Tasman Peninsula, southeastern Tasmania. In: Harris P, Baker E, editors. Seafloor geomorphology as benthic habitat: GeoHab atlas of seafloor geomorphic features and benthic habitats. Amsterdam, The Netherlands: Elsevier. p. 481-492.

Lucieer V, Nau AW, Forrest AL, Hawes I. 2016. Fine-scale sea ice structure characterized using underwater acoustic methods. Remote Sensing 8(10): 821. doi.org/10.3390/rs8100821.

Michel J, Bejarano A, Peterson C, Voss C. 2013. Review of biological and biophysical impacts from dredging and handling of offshore sand. Herndon, VA: U.S. Department of the Interior, Bureau of Ocean Energy Management. OCS Study BOEM 2013-0119. 258 pp.

Olsen Associates. 2013. Brevard County, Florida, Federal Shore Protection Project, South Reach: 3-Year post-construction monitoring of the Canaveral Shoals II offshore borrow area (June 2013). Jacksonville, Florida: 15 p.

Roman C, Singh H. 2006. Consistency based error evaluation for deep sea bathymetric mapping with robotic vehicles. Proceedings 2006 IEEE International Conference on Robotics and Automation, 2006 ICRA 2006: 3568-3574.

Sappington JM, Longshore KM, Thompson DB. 2007. Quantifying landscape ruggedness for animal habitat analysis: A case study using Bighorn Sheep in the Mojave Desert. The Journal of Wildlife Management 71: 1419-1426. doi.org/10.2193/2005-723.

Wenger A, Harvey E, Wilson S, Rawson C, Newman S, Clarke D, Saunders B, Browne N, Travers M, Mcilwain J. 2016. A critical analysis of the direct effects of dredging on fish. Fish and Fisheries 2017: 1-19. doi:10.1111/faf.12218.
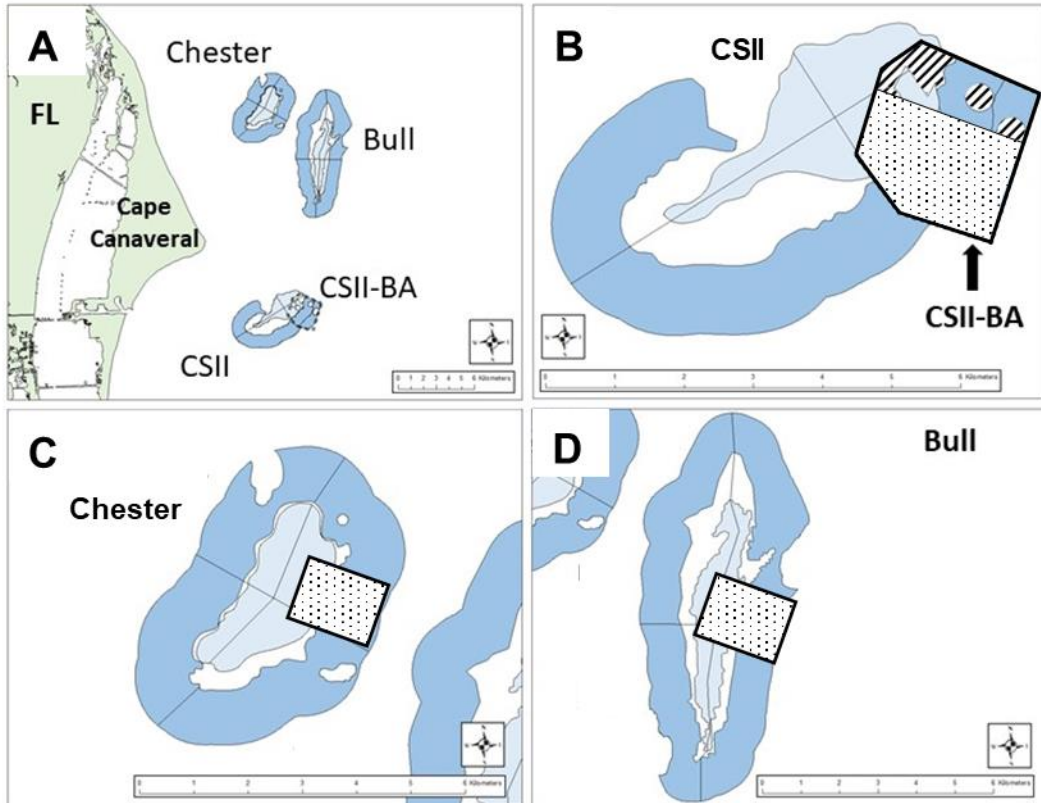
Figure 3-1. Location of A) all study shoals off the east coast of Florida; and designated multibeam bathymetric survey areas (gray stipple) for B) the borrow area (CSII-BA) of Canaveral Shoal II (CSII); C) Chester Shoal; and D) Bull Shoal.

For each shoal, the ridge area is outlined in light blue, the swale area in dark blue, with the buffer zone (white) between the ridge and swale areas (i.e., side of ridge). Hatched areas in CSII-BA represent exclusion areas (i.e., not open to dredging or sampling) (BOEM (Bureau of Ocean Energy Management) 2013).
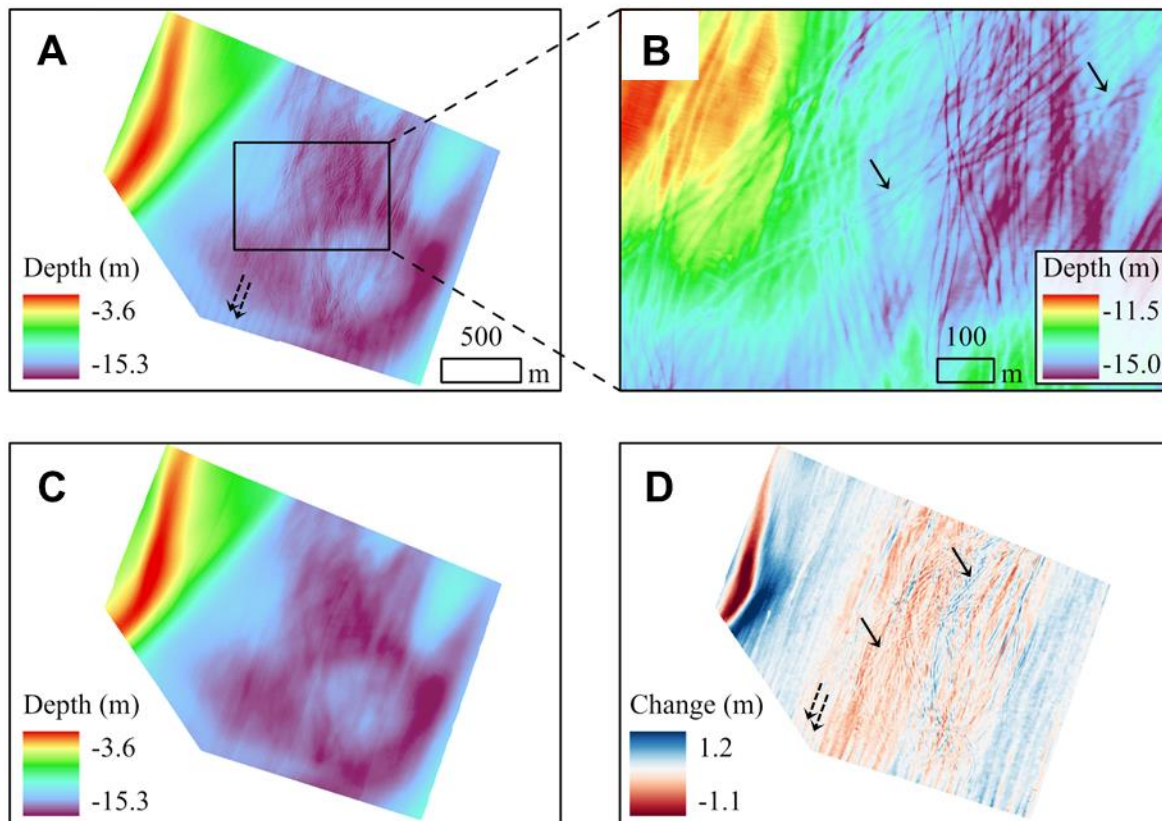
Figure 3-2. CSII-BA shoal bathymetry in A) May 2014 (immediate post-dredge); B) draghead furrows (solid arrows) in swale area dredged in fall 2013–spring 2014; C) June 2015 (1-year post-dredge); and D) bathymetry differences between 2014 and 2015.
Vertical offsets caused by along-track motion artifacts in the survey data are indicated by dashed arrows and run parallel to one another versus draghead furrows (noted by solid arrows) that cross multiple survey tracks. The scale on the difference map (D) is centered around 0 m (white) that indicates no change.
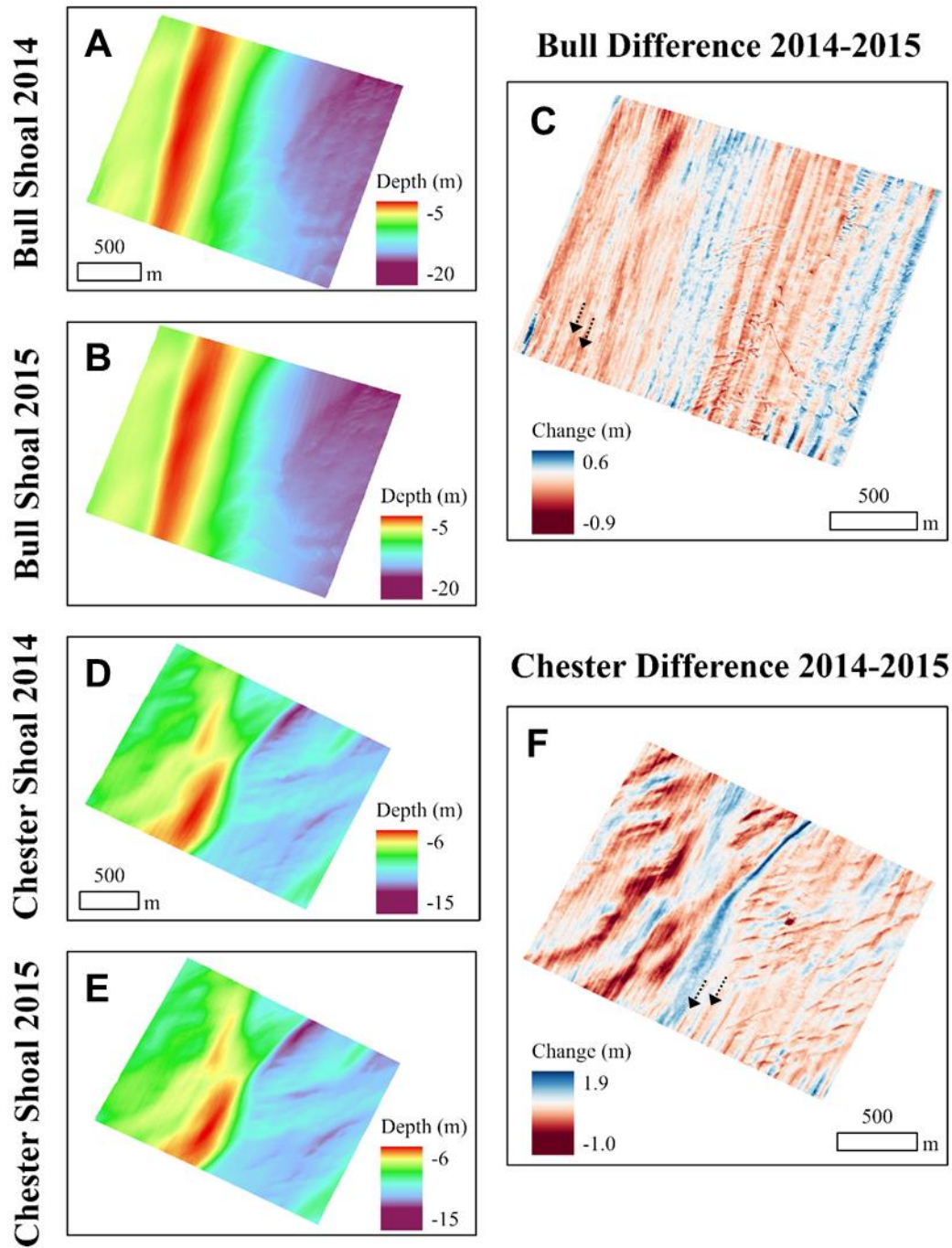
Figure 3-3. Chester Shoal and Bull Shoal bathymetry from 2014 and 2015, as well as the bathymetry difference between the 2 years.
Vertical offsets caused by along-track motion artifacts in the survey data are shown as parallel lines running southwest to northeast (dashed arrows). The scale on the difference maps is centered around 0 m (white) that indicates no change.
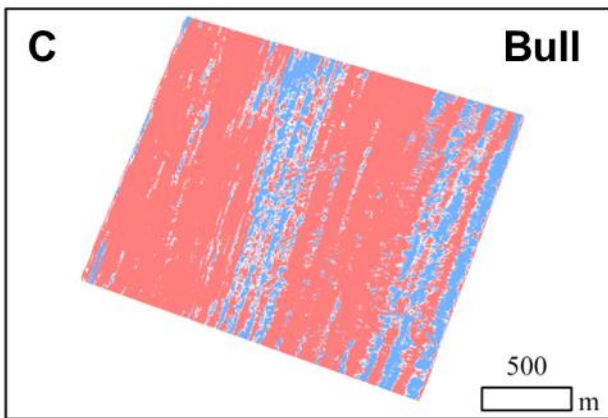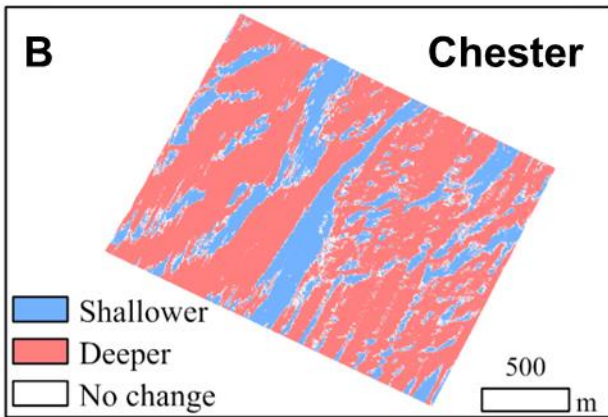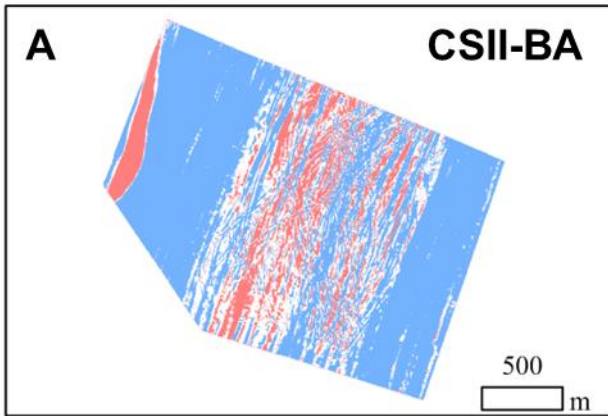
Figure 3-4. CSII-BA, Chester, and Bull Shoals showing areas that experienced accretion (shallower), erosion (deeper), or no change from the 2014 survey to the 2015 survey.
Areas marked as no change (white) are within the margin of error for the survey.
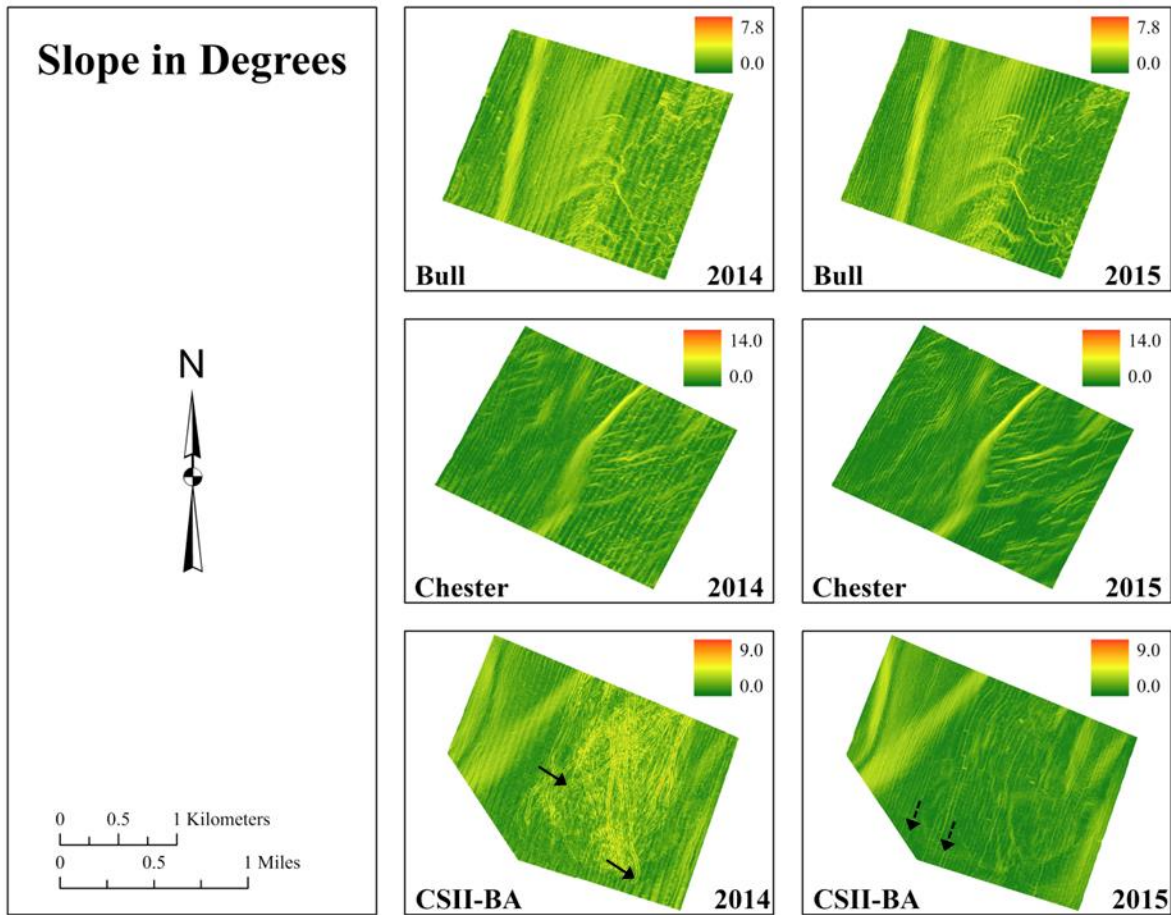
Figure 3-5. Slope for each shoal and year surveyed.
Note that the scale of slope is specific to each shoal to best visualize the changes. Vertical offsets caused by along-track motion artifacts in the survey data are indicated by dashed arrows and run parallel to one another versus draghead furrows (noted by solid arrows) that cross multiple survey tracks.
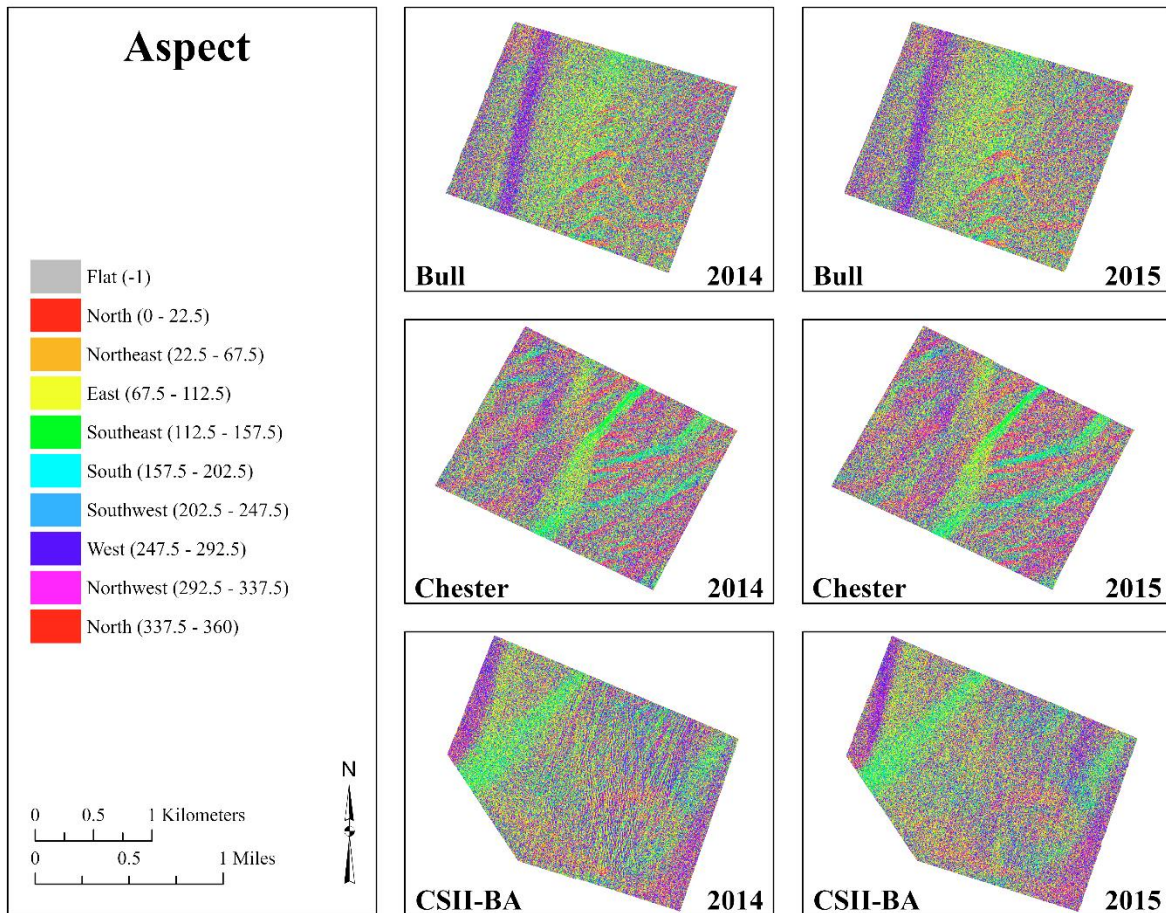
Figure 3-6. Aspect for each shoal for each surveyed year.
Legend shows the aspect in degrees from 0–360°, with 0° and 360° indicating due north. Flat areas showing no direction of the slope are indicated as -1. The degrees area binned to show general direction.
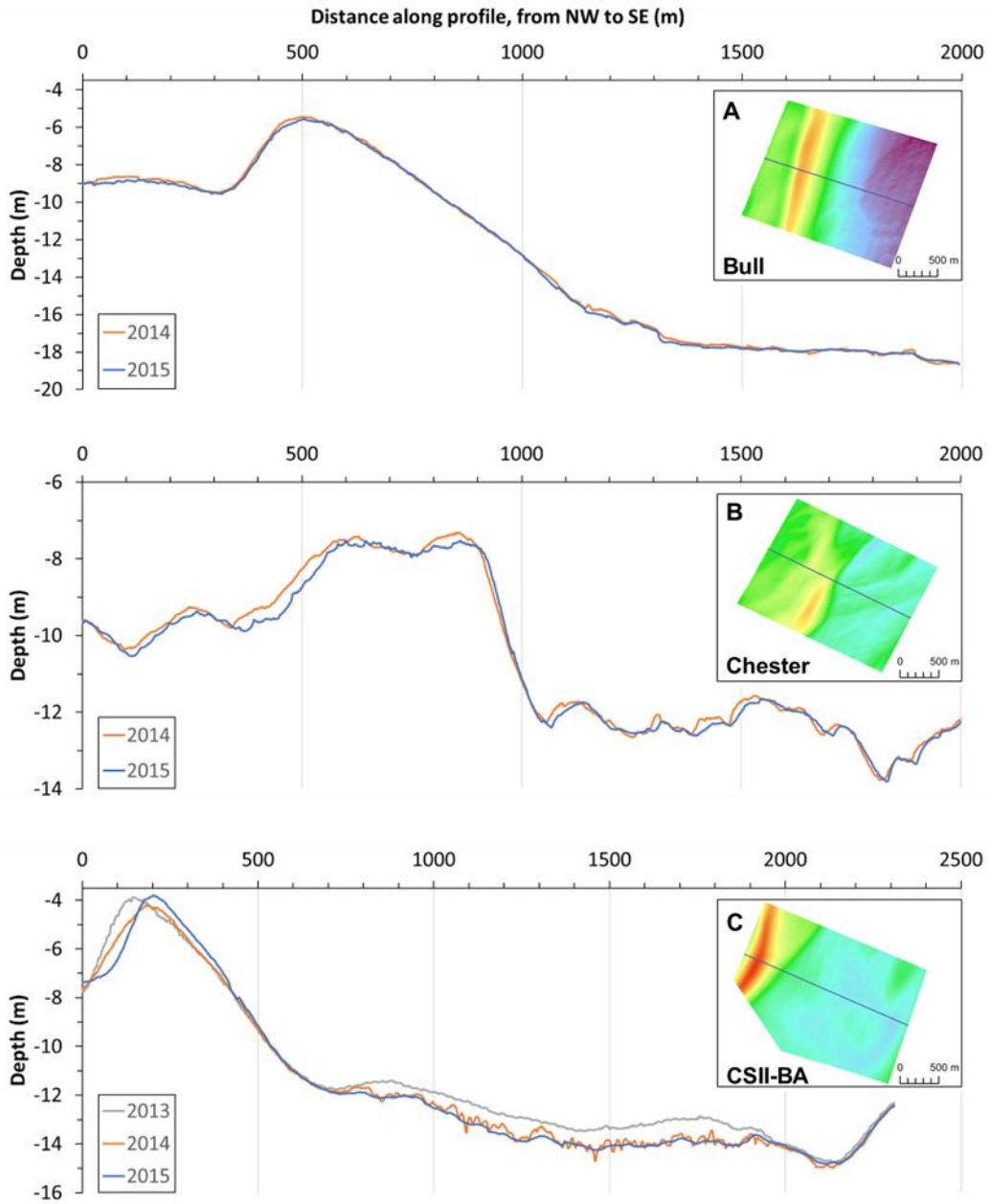
Figure 3-7. Bathymetric profiles for Bull, Chester, and CSII-BA shoals for 2014 and 2015.
The profile transects run NW to SE (insets). The bathymetric profile for CSII-BA includes a pre-dredge survey (June–July 2013) based on survey data supplied to BOEM by U.S. Army Corps of Engineers (survey done by Whidden Surveying & Mapping, Inc.).

Table 3-1. Terrain attributes used in this study, along with definition of the attribute.

Terrain Attribute (* denotes non-correlated)	Definition
Easterness*	Represents the sine of aspect in radians, i.e., the orientation of the slope. Thus, it represents the deviation of the slope from east. It ranges between -1 (fully West) and 1 (fully East).
General Curvature	Measures the overall curvature of the terrain from planar coordinates.
Mean Bathymetry	Statistical measure of the average depth within the window of analysis. It is known to remove local noise in bathymetry.
Mean Curvature	Measures the overall curvature of the terrain by averaging the minimum and maximum curvatures.
Median Bathymetry	Median depth value within the window of analysis.
Northerness*	Represents the cosine of aspect in radians, i.e., the orientation of the slope. Thus, it represents the deviation of the slope from north. It ranges between -1 (fully South) and 1 (fully North).
Planar Curvature	Quantifies the level of convexity or concavity perpendicular to the direction of maximum slope.
Profile Curvature	Quantifies the level of convexity or concavity along the direction of maximum slope.
Normal Curvature*	Measures the curvature perpendicular to the contour line.
Bathymetric Range	Represents the absolute variation of depth within a window of analysis.
Relative Deviation from Mean Value*	Unit-less measure of relative position proposed by Lecours et al. (2017b) that identifies local peaks (positive values) and pits (negative values).
Surface Area to Planar Area Ratio*	Proposed by Jenness (2004), it calculates the ratio of the 3D surface and the 2D surface within the window of analysis.
Slope*	Gradient of change in bathymetry within the window of analysis.
Slope of Slope*	Variation in slope gradient that can reveal the complexity and roughness of the terrain.
Standard Deviation of Bathymetry	Statistical measure of how much depth varies within the window of analysis. It is a proxy of local rugosity.
Surface Area	Calculates the surface area, or the 3D space filled within a window of analysis.
Tangential Curvature*	Measures the geometric normal curvature perpendicular to the slope line, tangent to the contour line.
Vector Ruggedness Measure*	Proposed by Sappington et al. (2007), it quantifies terrain ruggedness by measuring the dispersion of vectors orthogonal to the terrain surface.

Table 3-2. Summary statistics of the bathymetry differences between 2015 and 2014 at each shoal.

Depth Differences (m)	CSII-BA 2015–2014	Bull 2015–2014	Chester 2015–2014
Mean	0.111	-0.092	-0.087
Median	0.119	-0.089	-0.079
Std Dev	0.194	0.012	0.168
Maximum accretion	1.162	0.626	1.856
Maximum erosion	-1.146	-0.867	-1.023
Skewness	-0.032	-0.168	-0.121
Kurtosis	4.267	3.193	4.930

Note: Depth differences less than ± 0.06096 m were considered to be "no change" based on the combined vertical error of the surveys. All measurements are in meters.

4 Habitat Classification of Shoals and Surrounding Area Based on Direct Sampling Using Sediment Grabs

Debra Murie and Geoffrey Smith, Jr.

> **Key Points**
> - Based on benthic grab cores, the majority of sediment grain size on CSII, CSII-BA, Chester, and Bull Shoals was 0.25–1.00 mm and consisted of mostly fine, medium, and coarse sands, of both geologic and biogenic origin. Canaveral Bight had sediment mostly < 0.0625 mm and comprising muddy sand with ~2% organic content.
> - Based on benthic grab surface views (photographs), the majority of the substrate on the shoals was medium and coarse shell sand, and medium shell hash (biogenic origin).
> - Surface views of the substrate indicated a higher proportion of larger-sized biogenic particles from primarily mollusk shell fragments, which increased the complexity of the substrate compared to the sand observed in the majority of the benthic grab cores.

4.1 Introduction

For fisheries, the survival of larval and juvenile fishes ultimately drives recruitment (Houde 1997). Fish use physical habitat for refuge from predators as well as for foraging on prey resources, and many use specific habitat features or microhabitats depending on their life cycle stage (Auster et al. 1991; Gotceitas and Brown 1993). Larval and juvenile fishes, in particular, can be susceptible to habitat change because of strong fish-habitat interactions (Diaz et al. 2003). In addition, known associations between fish abundance and habitat can provide management agencies with information that can guide monitoring programs for activities that may have more consequential impacts to EFH. EFH is defined as "those waters and substrate necessary to fish for spawning, breeding, feeding or growth to maturity'' (SFA 1996) and includes habitat necessary for any phase in the life cycle of a federally managed species (SAFMC 2011). In addition, HAPCs, a subset of EFH, include habitats that provide an important ecological function, are sensitive to human-induced degradation, are currently stressed or will be stressed by development activities, or are a rare type of habitat (SAFMC 2011).

As a source of sand for beach renourishment following the storm damage by Hurricane Sandy in 2012, the northeast quadrant of Canaveral Shoal (CSII-BA) off the east coast of Cape Canaveral was dredged for sand (Figures 1-1 and 1-2). Whereas the sediment grain size and type was well known for CSII-BA because of the requirements of the sand grain size for renourishment purposes, the sediment characteristics were only generally known for the major (non-dredged) portion of Canaveral Shoal (CSII) and the surrounding area, as well as the two other reference shoals, Chester Shoal and Bull Shoal (Figure 1-2).

The overall goal of this chapter was therefore to determine the sediment characteristics of the study shoals and surrounding habitat in order to integrate habitat information with the abundance and biomass of invertebrates and fishes (in Chapters 11–13) and fish movements (in Chapter 14). Specific methods and objectives to meet this goal included the following: 1) to use conventional benthic grab samples to classify substrate; 2) alternatively, to use photographs of the surface of the benthic grabs to classify the substrate; and 3) to compare the two substrate classification methods in relation to potential invertebrate and fish habitat. Sediment features based on benthic grab samples that are three-dimensional (i.e., include a depth component) may be more applicable to infaunal and benthic invertebrates that are sedentary or

burrow in the bottom substrate. Two-dimensional surface sediment features observed in photographs may be more applicable to relatively larger, mobile, demersal invertebrates and fishes that primarily traverse over the bottom instead of burrowing into it. However, the distribution of these latter groups may also ultimately rely on the former due to their trophic relationships.

4.2   Methods

Benthic grab sampling was conducted in an approximately 22 km x 27 km sampling area that encompassed all three study shoals and adjoining coastal areas (Figure 4-1). This sampling area was overlain with a 1 km x 1 km sampling grid except in areas within the multibeam survey areas (Chapter 3), where sampling sites were spaced at 0.5 km (Figure 4-1). Sediment samples were collected every 2 km (i.e., every other sampling site in the grid) in areas outside of the study shoals (Figure 4-1). All sediment samples were collected in June 2017.

Samples were collected using a modified Young grab (as detailed in Chapter 11). If a Young grab sample was not at least ¾ full, the sample was discarded, and the Young grab was deployed again. This process was done up to five times, upon which it was assumed that there was some type of benthic feature (e.g., rock below the sediment layer) that was preventing a full sample from being collected rather than an equipment malfunction (e.g., grab closing too early, shells or sand dollars preventing the grab from closing all the way, etc.). If a grab was not full, it was noted and the approximate fullness of the grab was recorded (e.g., ½ or ¾ full). Along with each benthic grab, a digital photograph was taken of the surface of each grab with its unique station identification number in the frame. A 1.5-in (35-mm) inside diameter by 6-in (152 mm) long plastic plumbing tailpiece (straight pipe with a lip) was used to collect a sediment core from the center point of each grab sample. The depth of each core was 50 mm. Samples were placed in labeled ziplock bags and stored on ice during collection and then frozen until processed in the lab.

4.2.1   Processing Cores from Benthic Grabs

Samples were wet sieved through a series of US standard sieves decreasing in size, including sieve sizes 5, 10, 18, 35, 60, 120, and 230 (Table 4-1). Sediment was sequentially washed through the sieves using a handheld garden sprayer. Water and sediments passing through sieve 230 were collected in a clean plastic bucket (i.e., the wet sieving process collected all sediment). The sediment retained by each sieve layer was collected in a pre-labeled and pre-weighed aluminum pan; multiple pans were necessary for some sieve layers. If there was only a small amount of mud/silt in the water collected below the 230 sieve, then the water was filtered immediately through a pre-weighed 0.7 µm glass fiber filter using a vacuum pump, with the filter then placed in a pre-labeled/pre-weighed aluminum pan. A water-filled squirt bottle was used to wash out all sediment from the bucket with a minimum of rinse water. For samples with larger quantities of mud/silt collected in the water passing through the 230 sieve, the water in the bucket was allowed to settle for 12–24 hours. After settling, the top water was carefully decanted off as much as possible without disturbing the bottom of the bucket containing the sediment and the volume recorded. A 500 ml subsample of the top water was then filtered through a pre-weighed 0.7 µm glass fiber filter, which was then placed in a pre-labeled/pre-weighed aluminum pan. The remaining water was stirred to resuspend the sediment and the slurry was immediately transferred to large pre-labeled/pre-weighed aluminum loaf pans; multiple loaf pans were necessary to capture all of the water and sediment left in the bucket. If the bucket water was not clear following settling (i.e., suspended mud/clay particles) then the bucket was stirred to resuspend all of the sediment and a 500 ml subsample of the slurry was immediately collected. This subsample was filtered through a pre-weighed 0.7 µm glass fiber filter, which was then placed in a pre-labeled/pre-weighed aluminum pan. The total volume of the slurry in the bucket was then determined in order to estimate the total amount of sediment in the bucket based on the proportion represented by the subsample.

All filled pre-labeled/pre-weighed aluminum pans were dried in an oven at 105 °C for 24–36 hours to constant mass (O'Kelly 2005). After drying, pans were cooled in a dessicator and then re-weighed. The pan weight (and filter weight for those with glass fiber filters) was subtracted from the dry weight to determine the dry weight of the sediment in each sieve layer. We placed the aluminum pans in a muffle furnace at 500 °C for 4 h to ash any organic matter in the samples. After ashing, the pans were cooled in a dessicator and re-weighed with the ashed weight subtracted from the dry weight to determine the weight of organic matter in each sieve layer for each sample (i.e., loss-on-ignition).

We classified the sediment samples using the Coastal and Marine Ecological Classification Standard (CMECS), which is based on a modified Wentworth scale for particle size (FGDC 2012) (Table 4-1). Geologic sediments were classified based on CMECS, which uses a modified Folk (1954) ternary diagram of Gravel-Sand-Mud (FGDC 2012). Initially, each processed core sample taken from the grab was assessed for the percentage of grain sizes (Table 4-1) based on dry weight and the CMECS classification applied (FGDC 2012). In CMECS for geologic substrate, Gravel is considered to be all rock particles with a median size of > 2 mm or larger, and Mud is considered to be all particles with a median size < 0.0625 mm (i.e., smaller than fine sand) (FGDC 2012).

We plotted each core as a pie diagram based on the percentage of each particle size based on its sampling location to form a distribution map of particle sizes over the entire sampling frame. In addition, the distribution of Mud (fine sediments < 0.0625 mm) in the samples was plotted over the sampling frame and then interpolated using the IDW (inverse distance weighted) tool within the interpolation folder of Geostatistical Analysts Tools in ArcMap 10.8.1. The interpolated cell size was set at 0.005 x 0.005 (~ 0.5 km x 0.5 km). The search distance was set at 0.02 (~ 2 km) with a minimum number of neighbors set at 5 and maximum number of neighbors set at 10. If the minimum number of neighbors was not met, the search distance was increased until the minimum number of neighbors was achieved. The measurements for the cells and search distance were based on degrees, so the distances in km were approximate. The total % organic matter in the sediments also was plotted by sampling stations and interpolated to give a map of % total organic matter.

After each core was assessed for particle size distribution, it was then assigned to a substrate classification based on its substrate origin and mixture (FGDC 2012). Initially, we classified each processed core sample from the grab as either of geologic or biogenic origin based on whichever substrate component represented > 50% of the dry weight of the sample. Geologic sediments were classified based on CMECS, which uses a modified (Folk (1954) ternary diagram of Gravel-Sand-Mud (FGDC 2012). This ternary diagram classifies mixtures based on the percentages of each type of sediment; for core samples the percentages were based on % dry weight. Biogenic components in the present study were derived from shell substrate (shells and shell fragments) based on CMECS (FGDC 2012). For biogenic substrate, CMECS categories include Shell Rubble, Shell Hash, and Shell Sand (Table 4-2). For this study, based on the size of shell substrate particles in the sieve series, we further subdivided the Shell Hash category into Coarse versus Medium Shell Hash and subdivided the Shell Sand category into Coarse and Medium Shell Sand (Table 4-2). For all core samples, particles < 0.5 mm could not be visually identified as geologic versus biogenic and were therefore assumed to be of geologic origin, as per FGDC (2012). Silt and clay material passing through the lowest sieve (#230) that was < 0.0625 mm was all classified as Mud, as per FGDC (2012).

4.2.2 Processing Surface-view Photographs of Benthic Grabs

We initially scored each digital photograph taken of a benthic grab visually into either a geologic or biogenic substrate component based on which component represented > 50% of the surface area of the grab. The photograph was then scored visually as to the size and character of the visible components of substrate (Figure 4-2) and assigned into a substrate classification that represented the greatest percentage of the surface area (Table 4-2). Size of particles in the photograph were scaled against the known size of

the site label. Biogenic substrate could only be scored down to Medium Shell Sand and substrates with particles smaller than 0.5 mm were assigned into a geologic Sand or Mud category because it was not possible to visually distinguish shell particles from sand particles at sizes < 0.5 mm.

4.2.3   Visual Representation of Habitat Classification Schemes

Benthic grabs classified by % dry weight and surface-view photographs classified by % surface area had substrate types assigned a numerical value based on a common scale of increasing size of particles, from Mud=1 to Coarse Shell Hash=8. The distribution of substrate type based on both methods was then interpolated over the sampling frame using the same interpolation method as outlined in Section 4.2.1.

4.3   Results

4.3.1   Sediment Particle Size and Organic Content

Particle size distribution in the cores based on % dry weight did not contain any particles with a median size distribution > 64 mm (i.e., no particles in the Gravel category, including no Cobble or Boulder, and no Shell Rubble, Tables 4-1 and 4-2). In the northern region of the sampling frame, inclusive of Chester and Bull Shoals (Figure 4-3), the majority of particles in the cores were between 0.25 to 1 mm. An area on the southern end of Chester Shoal and southwest of it contained finer sediment particle sizes mostly in the range of 0.125 mm and smaller. A conspicuous area of larger particle sizes (> 1 mm) occurred to the south-southwest of both Chester and Bull Shoals, as well as off the east coast of Bull Shoal (Figure 4-3). In the southern region of the sampling frame, inclusive of CSII and CSII-BA (Figure 4-4), the majority of particle sizes were between 0.25 to 1 mm, similar to the northern region. However, west and southwest of CSII, the particle size was much smaller, with the majority < 0.125 mm.

Interpolated distribution of finer sediments inclusive of Mud (Silt/Clay) (i.e., < 0.0625 mm) indicated a higher percentage in the Canaveral Bight area (Figure 4-5), with the majority of the Bight sediments having 10–20% Mud. Areas southwest of both Chester and Bull Shoals also were observed to have pockets of higher percentages of Mud. Areas with higher percentages of Mud on the study shoals were in the swales of the shoals.

Interpolated distribution of % total organic matter (Figure 4-6) indicated a relatively low level (1–2%) of organic matter over most of the sampling area, with some isolated pockets of higher % organic matter. Canaveral Bight, in general, had a broader area of relatively higher organic matter (Figure 4-6).

4.3.2   Sediment Classification

4.3.2.1   Benthic Grab Cores

Benthic grab cores had no geologic substrate classified as Gravel (i.e., particles of geologic origin > 2 mm median size) (Table 4-1); all particles > 2 mm were of biogenic origin (shell and shell fragments) (Table 4-2). The complete absence of Gravel from the cores reduced the modified Folk (1954) ternary diagram to the last level of the triangle, which was based on the ratio of Sand to Mud and included: Sand (≥ 90% Sand and ≤ 10% Mud), Muddy Sand (≥ 50% Sand and ≤ 50% Mud), Sandy Mud (≤ 50% Sand and ≥ 50% Mud), and Mud (≥ 90% Mud and ≤ 10% Sand) (FGDC 2012).

Based on % dry weight in the benthic grab cores, the study shoals and surrounding area were primarily categorized as Sand, with Muddy Sand apparent in the bight area of Cape Canaveral (Figure 4-7); no cores were classified as having 50% or more Sandy Mud or Mud. There were areas of Coarse and Medium Shell Hash to the south/southwest of Chester and Bull Shoals and a patch of Medium Shell Hash on the east coast of Bull Shoal.

Interpolated substrate classification based on dry weight of the grab cores distributed the Sand category broadly across the study area (Figure 4-8). The area of Medium and Coarse Shell Hash to the south of Chester Shoal and to the southwest of Bull Shoal was also interpolated to be more extensive based on neighboring grabs. Muddy Sand was also extensive in the Canaveral Bight and southwest of CSII.

4.3.2.2 Surface-view Photographs

Classifying the bottom habitat based on visual scoring of habitat categories representing the greatest % surface area indicated that biogenic substrate components dominated the sampling area (Figure 4-9). CSII/CSII-BA had Sand substrate in the southeast quadrant but Medium Shell Hash on the ridge and Coarse and Medium Shell Sand across the northwest and northeast quadrants (Figure 4-9). Chester Shoal had Sand substrate in its southeastern swale, but its ridge was mostly Coarse Shell Sand with some Medium Shell Hash and Medium Shell Sand (Figure 4-9). Bull Shoal still showed some Coarse Shell Hash in its eastern swale but had Medium Shell Hash along its ridge, with the rest of the shoal primarily covered with Coarse and Medium Shell Sand (Figure 4-9).

Interpolation based on the surface view of the grabs demonstrated the extent of the biogenic substrate in the study area (Figure 4-10). In general, swales were comprised of Medium Shell Sand and Sand except the eastern swale of Bull Shoal that notably had a small patch of Coarse and Medium Shell Hash (Figure 4-10). Ridges on all the shoals had Coarse Shell Sand, with Bull Shoal also having Medium Shell Hash.

4.3.2.3 Comparison of Benthic Classification Based on Methods

Overall, classifying substrates of the shoals and surrounding area using cores taken from benthic grabs resulted in a more homogeneous (i.e., mostly Sand) spatial map compared to the heterogeneous bottom substrate observed when categorizing the surface view of the benthic grabs using photographs (Figures 4-7 and 4-9). The difference between the two methods was not extreme when comparing the methods for CSII/CSII-BA or Chester Shoal, other than the surface-view method showing the presence of small areas of Medium Shell Hash on the ridges. Bull Shoal, however, appeared much more heterogeneous when categorized using the surface-views compared to the grab cores.

4.4 Discussion

As expected, the study shoals and surrounding area had primarily sand substrate based on extensive benthic grab sampling. The entire Cape Canaveral and surrounding area has been explored since the 1970s as a source of sand for beach renourishment (Field and Duane 1974), and CSII-BA has been dredged repeatedly since 2000 for its sand resources (Table 1-1). Cores 5-cm deep taken from the benthic grabs collected over the shoal areas were comprised of mostly medium to coarse sands ranging from 0.25 to 1 mm that were of both geologic and biogenic origin. Finer sediments (< 0.0625 mm) that were primarily muddy sand with higher organic content were restricted mostly to Canaveral Bight and secondarily to areas directly south of Chester Shoal. This observation was similar to the surficial sediments reported by Field and Duane (1974) that were primarily medium to coarse sand over the shoals in the Cape Canaveral area and fine sand and silt in Canaveral Bight. Field and Duane (1974) also noted that the sands were made up of both "terrigenous" (= geologic) and biogenic sources and primarily "quartzose-mollusk sand." Further, they considered the sand over the shoal areas to be actively reworked by currents and storms in the area, as evidenced by the general lack of fine-grained sediments in the sands, along with polished shell fragments. Active reworking of the sediments over the shoals was also supported by both the sediment sampling in the current study as well as the currents and turbidity noted (Chapters 2 and 6).

Surface-views of the substrate of the benthic grabs indicated a higher proportion of larger-sized biogenic particles from primarily mollusk-shell fragments, which increased the complexity of the substrate

compared to the sand observed in the majority of the cores from the benthic grabs. There were some technical difficulties in assigning substrate categories to surface-view photographs. Although some Coarse Shell Hash had larger shells and shell fragments that corresponded to Shell Rubble (particles > 64 mm, Table 4-2), the median size of the shells/shell fragments were < 64 mm, and therefore the overall surface view of the grab was assigned to Coarse Shell Hash. Shell Rubble, even in low quantities, has a large enough size that it may be important to larval and juvenile fishes as a refuge from predation (Gotceitas and Brown 1993). Another technical difficulty was the inability to distinguish biogenic (shell) sand from geologic sand at particle sizes < 0.5 mm without physically sampling the surface (e.g., identify the presence or absence of shell particles using a microscope). However, from the comparative spatial maps, it would appear that the complexity observed in the biogenic substrate of the surface-view photographs occurred in much larger particle sizes (Coarse Shell Hash, Medium Shell Hash, and Coarse Shell Sand) that were not observed in large proportions in the benthic grab cores.

Both methods of classifying the substrate have advantages and disadvantages and should be interpreted relative to habitats important to various trophic levels. For example, many infaunal invertebrates prefer specific sediment grain sizes, whereas other invertebrates need structure for attachment (e.g., hydroids) and therefore benefit from increased complexity of the substrate (e.g., presence of shells and shell fragments). Associations of invertebrates, in particular, with specific substrate types would also be important to fishes that use invertebrates as a prey resource.

In this study, changes to the sediment particle size and classification were not assessed relative to specific dredging events. However, it was noteworthy that sediment on CSII-BA, the dredged shoal, was primarily medium to coarse sand with low amounts of fine particles < 0.0625 mm and low organic content, similar to the non-dredged shoals (CSII, Chester, and Bull Shoals). This similarity could be ascribed to repeated dredging of CSII-BA having no surficial effect on the sediments of CSII-BA, or that the dynamic nature of the currents and storms of the area continually rework the sediments and any impacts due to dredging are short-lived.

4.5 Acknowledgments

4.6 References

Auster PJ, Malatesta RJ, LaRosa SC, Cooper RA, Stewart LL. 1991. Microhabitat utilization by the megafaunal assemblage at a low relief outer continental shelf Site - Middle Atlantic Bight, USA. Journal of Northwest Atlantic Fishery Science 11: 59-69. doi:10.2960/j.v11.a7.

Diaz RJ, Cutter GR, Able KW. 2003. The importance of physical and biogenic structure to juvenile fishes on the shallow inner continental shelf. Estuaries 26(1): 12-20. doi:10.1007/BF02691689.

FGDC (Federal Geographic Data Committee). 2012. Coastal and marine ecological classification standard. Washington, DC: Report No.: FGDC-STD-018-2012.

Field M, Duane D. 1974. Geomorphology and sediments of the inner continental shelf, Cape Canaveral, Florida. Fort Belvoir, Virginia: U.S. Army, Corps of Engineers, Coastal Engineering Research Center. Technical Memorandum 42.

Folk RL. 1954. The distinction between grain size and mineral composition in sedimentary-rock nomenclature. The Journal of Geology 62(4): 344-359.

Gotceitas V, Brown JA. 1993. Substrate selection by juvenile Atlantic cod (*Gadus morhua*): effects of predation risk. Oecologia 93(1): 31-37. doi:10.1007/BF00321187.

Houde ED. 1997. Patterns and consequences of selective processes in teleost early life histories. In: Chambers RC, Trippel EA, editors. Early Life History and Recruitment in Fish Populations. Dordrecht: Springer Netherlands. p. 173-196. doi.org/10.1007/978-94-009-1439-1_6.

O'Kelly B. 2005. Oven-Drying Characteristics of Soils of Different Origins. Drying Technology 23: 1141-1149. doi:10.1081/DRT-200059149.

SAFMC (South Atlantic Fisheries Management Council). 2011. Comprehensive ecosystem-based amendment 2 for the South Atlantic region. South Atlantic Fisheries Management Council, North Charleston, SC. 178 pp.

SFA (Sustainable Fisheries Act). 1996. Amendment of Magnuson Fishery Conservation and Management Act (16 U.S.c. 1801 et seq.). Public Law 104-297, 104th Congress.
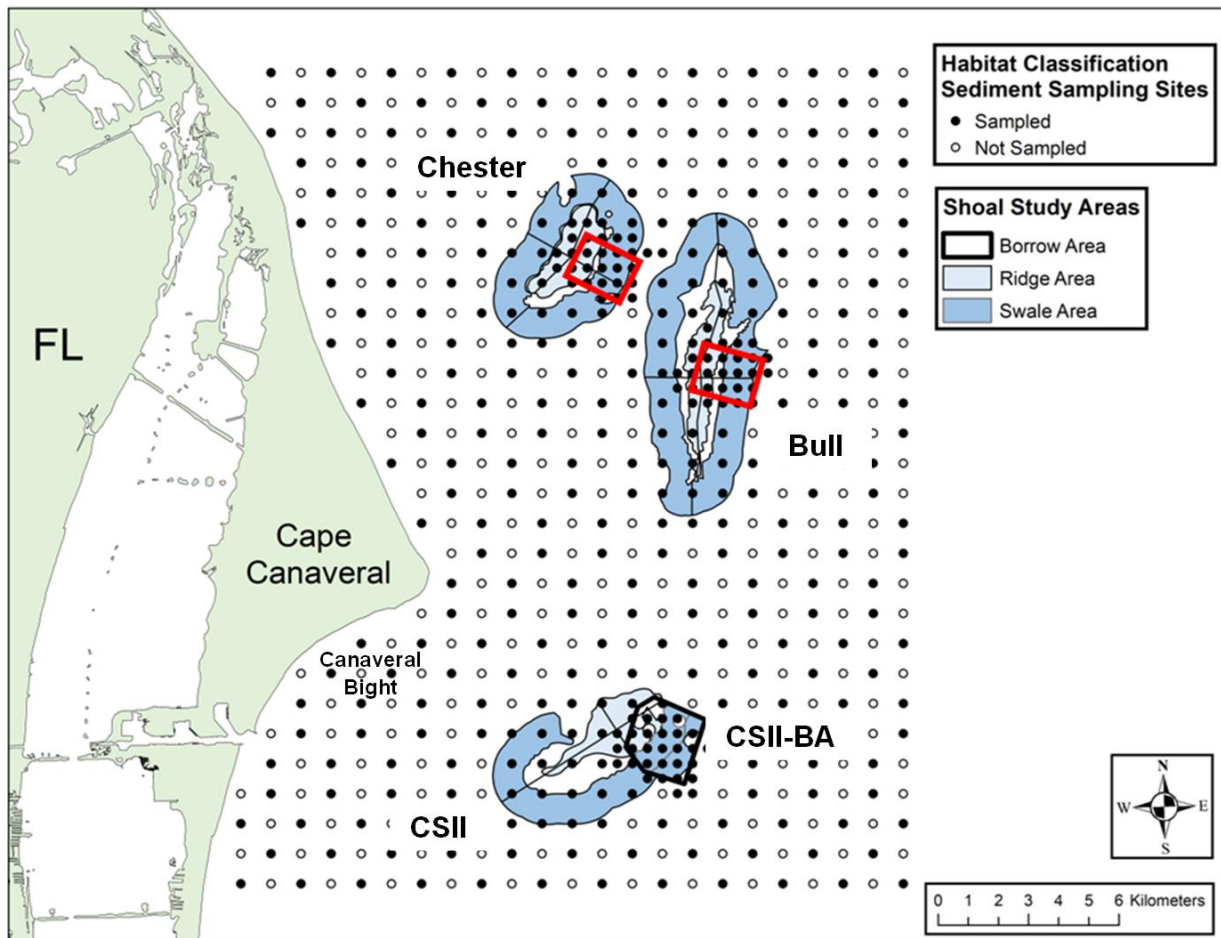
Figure 4-1. Sampling grid for benthic grabs overlain on all three study shoals and surrounding area.
Sampling sites on the study shoals were every 1 km, with areas that were surveyed using multibeam hydroacoustics (see Chapter 3) sampled every 0.5 km, including the potential dredge area (black outline) and comparable areas on Chester and Bull Shoals (red outlines); all other areas surrounding the shoals were sampled every 2 km.
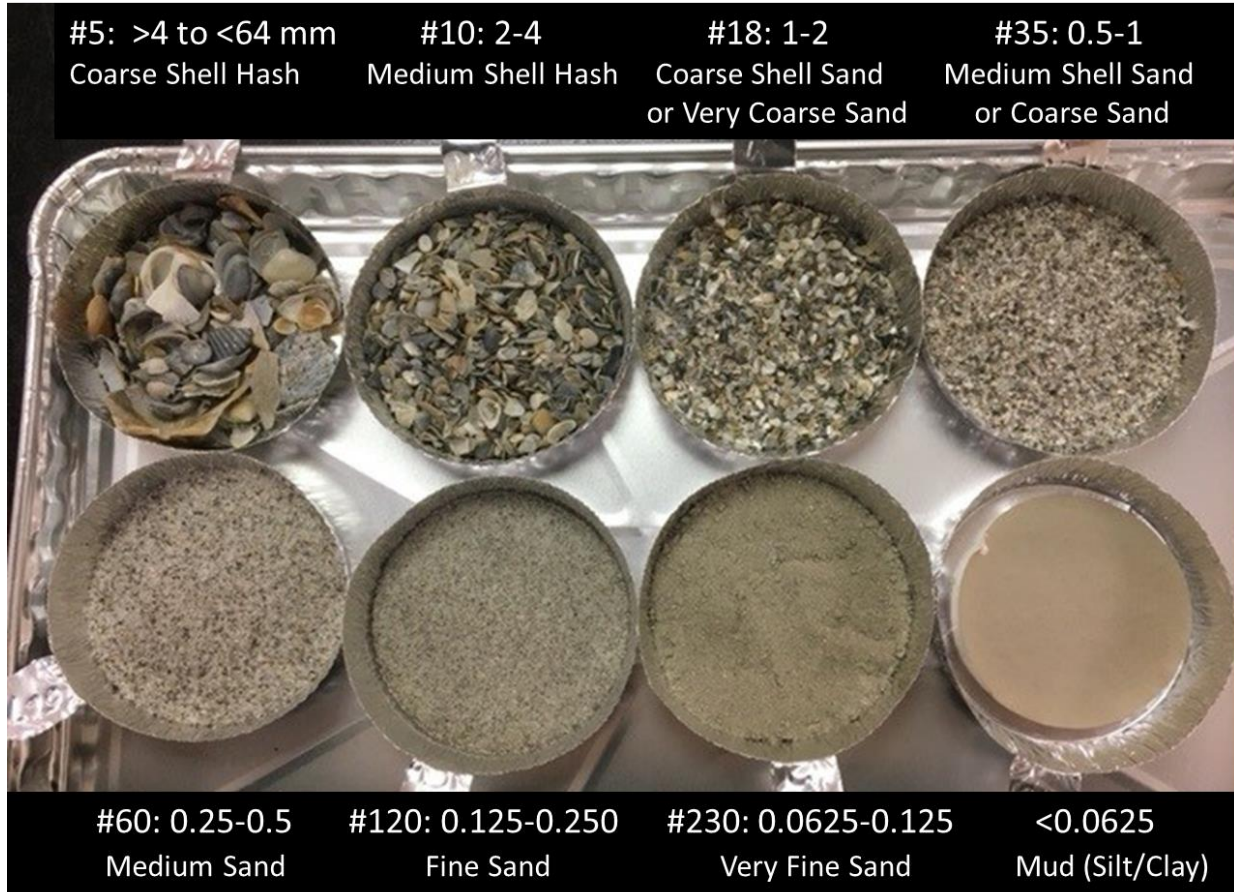
Figure 4-2. Example of a sieve series giving geologic and biogenic classification of sediments based on substrate type and sediment size.

Labels indicate the sieve number, range of particle sizes (mm), and a brief descriptor of the sediment type. Geologic sediments were classified based on CMECS, which uses a modified Folk (1954) ternary diagram of Gravel-Sand-Mud (FGDC 2012). Biogenic components were classified using CMECS based on shell substrate (shells and shell fragments) (FGDC 2012). Photo: D. Murie.
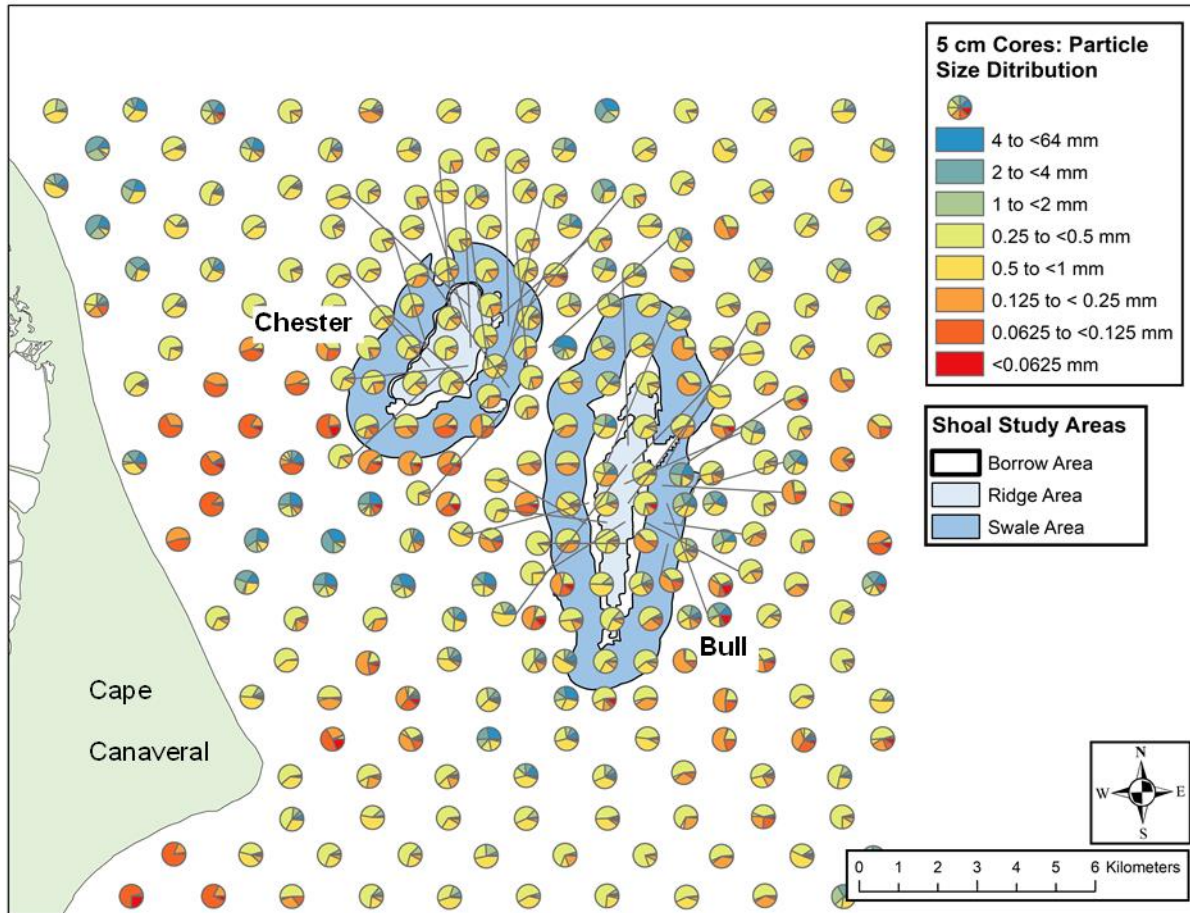
Figure 4-3. Northern region of sampling frame showing particle size distribution on Chester and Bull Shoals and surrounding area.

Each benthic grab was represented by a pie diagram based on the % of particles by size based on dry weight. Sediment samples were characterized using the CMECS, which is based on a modified Wentworth scale for particle size (FGDC 2012).
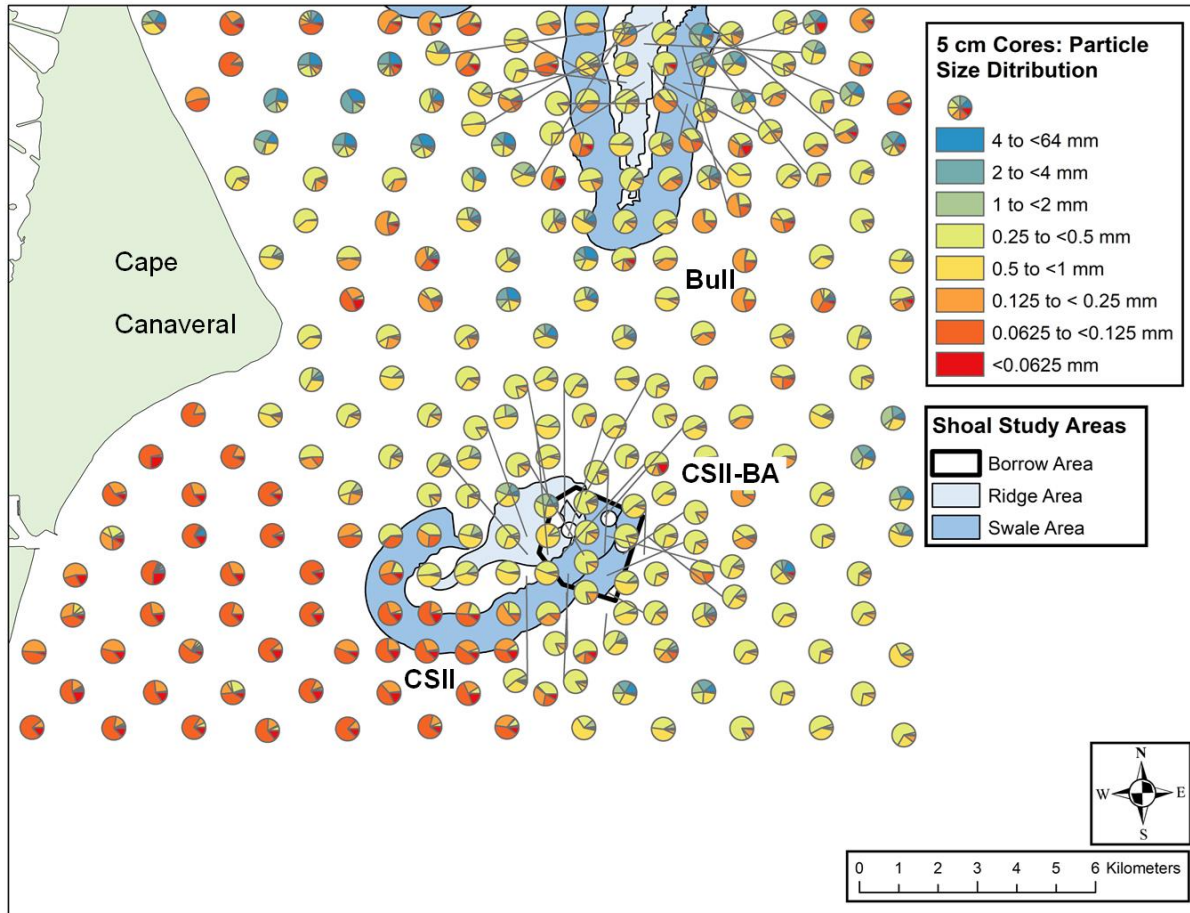
Figure 4-4. Southern region of sampling frame showing particle size distribution on CSII and CSII-BA (dredged area, as outlined in the northeastern quadrant of CSII) and surrounding area.
Each benthic grab was represented by a pie diagram based on the % of particles by size based on dry weight. Sediment samples were characterized using the CMECS, which is based on a modified Wentworth scale for particle size (FGDC 2012).
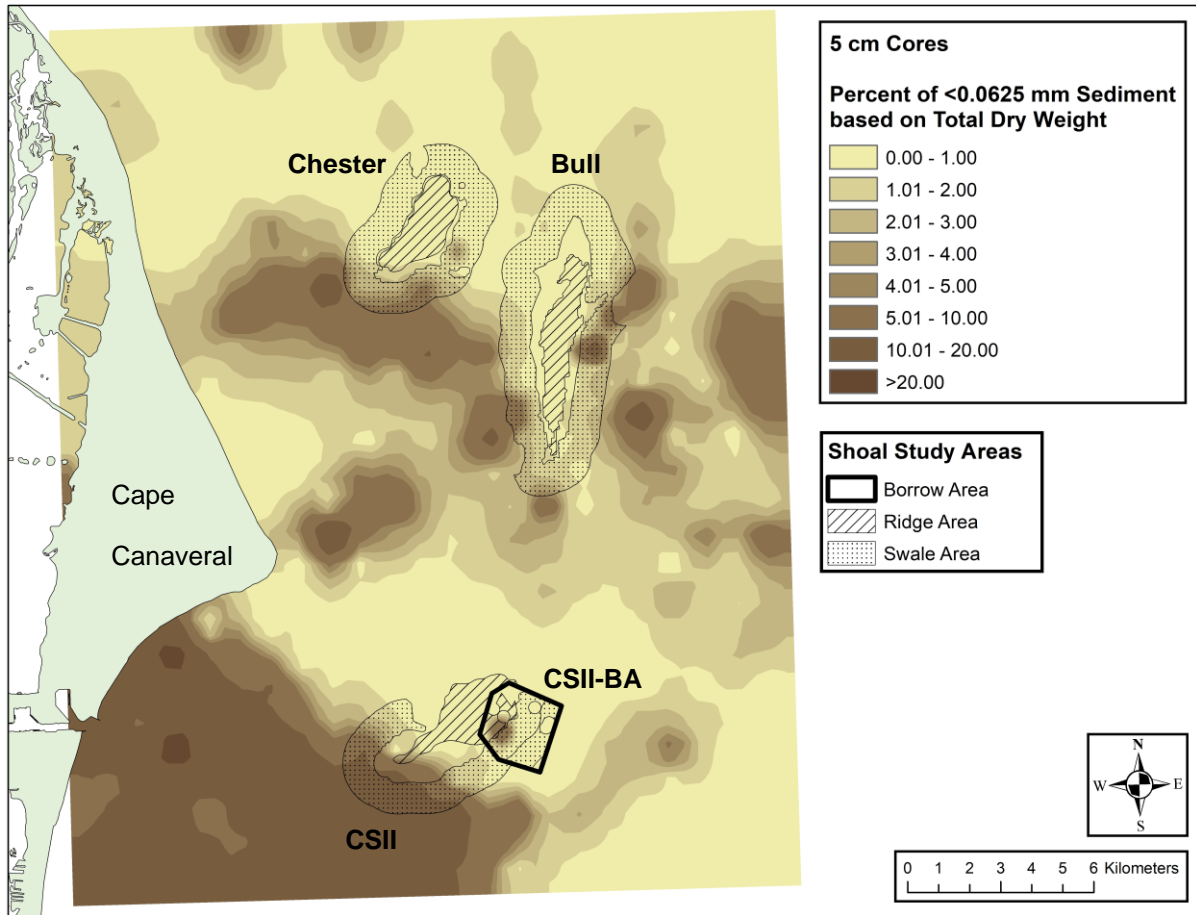
Figure 4-5. Interpolated distribution of Mud (silt/clay) (particles < 0.0625 mm) over the shoals and surrounding area.

Percentage of Mud was based on % dry weight. Sediment samples were characterized using the CMECS, which is based on a modified Wentworth scale for particle size (FGDC 2012).
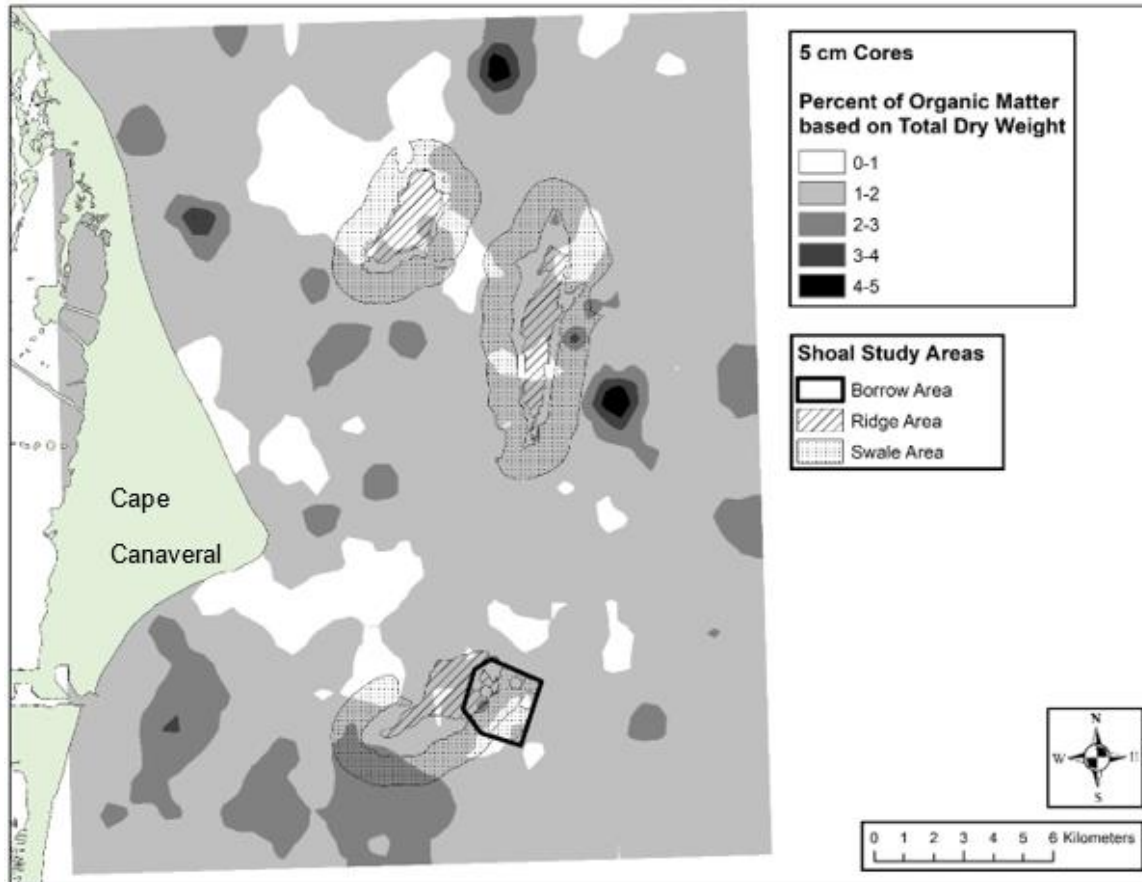
Figure 4-6. Interpolated distribution of % organic matter over the shoals and surrounding area.
Percentage of organic matter was based on % dry weight.
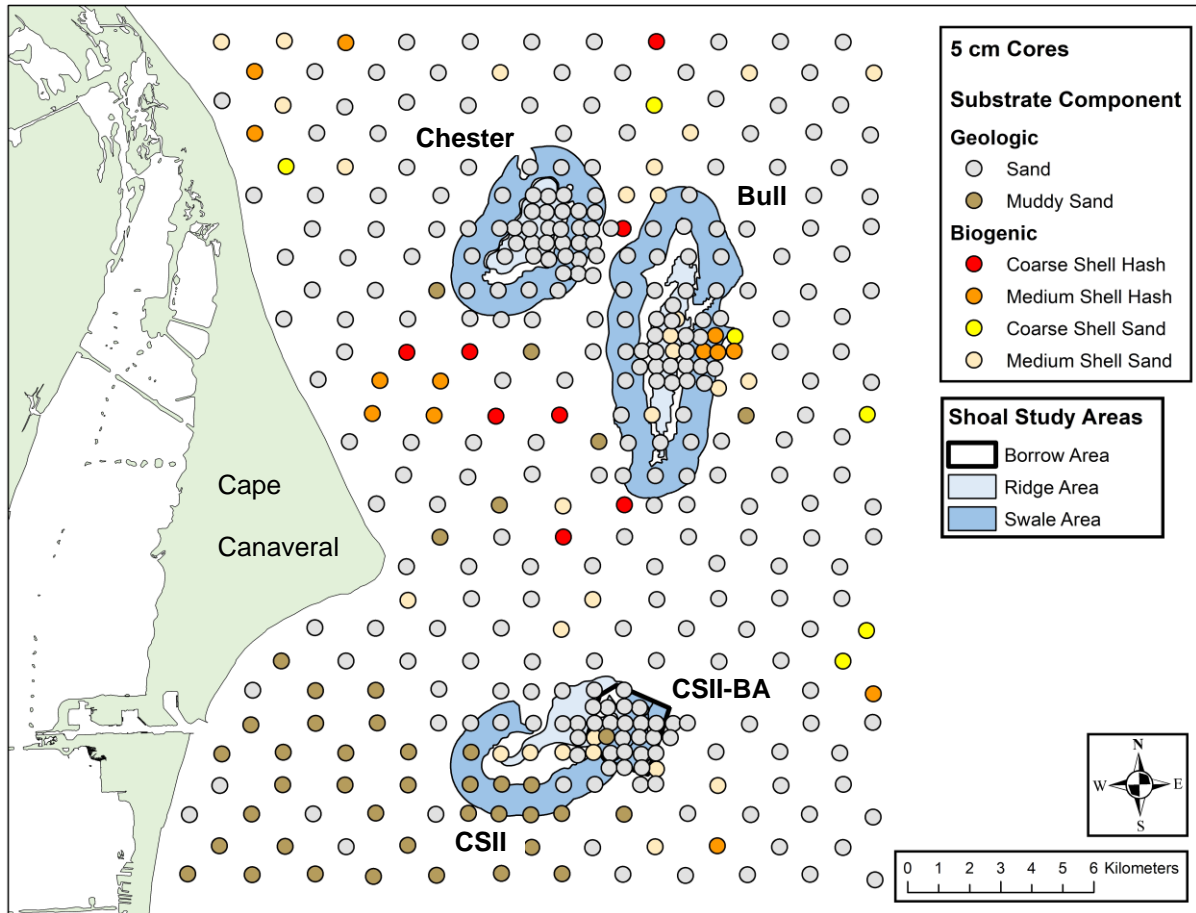
Figure 4-7. Spatial map of the study area with classification of benthic grab cores based on % dry weight.
Geologic sediments were classified based on CMECS, which uses a modified Folk (1954) ternary diagram of Gravel-Sand-Mud (FGDC 2012). Biogenic components were classified using CMECS based on shell substrate (shells and shell fragments) (FGDC 2012).
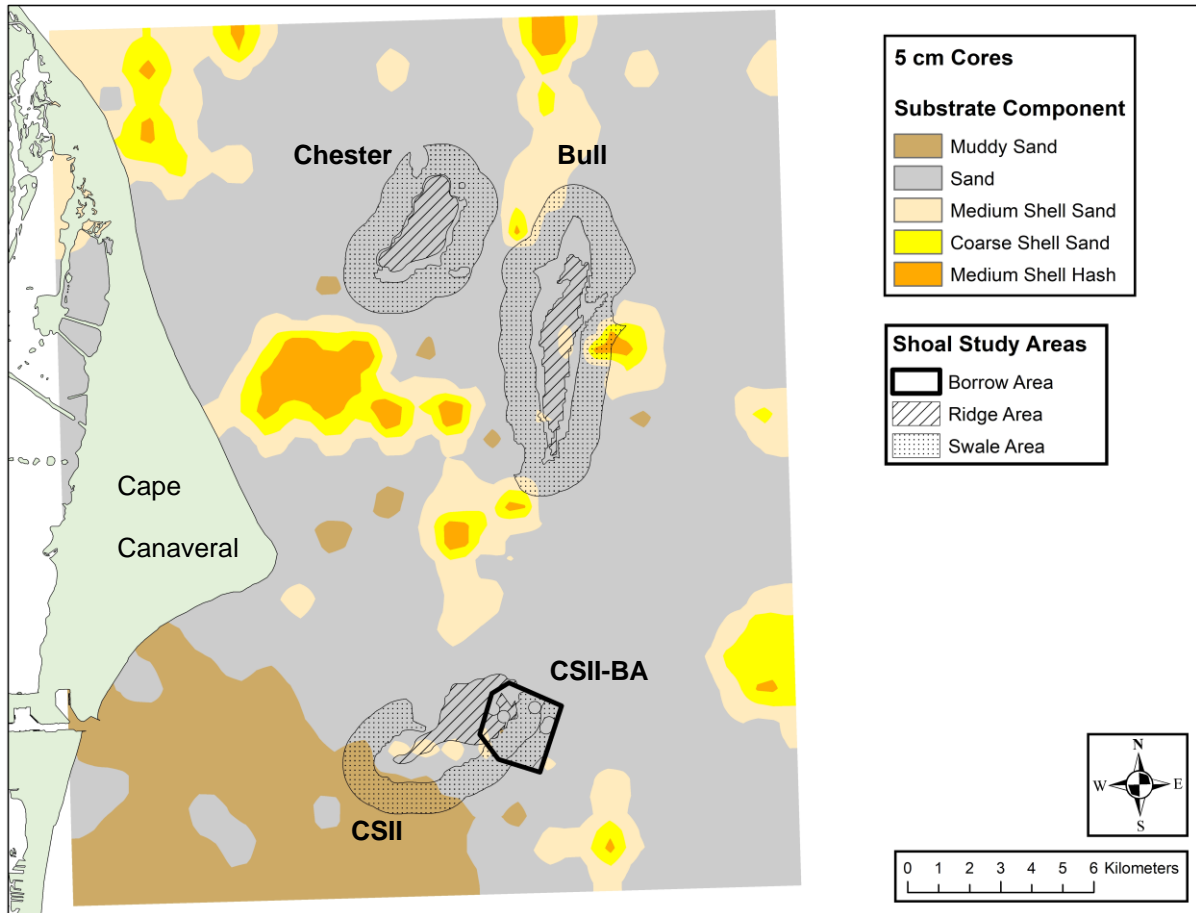
Figure 4-8. Spatial map of the study area with interpolated classification based on the benthic grab cores as % dry weight.

Geologic sediments were classified based on CMECS, which uses a modified Folk (1954) ternary diagram of Gravel-Sand-Mud (FGDC 2012). Biogenic components were classified using CMECS based on shell substrate (shells and shell fragments) (FGDC 2012).
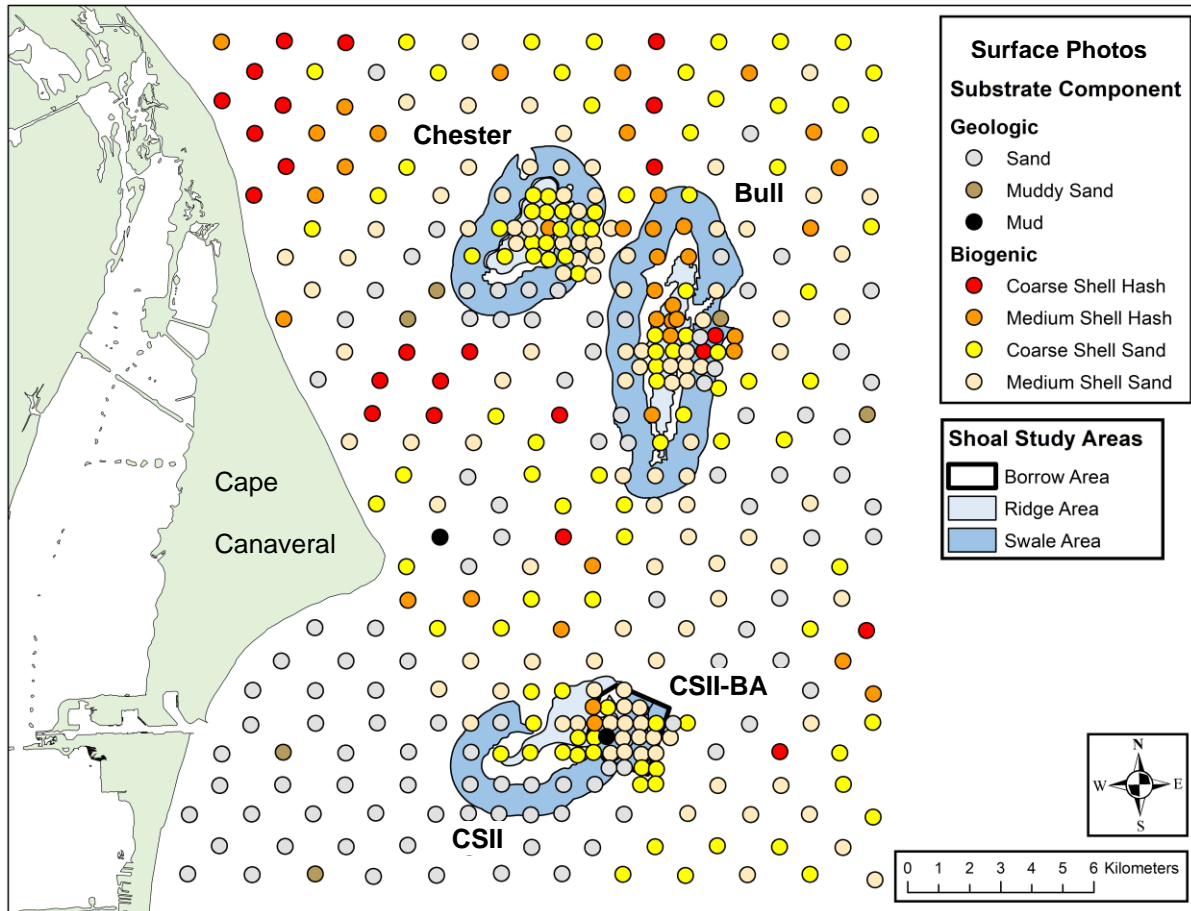
Figure 4-9. Spatial map of the study area with classification based on the surface view of the benthic grabs based on % surface area.

Geologic sediments were classified based on CMECS, which uses a modified Folk (1954) ternary diagram of Gravel-Sand-Mud (FGDC 2012). Biogenic components were classified using CMECS based on shell substrate (shells and shell fragments) (FGDC 2012).
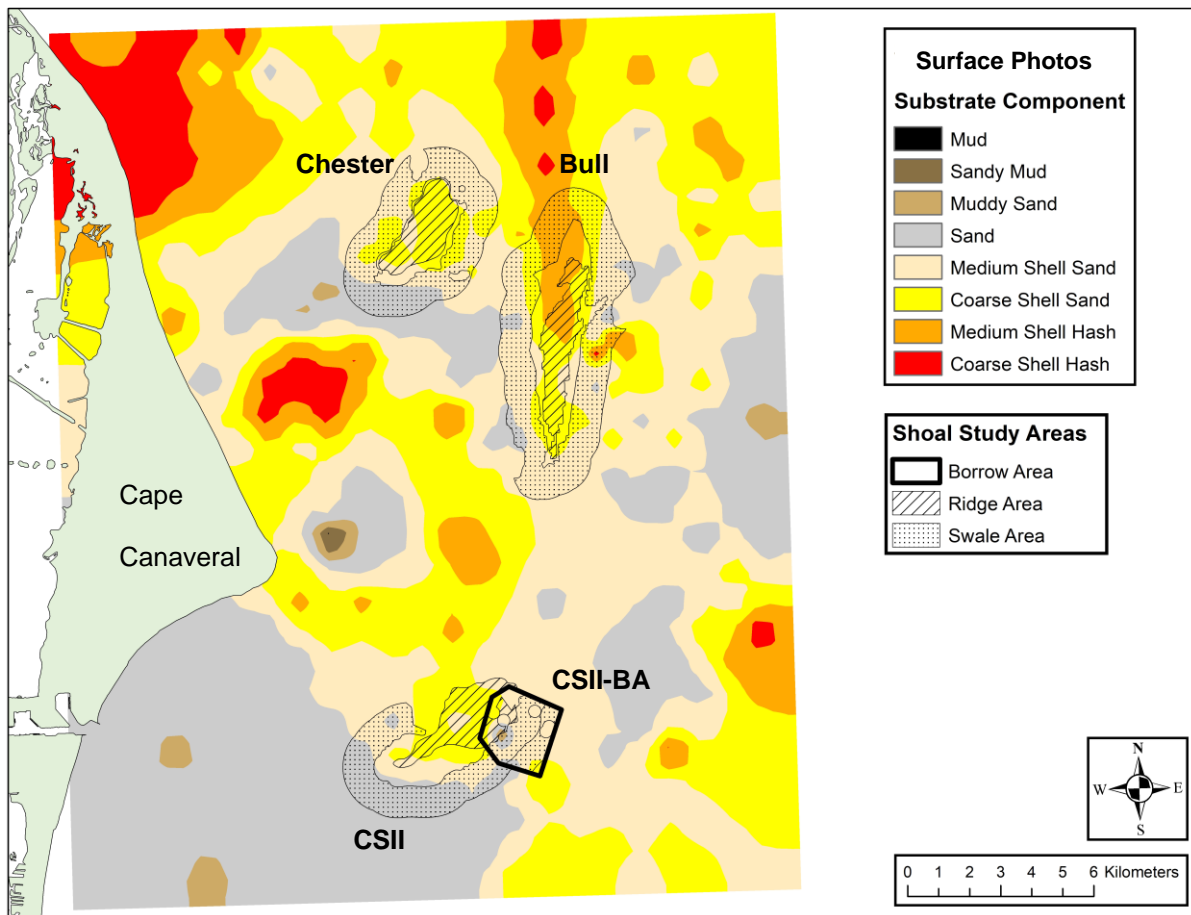
Figure 4-10. Spatial map of the study area with interpolated classification based on the surface view of benthic grabs by % surface area.

Geologic sediments were classified based on CMECS, which uses a modified Folk (1954) ternary diagram of Gravel-Sand-Mud (FGDC 2012). Biogenic components were classified using CMECS based on shell substrate (shells and shell fragments) (FGDC 2012).

Table 4-1. Standard sieve series used in benthic grab processing and associated CMECS geologic substrate classification with grain size based on modified Wentworth ([FGDC 2012](#)).

CMECS Descriptor	CMECS Grain Size (mm)	US Sieve #
Gravel[a]	2 to < 4,096	10 and above
Boulder	256 to < 4,096	above 5
Cobble	64 to < 256	above 5
Pebble	4 to < 64	5
Granule	2 to < 4	10
Sand	0.0625 to < 2	230 to 18
Very Coarse Sand	1 to < 2	18
Coarse Sand	0.5 to < 1	35
Medium Sand	0.25 to < 0.5	60
Fine Sand	0.125 to < 0.25	120
Very Fine Sand	0.0625 to < 0.125	230
Mud/Silt/Clay	< 0.0625	below 230
Mud	< 0.0625	below 230
Silt	0.004 to < 0.0625	below 230
Clay	< 0.004	below 230

[a] In CMECS, gravel is all rock particles > 2 mm or larger.
[b] In CMECS, mud is all particles smaller than sand (< 0.0625 mm).

Table 4-2. Standard sieve series used in benthic grab processing and associated CMECS biogenic substrate classification with grain size (FGDC 2012).

CMECS Descriptor	Grain Size (mm)	US Sieve #
Shell Rubble	64 to < 4,096	above 5
Shell Hash[a]	2 to < 64	5, 10
Coarse Shell Hash	4 to < 64	5
Medium Shell Hash	2 to < 4	10
Shell Sand[b]	0.0625 to < 2	230 to 18
Coarse Shell Sand	1 to < 2	18
Medium Shell Sand	0.5 to < 1	35
Sand[c]	0.0625 to 0.5	60, 120, 230
Mud (Silt/Clay)[d]	< 0.0625	below 230

[a] Shell Hash was further subdivided in the present study into recognizable Coarse versus Medium Shell Hash.
[b] Shell Sand was further subdivided in the present study into recognizable Coarse versus Medium Shell Sand.
[c] Composition of Sand particles of median size > 0.0625 to 0.5 mm was unknown and was assumed to be of geologic origin, as per FGDC (2012).
[d] Composition of particles of median size < 0.0625 mm was unknown and was assumed to be of geologic origin, as per FGDC (2012).

5 Using Satellite Imagery to Assess Large-scale Variation in Phytoplankton Productivity Relative to a Sand Dredging Event

Michael Dickson and Debra Murie

> **Key Points**
> - Chlorophyll *a* concentration, as a proxy for surface phytoplankton productivity, varied widely on CSII-BA, CSII, Chester, and Bull Shoals, and in the surrounding area, during pre-dredge and post-dredge periods and encompassed a range of higher chlorophyll *a* levels than those observed during active dredging.
> - Dredging activities on CSII-BA in December 2013 to March 2014 did not result in an increase in primary productivity in the surface waters of CSII-BA or any of the study shoals overall.

5.1 Introduction

Dredging sand borrow areas can result in changes in water quality parameters with one of the primary concerns being an increase in the suspended solids from the draghead action or over-wash (Michel et al. 2013). This increase in suspended particles can lead to a decrease in phytoplankton productivity due to light limitation (Su et al. 2015) and sedimentation of nearby habitats such as reefs (Michel et al. 2013), as well as cause physiological and behavioral changes in fishes (Wenger et al. 2017). Other important water quality impacts include a reduction of dissolved oxygen in the water column and at the water-sediment interface, especially if the dredging activity creates deep pits with reduced water circulation (Michel et al. 2013). Dredging, however, can also resuspend nutrients from the sediment (Su et al. 2015; Chen et al. 2020) or increase organic content in the water due to maceration of entrained invertebrates (Newell et al. 1999). Resuspension of nutrients, in contrast to increasing turbidity, can increase phytoplankton productivity (Su et al. 2015), whether the resuspension occurs due to naturally occurring tidal and current fluxes or through human-induced perturbations such as dredging activities.

From 27 November 2013 to 22 April 2014, the borrow area of Canaveral Shoal II (CSII-BA) (Figure 5-1) was dredged to supply sand for beach renourishment to offset the storm damage from Hurricane Sandy in 2012. To assess whether dredging activity on CSII-BA resuspended nutrients into the water column and increased phytoplankton productivity, we used satellite ocean-color images of chlorophyll *a* concentration to track phytoplankton productivity. The use of the spectral properties of chlorophyll *a* in satellite imagery as a proxy for phytoplankton biomass has been well established (Huot et al. 2007; Boyer et al. 2009). Specifically, our objectives were to visually compare averaged monthly satellite chlorophyll *a* images of the dredged shoal (CSII-BA) relative to non-dredged reference shoals (CSII, Chester, and Bull Shoals) in the months prior to, during, and after dredging of CSII-BA.

5.2 Methods

The study shoals were located off Cape Canaveral on the east coast of Florida (Figure 5-1) and included CSII-BA, the non-dredged portion of Canaveral Shoal (referred to as CSII), Chester Shoal, and Bull Shoal. Canaveral and Chester Shoals are approximately 5-15 m in depth, and Bull Shoal ranges from 7-20 m. Each shoal has shallower ridge and deeper swale habitats. CSII-BA has been dredged multiple times (Table 1-1). Each pixel value was derived from sensor-specific spectral reflectance algorithms and represented the mean daily chlorophyll *a* concentration for the square kilometer. In this study, pre-

processing of the image products was first performed using SEAWIFS Data Analysis System (SeaDAS) 7 and involved removing low quality images with extreme cloud cover. The images with minimal cloud interference were then exported to ArcGIS 10.3 and superimposed on an Environmental Systems Research Institute (ESRI) shapefile of the shoals. A second filter pass eliminated those images where chlorophyll estimations were not available for any portion of any shoal. Chlorophyll values from the final viable images were extracted from the pixels within the shoal and dredge area footprints and averaged over monthly time frames from October to March, including 1) a pre-dredge period of October 2012 to March 2013; 2) a pre-dredge period of October–November 2013 transitioning into the active dredging period of December 2013 to March 2014; and 3) a post-dredge period of October 2014 to March 2015.

5.3 Results

Chlorophyll *a* concentration, as a proxy for surface phytoplankton productivity, varied widely on the study shoals and in the surrounding area irrespective of dredging activity (Figures 5-2, 5-3, 5-4). Most notably, surface phytoplankton concentration was higher during October through December in both the pre-dredge time period during October–December 2012 (Figure 5-2) and in the time period encompassing the transition from pre- to active dredging in October–December 2013 (Figure 5-3). Following December, the chlorophyll *a* concentration in the coastal waters over all the shoals decreased. Higher surface phytoplankton concentrations were also observed in the post-dredge months of October–December 2014, but continued to increase into January–March 2015 (Figure 5-4).

During the pre-dredge period from October 2012 to March 2013, the chlorophyll *a* concentration directly over the study shoals remained below ~4 mg/m^3 (Figure 5-2), whereas isolated areas in the nearshore waters northwest of Chester Shoal reached levels of ~9 mg/m^3. This same area of Chester Shoal also had high chlorophyll *a* concentration in the months of October 2013 and November 2013 immediately prior to the start of dredging, with some isolated areas exceeding ~15 mg/m^3 (Figure 5-3). During active dredging in December 2013 and January–March 2014, chlorophyll *a* concentration on the shoals, and CSII-BA specifically, was < 4 mg/m^3 (Figure 5-3). Chlorophyll *a* concentration over all the shoals (including both the dredged and reference shoals) and surrounding waters during a post-dredge period of October 2014 to March 2015, approximately 1 year following the start of dredging in 2013, were relatively high (~6–12 mg/m^3) along the nearshore coastal waters, especially northwest of Chester Shoal (Figure 5-4).

5.4 Discussion

If nutrients were resuspended through dredging activities on CSII-BA in December 2013 to March 2014, it did not result in an increase in primary productivity in the area of CSII-BA or the study shoals overall. Furthermore, the natural variability observed in chlorophyll *a* concentrations in pre-dredge and post-dredge periods was high and encompassed a range of higher chlorophyll *a* levels than those observed during active dredging. Overall, the chlorophyll *a* concentration over the shoal areas observed via satellite imagery was consistent with results from direct phytoplankton sampling which ranged from 1 mg/m^3 to 5 mg/m^3 (Chapter 7) (Tate et al. 2020).

Periodic, rapid, and large increases in phytoplankton or "blooms" were also observed via satellite imagery in waters inshore of the study shoals, in particular northwest of Chester Shoal. Tate et al. (2020) coincidentally sampled a bloom of primarily *Trichodesmium,* a cyanobacterium, as well as a mix of dinoflagellates in fall 2013 (October) in the pre-dredge period that had chlorophyll levels of ~15 mg/m^3. Similarly, surface slicks of most likely *Trichodesmium* were also physically observed in the study area outside of the dredging timeline (e.g., November 2015, Figure 5-5).

5.5 References

Boyer J, Kelble C, Ortner P, Rudnick D. 2009. Phytoplankton bloom status: Chlorophyll a biomass as an indicator of water quality condition in the southern estuaries of Florida, USA. Ecological Indicators 9: S56-S67. doi:10.1016/j.ecolind.2008.11.013.

Chen C, Kong M, Wang YY, Shen QS, Zhong JC, Fan CX. 2020. Dredging method effects on sediment resuspension and nutrient release across the sediment-water interface in Lake Taihu, China. Environmental Science and Pollution Research 27(21): 25861-25869. doi:10.1007/s11356-019-06192-w.

FGDC (Federal Geographic Data Committee). 2012. Coastal and marine ecological classification standard. Washington, DC: Report No.: FGDC-STD-018-2012.

Folk RL. 1954. The distinction between grain size and mineral composition in sedimentary-rock nomenclature. The Journal of Geology 62(4): 344-359.

Huot Y, Babin M, Bruyant F, Grob C, Twardowski MS, Claustre H. 2007. Relationship between photosynthetic parameters and different proxies of phytoplankton biomass in the subtropical ocean. Biogeosciences 4(5): 853-868. doi:10.5194/bg-4-853-2007.

Michel J, Bejarano A, Peterson C, Voss C. 2013. Review of biological and biophysical impacts from dredging and handling of offshore sand. Herndon, VA: U.S. Department of the Interior, Bureau of Ocean Energy Management. OCS Study BOEM 2013-0119. 258 pp.

Newell RC, Hitchcock DR, Seiderer LJ. 1999. Organic enrichment associated with outwash from marine aggregates dredging: A probable explanation for surface sheens and enhanced benthic production in the vicinity of dredging operations. Marine Pollution Bulletin 38(9): 809-818. doi.org/10.1016/S0025-326X(99)00045-4.

Su J, Tian T, Krasemann H, Schartau M, Wirtz K. 2015. Response patterns of phytoplankton growth to variations in resuspension in the German Bight revealed by daily MERIS data in 2003 and 2004. Oceanologia 57(4): 328-341. doi.org/10.1016/j.oceano.2015.06.001.

Tate MC, Phlips EJ, Stelling B, Badylak S, Landauer L, West-Valle A, Murie D. 2020. Phytoplankton composition in the subtropical coastal shelf environment of Cape Canaveral, Florida. Bulletin of Marine Science 96(4): 593-616. doi:10.5343/bms.2019.0079.

Wenger AS, Harvey E, Wilson S, Rawson C, Newman SJ, Clarke D, Saunders BJ, Browne N, Travers MJ, Mcilwain JL, Erftemeijer PLA, Hobbs J-PA, Mclean D, Depczynski M, Evans RD. 2017. A critical analysis of the direct effects of dredging on fish. Fish and Fisheries 18(5): 967-985. doi.org/10.1111/faf.12218.
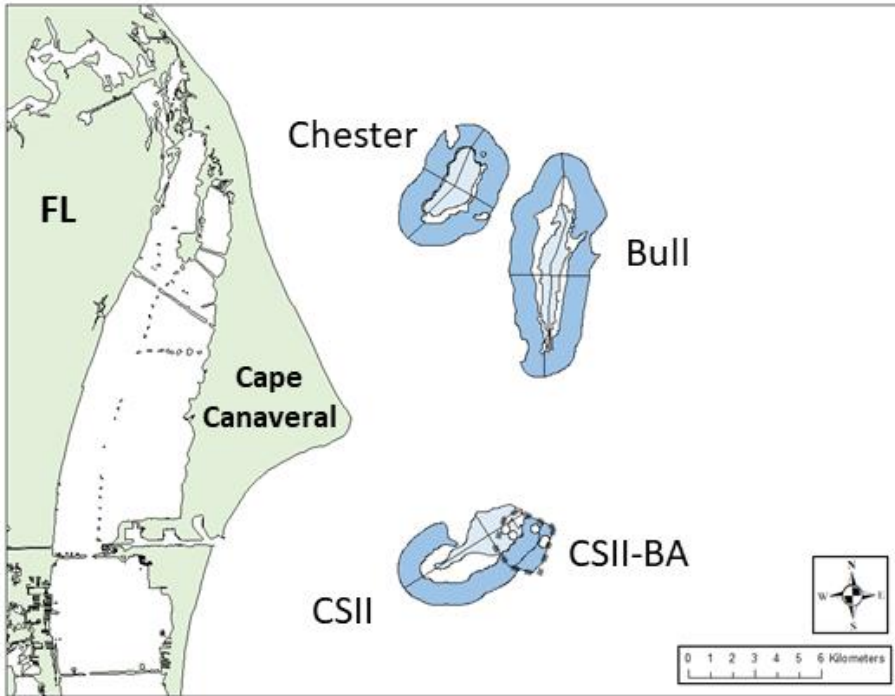
Figure 5-1. Study shoals offshore of Cape Canaveral on the east coast of Florida.
Ridge habitat (light blue) and swale habitat (dark blue) is shown for each shoal, with CSII-BA outlined in dashed line.
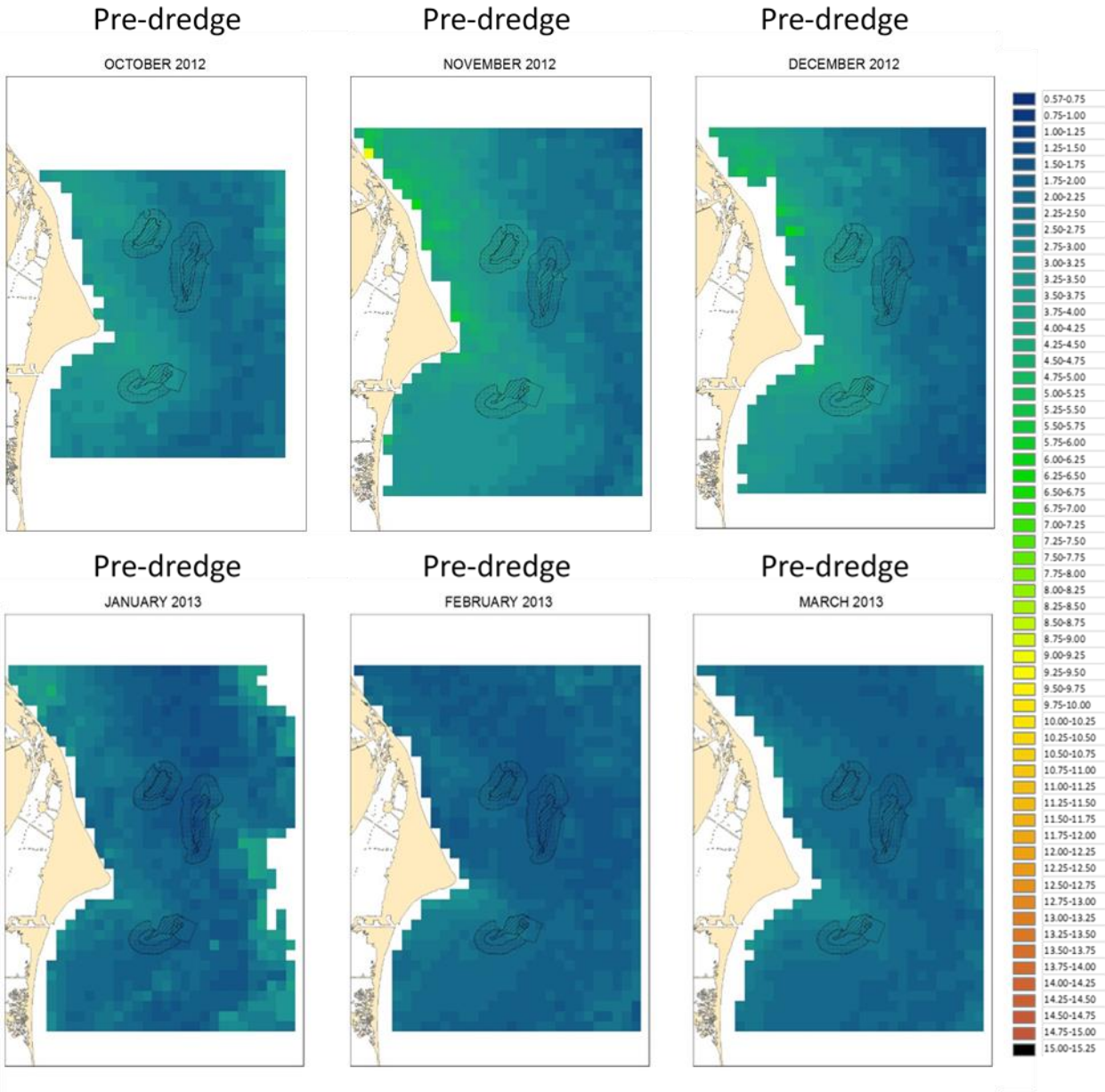
Figure 5-2. Surface chlorophyll *a* concentration over study shoals and surrounding area during a pre-dredge period from October 2012 to March 2013.
Shoals are outlined in black.
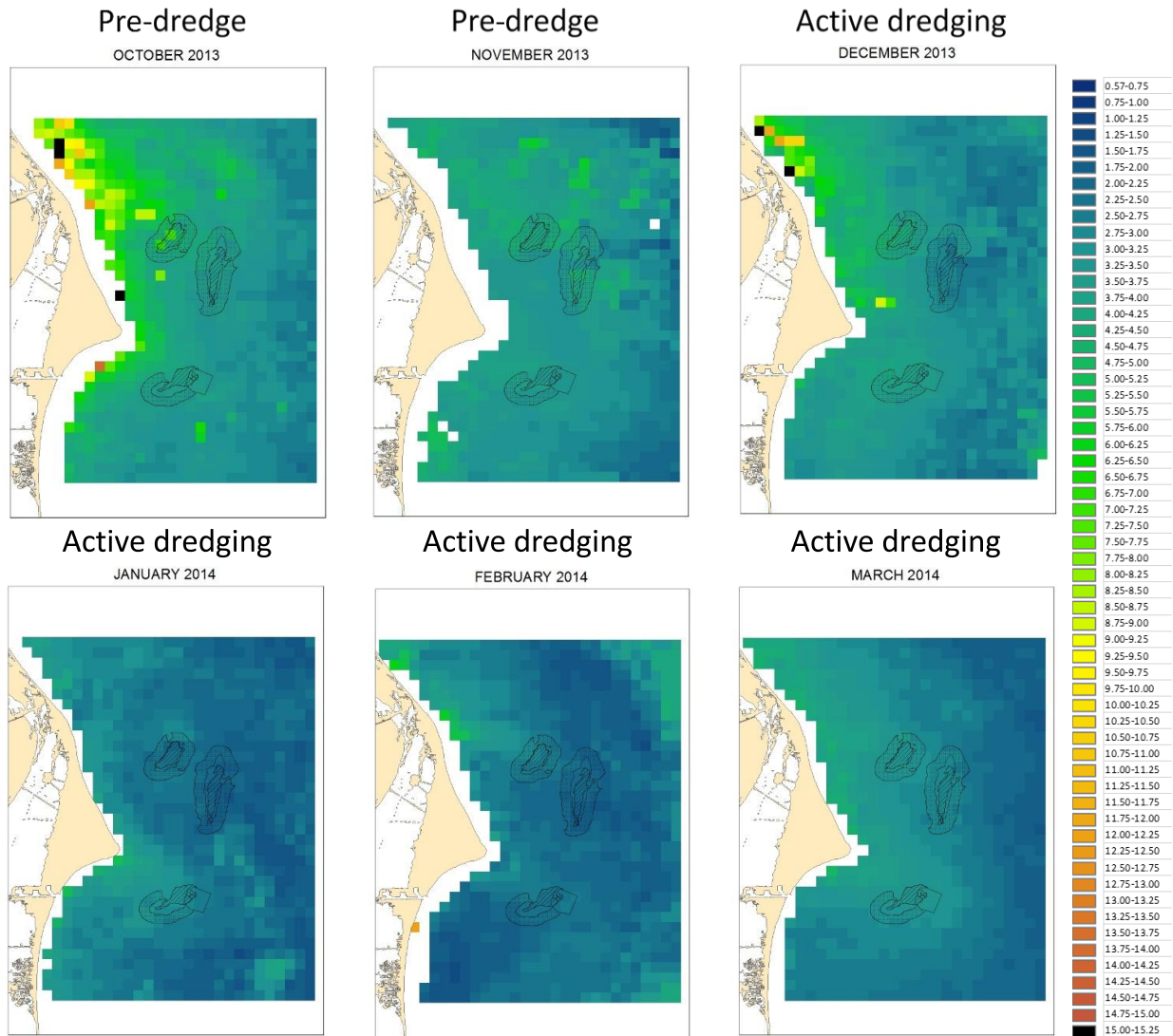
Figure 5-3. Surface chlorophyll *a* concentration over the study shoals and surrounding area during a pre-dredge period in October 2013 and November 2013 immediately before dredging started on 27th November 2013 and throughout the spring of 2014.
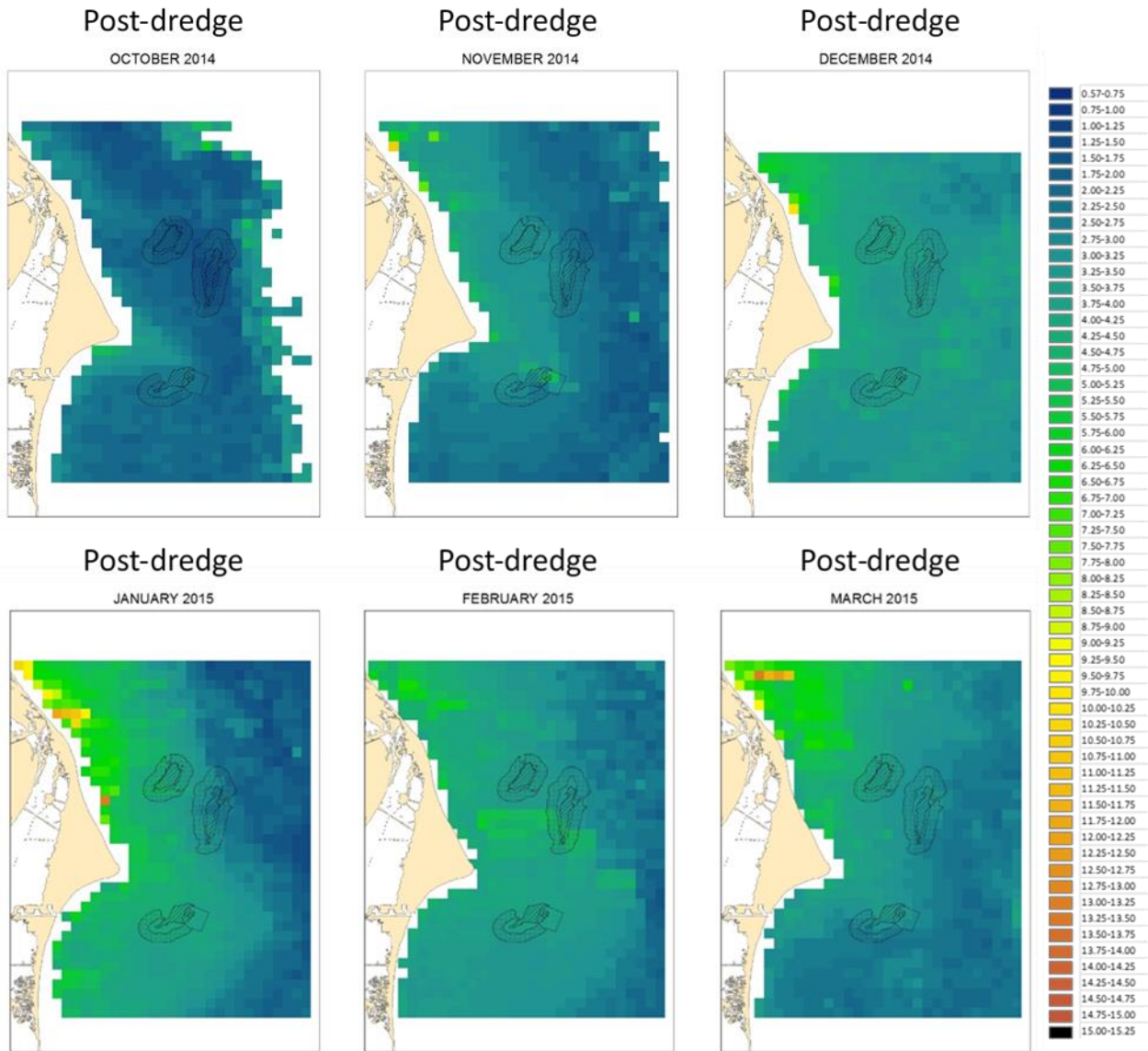
Figure 5-4. Surface chlorophyll *a* concentration over the study shoals and surrounding area during a post-dredge period (approximately 1 year later), October 2014 through March 2015.

Figure 5-5. Surface bloom observed on 3 November 2015 in the shoal study area, most probably the cyanobacterium *Trichodesmium*, locally known as "sea sawdust."
Photo Credit: University of Florida (B. Gillett).

Appendix A: Deployment of ADCP Instruments

Table A-1. List of moored ADCP deployments during the study with season and year of deployment, location of deployment, instrument type used, upward- or downward-facing deployment, and start and end date of deployment.

| Season-Year	Deployment #	Location	Instrument	Upward or Downward	Date Start	Date End
Fall 2013	1	Shoal E Swale West (=CSII-BA)	Aquadopp	Upward	23-Sep-2013	3-Dec-2013
Fall 2013	1	Shoal E Swale East	AWAC	Upward	23-Sep-2013	3-Dec-2013
Fall 2013	1	Chester Swale West	RDI Workhorse	Upward	23-Sep-2013	15-Nov-2015
Spring 2014	2	Shoal E Swale West (=CSII-BA)	Aquadopp	Upward	6-May-2014	6-Jun-2014
Spring 2014	2	Shoal E Swale East	AWAC	Upward	6-May-2014	6-Jun-2014
Spring 2014	2	Chester Swale West	RDI Workhorse	Upward	6-May-2014	6-Jun-2014
Spring 2014	2	Chester Swale East	RDI Workhorse	Upward	6-May-2014	6-Jun-2014
Summer 2014	3	Ridge West (CSII-BA Ridge)	RDI Workhorse	Upward	29-Jul-2014	3-Sep-2014
Summer 2014	3	Ridge West (CSII-BA Ridge)	RDI Workhorse	Downward	29-Jul-2014	ND
Summer 2014	3	Chester Ridge (East)	RDI Workhorse	Upward	28-Jul-2014	3-Sep-2014
Summer 2014	3	Chester Ridge (East)	RDI Workhorse	Downward	28-Jul-2014	3-Sep-2014
Summer 2014	3	Bull Ridge (East)	Sentinel V	Upward	28-Jul-2014	3-Sep-2014
Summer 2014	3	Bull Ridge (East)	RDI Workhorse	Downward	28-Jul-2014	3-Sep-2014
Fall 2014	4	Shoal E Swale West (=CSII-BA)	Sentinel V	Upward	7-Oct-2014	13-Nov-2014
Fall 2014	4	Shoal E Swale West (=CSII-BA)	RDI Workhorse	Downward	7-Oct-2014	ND
Fall 2014	4	Shoal E Swale East	AWAC	Upward	8-Oct-2014	7-Jan-2015
Fall 2014	4	Chester Swale West	Aquadopp	Upward	8-Oct-2014	13-Nov-2014
Fall 2014	4	Chester Swale East	RDI Workhorse	Upward	8-Oct-2014	ND
Fall 2014	4	Bull Swale (East)	Sentinel V	Upward	7-Oct-2014	13-Nov-2014
Winter 2014—15	5	Shoal E Swale West (=CSII-BA)	RDI Workhorse	Upward	14-Dec-2014	23-Jan-2015
Winter 2014—15	5	Shoal E Swale West (=CSII-BA)	RDI Workhorse	Downward	14-Dec-2014	ND
Winter 2014—15	5	Shoal E Swale East	Aquadopp	Upward	14-Dec-2014	ND
Winter 2014—15	5	Chester Swale West	Aquadopp	Upward	14-Dec-2014	23-Jan-2015
Winter 2014—15	5	Chester Swale East	RDI Workhorse	Upward	14-Dec-2014	ND
Winter 2014—15	5	Chester Swale East	RDI Workhorse	Downward	14-Dec-2014	ND

Season-Year	Deployment #	Location	Instrument	Upward or Downward	Date Start	Date End
Winter 2014—15	5	Bull Swale (East)	Sentinel V	Upward	14-Dec-2014	19-Jan-2015
Winter 2014—15	5	Bull Swale (East)	RDI Workhorse	Downward	14-Dec-2014	ND
Spring 2015	6	Shoal E Swale West (=CSII-BA)	Sentinel V	Upward	24-Apr-2015	26-May-2015
Spring 2015	6	Shoal E Swale West (=CSII-BA)	Sentinel V	Downward	24-Apr-2015	ND
Spring 2015	6	Shoal E Swale East	Aquadopp	Upward	24-Apr-2015	ND
Spring 2015	6	Chester Swale West	AWAC	Upward	23-Apr-2015	3-Jun-2015
Spring 2015	6	Chester Swale East	Sentinel V	Upward	23-Apr-2015	26-May-2015
Summer 2015 A	7	Shoal E Swale West (=CSII-BA)	Sentinel V	Upward	9-Jul-2015	30-Jul-2015
Summer 2015 A	7	Shoal E Swale West (=CSII-BA)	RDI Workhorse	Downward	9-Jul-2015	30-Jul-2015
Summer 2015 A	7	Shoal E Swale East	Aquadopp	Upward	8-Jul-2015	30-Jul-2015
Summer 2015 A	7	Ridge West (CSII-BA Ridge)	Sentinel V	Upward	14-Jul-2015	30-Jul-2015
Summer 2015 A	7	Ridge West (CSII-BA Ridge)	RDI Workhorse	Downward	14-Jul-2015	30-Jul-2015
Summer 2015 A	7	Chester Swale West	AWAC	Upward	9-Jul-2015	30-Jul-2015
Summer 2015 A	7	Chester Swale East	Sentinel V	Upward	9-Jul-2015	30-Jul-2015
Summer 2015 A	7	Chester Swale East	RDI Workhorse	Downward	9-Jul-2015	20-Jul-2015
Summer 2015 A	7	Chester Ridge (East)	Sentinel V	Upward	14-Jul-2015	30-Jul-2015
Summer 2015 A	7	Chester Ridge (East)	RDI Workhorse	Downward	14-Jul-2015	20-Jul-2015
Summer 2015 B	8	Shoal E Swale West (=CSII-BA)	Sentinel V	Upward	13-Aug-2015	2-Sep-2015
Summer 2015 B	8	Shoal E Swale West (=CSII-BA)	RDI Workhorse	Downward	14-Aug-2015	4-Sep-2015
Summer 2015 B	8	Ridge West (CSII-BA Ridge)	Sentinel V	Upward	13-Aug-2015	2-Sep-2015
Summer 2015 B	8	Ridge West (CSII-BA Ridge)	RDI Workhorse	Downward	14-Aug-2015	24-Aug-2015
Summer 2015 B	8	Bull Ridge (East)	Sentinel V	Upward	13-Aug-2015	2-Sep-2015
Summer 2015 B	8	Bull Ridge (East)	RDI Workhorse	Downward	14-Aug-2015	5-Sep-2015
Summer 2015 B	8	Bull Swale (East)	Sentinel V	Upward	13-Aug-2015	2-Sep-2015
Summer 2015 B	8	Bull Swale (East)	RDI Workhorse	Downward	14-Aug-2015	23-Aug-2015
Fall 2015 A	10	Shoal E Swale West (=CSII-BA)	Sentinel V	Upward	30-Oct-2015	13-Nov-2015
Fall 2015 A	10	Shoal E Swale West (=CSII-BA)	RDI Workhorse	Downward	30-Oct-2015	15-Nov-2015
Fall 2015 A	10	Ridge West (CSII-BA Ridge)	Sentinel V	Upward	30-Oct-2015	9-Nov-2015
Fall 2015 A	10	Ridge West (CSII-BA Ridge)	RDI Workhorse	Downward	31-Oct-2015	7-Nov-2015

Season-Year	Deployment #	Location	Instrument	Upward or Downward	Date Start	Date End
Fall 2015 A	10	Chester Swale East	Sentinel V	Upward	29-Oct-2015	10-Nov-2015
Fall 2015 A	10	Chester Swale East	RDI Workhorse	Downward	30-Oct-2015	4-Nov-2015
Fall 2015 A	10	Chester Ridge (East)	Sentinel V	Upward	29-Oct-2015	13-Nov-2015
Fall 2015 B	10	Shoal E Swale West (=CSII-BA)	AWAC	Upward	17-Dec-2015	14-Jan-2016
Fall 2015 B	10	Chester Swale West	Aquadopp	Upward	17-Dec-2015	6-Jan-2016
Winter 2015—16	11	Shoal E Swale West (=CSII-BA)	AWAC	Upward	3-Feb-2016	29-Mar-2016
Winter 2015—16	11	Shoal E Swale West (=CSII-BA)	RDI Workhorse	Downward	3-Feb-2016	19-Feb-2016
Winter 2015—16	11	Ridge West (CSII-BA Ridge)	Sentinel V	Upward	3-Feb-2016	27-Feb-2016
Winter 2015—16	11	Ridge West (CSII-BA Ridge)	RDI Workhorse	Downward	3-Feb-2016	10-Feb-2016
Winter 2015—16	11	Bull Swale (East)	Sentinel V	Upward	2-Feb-2016	28-Feb-2016
Winter 2015—16	11	Bull Swale (East)	RDI Workhorse	Downward	3-Feb-2016	13-Feb-2016
Summer 2016 A	12	Shoal E Swale West (=CSII-BA)	AWAC	Upward	20-Jul-2016	5-Aug-2016
Summer 2016 A	12	Shoal E Swale West (=CSII-BA)	RDI Workhorse	Downward	ND	ND
Summer 2016 A	12	Ridge West (CSII-BA Ridge)	Sentinel V	Upward	22-Jul-2016	5-Aug-2016
Summer 2016 A	12	Ridge West (CSII-BA Ridge)	RDI Workhorse	Downward	20-Jul-2016	23-Jul-2016
Summer 2016 A	12	Chester Swale East	Sentinel V	Upward	20-Jul-2016	5-Aug-2016
Summer 2016 A	12	Chester Swale East	RDI Workhorse	Downward	20-Jul-2016	23-Jul-2016
Summer 2016 A	12	Chester Swale West	Sentinel V	Upward	20-Jul-2016	5-Aug-2016
Summer 2016 A	12	Chester Swale West	RDI Workhorse	Downward	20-Jul-2016	24-Jul-2016
Summer 2016 B	13	Shoal E Swale West (=CSII-BA)	AWAC	Upward	30-Sep-2016	4-Nov-2016

Table A-2. List of towed-ADCP deployments during the study for the northern transect (control at Chester Shoal) and southern transect (CSII-BA to Shoal E) with date of towed transect.
See Figure 2-1 for location and specifics of transects.

Location	Date
Northern Transect	18-Oct-13
Northern Transect	16-Jun-14
Northern Transect	17-Dec-14
Northern Transect	1-Apr-15
Northern Transect	17-Jun-15
Southern Transect	24-Sep-13
Southern Transect	17-Jun-14
Southern Transect	15-Dec-14
Southern Transect	22-Mar-15
Southern Transect	4-Jun-15

Appendix B: Derivation of the Ursell Number

The Ursell number, Ur, may be thought of as the ratio between the amplitudes of the secondary-order, $\eta_2 = (3\epsilon^2)/(4h\kappa^3)\cos 2\theta$, and the leading-order, $\eta_1 = \epsilon h \cos\theta$, Stokes free surface elevation solutions to the Korteweg-deVries equation for progressive, sinusoidal waves, where $\epsilon = a/h$ is considered $\ll 1$, $\theta = \kappa x - \omega t$, and ω is the short-wave radian frequency (Doering and Bowen 1986 equation following Fig. 6; see also Whitham 1999 section 13.13). In such case, Ur is given by:

$$Ur = \frac{|\eta_2|_{max}}{|\eta_1|_{max}} = \frac{3}{4}\frac{a}{h}\frac{1}{(\kappa h)^2} \tag{B-1}$$

After accounting for the wave amplitude in terms of the sea-swell significant wave height (H_{SGW}) as $a = \sqrt{2}H_{SGW}/4$ (Holthuijsen 2007 equation 4.2.26), and considering that $\omega^2 = g\kappa\tanh(\kappa h)$, with $\omega = 2\pi/T_p$ (Guo 2002), Ur reads:

$$Ur = \alpha\frac{H_{SGW}}{h}\left(\frac{L}{h}\right)^2 \tag{B-2}$$

with $\alpha = (3\sqrt{2})/(64\pi^2) \approx 0.0067$. Although a more recent parameterization that performs better for intermediate water waves has been proposed (Beji 1995), we preferred the original formulation to include Ur in the surf-beat similarity parameterization. In such case, $0 < Ur < O(1)$ and $0 < \xi_{surfbeat} < O(1)$, and both lower and upper bounds relate to the same regimes: deep-water (frequency dispersive) and shallow-water (amplitude dispersive) waves, respectively.

Appendix C: Spectral Parameters of the Wave Field

The SGWs (sea-swell) significant wave heights, $H_{m0,SGW}$, were quantified for each spectrum of water level as (Holthuijsen 2007 equation 4.2.24):

$$H_{m0,SGW} \approx 4\sqrt{m_{0,SGW}} \tag{C-1}$$

with $m_{0,SGW}$ as the SGWs (sea-swell) zeroth-moment of the spectrum defined by (Thomson and Emery 2014 equation 5.121):

$$m_{0,SGW} = \int_{0.05\,Hz}^{0.3\,Hz} S(f)df \tag{C-2}$$

where df is the frequency resolution of the power spectrum $S(f)$, $S(f)$ represents the spectral density (in m²/Hz) at the frequency f (in Hz) given by the one-sided spectrum of pressure data x as (Thomson and Emery 2014 section 5.6.3):

$$S(f) = \frac{2}{N\Delta t}[X^*(f)X(f)] \tag{C-3}$$

where N is the number of elements of the time series x, Δt is the time resolution, "*" denotes complex conjugation, and X is the Fourier transform of the pressure data (Thomson and Emery 2014 equation 5.27).

The LGWs significant wave heights H_{LGW} were calculated using aforementioned expressions for the LGW frequency range. We subsequently dropped subindices "$m0$" for clarity, so $H_{m0,SGW} \equiv H_{SGW}$ and $H_{m0,LGW} \equiv H_{LGW}$. The peak periods T_p were calculated as the inverse of the frequency at which $S(f)$ were maxima. The peak directions D_p corresponded to directions with maximum spectral density at peak frequencies f_p in the directional spectrum calculated by the Iterative Maximum Likelihood Method (Benoît et al. 1997).

Appendix D: Statistical Inference About Two Time Series

Given that sample sizes were large ($N > 40$), a test statistic value z that compares the means of two pair of datasets (e.g., inner and outer reflection coefficients R^2) was calculated as (Devore and Berk 2012 equation 10.1):

$$z = \frac{\overline{R^2_{inner}} - \overline{R^2_{outer}}}{\sqrt{\frac{s^2_{inner}}{N_{inner}} + \frac{s^2_{outer}}{N_{outer}}}} \tag{D-1}$$

with N_{inner} as the number of samples at the inner swale, s_{inner} as the standard deviation of R^2_{inner} values, and overbar indicating averaging. Even if distributions were not normal in all experiments, the difference between means can be considered as normally distributed regardless of the population distributions (Devore and Berk 2012).

Similarly, we tested correlation coefficients for statistical significance at the 99% using (Bendat and Piersol 2010 equation 4.61):

$$\left[-z_{\alpha/2} < \frac{\sqrt{N-3}}{2} \ln\left(\frac{1+r_{xy}}{1-r_{xy}}\right) < z_{\alpha/2} \right] \tag{D-2}$$

where $z_{\alpha/2}$ was the standardized normal variable at level of significance $\alpha/2$ (for a two-tailed test), N was the number of samples, and r_{xy} was the correlation coefficient between variables x and y. This test used the nearly normal function of r_{xy} $w = 0.5 \ln\left[(1 + r_{xy})/(1 - r_{xy})\right]$ to test its significance (see Bendat and Piersol 2010 section 4.6.1 for details). Values outside of the interval given by Equation D-2 indicate statistical correlation between x and y at the α level of significance.

The wavelet coherence, $WTC_n(s)$, indicated the cross correlation between time series x_1 and x_2 both in time and frequency and was given by (Torrence and Webster 1999 their appendix):

$$WTC_n(s) = \frac{\left|\langle s^{-1} W_n^{(12)}(s)\rangle\right|^2}{\langle s^{-1}|W_n^{(1)}(s)|^2\rangle \langle s^{-1}|W_n^{(2)}(s)|^2\rangle} \tag{D-3}$$

where $W_n^{(1)}(s)$ and $W_n^{(2)}(s)$ were the wavelet transforms of x_1 and x_2, respectively, $W_n^{(12)}(s)$ was the cross-wavelet spectrum, s was the scale, n was the time index, and $\langle \ldots \rangle$ represents smoothing in time and scale. The phase difference per scale between time series, $\phi_n(s)$ reads:

$$\phi(s) = \arctan\left\{ \frac{\Im[\langle s^{-1} W_n^{(12)}(s)\rangle]}{\Re[\langle s^{-1} W_n^{(12)}(s)\rangle]} \right\} \tag{D-4}$$

Statistical confidence of the wavelet coherence values was calculated by means of Monte Carlo simulations by Grinsted et al. (2004) methodology.

Appendix E: Spatial Evolution of Wave Energy

Assuming waves propagated across the shoal, the bulk LGW energy flux evolution in space, $\partial F / \partial x$ may be modeled as (Komen et al. 1994; Herbers et al. 2000; Ardhuin et al. 2001):

$$\frac{\partial F}{\partial x} = S \tag{E-1}$$

where $F(x) = \int_{f_{min}}^{50\ mHz} df\ \mathcal{F}(f, x)$, $\mathcal{F}(f, x) = C_g \mathcal{S}(f, x)$, $\mathcal{S}(f, x)$ was the spectral density at frequency f and location across shoal x, and $S = S_{nl} + S_{dis,bf}$ represented the sum of bulk LGW source terms (nonlinear interactions and dissipation by bottom friction). A discrete version for the difference in net LGW energy flux between swales, ΔF_{LGW} may read (Elgar et al. 1997):

$$\frac{\Delta F_{LGW}}{\Delta x} \approx \bar{S} \tag{E-2}$$

with $\Delta F_{LGW} = F_{LGW,inner} - F_{LGW,outer}$ and $F_{LGW} = h \int_{f_{min}}^{50\ mHz} Co_{PV} df$ (cf. Sheremet et al. 2002 section b.3) $\Delta x \approx 1.6\ km$, and $\bar{S} = (S_{inner} + S_{outer})/2$. The bulk source term related to bottom dissipation, $S_{dis,bf}$, reads (Madsen et al. 1988; Ardhuin et al. 2001):

$$S_{dis,bf} = \int_{f_{min}}^{50\ mHz} df \left\{ -\frac{1}{2g} f_w u_{br} \left[\frac{2\pi f}{\sinh(\kappa h)} \right]^2 \mathcal{S}(f) \right\} \tag{E-3}$$

with the bulk wave orbital velocity $u_{br} = \left\{ \int_{f_{min}}^{f_{max}} df \left[\frac{8\pi^2 f^2}{\sinh^2(\kappa h)} \mathcal{S}(f) \right] \right\}^{1/2}$, and f_w as a total friction factor (cf. Ardhuin et al. 2001 their appendix A). Similarly, the bulk source term representing the triad interactions involving LGWs, S_{nl} was calculated as (Herbers et al. 2000; de Bakker et al. 2015):

$$S_{nl} = \int_{f_{min}}^{50\ mHz} df\ \Im \left\{ \frac{3\pi f}{h} \left(\int_{f_{min}}^{f} df'\ \mathcal{B}(f', f - f') - 2 \int_{f_{min}}^{f_{max}} df'\ \mathcal{B}(f', f) \right) \right\} \tag{E-4}$$

where $\mathcal{B}(f_1, f_2) = E[X(f_1) X(f_2) X^*(f_1 + f_2)]$ represented the bispectrum, and $X(f)$ was the Fourier transform of x. We quantified the bispectrum for hourly data (to capture the tidal variability) with 75% overlapping (see Table E-1). We averaged each bispectral value over contiguous frequencies using squares of five elements of side (Elgar and Guza 1985). Degrees of freedom, DOF, were calculated as $DOF = 4 \times 25 \times N_{tot,b}$, with $N_{tot,b} = N_b + 3(N_b - 1)$, $N_b = \lfloor N/N_{elem} \rfloor$, and $N_{elem} = 512$. Positive values of S_{nl} represent bulk energy transfer to LGWs by sum (positive term in Equation E-4) and difference interactions (negative term in E-4). See de Bakker et al. (2015) and references therein.

Finally, the spatial change in short-wave energy fluxes, $\Delta F_{SGW}/\Delta x$ was calculated as

$$\frac{\Delta F_{SGW}}{\Delta x} = \left(F_{SGW,inner} - F_{SGW,outer} \right)/\Delta x \tag{E-5}$$

with $F_{SGW} = C_g E$, $C_g = 0.5\omega_p/\kappa(1 - 2\kappa h/\sinh 2\kappa h)$ and $E = H_{SGW}^2/16$.

Table E-1. Details of the bispectral calculation for each experiment.
DOFs: degrees of freedom (Elgar and Guza 1985; see also Thomson and Emery 2014 section 5.4.6).

Experiment	Swale	Number of elements	DOFs
Fall 2013	Inner	1,200	500
Fall 2013	Outer	2,048	2,900
Spring 2014	Inner	2,400	1,300
Spring 2014	Outer	2,400	1,300
Fall 2014	Inner	7,200	5,300
Fall 2014	Outer	2,400	1,300

References for Appendices

Ardhuin F, Herbers THC, O'Reilly WC. 2001. A hybrid Eulerian–Lagrangian model for spectral wave evolution with application to bottom friction on the continental shelf. Journal of Physical Oceanography 31(6): 1498-1516. doi:10.1175/1520-0485(2001)031<1498:Ahelmf>2.0.Co;2.

Beji S. 1995. Note on a nonlinearity parameter of surface waves. Coastal Engineering 25(1): 81-85. doi.org/10.1016/0378-3839(94)00031-R.

Bendat JS, Piersol AG. 2010. Random data: analysis and measurement procedures. 4th ed. Hoboken, NJ: John Wiley & Sons.

Benoît M, Frigaard P, Schäffer HA. 1997. Analysing multidirectional wave spectra: A tentative classification of available methods. In: Mansard E, editor. Proceedings of the 27th IAHR Congress on Multidirectional Waves and their Interaction with Structures (10-15 August 1997); San Francisco, CA. Canadian Government Publishing.

de Bakker ATM, Herbers THC, Smit PB, Tissier MFS, Ruessink BG. 2015. Nonlinear infragravity–wave interactions on a gently sloping laboratory beach. Journal of Physical Oceanography 45(2): 589-605. doi:10.1175/jpo-d-14-0186.1.

Devore JL, Berk KN. 2012. Modern mathematical statistics with applications. 2nd ed. New York, NY: Springer.

Doering JC, Bowen AJ. 1986. Shoaling surface gravity waves: A bispectral analysis. In: Coastal Engineering Proceedings, 20th International Conference in Coastal Engineering, January 1986; 150-162 p.

Elgar S, Guza RT. 1985. Observations of bispectra of shoaling surface gravity waves. Journal of Fluid Mechanics 161: 425-448. doi:10.1017/S0022112085003007.

Elgar S, Guza RT, Raubenheimer B, Herbers THC, Gallagher EL. 1997. Spectral evolution of shoaling and breaking waves on a barred beach. Journal of Geophysical Research: Oceans 102(C7): 15797-15805. doi.org/10.1029/97JC01010.

Grinsted A, Moore JC, Jevrejeva S. 2004. Application of the cross wavelet transform and wavelet coherence to geophysical time series. Nonlinear Processes in Geophysics 11(5/6): 561-566. doi:10.5194/npg-11-561-2004.

Guo J. 2002. Simple and explicit solution of wave dispersion equation. Coastal Engineering 45: 71-74.

Herbers THC, Russnogle NR, Elgar S. 2000. Spectral energy balance of breaking waves within the surf zone. Journal of Physical Oceanography 30(11): 2723-2737. doi:10.1175/1520-0485(2000)030<2723:Sebobw>2.0.Co;2.

Holthuijsen LH. 2007. Waves in Oceanic and Coastal Waters. 1st ed. New York, NY: Cambridge University Press.

Komen GJ, Cavaleri L, Donelan M, Hasselmann K, Hasselmann S, Janssen P. 1994. Dynamics and modelling of ocean waves. New York, NY: Cambridge University Press. https://www.cambridge.org/core/books/dynamics-and-modelling-of-ocean-waves/767155B50D6E29B0F62729F29C2DE124.

Madsen O, Poon Y-K, Graber H. 1988. Spectral wave attenuation by bottom friction: Theory. In: Coastal Engineering Proceedings 1 (21): 34.

Sheremet A, Guza RT, Elgar S, Herbers THC. 2002. Observations of nearshore infragravity waves: Seaward and shoreward propagating components. Journal of Geophysical Research: Oceans 107 (C8, 3095). doi10.1029/2001JC000970(C8). doi.org/10.1029/2001JC000970.

Thomson RE, Emery WJ. 2014. Data analysis methods in physical oceanography. 3rd ed. Waltham, MA: Elsevier.

Torrence C, Webster PJ. 1999. Interdecadal changes in the ENSO-monsoon system. Journal of Climate 12: 2679-2690.

Whitham G. 1999. Linear and nonlinear waves. New York, NY: Wiley-Interscience. https://onlinelibrary.wiley.com/doi/abs/10.1002/9781118032954.fmatter.

U.S. Department of the Interior (DOI)

DOI protects and manages the Nation's natural resources and cultural heritage; provides scientific and other information about those resources; and honors the Nation's trust responsibilities or special commitments to American Indians, Alaska Natives, and affiliated island communities.

Bureau of Ocean Energy Management (BOEM)

BOEM's mission is to manage development of U.S. Outer Continental Shelf energy and mineral resources in an environmentally and economically responsible way.

BOEM Environmental Studies Program

The mission of the Environmental Studies Program is to provide the information needed to predict, assess, and manage impacts from offshore energy and marine mineral exploration, development, and production activities on human, marine, and coastal environments. The proposal, selection, research, review, collaboration, production, and dissemination of each of BOEM's Environmental Studies follows the DOI Code of Scientific and Scholarly Conduct, in support of a culture of scientific and professional integrity, as set out in the DOI Departmental Manual (305 DM 3).